

Wavelet Based Damage Detection in Civil Structures Subjected to Earthquake Loads

By

LUIS ROBERTO VELÁZQUEZ CARRASQUILLO

A thesis submitted in partial fulfillment of
the requirements for the degree of

**MASTER OF SCIENCE
IN
CIVIL ENGINEERING**

**UNIVERSITY OF PUERTO RICO
MAYAGUEZ CAMPUS
2011**

Approved by:

Luis E. Suárez, Ph.D.
Member, Graduate Committee

Date

José A. Martínez Cruzado, Ph.D.
Member, Graduate Committee

Date

Luis A. Montejo, Ph.D.
President, Graduate Committee

Date

Omar Colón, Ph.D.
Representative of Graduate School

Date

Ismael Pagán Trinidad, M.S.
Chairman of Civil Engineering and Surveying Department

Date

ABSTRACT

During a seismic event, structural damage may result from the vibration of the structure in response to ground shaking at its foundation. The assessment of structural damage after a seismic event is required to identify unsafe structures. However, a comprehensive application of localized damage detection methods to a complex structure is a lengthy and expensive assignment that can even become dangerous in the case of post-earthquake inspections. Current efforts have focused on the possibility of real time (or near real-time) damage identification from the examination of the dynamic response of the structure. Analysis of the structural response registered during the earthquake is performed using advanced mathematical tools (like the Wavelet or Hilbert-Huang Transforms) that allow for simultaneous time frequency examination. The occurrence of damage is then associated with any changes in the instantaneous frequency (IF) or singularities in the high frequency response. Unfortunately, most of the proposed methodologies have been validated through numerical models in which the hysteretic and non-linear behavior proper of the elements of a civil structure is misrepresented by assuming linear or multi-linear behavior at most. In this research we evaluate the application of wavelet based methods for damage identification of reinforced concrete structures subjected to seismic loads. Evaluation of the methods is performed using state-of-the-art nonlinear-fiber-based models capable of replicating the actual nonlinear hysteretic response of reinforced concrete members. It was found that application of such techniques is largely limited by the high frequency content of the excitation and the modeling assumptions. Methodology refinements are proposed to ameliorate these problems.

RESUMEN

Durante un evento sísmico, la vibración de la estructura en respuesta al suelo que vibra en sus cimientos puede ocasionar daños en esta. La evaluación de los daños estructurales después de un evento sísmico es necesaria para poder identificar estructuras vulnerables. Sin embargo, una inspección completa usando métodos localizados para identificar los daños en una estructura compleja es una tarea larga y costosa que incluso puede llegar a ser peligrosa en el caso de las inspecciones después de un terremoto. Los esfuerzos actuales se han centrado en la posibilidad de identificar los daños en tiempo real (o casi en tiempo real) a partir del análisis de la respuesta dinámica de la estructura. El análisis de la respuesta estructural registrado durante el terremoto se realiza utilizando herramientas matemáticas avanzadas (como las transformadas de Wavelet o Hilbert-Huang) que permiten la exploración simultánea en el dominio de la frecuencia y el tiempo. La ocurrencia de daños es entonces asociada con cambios en la frecuencia instantánea (IF, por sus siglas en inglés) o con singularidades en las frecuencias altas de la respuesta. Desafortunadamente, la mayoría de las metodologías propuestas han sido validadas a través de modelos numéricos en los que se tergiversó el comportamiento histerético y no-lineal propios de los elementos de una estructura civil, asumiendo un comportamiento lineal o multi-lineal. En esta investigación se evalúa la aplicación de métodos basados en la transformada Wavelet para la identificación de daños en estructuras de hormigón armado sometidos a cargas sísmicas. La evaluación de los métodos se realiza utilizando modelos no lineales a base de fibras capaces de reproducir la respuesta real histerética no lineal de elementos de hormigón armado. Se encontró que la aplicación de estas técnicas es en gran medida limitada por el contenido de altas frecuencias en la excitación y las suposiciones en la modelación. Refinamientos a las metodologías actuales son propuestos para aminorar estos problemas.

Dedicated to my family...

My Mother: Gloria Carrasquillo Hernández

My Father: Luis R. Velázquez Rodríguez

My Sister: Glorimar Velázquez Carrasquillo

ACKNOWLEDGMENTS

First of all, I want to thank God for blessing me every day. All this research experience would not have been accomplished without him.

I would like to express my gratitude to my advisor, Dr. Luis A. Montejo for all his support, advice and guidance during this research. More than my advisor, I consider him a true friend.

Also, I want to thanks my graduate committee, Dr. Luis E. Suárez, Dr. José A. Martínez Cruzado, Dr. Omar Colón and Ismael Pagán Trinidad for taking the time to review this manuscript.

I would like to thank the Puerto Rico Strong Motion Program under the Civil Engineering and Surveying Department of the University of Puerto Rico at Mayaguez under the direction of Dr. José A. Martínez Cruzado for the support to this research.

I would like to thank the administrative staff, Myriam Henández from the Civil Engineering Department and Glorimer Torres from the Puerto Rico Strong Motion Program for their help on the administrative affairs.

I want to thank my family, especially my mother, for their unconditional support, prayers and blessings since without them this research would not have been carried out at all.

TABLE OF CONTENTS

ABSTRACT.....	ii
RESUMEN.....	iii
DEDICATION.....	iv
ACKNOWLEDGMENTS.....	v
TABLE OF CONTENTS.....	vi
LIST OF FIGURES.....	x
LIST OF TABLES.....	xvii

CHAPTER I..... 1

INTRODUCTION.....	1
1.1 Problem Statement	1
1.2 Justification	2
1.3 Hysteresis models used in this research.....	3
1.3.1 Introduction.....	3
1.3.2 Bilinear model.....	4
1.3.3 Hysteretic – “Takeda” like model.....	5
1.3.4 Fiber-based model	8
1.4 Wavelet Theory	10
1.4.1 Introduction.....	10
1.4.2 Wavelet Analysis.....	11
1.4.3 Continuous Wavelet Transform (CWT).....	13
1.4.4 Discrete Wavelet Transform (DWT).....	17
1.5 Scope of the research work	18
1.6 Thesis Organization.....	19
1.6.1 Development and validation of structural models	19
1.6.2 Evaluation and calibration of wavelet parameters	19
1.6.3 The effects of modeling assumptions and load excitation characteristics on the effectiveness of current Wavelet based damage detection methodologies.....	19
1.6.4 Proposed methodology for damage detection in civil structures subjected to earthquake loads.....	19
1.7 References	20

CHAPTER II 22

DEVELOPMENT AND VALIDATION OF STRUCTURAL MODELS..... 22

2.1	Introduction	22
2.2	Development of structural models.....	23
2.2.1	Uniaxial materials.....	23
2.2.2	Sections generation	33
2.2.3	Elements generation	37
2.3	Calibration and validation of structural models.....	40
2.3.1	FL-89A.....	41
2.3.2	SL-P20	50
2.3.3	EUCENTRE.....	55
2.3.4	UCSD.....	61
2.4	Conclusions	74
2.5	References	75

CHAPTER III..... 76

EVALUATION AND CALIBRATION OF WAVELET PARAMETERS..... 76

3.1	Introduction	76
3.2	Continuous Wavelet Transform (CWT).....	77
3.3	Discrete Wavelet Transform (DWT).....	83
3.3.1	Decomposition and reconstruction of wavelets	83
3.4	Mother wavelets used on the research.....	89
3.5	Evaluation and Calibration of the CWT	91
3.6	Evaluation and Calibration of the DWT	96
3.7	Conclusions	99
3.8	References	100

CHAPTER IV 101

WAVELET BASED DAMAGE DETECTION METHODOLOGY APPLIED TO CIVIL STRUCTURES. 101

4.1	Introduction	101
4.2	Description of the Dynamic Load Excitations.....	101
4.3	Acceleration and Force-Displacement Responses	105
4.4	Evaluation of the CWT Applied to Civil Structures.....	108
4.5	Evaluation of the DWT Applied to Civil Structures.....	130
4.6	Summary of the results obtained.....	140
4.7	Conclusions	143
4.8	References	145

CHAPTER V 146

FURTHER REFINEMENTS FOR DAMAGE DETECTION IN REINFORCED CONCRETE STRUCTURES SUBJECTED TO EARTHQUAKE LOADS 146

5.1	Introduction	146
5.2	FL-89A modification	147
5.3	Dynamic Excitation Loads	147
5.4	Incremental Dynamic Analysis (IDA)	150
5.5	CWT analysis – Low and High Frequency analyzes	151
5.5.1	White Noise <20Hz	151
5.5.2	White Noise <40Hz	158
5.5.3	Loma Prieta earthquake	164
5.5.4	Whittier Narrows earthquake	170
5.6	DWT analysis – Single Decomposition	176
5.6.1	White Noise <20Hz	176
5.6.2	White Noise <40Hz	177
5.6.3	Loma Prieta earthquake	179
5.6.4	Whittier Narrows earthquake	180
5.7	DWT analysis – Wavelet Package Decomposition	182
5.8	Proposed Refinements	183
5.9	CWT analysis – High Frequency	184
5.9.1	White Noise <20Hz	184
5.9.2	White Noise <40Hz	187
5.9.3	Loma Prieta earthquake	190
5.9.4	Whittier Narrows earthquake	193
5.10	DWT analysis results with the proposed refinement	196
5.10.1	White Noise <20Hz	196
5.10.2	White Noise <40Hz	198
5.10.3	Loma Prieta earthquake	199
5.10.4	Whittier Narrows earthquake	200
5.11	Conclusions	201
5.12	References	206

CHAPTER VI 207

CONCLUSIONS AND RECOMMENDATIONS 207

6.1	Summary	207
6.2	Conclusions	208
6.3	Recommendations for future works	219

APPENDIX A..... 220

OPENSEES CODES.....220

A.1	Cantilever Circular Column: FL-89A (bilinear model) used in Chapter II.....	220
A.2	Cantilever Circular Column: FL-89A (Takeda model) used in Chapter II.....	222
A.3	Cantilever Circular Column: FL-89A (Fiber-based model) used in Chapter II.....	224
A.4	Cantilever Circular Column: SL-P20 (Fiber-based model) used in Chapter II	228
A.5	Cantilever Circular Column: EUCENTRE (Fiber-based model) used in Chapter II.....	231
A.6	Cantilever Circular Column: UCSD (Fiber-based model) used in Chapter II.....	235
A.7	Cantilever Circular Column: FL-89A (Fiber-based model) used in Chapter V	238
A.8	Build Reinforced Concrete Circular Section code.....	242
A.9	Static Reversed-Cyclic Analysis (used in Chapter II)	243
A.10	Static Cyclic Analysis Parameters (needed for the Static Reversed-Cyclic Analysis code)..	245
A.11	Dynamic Analysis (used in Chapters II, IV and V)	247
A.12	Dynamic Analysis Parameters (needed for the Dynamic Analysis code).....	249

LIST OF FIGURES

Figure 1-1: Total Horizontal earthquake forces in a building increase downward along its height. ...	2
Figure 1-2: (a) Elasto-plastic model, (b) Bilinear model, (c) Degrading Bilinear model (Otani, 2002)	4
Figure 1-3: Bilinear Hysteresis model	5
Figure 1-4: Stiffness degrading model by Takeda et al. (1970)	6
Figure 1-5: (a) No-degrading; (b) Low-Degrading: $\alpha=0.002$, $\beta=0.0015$; (c) Moderate-Degrading: $\alpha=0.0035$, $\beta=0.003$; (d) High-Degrading: $\alpha=0.005$, $\beta=0.0045$	7
Figure 1-6: Hysteretic model.....	8
Figure 1-7: Fiber-based model (Montejo 2008)	8
Figure 1-8: (a) Fiber-based Experimental Test (b) OpenSees Fiber-based model	9
Figure 1-9: (a) Experimental Test (b) OpenSees Bilinear model (c) OpenSees Hysteretic model (d) OpenSees Fiber-based model	10
Figure 1-10: (a) Representation of a Sine Wave. (b) Representation of a Wavelet (Morlet).....	11
Figure 1-11: (a) Signal in the time domain (b) Fourier spectrum.....	12
Figure 1-12: The Fourier and Inverse Fourier transform (Misiti <i>et al.</i> 2000)	13
Figure 1-13: The Wavelet and Inverse Wavelet transform (Misiti <i>et al.</i> 2000).....	14
Figure 1-14: (a) 3D plot of the wavelet coefficients, (b) Wavelet Map and (c) Instantaneous frequencies from wavelet ridges.....	16
Figure 1-15: CWT of the artificially signal at high frequencies	16
Figure 1-16: (a) Original Signal with a discontinuity, (b) DWT approximations and (c) DWT details	18
Figure 2-1: Elastic Material behavior.....	24
Figure 2-2: Steel01 Material behavior (Mazzoni, 2007)	25
Figure 2-3: Hysteretic Material behavior	26
Figure 2-4: Unconfined and Confined concrete parameters from CUMBIA (Montejo <i>et al.</i> 2007).....	28
Figure 2-5: Hysteretic model for the unconfined concrete	28
Figure 2-6: Hysteretic model for the confined concrete	29
Figure 2-7: Longitudinal Reinforcing Steel parameters (Montejo <i>et al.</i> 2007).....	30
Figure 2-8: Hysteretic model for the reinforcing steel	31
Figure 2-9: Fatigue and degradation parameters example.....	32
Figure 2-10: Example of OpenSees sections to describe force-deformation relationship (Mazzoni, 2007)	33
Figure 2-11: Group previously-defined materials to describe stress resultant section behavior	34
Figure 2-12: Fibers-based section	35
Figure 2-13: (a) Circular layer parameters (b) Circular patch parameters (Mazzoni, 2007)	36
Figure 2-14: Concentrated plasticity model (Montejo, 2008)	37
Figure 2-15: Distributed plasticity model (Montejo, 2008).....	39
Figure 2-16: Beam With Hinges Element.....	40
Figure 2-17: FL89A Geometric Properties.....	42
Figure 2-18: Cyclic Test: Displacement Loading History for FL-89A.....	43

Figure 2-19: FL-89A bilinear model generation.....	44
Figure 2-20: FL-89A hysteretic model generation	45
Figure 2-21: FL-89A fiber-based model generation.....	46
Figure 2-22: Bilinear experimental response and predictions for FL-89A	48
Figure 2-23: Hysteretic experimental response and predictions for FL-89A	49
Figure 2-24: Fiber-based experimental response and predictions for FL-89A.....	49
Figure 2-25: SL-P20 geometric properties	50
Figure 2-26: Cyclic Test: Displacement Loading History for SL-P20	51
Figure 2-27: SL-P20 fiber-based model generation.....	52
Figure 2-28: Fiber-based experimental response and predictions for SL-P20.....	54
Figure 2-29: (a) Stress-Strain for Reinforcing Steel (b) Stress-Displacement Relationship	54
Figure 2-30: EUCENTRE bridge pier geometric properties.....	55
Figure 2-31: EUCENTRE Cyclic Test: Displacement Loading History.....	56
Figure 2-32: Shaking table test: input ground motion (Morgan Hill - 1984 scaled to 1.2g PGA).....	57
Figure 2-33: EUCENTRE Fiber-based model generation	58
Figure 2-34: Fiber-based response and predictions for EUCENTRE	59
Figure 2-35: Experimental response and predicted displacement time-histories for dynamic test..	61
Figure 2-36: UCSD Geometric Properties.....	62
Figure 2-37: UCSD Cyclic Test: Displacement Loading History.....	63
Figure 2-38: UCSD Shake Table	63
Figure 2-39: UCSD Dynamic test: Acceleration time-history	64
Figure 2-40: UCSD Fiber-based Model Generation.....	65
Figure 2-41: Fiber-based simulation and CUMBIA prediction for UCSD.....	66
Figure 2-42: (a) Displacement time-histories for EQ1, (b) Acceleration time-histories for EQ1.....	68
Figure 2-43: (a) Displacement time-histories for EQ2, (b) Acceleration time-histories for EQ2.....	69
Figure 2-44: (a) Displacement time-histories for EQ3, (b) Acceleration time-histories for EQ3.....	70
Figure 2-45: (a) Displacement time-histories for EQ4, (b) Acceleration time-histories for EQ4.....	71
Figure 2-46: (a) Displacement time-histories for EQ5, (b) Acceleration time-histories for EQ5.....	72
Figure 2-47: (a) Displacement time-histories for EQ6, (b) Acceleration time-histories for EQ6.....	73
Figure 3-1: (a) Sinusoid scaling factor, (b) Wavelet.....	77
Figure 3-2: (a) Wavelet function $\psi(t)$, (b) Shifted Wavelet function $\psi(t-k)$	78
Figure 3-3: CWT Wavelet Map	80
Figure 3-4: 3D plot of the CWT	81
Figure 3-5: CWT - Low and High scales comparison (Misiti <i>et al.</i> 2000)	81
Figure 3-6: Representation of CWT High-scales to get CWT Low-Frequencies	82
Figure 3-7: Representation of CWT Low-Scales to get CWT High-Frequencies.....	83
Figure 3-8: DWT decomposition for level 1 (Misiti <i>et al.</i> 2000)	84
Figure 3-9: Schematic diagram for DWT single-decomposition.....	85
Figure 3-10: Wavelet packet decomposition tree at level 3 (Misiti <i>et al.</i> 2000)	86
Figure 3-11: Wavelet Packet Tree organized at level 3 (Misiti <i>et al.</i> 2000).....	87
Figure 3-12: Wavelet Packet Tree (WPT)	88
Figure 3-13: Fourier Spectrum for second-level decomposition of the WPT.....	88

Figure 3-14: Mother Wavelets: (a) Complex Morlet, (b) Mexican Hat, (c) Haar, (d) db8, (e) Bior6.8 (PyWavelet, 2006)*	91
Figure 3-15: 6Hz Sinusoid + Chirp (3Hz to 1Hz)	92
Figure 3-16: Mexican Hat Wavelet: (a) 3D plot, (b) CWT Wavelet Map, (c) IF from wavelet ridges..	92
Figure 3-17: Bior6.8 Wavelet: (a) 3D plot, (b) CWT Wavelet Map, (c) IF from wavelet ridges	92
Figure 3-18: Complex Morlet Wavelet: (a) 3D plot, (b) CWT Wavelet Map, (c) IF from wavelet ridges	93
Figure 3-19: 1Hz sinusoidal signal + 10% discontinuity at 4.75s	94
Figure 3-20: 1Hz sinusoidal signal + 1% discontinuity at 4.75s.....	95
Figure 3-21: 1Hz sinusoidal signal + 0.1% discontinuity at 4.75s	95
Figure 3-22: Sinusoidal with a change in frequency from 1Hz to 2Hz at t = 5 sec	97
Figure 3-23: Signal with a discontinuity of 10% at t = 4.75 sec	98
Figure 3-24: Signal with a discontinuity of 1% at t = 4.75 sec.....	98
Figure 3-25: Signal with a discontinuity of 0.1% at t = 4.75 sec	99
Figure 4-1: (a) 5Hz Tapered Sinusoid, (b) Fourier Spectrum	102
Figure 4-2: (a) White Noise with frequency content of 20Hz, (b) Fourier Spectrum	103
Figure 4-3: (a) White Noise with a frequency content of 40Hz, (b) Fourier Spectrum	103
Figure 4-4: (a) Round Valley earthquake from McGee Creek Surface Station - 11/23/1984, (b) Fourier Spectrum.....	104
Figure 4-5: Loma Prieta earthquake from Treasure Island Station - 10/17/1989: (a) Original, (b) Edited to 25 s, (c) Fourier Spectrum	104
Figure 4-6: Bilinear: Top Acceleration Responses (left) and the Force-Displacement Responses (Right)	105
Figure 4-7: Takeda: Top Acceleration Responses (left) and the Force-Displacement Responses (Right)	106
Figure 4-8: Fibers: Top Acceleration Responses (left) and the Force-Displacement Responses (Right)	107
Figure 4-9: Bilinear model: (a) Force Response, (b) Stiffness, (c) Low-Frequency Analysis, (d) IF from wavelet ridges.....	110
Figure 4-10: Hysteretic model: (a) Force Response, (b) Stiffness, (c) Low-Frequency Analysis, (d) IF from wavelet ridges.....	110
Figure 4-11: Fibers model: (a) Force Response, (b) Stiffness, (c) Low- Frequency Analysis, (d) IF from wavelet ridges.....	111
Figure 4-12: Bilinear model: (a) Force Response, (b) Stiffness, (c) High-Frequency Analysis, (d) Coefficients for 80Hz frequency	112
Figure 4-13: Hysteretic model: (a) Force Response, (b) Stiffness, (c) High-Frequency Analysis, (d) Coefficients for 80Hz frequency	113
Figure 4-14: Fibers model: (a) Force Response, (b) Stiffness, (c) High-Frequency Analysis, (d) Coefficients for 80Hz frequency	113
Figure 4-15: Bilinear model: (a) Force Response, (b) Stiffness, (c) Low-Frequency Analysis, (d) IF from wavelet ridges.....	114
Figure 4-16: Hysteretic model: (a) Force Response, (b) Stiffness, (c) Low-Frequency Analysis, (d) IF from wavelet ridges.....	115

Figure 4-17: Fibers model: (a) Force Response, (b) Stiffness, (c) Low-Frequency Analysis, (d) IF from wavelet ridges.....	115
Figure 4-18: Bilinear model: (a) Force Response, (b) Stiffness, (c) High-Frequency Analysis, (d) Coefficients for 80Hz frequency	116
Figure 4-19: Hysteretic model: (a) Force Response, (b) Stiffness, (c) High-Frequency Analysis, (d) Coefficients for 80Hz frequency	117
Figure 4-20: Fibers model: (a) Force Response, (b) Stiffness, (c) High-Frequency Analysis, (d) Coefficients for 80Hz frequency	117
Figure 4-21: Bilinear model: (a) Force Response, (b) Stiffness, (c) Low-Frequency Analysis, (d) IF from wavelet ridges.....	118
Figure 4-22: Hysteretic model: (a) Force Response, (b) Stiffness, (c) Low-Frequency Analysis, (d) IF from wavelet ridges.....	119
Figure 4-23: Fibers model: (a) Force Response, (b) Stiffness, (c) Low-Frequency Analysis, (d) IF from wavelet ridges.....	119
Figure 4-24: Bilinear model: (a) Force Response, (b) Stiffness, (c) High-Frequency Analysis, (d) Coefficients for 80Hz frequency	120
Figure 4-25: Hysteretic model: (a) Force Response, (b) Stiffness, (c) High-Frequency Analysis, (d) Coefficients for 80Hz frequency	121
Figure 4-26: Fibers model: (a) Force Response, (b) Stiffness, (c) High-Frequency Analysis, (d) Coefficients for 80Hz frequency	121
Figure 4-27: Bilinear model: (a) Force Response, (b) Stiffness, (c) Low-Frequency Analysis, (d) IF from wavelet ridges.....	122
Figure 4-28: Hysteretic model: (a) Force Response, (b) Stiffness, (c) Low-Frequency Analysis, (d) IF from wavelet ridges.....	123
Figure 4-29: Fibers model: (a) Force Response, (b) Stiffness, (c) Low-Frequency Analysis, (d) IF from wavelet ridges.....	123
Figure 4-30: Bilinear model: (a) Force Response, (b) Stiffness, (c) High-Frequency Analysis, (d) Coefficients for 80Hz frequency	124
Figure 4-31: Hysteretic model: (a) Force Response, (b) Stiffness, (c) High-Frequency Analysis, (d) Coefficients for 80Hz frequency	125
Figure 4-32: Fibers model: (a) Force Response, (b) Stiffness, (c) High-Frequency Analysis, (d) Coefficients for 80Hz frequency	125
Figure 4-33: Bilinear model: (a) Force Response, (b) Stiffness, (c) Low-Frequency Analysis, (d) IF from wavelet ridges.....	126
Figure 4-34: Hysteretic model: (a) Force Response, (b) Stiffness, (c) Low-Frequency Analysis, (d) IF from wavelet ridges.....	127
Figure 4-35: Fibers model: (a) Force Response, (b) Stiffness, (c) Low-Frequency Analysis, (d) IF from wavelet ridges.....	127
Figure 4-36: Bilinear model: (a) Force Response, (b) Stiffness, (c) High-Frequency Analysis, (d) Coefficients for 80Hz frequency	128
Figure 4-37: Hysteretic model: (a) Force Response, (b) Stiffness, (c) High-Frequency Analysis, (d) Coefficients for 80Hz frequency	129

Figure 4-38: Fibers model: (a) Force Response, (b) Stiffness, (c) High-Frequency Analysis, (d) Coefficients for 80Hz frequency	129
Figure 4-39: Bilinear model: (a) Force Response, (b) Stiffness, (c) DWT Detail analysis	131
Figure 4-40: Hysteretic "Takeda" model: (a) Force Response, (b) Stiffness, (c) Detail DWT analysis	131
Figure 4-41: Fibers model: (a) Force Response, (b) Stiffness, (c) DWT Detail analysis	132
Figure 4-42: Bilinear model: (a) Force Response, (b) Stiffness, (c) DWT Detail analysis	133
Figure 4-43: Hysteretic "Takeda" model: (a) Force Response, (b) Stiffness, (c) DWT Detail analysis	133
Figure 4-44: Fibers model: (a) Force Response, (b) Stiffness, (c) DWT Detail analysis	134
Figure 4-45: Bilinear model: (a) Force Response, (b) Stiffness, (c) DWT Detail analysis	135
Figure 4-46: Hysteretic "Takeda" model: (a) Force Response, (b) Stiffness, (c) DWT Detail analysis	135
Figure 4-47: Fibers model: (a) Force Response, (b) Stiffness, (c) DWT Detail analysis	136
Figure 4-48: Bilinear model: (a) Force Response, (b) Stiffness, (c) DWT Detail analysis	137
Figure 4-49: Hysteretic "Takeda" model: (a) Force Response, (b) Stiffness, (c) DWT Detail analysis	137
Figure 4-50: Fibers model: (a) Force Response, (b) Stiffness, (c) DWT Detail analysis	138
Figure 4-51: Bilinear model: (a) Force Response, (b) Stiffness, (c) DWT Detail analysis	139
Figure 4-52: Hysteretic "Takeda" model: (a) Force Response, (b) Stiffness, (c) DWT Detail analysis	139
Figure 4-53: Fibers model: (a) Force Response, (b) Stiffness, (c) DWT Detail analysis	140
Figure 4-54: (a) Round Valley earthquake, (b) Bilinear model, (c) Takeda model, (d) Fibers model	144
Figure 4-55: (a) Round Valley earthquake, (b) Bilinear model, (c) Takeda model, (d) Fibers model	144
Figure 5-1: FL-89A - geometric properties modification.....	147
Figure 5-2: (a) White Noise with frequency content of 20Hz, (b) Fourier Spectrum	148
Figure 5-3: (a) White Noise with frequency content of 40Hz, (b) Fourier Spectrum	148
Figure 5-4: (a) Loma Prieta earthquake from Treasure Island - 10/17/89, (b) Fourier Spectrum.	149
Figure 5-5: (a) Whittier Narrows from LA Baldwin Hills Station - 10/1/87, (b) Fourier Spectrum	149
Figure 5-6: Displacement histories for different levels of ground motion intensities.....	152
Figure 5-7: White Noise 20Hz - Incremental Dynamic Analysis (IDA Curve)	153
Figure 5-8: (a) Stress - Strain Relationship, (b) Stress-Time Relation	153
Figure 5-9: Force (left) and Acceleration (right) histories for different PGA.....	154
Figure 5-10: CWT - Low Frequency analysis	155
Figure 5-11: CWT - High Frequency analysis.....	156
Figure 5-12: CWT - High Frequency analysis showing the coefficients for 80Hz.....	157
Figure 5-13: CWT Spike Amplitude vs Ductility	157
Figure 5-14: Displacement histories for different levels of ground motion intensities.....	158
Figure 5-15: White Noise 40Hz - Incremental Dynamic Analysis (IDA curve)	159
Figure 5-16: (a) Stress - Strain Relationship, (b) Stress - Time Relation	159

Figure 5-17: Force (left) and Acceleration (right) for different levels of PGA	160
Figure 5-18: CWT - Low Frequency analysis	161
Figure 5-19: CWT - High Frequency analysis.....	162
Figure 5-20: CWT - High Frequency analysis showing the coefficients for 80Hz.....	163
Figure 5-21: CWT Spike Amplitude vs Ductility	163
Figure 5-22: Displacement histories for different levels of ground motion intensities.....	164
Figure 5-23: Loma Prieta earthquake - Incremental Dynamic Analysis (IDA curve)	165
Figure 5-24: (a) Stress-Strain Relationship, (b) Stress-Time Relation	165
Figure 5-25: Force (left) and Acceleration (right) histories for different levels of PGA.....	166
Figure 5-26: CWT - Low Frequency analysis	167
Figure 5-27: CWT - High Frequency analysis.....	168
Figure 5-28: CWT - High Frequency analysis showing the coefficients for 80Hz.....	169
Figure 5-29: CWT Spike Amplitude vs Ductility	169
Figure 5-30: Displacement histories for different levels of ground motion intensities.....	170
Figure 5-31: Loma Prieta EQ - Incremental Dynamic Analysis (IDA curve)	171
Figure 5-32: (a) Stress-Strain Relationship, (b) Stress-Time Relation	171
Figure 5-33: Force (left) and Acceleration (right) histories for different levels of PGA.....	172
Figure 5-34: CWT - Low Frequency analysis	173
Figure 5-35: CWT - High Frequency analysis.....	174
Figure 5-36: CWT - High Frequency analysis showing the coefficients for 80Hz.....	175
Figure 5-37: CWT Spike Amplitude vs Ductility	175
Figure 5-38: WN20 - Force histories (left) and DWT detail analysis (right)	176
Figure 5-39: WN20 - Maximum Peak Amplitude vs Ductility	177
Figure 5-40: WN40 - Force histories (left) and DWT detail analysis (right)	178
Figure 5-41: WN40 - Maximum Peak Amplitude vs Ductility	178
Figure 5-42: Loma Prieta EQ - Force histories (left) and DWT detail analysis (right)	179
Figure 5-43: Loma Prieta EQ - Maximum Peak Amplitude vs Ductility	180
Figure 5-44: Whittier Narrows EQ - Force histories (left) and DWT detail analysis (right).....	181
Figure 5-45: Whittier Narrows EQ - Maximum Peak Amplitude vs Ductility.....	181
Figure 5-46: WN20 - DWT Detail Decomposition (left) and the Fourier Spectrum (right).....	182
Figure 5-47: (a) CWT coefficients for 80Hz, (b) Proposed methodology, (c) Final results	184
Figure 5-48: WN20 - Force histories (left) and CWT High Frequencies (right) for different PGA... 185	
Figure 5-49: WN20 - Force histories (left) and High Frequency coefficients (right) for different PGA	186
Figure 5-50: WN20 - (a) High Frequency analysis, (b) CWT coefficients, (c) 3D plot	187
Figure 5-51: WN40 - Force histories (left) and CWT High Frequencies (right) for different PGA... 188	
Figure 5-52: WN40 - Force histories (left) and High Frequency coefficients (right) for different PGA	189
Figure 5-53: WN40 - (a) High Frequency analysis, (b) CWT coefficients, (c) 3D plot	190
Figure 5-54: Loma Prieta EQ - Force histories (left) and High Frequencies (right) for different PGA	191
Figure 5-55: Loma Prieta EQ - Force histories (left) and High Frequencies coefficients (right) for different PGA	192

Figure 5-56: Loma Prieta EQ - (a) High Frequency analysis, (b) CWT coefficients, (c) 3D plot	193
Figure 5-57: Whittier Narrows EQ - Force histories (left) and High Frequencies (right) for different PGA	194
Figure 5-58: Whittier Narrows EQ - Force histories (left) and High Frequencies coefficients (right) for different PGA	195
Figure 5-59: Whittier Narrows EQ - (a) High Frequency analysis, (b) CWT coefficients, (c) 3D plot	196
Figure 5-60: White Noise 20Hz - Force histories (left) and DWT detail (right) for different PGA...	197
Figure 5-61: White Noise 40Hz - Force histories (left) and DWT detail (right) for different PGA...	198
Figure 5-62: Loma Prieta EQ - Force histories (left) and DWT detail (right) for different PGA.....	199
Figure 5-63: Whittier Narrows EQ - Force histories (left) and DWT detail (right) for different PGA	200
Figure 5-64: EQ1 - (a) Force history, (b) CWT high frequency analysis, (c) Proposed methodology	202
Figure 5-65: EQ1 - (a) Force history, (b) CWT high frequency analysis, (c) Proposed methodology	202
Figure 5-66: EQ2 - (a) Force history, (b) CWT high frequency analysis, (c) Proposed methodology	203
Figure 5-67: EQ2 - (a) Force history, (b) DWT Detail analysis, (c) Proposed methodology	203
Figure 5-68: White Noise 20Hz - Ductility vs Period	204
Figure 5-69: White Noise 40Hz - Ductility vs Period	204
Figure 5-70: Loma Prieta earthquake - Ductility vs Period	205
Figure 5-71: Whittier Narrows earthquake - Ductility vs Period	205
Figure 6-1: WN20 (PGA ₄): (a) Acceleration, (b) Force, (c) CWT low-freq, (d) CWT high freq, (e) DWT detail	211
Figure 6-2: WN20 (PGA ₇): (a) Acceleration, (b) Force, (c) CWT low-freq, (d) CWT high freq, (e) DWT detail	212
Figure 6-3: WN40 (PGA ₄): (a) Acceleration, (b) Force, (c) CWT low-freq, (d) CWT high freq, (e) DWT detail	213
Figure 6-4: WN40 (PGA ₇): (a) Acceleration, (b) Force, (c) CWT low-freq, (d) CWT high freq, (e) DWT detail	214
Figure 6-5: EQ1 (PGA ₄): (a) Acceleration, (b) Force, (c) CWT low-freq, (d) CWT high freq, (e) DWT detail	215
Figure 6-6: EQ1 (PGA ₇): (a) Acceleration, (b) Force, (c) CWT low-freq, (d) CWT high freq, (e) DWT detail	216
Figure 6-7: EQ2 (PGA ₄): (a) Acceleration, (b) Force, (c) CWT low-freq, (d) CWT high freq, (e) DWT detail	217
Figure 6-8: EQ2 (PGA ₇): (a) Acceleration, (b) Force, (c) CWT low-freq, (d) CWT high freq, (e) DWT detail	218

LIST OF TABLES

Table 2-1: Elastic material parameters	23
Table 2-2: Steel01 material parameters	24
Table 2-3: Hysteretic material parameters.....	26
Table 2-4: OpenSees Concrete01 material parameters	27
Table 2-5: Reinforcing Steel parameters	30
Table 2-6: Aggregator Section parameters.....	34
Table 2-7: Fibers Section Parameters	35
Table 2-8: Nonlinear Beam-Column Parameters	38
Table 2-9: Beam With Hinges Parameters	39
Table 2-10: Numerical vs Experimental positive and negative peak displacements.....	61
Table 2-11: Ground motions induced to the UCSD bridge pier	64
Table 2-12: Numerical vs Experimental positives and negatives peak displacements.....	74
Table 2-13: Numerical vs Experimental positives and negatives peak ground accelerations	74
Table 3-1: Summary of the Wavelets and Associated Parameters	89
Table 4-1: Ground Motions.....	103
Table 4-2: Frequencies after the dynamic load excitation was applied in Hz.....	109
Table 4-3: Summary of the CWT Low Frequencies analysis results for each model.....	141
Table 4-4: Summary of the CWT High Frequencies analysis results for each model.....	142
Table 4-5: Summary of the DWT detail analysis results for each model.....	142
Table 5-1: PGA for each dynamic excitation load.....	150

CHAPTER I

INTRODUCTION

1.1 Problem Statement

Earthquakes are natural phenomena that directly affect mankind, having a great impact in our lives. Most global cities have at least tripled their populations in the last hundred years, so it is quite likely that a major earthquake hitting close to a city could collapse structures such as power plants, skyscrapers, factories and bridges. Earthquakes have the power to uproot trees and send them crashing into buildings, but also they can trigger landslides and avalanches, and cause flooding and tsunamis (TQ, 2000). Moreover, violent earthquakes often cause structures to collapse, burying people underneath. An earthquake can cause devastation that continues for years after the first impact. An example is the earthquake occurred at Managua, Nicaragua, in 1972. After the event, a series of severe earthquakes hit the city. Fifteen years later, the city looked very similar as a week after the earthquake, because the country did not have the money necessary to rebuild (TQ, 2000).

During a seismic event, structural damage may result from the vibration of the structure in response to ground shaking at its foundation. Earthquake shaking generates inertia forces in the building, which are proportional to the building mass. Since most of the building mass is present at floor levels, earthquakes-induced inertia forces primarily develop at the floor levels. These forces travel downwards through slab and beams to the columns and walls, and then to the foundations from where they are dispersed to the ground. As inertia forces accumulates downwards from the top of the building, the columns and walls at lower level floors experiences higher earthquake-induced forces (Murty, 2005), see Figure 1-1.

Over the last decades different methods to identify damage in Reinforced Concrete (RC) structures have been developed. There are visual and localized experimental damage-detection methods (such as acoustic, ultrasonic, magnetic or thermal methods) that are capable of identify and determine the extent of damage, but an effective application of these techniques require previous knowledge of the damage location and its spot to be easily accessed. Also, application of these techniques are lengthy and expensive assignments that many times are too difficult to carry out. Current efforts have focused on the possibility of real time (or near real-time) damage identification from the examination of the dynamic response of the structure.



Figure 1-1: Total Horizontal earthquake forces in a building increase downward along its height.

1.2 Justification

Puerto Rico is located in a zone with very high seismic activity, and therefore essential structures such as factories, hospitals, schools, and bridges must be able to withstand the events of a large earthquake. However, many times the structures will experience some level of damage during an earthquake and it is essential to examine the condition in that the structure remained to appreciate the extent of damage, and look for possible solutions. Moreover, after a large earthquake occurs the assessment of structural damage is required to identify unsafe structures (to be evacuated and close down) and safe structures (that eventually may serve as temporal shelters). Nevertheless, a visual inspection of all the structures affected by the earthquake is a lengthy and dangerous task due to the chaotic environment and the eminent risk of an aftershock. A system capable of remotely examine

the health of the affected structures is then highly desirable. This research is focused on methodologies based on the analysis of the nonlinear/nonstationary characteristics of the dynamic response of the structure. In this type of approaches the analysis of the structural response registered during the earthquake is performed using advanced mathematical tools (like the Wavelet or Hilbert-Huang Transforms) that allow for simultaneous time frequency examination. The occurrence of damage is then associated with any changes in the instantaneous frequency (IF) or singularities in the high frequency response. Unfortunately, most of the proposed methodologies have been validated through numerical models in which the hysteretic and non-linear behavior proper of the elements of a civil structure is misrepresented by assuming linear or multi-linear behavior at most. The main objective of this research is to develop a damage identification technique that can be implemented in the damage identification of reinforced concrete structures subjected to seismic loads. Validation and calibration of the proposed technique will be performed through the use of state-of-the-art nonlinear-fiber-based models.

1.3 Hysteresis models used in this research

1.3.1 Introduction

In the last two decades a large number of hysteresis models have been developed that can predict reasonably well the hysteretic response of RC members. Structures subjected to strong earthquake excitation are designed to dissipate energy by inelastic material behavior, interface friction, etc. However, under repeated cyclic deformations there is invariably deterioration in the characteristics of such hysteretic behavior. Such deterioration must be taken into account in the modeling and design of seismic-resistant structural systems (Mettupalayam and Reinhorn, 2000). For this reason, the dynamic inelastic response of RC structures requires realistic models that can simulate strength, stiffness, and energy-dissipation characteristics of members as well as strength and stiffness degradation.

On this research, it is essential to model the structure in detail because we need to represent the actual behavior that would have the structure when is subjected to an

earthquake excitation. Therefore, the use of different non-linear structural models will be considered (from simpler models to more complex). Models will be implemented in the OpenSees platform. Moreover, they will be compared and evaluated to know the effects that each model assumption has on the efficacy of the damage methodology that will be developed. The different models that will be evaluated, in ascending complexity order, are the bilinear model, the hysteretic model (i.e. Takeda) and the fiber-based model.

1.3.2 Bilinear model

At the initial development stage of nonlinear dynamic analysis, the elastic-perfectly plastic hysteretic model ("elasto-plastic model") was used by many investigators because the model was simple (Figure 1-2a). The response point moves on the elastic stiffness line before the yield stress is reached. After yielding, the response point moves on the perfectly plastic line until unloading takes place. Upon unloading, the response point moves on the line parallel to the initial elastic line (Otani, 1980). In the bilinear model a finite positive slope was assigned to the post yield stiffness to account for the strain-hardening characteristic (Figure 1-2b). Unloading stiffness after yielding is equal to the initial elastic stiffness. The stiffness and strength degradation within elastic deformation and energy dissipation during small amplitude oscillation are not considered in the model (Otani, 1980). Neither the elasto-plastic model nor the bilinear model represents the degradation of loading and unloading stiffnesses with increasing displacement amplitude reversals, therefore these models are not suited for a refined nonlinear analysis of a reinforced concrete structure. A degrading bilinear model is displayed in Figure 2-1c (Otani, 2002).

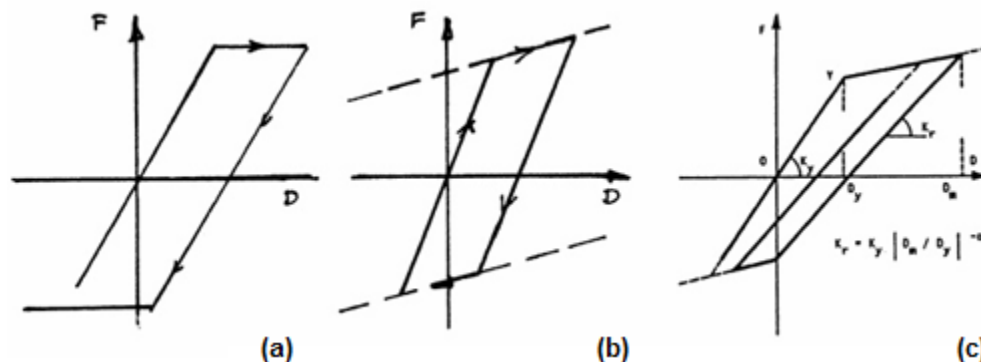


Figure 1-2: (a) Elasto-plastic model, (b) Bilinear model, (c) Degrading Bilinear model (Otani, 2002)

To implement the bilinear model in OpenSees some parameters are needed such as the effective stiffness (El_{eff}) and the strain-hardening ratio (b , for the positive slope). For RC members these parameters are calculated based on the results of moment-curvature analyses ($M-C$). In this research we will use the computer code CUMBIA (Montejo and Kowalsky, 2007) to obtain the theoretical monotonic $M-C$ response of the RC section. The effective stiffness is calculated as the slope of the line from the origin to the point in the $M-C$ curve that corresponds to first yield of the longitudinal steel. The response of the OpenSees bilinear model compared with an experimental test result of a reinforced concrete column is shown in Figure 1-3.

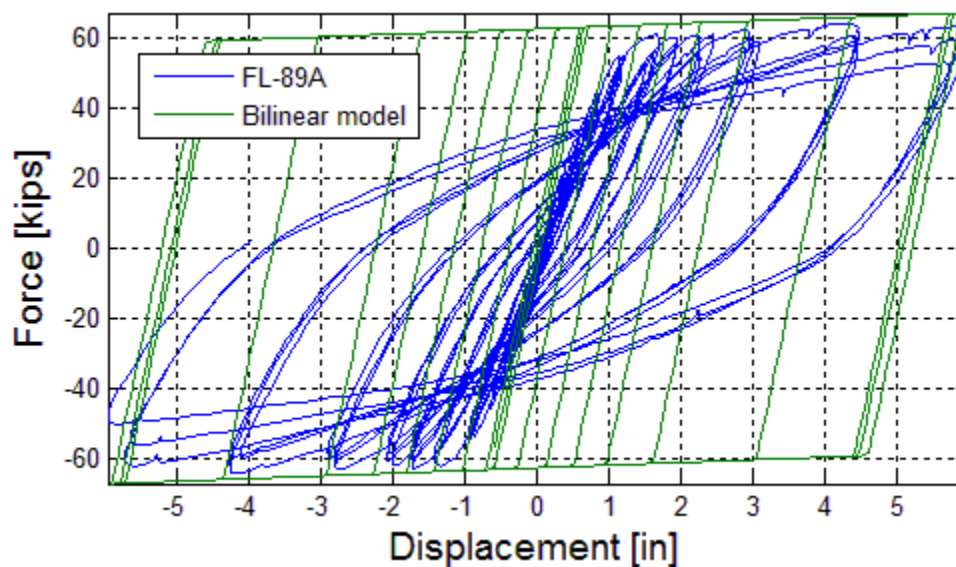


Figure 1-3: Bilinear Hysteresis model

1.3.3 Hysteretic – “Takeda” like model

An improved degrading stiffness model was developed by Takeda *et al.* (1970) on the basis of experimental observation (Otani, 1980). Figure 1-4 illustrates the basic features of the Takeda *et al.* model, which is applicable to RC members with stable hysteresis loops under constant axial load. The model included (a) stiffness changes at flexural cracking and yielding, and also strain-hardening characteristics utilizing a trilinear skeleton force-deformation relationship, (b) hysteresis rules for inner hysteresis loops inside the outer loop; i.e., the response point during loading moves toward a peak of the immediately outer

hysteresis loop, and (c) unloading stiffness degradation with a maximum deformation amplitude (Kabeyasawa *et al.* 1983).

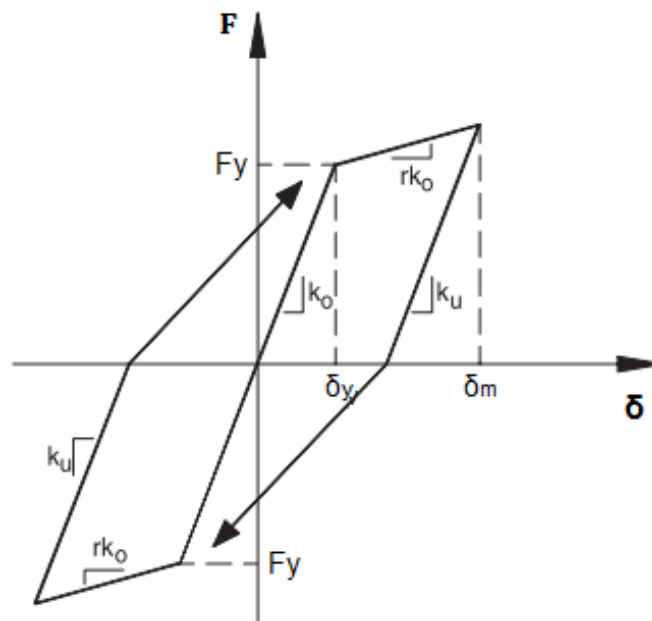


Figure 1-4: Stiffness degrading model by Takeda *et al.* (1970)

Degrading systems were modeled using the *Hysteresis* material in the OpenSees (2009) analysis platform. The parameters required for this material will be adjusted to emulate the Takeda model. Strength and stiffness degradation due to both ductility and energy dissipation were specified in the model. In OpenSees, α is the parameter used in the *Hysteresis* material to represent the damage due to ductility whereas the parameter β is used to symbolize damage due to energy dissipation (Erduran and Kunnath, 2010). The range values for these parameters are 0 - 0.5 for α and 0 - 0.6 for β (Silva, 2010). Figure 1-5 shows the resulting force-deformation behavior (or degradation magnitude) by changing the parameters α and β . It is shown that increasing α decrease the unloading stiffness and increasing β increases the reloading stiffness. The significant parameters in the force-deformation relationship such as the initial stiffness, yield moment and yield curvature are determined through section M-C analysis.

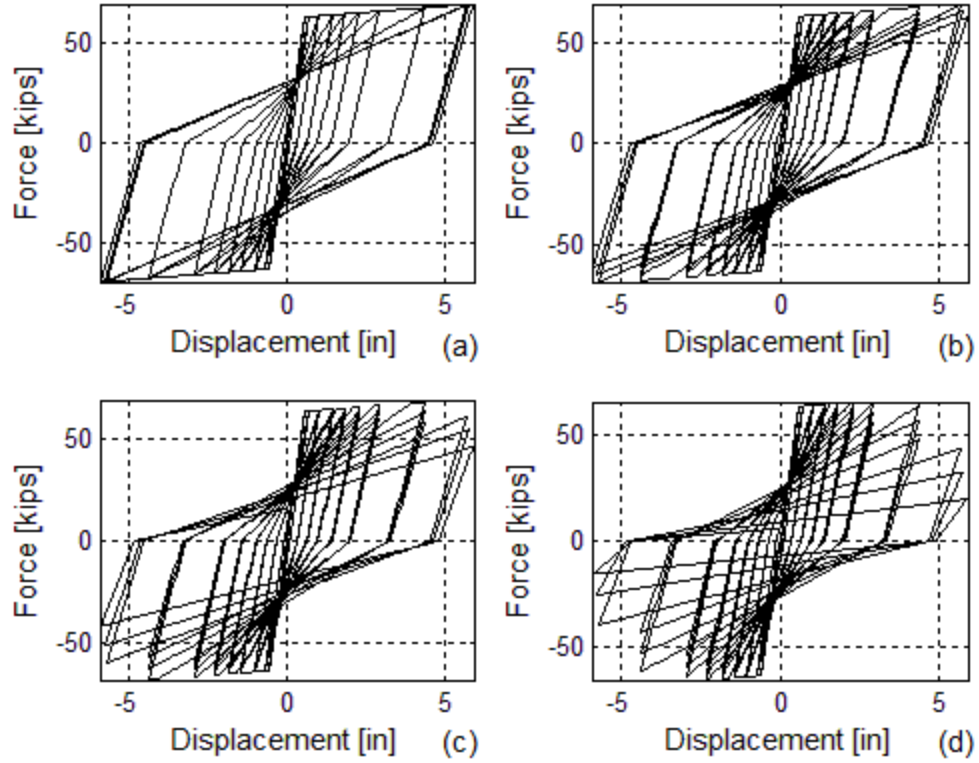


Figure 1-5: (a) No-degrading; (b) Low-Degrading: $\alpha=0.002$, $\beta=0.0015$; (c) Moderate-Degrading: $\alpha=0.0035$, $\beta=0.003$; (d) High-Degrading: $\alpha=0.005$, $\beta=0.0045$

This type of model has been used for many years by the structural engineers to analyze the non-linear behavior of civil structures, but their use for validation of damage detection techniques is not adequate because of the abrupt change in stiffness that any multilinear model will display. However, as with the bilinear model, they will be used on this research to evaluate the effect of different model assumptions on the results of different damage detection approaches.

The response of the OpenSees hysteretic model compared with an experimental test result of a reinforced concrete column is shown in Figure 1-6. To represent this model parameters as the inertia (I) and the young modulus (E) of the column; the yield moment and curvature (M_y , ϕ_y); the ultimate moment and curvature (M_u , ϕ_u); damages due to ductility and energy (α , β); pinching factors for force and deformation during reloading (p_x , p_y) and the degraded unloading stiffness (b) are required. To generate Figure 1-6 the

parameters were taken from CUMBIA; more detail on the determination of such parameters will be presented in Chapter II.

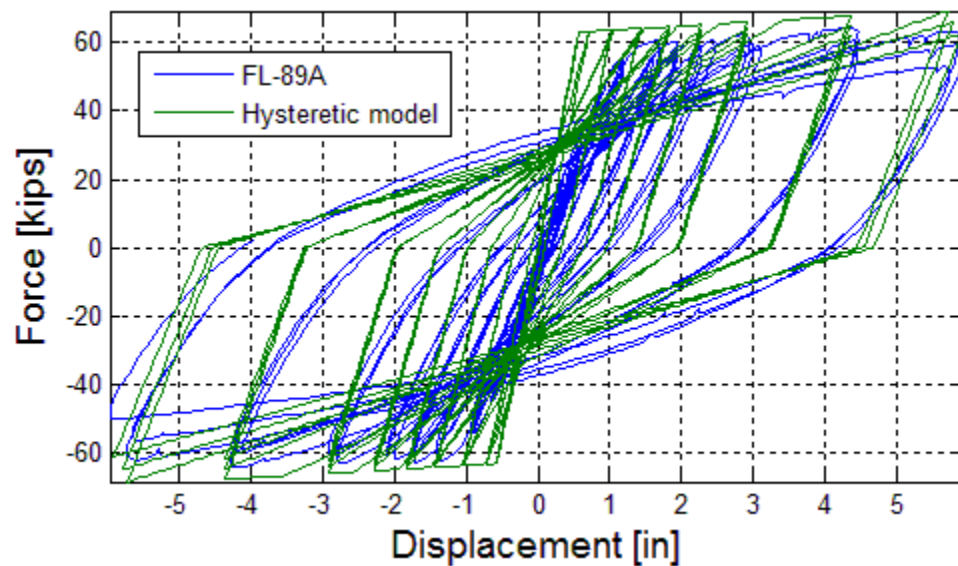


Figure 1-6: Hysteretic model

1.3.4 Fiber-based model

In a fiber-based model, the flexural member is represented by unidirectional fibers and constitutive-material relationships are specified to each type of fiber. In RC members, for example, fibers representing the reinforcing steel, cover concrete (unconfined) and core concrete (confined) can be employed (Figure 1-7).

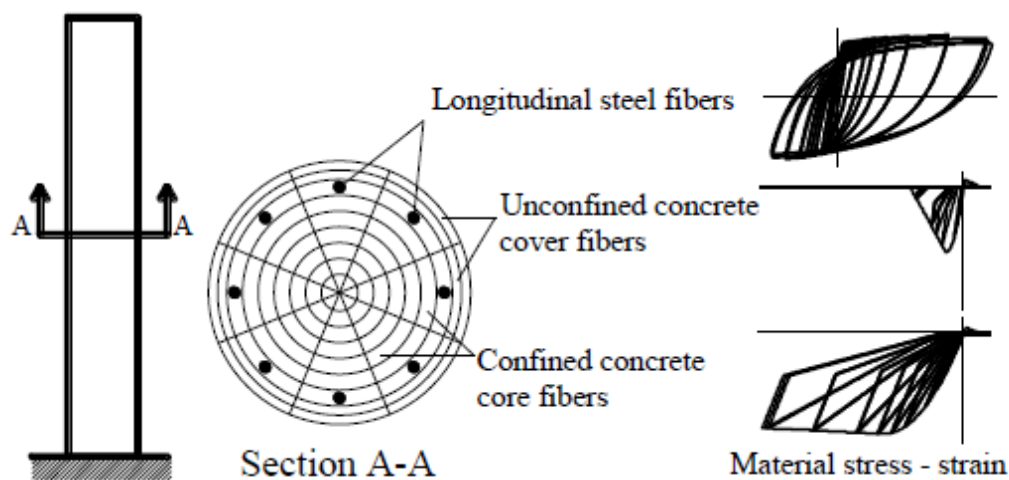


Figure 1-7: Fiber-based model (Montejo, 2008)

Figure 1-8a shows an experimental test result (actual behavior) of a reinforced concrete cantilever column. A typical hysteretic response using a fiber-based model in OpenSees is displayed in Figure 1-8b, it is seen that the resulting response closely resembles the actual behavior of the column. To represent this model in OpenSees, the following parameters are required: the inertia (I) and the young modulus (E) of the column; the unconfined and confined concrete compressive strengths (f'_c); strains for unconfined and confined concrete at maximum stress (ϵ); unconfined and confined concrete residual strength (f'_{cr}); and the unconfined and confined strain at ultimate strength (ϵ_u). In addition, the reinforcing steel parameters are: steel yield stress (F_y); maximum steel stress (F_u); steel modulus of elasticity (E_s); tangent at initial strain hardening (E_{sh}); strain corresponding to initial strain hardening (ϵ_{ish}) and the strain at peak stress (ϵ_u). All these parameters for reinforcing steel, cover concrete (unconfined) and core concrete (confined) were taken from CUMBIA and will be explained later in Chapter II.

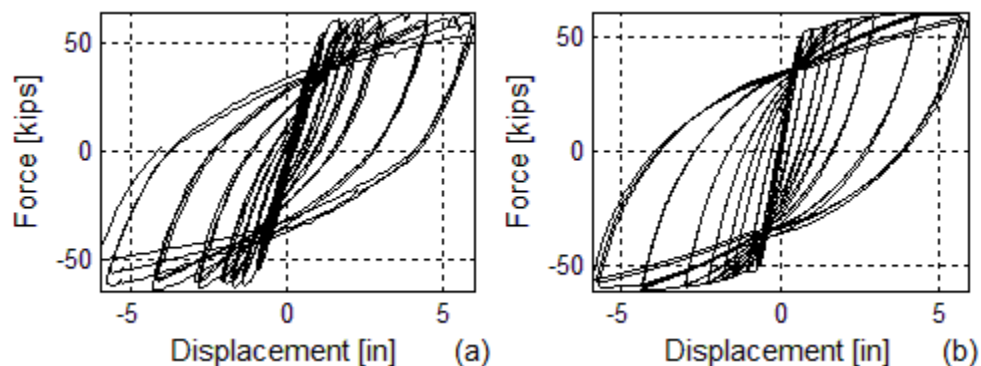


Figure 1-8: (a) Fiber-based Experimental Test, (b) OpenSees Fiber-based model

A summary of the hysteretic force-displacement response obtained by each of the three models considered is presented in Figures 1-9 b to d. For comparison purposes, the actual response of the column being modeled is also presented (Figure 1-9a). Notice that the actual response of the column is highly non-linear (even in the frequently called “linear range”) and that stiffness changes occur in a smooth fashion. Therefore, although multilinear hysteretic models have been successfully used for years by the structural engineering community to analyze the no-linear behavior of civil structures, their use for

validation of damage detection technique may not be adequate due to the unrealistic abrupt change in stiffness characteristic of these models.

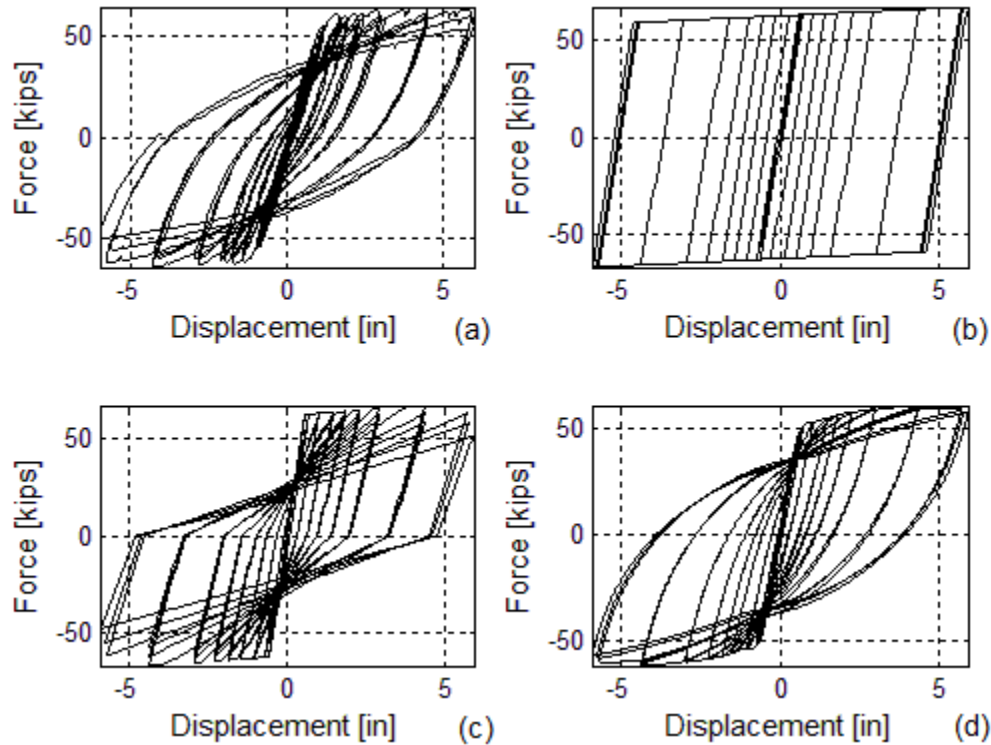


Figure 1-9: (a) Experimental Test (b) OpenSees Bilinear model (c) OpenSees Hysteretic model (d) OpenSees Fiber-based model

1.4 Wavelet Theory

1.4.1 Introduction

The history of Wavelets begins with Fourier. The Fourier transform is a great tool that has revolutionized the signal processing and its application to different disciplines, perhaps like no other development permitting analyze process that are stationary, i.e. there are no frequency changes over the time (Kijewski & Kareem, 2006). However, Fourier analysis has a serious drawback. It transforms the signal from a time-based or space-based domain to a frequency-based one. Unfortunately, in transforming to the frequency domain, the time or space information is lost. When we look at the Fourier transform of a signal it is impossible to determine when or where a particular event took place (Ovanesova and Suárez, 2004). Nevertheless, most interesting signals contain numerous nonstationary or transitory

characteristics such as drift, trends, abrupt changes, and beginning and ends of events (e.g. earthquakes). These characteristics are often the most important part of the signal, and Fourier does not detect them (Misiti *et al.* 2000). Because the time is lost when transforms the signal to the frequency-domain, an alternative transform should be used to reach the time-frequency analysis. An option is the wavelet transform.

1.4.2 Wavelet Analysis

As the Fourier transform, there are two type of Wavelet transform: the continuous and the discrete version. If we compare both (Fourier vs Wavelet), Fourier analysis is composed of basis sine waves (or sinusoids) of infinite duration, they extend from minus to plus infinity (Figure 1-10). Wavelet transforms use wavelets (“little waves”) with a limited duration. Moreover, where sinusoids are smooth and predictable (Figure 1-10a), wavelets tend to be irregular and asymmetric (Figure 1-10b).

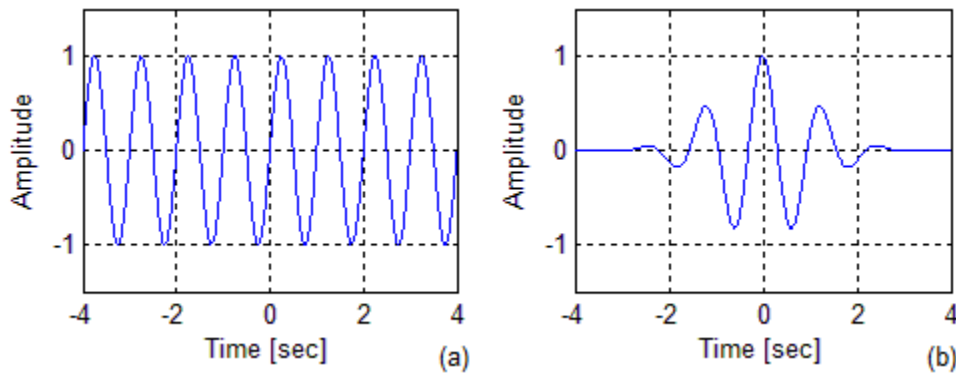


Figure 1-10: (a) Sine Wave. (b) Morlet Wavelet

To appreciate better the importance of wavelet transform an example of the Fourier analysis is presented next. A signal was artificially generated (Figure 1-11a) with two sinusoidals (of different frequencies). First, a sinusoidal with frequency of 1-Hz range from 0 to 5 seconds, then a sinusoidal with frequency of 2Hz goes from 5 to 10 seconds (a discontinuity is then generated at 5 seconds). The Fourier spectrum of the signal is presented in Figure 1-11b. It is seen that Fourier spectrum effectively captured the correct frequencies of the signal (at 1Hz and 2Hz), but the time in where the frequencies occurs is missed.

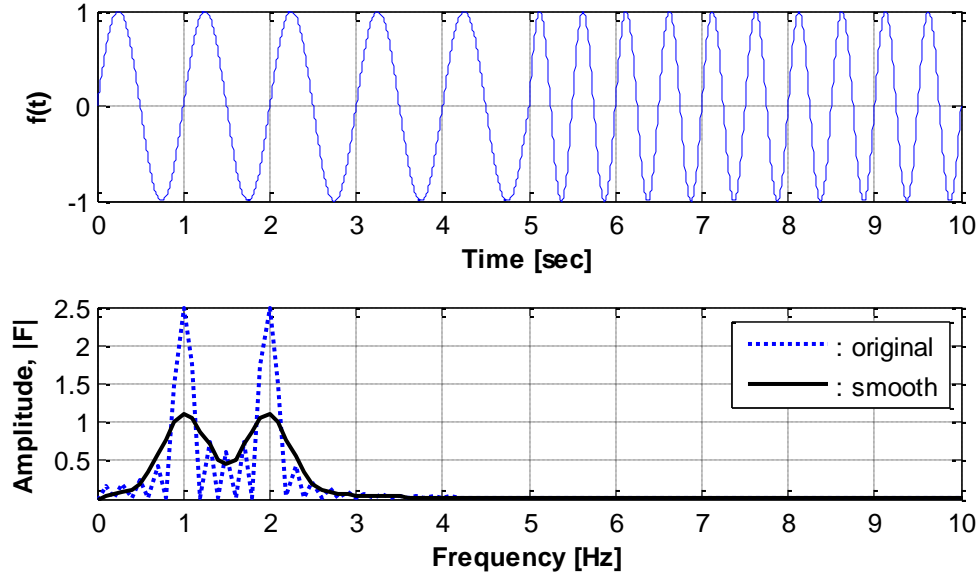


Figure 1-11: (a) Signal in the time domain (b) Fourier spectrum

Wavelets are a waveform oscillation of effectively limited duration that has an average value of zero (Misiti *et al.* 2000). They can be used to extract information from much different type of data, including but not limited to audio signals, sub-band coding, image processing, turbulence, earthquake-prediction and FBI fingerprint compression (Graps, 1995).

Wavelet analysis is the breaking up of a signal into shifted and scaled versions of the original (or mother) wavelet. It is a multi-resolution 3D analysis that has an alternative to obtain the time and frequency domains simultaneously (Kijewski and Kareem, 2003). This analysis is capable of revealing aspects of data that other signal analysis techniques miss, like trends, breakdown points and discontinuities. In this investigation we will evaluate both, the Continuous Wavelet Transform (CWT) and the Discrete Wavelet Transform (DWT) to determine their potential for damage identification purposes. An example using both transforms will be presented later on this chapter.

1.4.3 Continuous Wavelet Transform (CWT)

Conceptually, the wavelet transform can be explained by comparing it with the Fourier transform. Mathematically, the Fourier analysis is defined as:

$$F(\omega) = \int_{-\infty}^{\infty} f(t) e^{-j\omega t} dt \quad (1-1)$$

which is the sum over the all-time of the signal $f(t)$ multiplied by a complex exponential (that can be broken into real and imaginary sinusoidal components).

The results of the transform are the Fourier coefficients $F(\omega)$, which when multiplied by a sinusoid of appropriate frequency ω yields the constituent sinusoidal components of the original signal. Graphically, the process looks like shown in Figure 1-12.

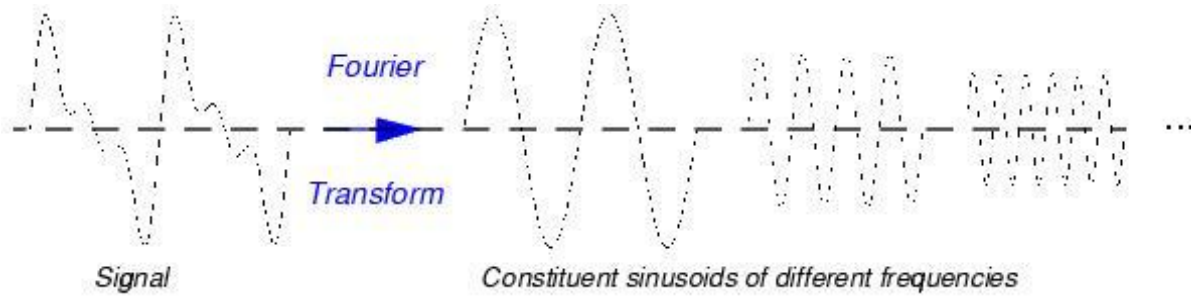


Figure 1-12: The Fourier and Inverse Fourier transform (Misiti *et al.* 2000)

Wavelet analysis extends this mathematical technique by, instead of breaking the signal down into a series of sinusoids which have constant amplitude with time, breaking the signal into a series of wavelets, which are functions that have particular frequency content and are also limited in length. The signal can be decomposed into a set of signals with different dominant frequencies occurring at different times. This decomposition is carried out by convoluting the signal with the wavelet of interest.

Similarly, the *continuous wavelet transform* (CWT) is defined as the sum over the all-time of the signal multiplied by scaled, shifted versions of the wavelet function ψ :

$$C(scale, position) = \int_{-\infty}^{\infty} f(t) \psi(scale, position, t) dt \quad (1-2)$$

The results of the CWT are many *wavelet coefficients* C , which are function of scale and position. Multiplying each coefficient by the appropriately scaled and shifted wavelet yields the constituent wavelets of the original signal:

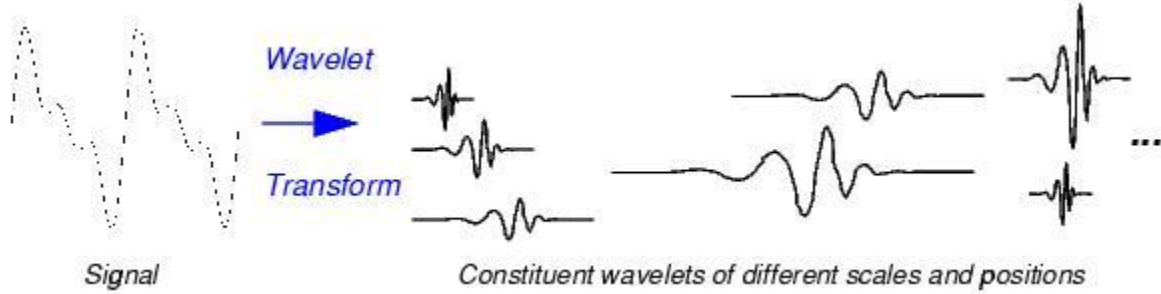


Figure 1-13: The Wavelet and Inverse Wavelet transform (Misiti *et al.* 2000)

Wavelet analysis starts by selecting from the existing wavelet families a basic wavelet function that can be a function of space x or time t . This basic wavelet function, known the “mother wavelet” $\psi(x)$, is then dilated (stretched or compressed) by a quantity a and translated in space by b to generate a set of basis functions $\psi_{a,b}(x)$ as follows:

$$\psi_{a,b}(x) = \frac{1}{\sqrt{a}} \psi\left(\frac{x-b}{a}\right) \quad (1-3)$$

The function is centered at b with a spread proportional to a . The wavelet transform (in its continuous or discrete version) correlates the function $f(x)$ with $\psi_{ab}(x)$. The CWT is the sum over all time of the signal multiplied by a scaled and shifted version of a mother wavelet:

$$C(a,b) = \frac{1}{\sqrt{a}} \int_{-\infty}^{\infty} f(x) \psi\left(\frac{x-b}{a}\right) dx = \int_{-\infty}^{\infty} f(x) \psi_{ab}(x) dx \quad (1-4)$$

Where the scale a and the position b are real numbers and $a > 0$. The results of the transform are wavelet coefficients that show how well a wavelet function correlates with the signal analyzed. Hence, sharp transitions in $f(x)$ create wavelet coefficients with large amplitudes.

The CWT has an inverse: the inverse CWT permits to recover the signal from its coefficients $C(a,b)$ and is defined as

$$f(x) = \frac{1}{K_{\psi}} \int_{a=-\infty}^{\infty} \int_{b=-\infty}^{\infty} C(a,b) \psi_{ab}(x) db \frac{da}{a^2} \quad (1-5)$$

where the constant K_ψ depends on the wavelet type. One of the drawback of the CWT is that a very large number of wavelet coefficients $C(a,b)$ are generated during the analysis. Moreover, few wavelets have an explicit expression, and most are defined with recursive equations.

To demonstrate the application of the CWT, the previous artificial signal presented for the Fourier analysis will be used here. An analysis in the time-frequency domain at low-frequencies (0-10Hz) using the CWT is shown in Figures 1-14. It is seen that the CWT allows us to identify the time where each event took place. Figure 1-14a shows the real values of the coefficients $C(s,p)$ that result from the application of the CWT (Eq. 4) using the Complex Morlet Wavelet. Figure 1-14b is similar to Fig. 1-14a, but now the wavelet coefficients $C(s,p)$ are shown in a two-dimensional graph with their absolute values plotted. This is the usual form to graph the coefficients and it is called a Wavelet Map. The darker colors indicate higher values of the wavelet coefficients. By observing the darker colors in the graph, one can perceive the frequency content of the signal at any time instant. A more precise estimation of the instantaneous dominant frequencies can be obtained by identifying each component by a distinct ridge in the time-frequency plane. There are several techniques to identify these ridges (Carmona *et al.* 1997). The instantaneous dominant frequencies in Figure 1-14c were obtained by locating the local maximas at each time instant. It is seen that the dominant frequencies and its evolution in time are successfully identified for most part of the signal. However, deviations in the identified IF are at the beginning and end of the signal due to the end effects. Aiming for a better visualization of the results obtained, in Figures 1-14 we have omitted parts of the beginning and end of the signal. Different methodologies haven proposed to meliorate the end effects in the CWT, e.g. padding the beginning and end of the signal with surrogate values (Kijewski and Kareem 2003). The results displayed in Figures 1-14 were obtained from the original signal without padding.

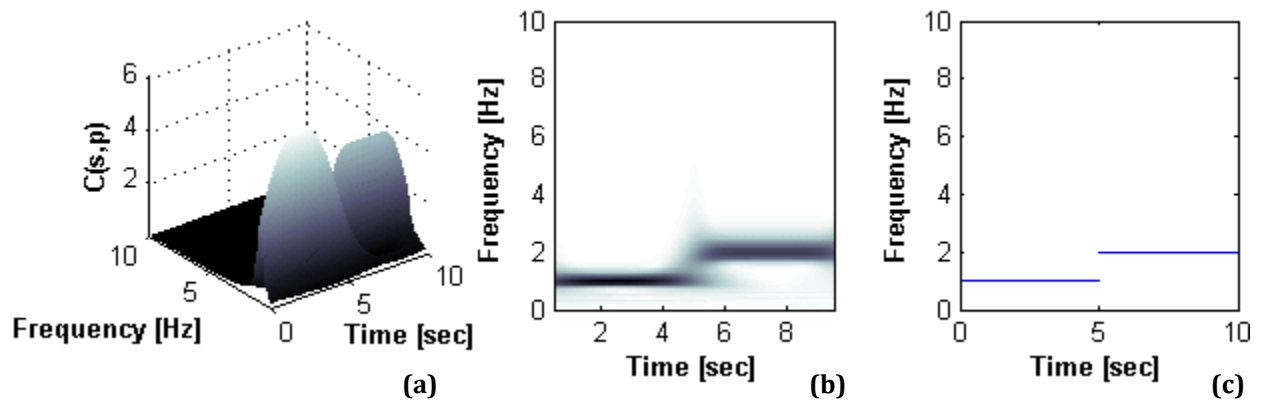


Figure 1-14: (a) 3D plot of the wavelet coefficients, (b) Wavelet Map and (c) Instantaneous frequencies from wavelet ridges

The CWT also permits us to identify singularities in the signal if the analysis is performed at high frequencies (e.g. frequencies near the nyquist frequency). Remember that in the signal we had a discontinuity at 5 seconds due to the change in frequency from 1Hz to 2 Hz. Figure 1-15 clearly presents that discontinuity.

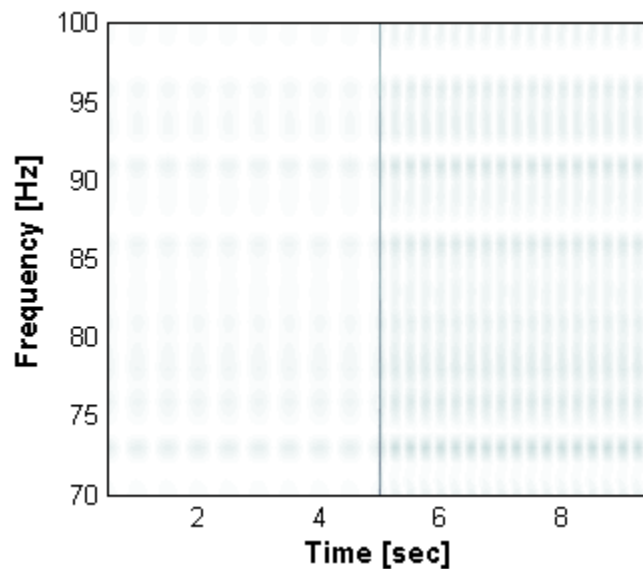


Figure 1-15: CWT of the artificially signal at high frequencies

1.4.4 Discrete Wavelet Transform (DWT)

It can be shown (Daubechies 1992) that the CWT is highly redundant, in the sense that it is not necessary to use the full domain of $C(a,b)$ to reconstruct $f(x)$. Therefore, instead of using a continuum of dilations and translations, discrete values of the parameters can be used. The dilation is defined as $a = 2^j$ and the translation parameter takes the values $b = k 2^j$, where $(j, k) \in Z$, and Z is set of integers. This sampling of the coordinates (a,b) is referred to as dyadic sampling because consecutive values of the discrete scales differ by a factor of 2. In the Discrete Wavelet Transforms the values of scale and position are choose based on a dyadic scale, for some special mother wavelets $\psi(t)$ the corresponding discretized wavelets $\psi_{s,p}(t)$ constitute an orthonormal basis. Mallat (1989) developed a fast wavelet decomposition and reconstruction algorithm for the DWT using a two-channel sub-band coder. In the DWT, a signal can be represented (Eq. 6) by its approximations (A) and details (D) at different levels of decomposition (j). The approximations are the high-scale, low-frequency components of the signal. The details are the low-scale, high-frequency components.

$$x(t) = A_j + \sum_{i \leq j} D_i \quad (1-6)$$

In a similar manner as the CWT, the DWT may also detect localized discontinuities in the signal being analyzed by inspection of the high frequency components (detail functions). The advantage of the DWT is that it takes the structural response and separates the discontinuities (with the details components) from the original signal. This allows localize the structural damage of an easier way only using the details of the DWT.

Continuing with the same example on prior applications we will show now the application of the DWT. Figure 1-16a shows the original signal previously generated with the discontinuity at 5 seconds. The DWT approximations (low-frequency components) are presented in Figure 1-16b. Figure 1-16c presents the absolute values of the detail functions (high frequency components) obtained via DWT with the Bior6.8 wavelet. The spike in the detail functions correspond to the time instant where the damage (or discontinuity) was induced. As for the CWT, it can see that the DWT also has undesirable end effects.

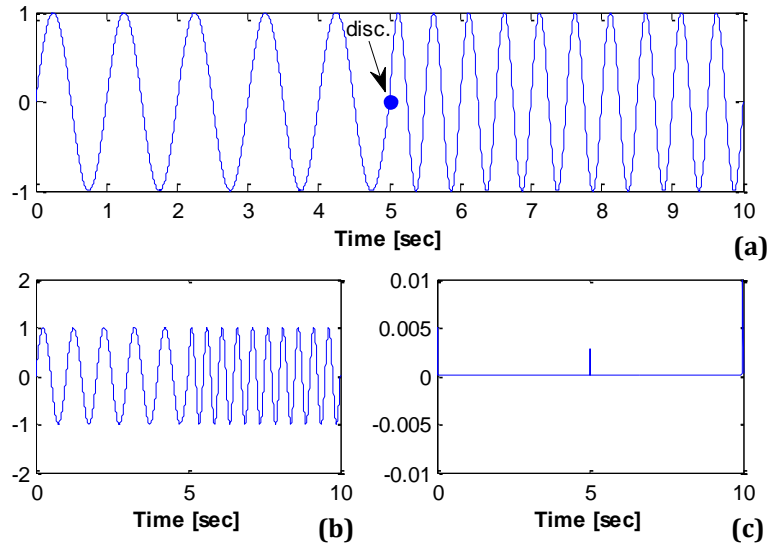


Figure 1-16: (a) Original Signal with a discontinuity, (b) DWT approximations and (c) DWT details

It can be conclude that each type of transform has its own advantages. Moreover, the information that can be obtained from each transform complements each other towards a more robust analysis. Different wavelets will be study for both applications (e.g., Daubechies, Morlet, Complex Morlet, Haas, Bior6.8, etc.) to finally choose the one that better results presents. Numerical examples will be presented on Chapter IV.

1.5 Scope of the research work

The goal of this research is to develop a damage identification technique that it can be implemented in the damage identification of RC structures subjected to seismic loads. Validation and calibration of the proposed technique will be performed through the use of non-linear-fiber-based models. Specifically the objectives are to:

- Study the effect of different modeling approaches (bilinear, hysteretic and fiber-based) on the results of current Wavelet based damage detection methodologies.
- Study the effect of different excitation loads (e.g. deterministic, non-stationary) on the results of current Wavelet based damage detection methodologies.
- Develop a methodology capable of identify the occurrence of damage in highly nonlinear structures subjected to earthquake type excitations.

1.6 Thesis Organization

1.6.1 Development and validation of structural models

Chapter II presents different columns modeled with the three hysteretic models mentioned at the beginning of this chapter. Models will be validated and calibrated based on available experimental data from pseudo-dynamic cyclic reversals tests and shake table tests. Each model will be subjected to non-linear cyclic push-over analyses and dynamic analyses. The push-over analyses consist of applying lateral force reversals at the tip of the column in displacement increments (in terms of story drift ratio). The dynamic analyses are achieved by applying an acceleration time history to the base of the column. Excitation loads ranges from sinusoids with particular frequencies to real accelerograms recorded during historic earthquakes (e.g., Loma Prieta, 10/17/89 & Round Valley, 11/23/84).

1.6.2 Evaluation and calibration of wavelet parameters

Chapter III includes the study of different types of wavelets. Evaluation and calibration of the wavelet parameters will be performed based on the capacity to detect natural frequencies and discontinuities.

1.6.3 The effects of modeling assumptions and load excitation characteristics on the effectiveness of current Wavelet based damage detection methodologies

Chapter IV describes the analysis evaluation of both applications, the CWT and DWT. This analysis consists in the use of low-and-high frequencies decompositions to identify the occurrence of structural damage using distinct modeling approached and dynamic load excitations.

1.6.4 Proposed methodology for damage detection in civil structures subjected to earthquake loads

Based on the results obtained from the evaluation performed in Chapter IV, a methodology will be developed aiming to specifically tackle the damage identification problem in RC structures subjected to seismic loads.

Appendix A presents the OpenSees codes developed during this research for the columns used in order to develop the RC members for the application of the wavelet transforms (CWT and DWT).

1.7 References

Erduran, E. and Kunnath, S. K. (2010). *“Enhanced Displacement Coefficient Method for Degrading Multi-Degree-of-Freedom Systems”*, Earthquake Spectra, Vol. 26, No. 2, pages 311 – 326.

Graps, A. (1995). *“An Introduction to Wavelets”*, Computational Science and Engineering, pages 1 – 18.

Kabeyasawa, T., Shiohara, H., Otani, S. and Aoyama, H. (1983). *“Analysis of the Full-scale Seven-story Reinforced Concrete Test Structure”*, The Faculty of Engineering, University of Tokyo, Vol. 37, No. 2, pages 432 – 478.

Kijewski, T. and Kareem, A. (2006). *“Efficacy of Hilbert and Wavelet Transforms for Time-Frequency Analysis”*, Journal of Engineering Mechanics, Vol. 132, No 10, pages 1037 – 1049.

Kijewski, T. and Kareem, A. (2003). *“Wavelet Transform for System Identification in Civil Engineering”*, Computed-Aided Civil and Infrastructure Engineering, Vol. 18, pages 339 – 355.

Mettupalayam, V. and Reinhorn, A. M. (2000). *“Hysteretic Models for Deteriorating Inelastic Structures”*, Journal of Engineering Mechanics, Vol. 126, No. 6, pages 633 – 640.

Misiti, M., Misiti, Y., Oppenheim, G. and Poggi, J. M. (2000). *“Wavelet toolbox user’s guide”*. The Math Works Inc., Natick, Massachusetts.

Montejo, L. A. (2008). *“Seismic Behavior of Reinforced Concrete Bridge Columns at Sub-Freezing Temperatures”*, PhD dissertation, North Carolina State University.

Murty, C. V. R. (2005). *“Earthquakes Tips – Learning Earthquake Design and Construction”*, National Information Center of Earthquake Engineering, pages 33 – 34.

Otani, S. (2002). *“Nonlinear Earthquake Response Analysis of Reinforced Concrete Buildings – Lecture Notes”*, Department of Architecture – Graduate School of Engineering, Chapter 11, pages 5 – 6.

Otani, S. (1980). *“Nonlinear Dynamic Analysis of Reinforced Concrete Buildings Structures”*, University of Toronto, Canadian Journal of Civil Engineering, Vol. 7 pages 333 – 344.

Ovanesova, A. and Suárez, L. E. (2004). *"Applications of Wavelet Transforms to Damage Detection in Frame Structures"*, Engineering Structures, Vol. 26, No. 1, pages 39 – 49.

Silva P. F. (2010). *"Hysteretic Rotation Model HRM4 for CFRP-Strengthened Joints"*, pages 105 – 116.

TQ, (2000). *"Force of Nature"*, Retrieved on April 23, 2011 from <http://library.thinkquest.org/C003603/english/earthquakes/earthquakedamage.shtml>

CHAPTER II

DEVELOPMENT AND VALIDATION OF STRUCTURAL MODELS

2.1 Introduction

In order to understand the process, development and influence in the damage detection results of the three modeling approaches described in Chapter I, four columns were analyzed. The modeling approach plays an important role since we need a realistic RC member representation to develop and validate the damage identification techniques to be presented on Chapters IV and V. These columns are evaluated as cantilever beam-column elements, each one subjected to cyclic pushover analyses. Dynamic analysis was carried out in two of them. The purpose of this chapter is the validation of each analytical model that simulates the behavior of the RC members, mainly the fiber-based model. Validation of this particular model is fundamental because we anticipate that this is the model that will be implemented on the damage detection technique in nonlinear civil structures. Damage (or yield episodes) detection in structural models developed using the bilinear and “Takeda” hysteretic models should be “easier” because of the multi-linear nature of such models, but their abrupt changes in stiffness does not represents the actual behavior of RC members. This will be demonstrated later in Chapter IV. That is why a more sophisticated model, like fibers approach has to be used. Each model generation was built in the OpenSees software framework system (McKenna *et al.* 2000). Explanation and calibration to different parameters of the OpenSees materials, sections and elements is presented in detail for each model. The results obtained with the analytical models for all four reinforced concrete columns are compared with the theoretical moment-curvature based monotonic prediction (i.e., CUMBIA, Montejo *et al.* 2007) and the actual experimental results. Finally, the chapter discusses the importance of using the fiber-based approach to simulate the behavior of civil structures.

2.2 Development of structural models

This section discusses the procedures to develop the three analytical models, especially the fiber-based model. When a fiber approach is used, separated material rules need to be specified for the reinforcing steel bars, unconfined concrete and confined concrete; material stress is assumed constant between integration points along the fiber segment. No prior moment-curvature analysis is required because the hysteretic response of the section is defined by the material properties, and hence does not need to be specified. Material models, sections and elements used in this research are described next and all are available in OpenSees.

2.2.1 Uniaxial materials

OpenSees has an extensive variety of materials representation to simulate different kind of models. For our study we focus on the following materials: *Elastic*, *Steel01*, *Hysteretic*, *Concrete01*, and the *ReinforcingSteel*. These materials were taken for the following purpose; the *Elastic* material was added to the *Steel01* and the *Hysteretic* materials to account for the axial actions in the bilinear and the hysteretic “Takeda” model. For the use of the three materials mentioned above, prior moment-curvature analysis is required. The *Concrete01* material in combination with the *ReinforcingSteel* material characterizes the third and final model, the fiber-based approach. These materials are described in detail below.

2.2.1.1 Elastic material

This command is used to construct an elastic uniaxial material object in the bilinear and hysteretic models as explain before. Table 2-1 shows the parameters that have to be entered for the *Elastic Material*. The behavior of the *elastic material* is presented in Figure 2-1.

Table 2-1: Elastic material parameters

uniaxialMaterial Elastic \$matTag \$E <\$eta>	
\$matTag	unique material object integer tag
\$E	tangent
\$eta	damping tangent (optional, default = 0.0)

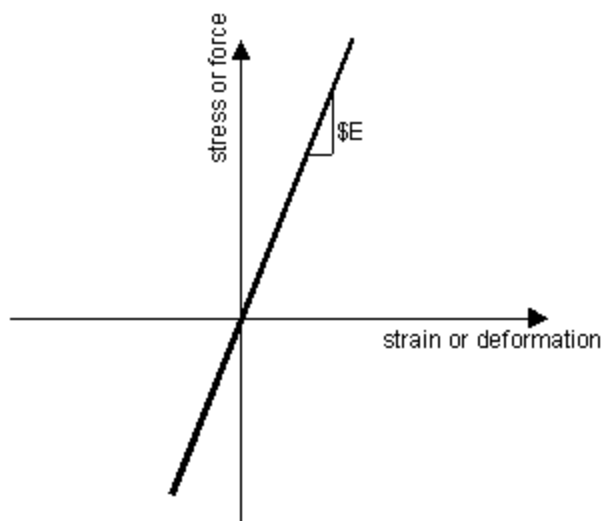


Figure 2-1: Elastic Material behavior

2.2.1.2 *Steel01 material*

The *Steel01* material command is used to construct a uniaxial bilinear steel material object with optional isotropic hardening. Table 2-2 presents the material parameters previously calculated from a moment-curvature analysis in CUMBIA, while the Figure 2-2 shows the behavior of the monotonic envelope.

Table 2-2: Steel01 material parameters

uniaxialMaterial Steel01 \$matTag \$Fy \$E0 \$b	
\$matTag	unique material object integer tag
\$Fy	yield strength
\$E0	initial elastic tangent
\$b	strain-hardening parameters (ratio between post-yield tangent and initial elastic tangent)

Code developed by Filip Filippou, UC Berkeley

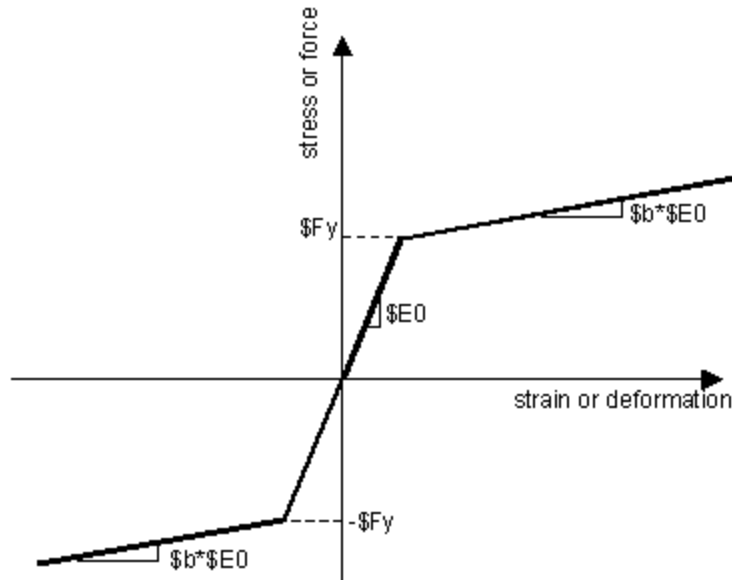


Figure 2-2: Steel01 Material behavior (Mazzoni, 2007)

2.2.1.3 *Hysteretic material*

The *Hysteretic* material command is used to construct a uniaxial bilinear hysteretic material object with pinching of force and deformation, damage due to ductility and energy, and degraded unloading stiffness based on ductility (input data also obtained from CUMBIA is summarized in Table 2-3). This material in junction with the *Elastic* material will emulate the Takeda model. Figure 2-3 illustrates the behavior of this model.

Table 2-3: Hysteretic material parameters

uniaxialMaterial Hysteretic \$matTag \$s1p \$e1p \$s2p \$e2p <\$s3p \$e3p>\$s1n \$e1n \$s2n \$e2n <\$s3n \$e3n> \$pinchX \$pinchY \$damage1 \$damage2 <\$beta>	
\$matTag	unique material object integer tag
\$s1p \$e1p	stress and strain (or force & deformation) at <i>first point</i> of the envelope in the <i>positive</i> direction
\$s2p \$e2p	stress and strain (or force & deformation) at <i>second point</i> of the envelope in the <i>positive</i> direction
\$s3p \$e3p	stress and strain (or force & deformation) at <i>third point</i> of the envelope in the <i>positive</i> direction (optional)
\$s1n \$e1n	stress and strain (or force & deformation) at <i>first point</i> of the envelope in the <i>negative</i> direction*
\$s1n \$e1n	stress and strain (or force & deformation) at <i>second point</i> of the envelope in the <i>negative</i> direction*
\$s1n \$e1n	stress and strain (or force & deformation) at <i>third point</i> of the envelope in the <i>negative</i> direction (optional)*
\$pinchX	pinching factor for strain (or deformation) during reloading
\$pinchY	pinching factor for stress (or force) during reloading
\$damage1	damage due to ductility
\$damage2	damage due to energy
\$beta	power used to determine the degrading unloading stiffness based on ductility (optional, default = 0.0)

*NOTE: negative backbone points should be entered as negative numeric values

Code Developed by Micheal Scott & Filip Filippou, UC Berkeley

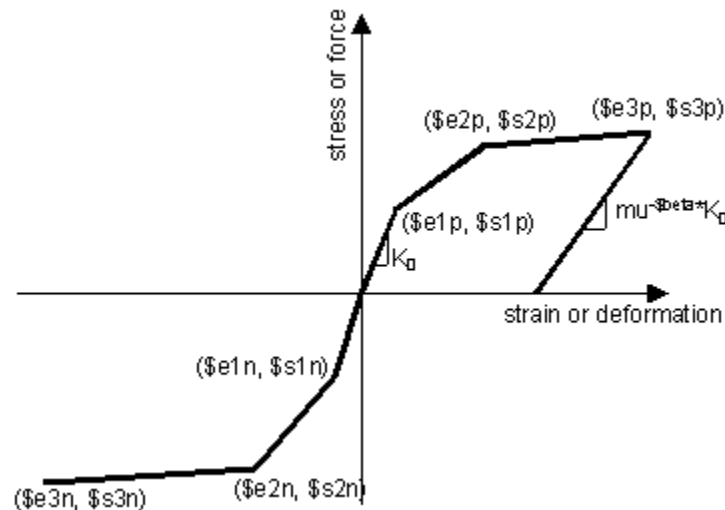


Figure 2-3: Hysteretic Material behavior

2.2.1.4 Concrete01 material

Confined and unconfined concrete are modeled with the OpenSees *Concrete01* material. The input data required for this model is presented in Table 2-4. As it was previously mentioned, no moment-curvature analysis is necessary, it just needs the constitutive properties for the unconfined and confined model obtained from CUMBIA. Figure 2-4 illustrates an example from CUMBIA of how obtain the input data for both constitutive models used in the *Concrete01* material. The constitutive model for the concrete has to be specified by the user. However, the code has some default models. The default models for the unconfined and confined concrete are those proposed by Mander, Priestly and Park (1988). Figures 2-5 and 2-6 show the hysteretic stress-strain relationship with degraded linear unloading/reloading stiffness and no tensile strength obtained with *Concrete01*.

Table 2-4: OpenSees Concrete01 material parameters

uniaxialMaterial Concrete01 \$matTag \$fpc \$epsc0 \$fpcu \$ epsU	
\$matTag	unique material object integer tag
\$fpc	concrete compressive strength at 28 days (compression is negative)*
\$epsc0	concrete strain at maximum strength*
\$fpcu	concrete crushing strength*
\$epsU	concrete strain at crushing strength*
*NOTE: Compressive concrete parameters should be input as negative values.	
Code developed by Filip Filippou, UC Berkeley	

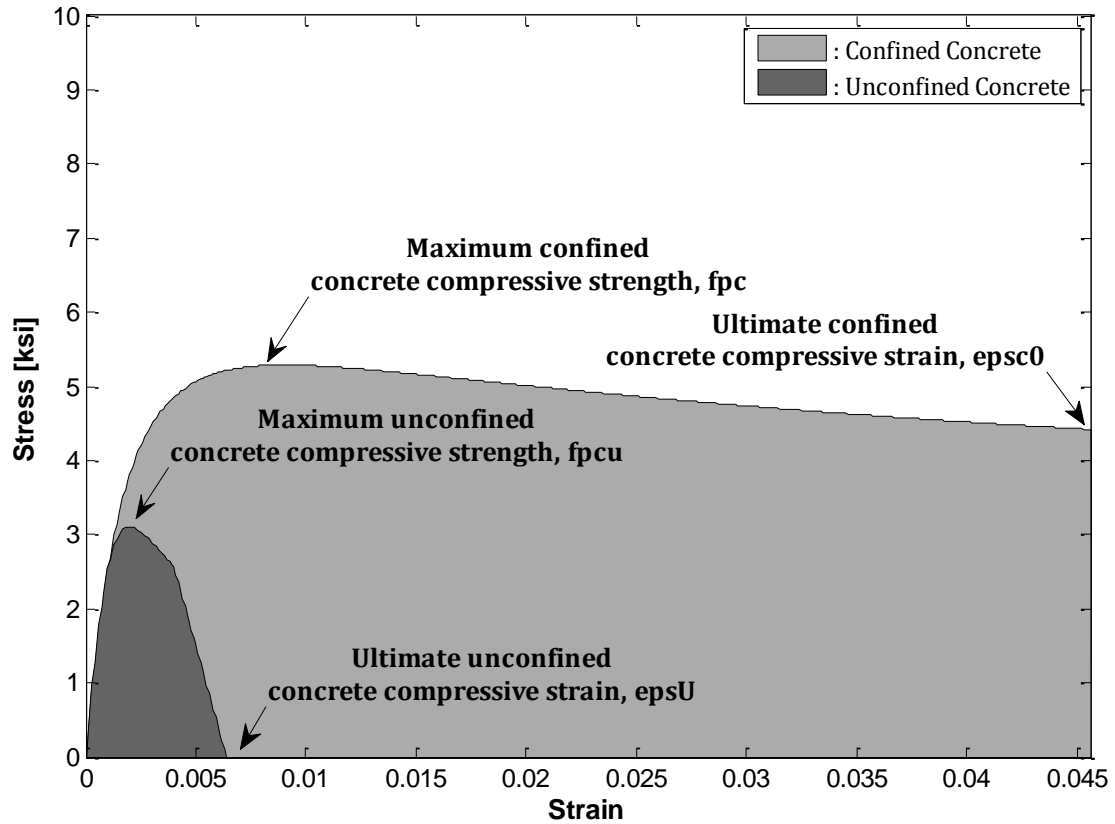


Figure 2-4: Unconfined and Confined concrete parameters from CUMBIA (Montejo *et al.* 2007)

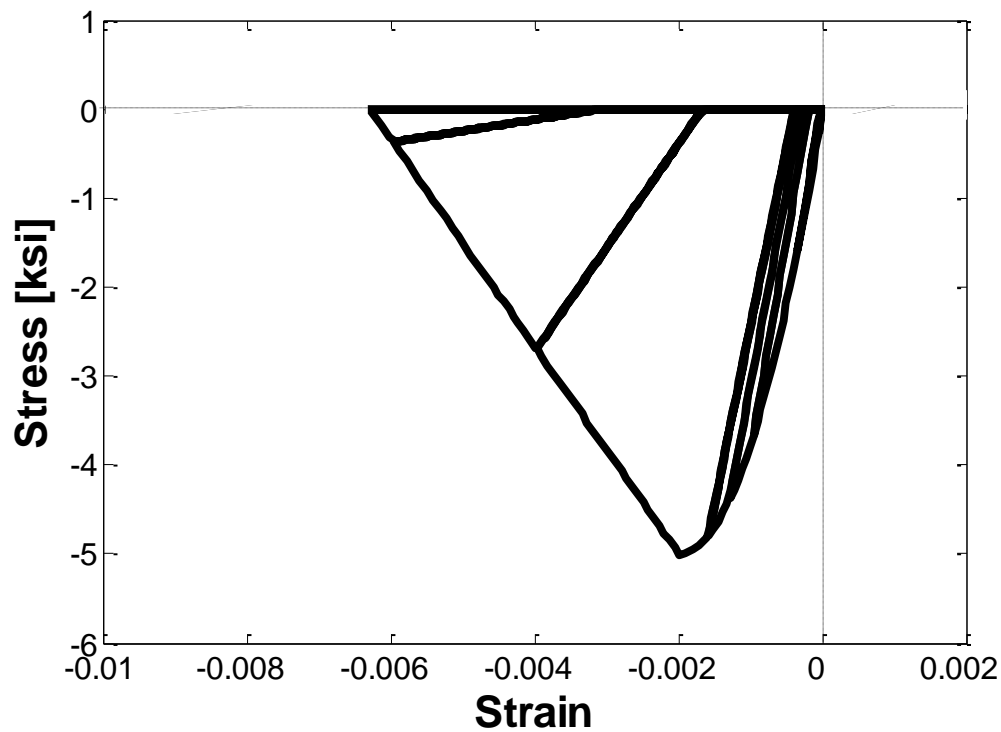


Figure 2-5: Hysteretic model for the unconfined concrete (compression values should be input as negative in OpenSees)

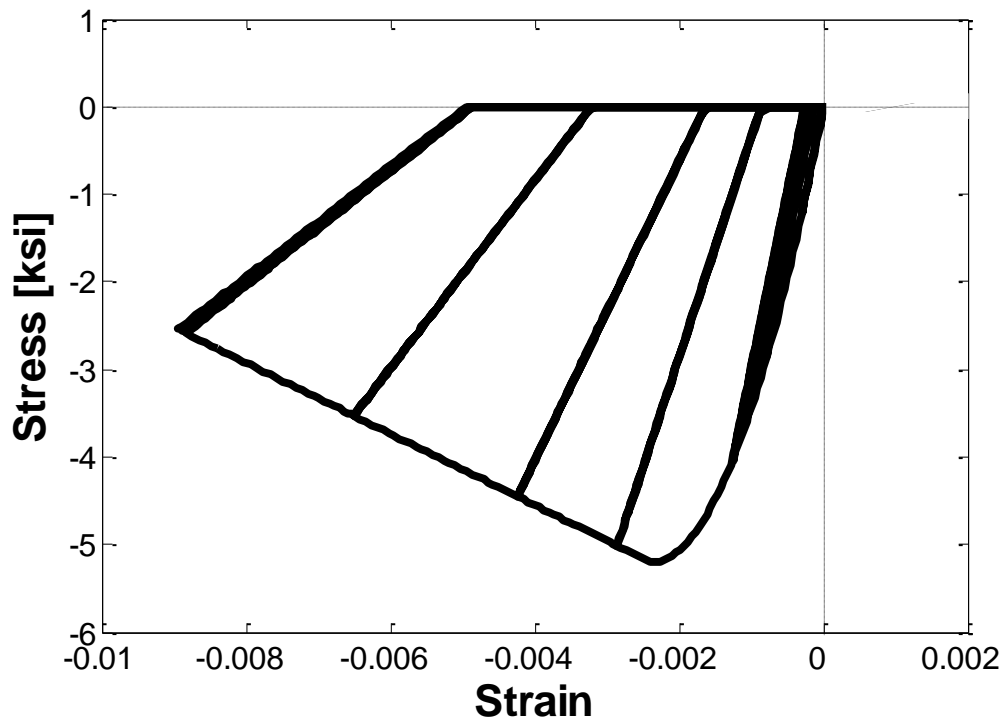


Figure 2-6: Hysteretic model for the confined concrete (compression values should be input as negative in OpenSees)

2.2.1.5 Reinforcing Steel material

Reinforcing steel bars are modeled using the *ReinforcingSteel* material suggested by Mohle and Kunnath (2006) which was specially intended to be used in a reinforced concrete fiber section as the steel reinforcing material. Table 2-5 summarizes the input data used to represent this model.. Figure 2-7 shows an example from CUMBIA of how obtain the input data for the constitutive model of the steel reinforcement that will be used in the *ReinforcingSteel* material. As the constitutive model for the concrete, the constitutive model for the steel also has to be specified by the user. For the steel, the model used will be the proposed by Raynor *et al.* (2002). The general hysteretic behavior of the *ReinforcingSteel* material is shown in Figure 2-8.

Table 2-5: Reinforcing Steel parameters

uniaxialMaterial ReinforcingSteel \$matTag \$fy \$fu \$Es \$Esh \$esh \$eult < -GABuck \$lsr \$beta \$r \$gamma> < -DMBuck \$lsr <alpha>> < -CM Fatigue \$Cf \$alpha \$Cd> < -IsoHard <\$a1 <\$limit> < -MPCurvesParams>>>	
\$matTag	unique material object integer tag
\$fy	yield stress in tension
\$fu	ultimate stress in tension
\$Es	initial elastic tangent
\$Esh	tangent at initial strain hardening
\$esh	strain corresponding to initial strain hardening
\$eult	strain at peak stress
Code developed by <i>Filip Filippou, UC Berkeley</i>	
- CMFatigue	Coffin - Manson Fatigue and Strength Reduction
\$Cf	Coffin and Mason constant, C
\$alpha	Coffin and Mason constant, a
\$Cd	Cyclic strength reduction constant
- MPCurveParams	Menegotto and Pinto Curve Parameters
\$R1	(default = 0.333)
\$R2	(default = 18)
\$R3	(default = 4)

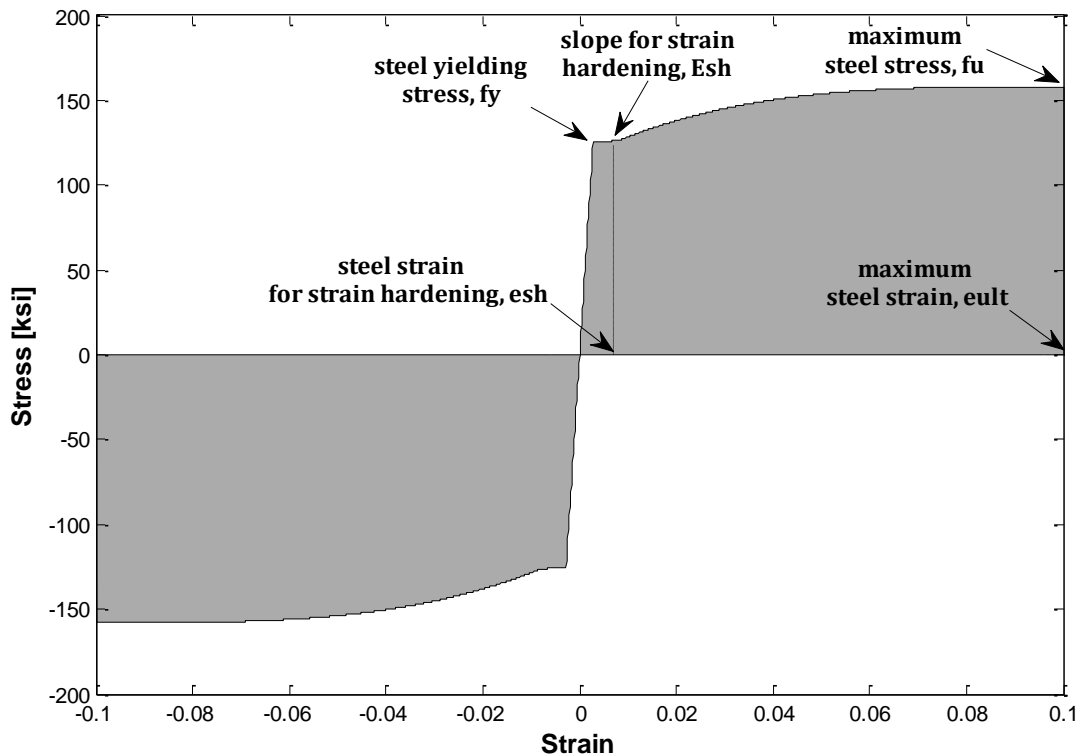


Figure 2-7: Longitudinal Reinforcing Steel parameters (Montejo *et al.* 2007)

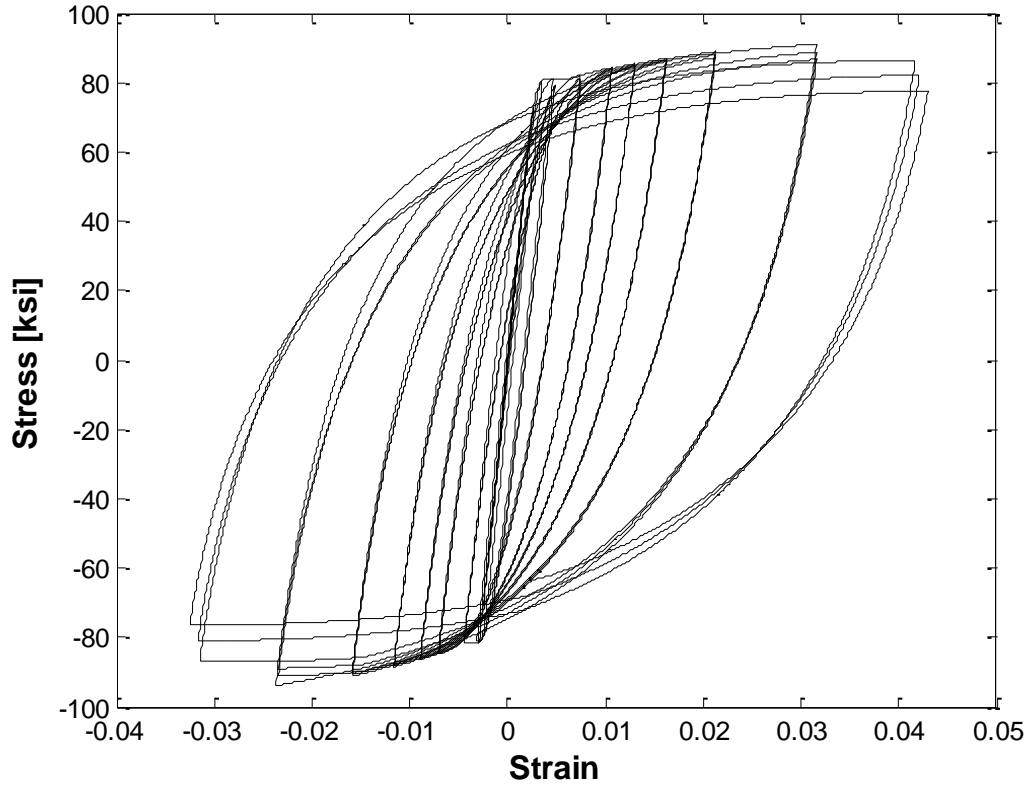


Figure 2-8: Hysteretic model for the reinforcing steel

If we take a look in Figure 2-8, it can see some degradation in the hysteresis response. This degradation of strength and stiffness due to cycling is calculated according to the Coffin and Mason fatigue model (i.e. *-CMFatigue*) through the factors α , C_f and C_d . The damage strain range constant, α , is used to relate damage from one strain range to an equivalent damage at another strain range and is constant for a material type. The ductility constant, C_f , is used to adjust the number of cycles to failure. A higher value translates to a larger number of cycles to failure. The strength reduction constant, C_d , controls the amount of degradation per cycle. A large value for C_d will result in a lower reduction of strength for each cycle. Suggested values by Mohle and Kunnath (2006) for bars with a slenderness (ratio between the bar unsupported length and the bar diameter) of 6 are $\alpha = 0.506$, $C_f = 0.26$, $C_d = 0.389$. In general, these values are expected to change with the steel type, bar diameter and confinement provided to the section.

Figure 2-9 demonstrate the effects that some of the variables have on the cyclic response.

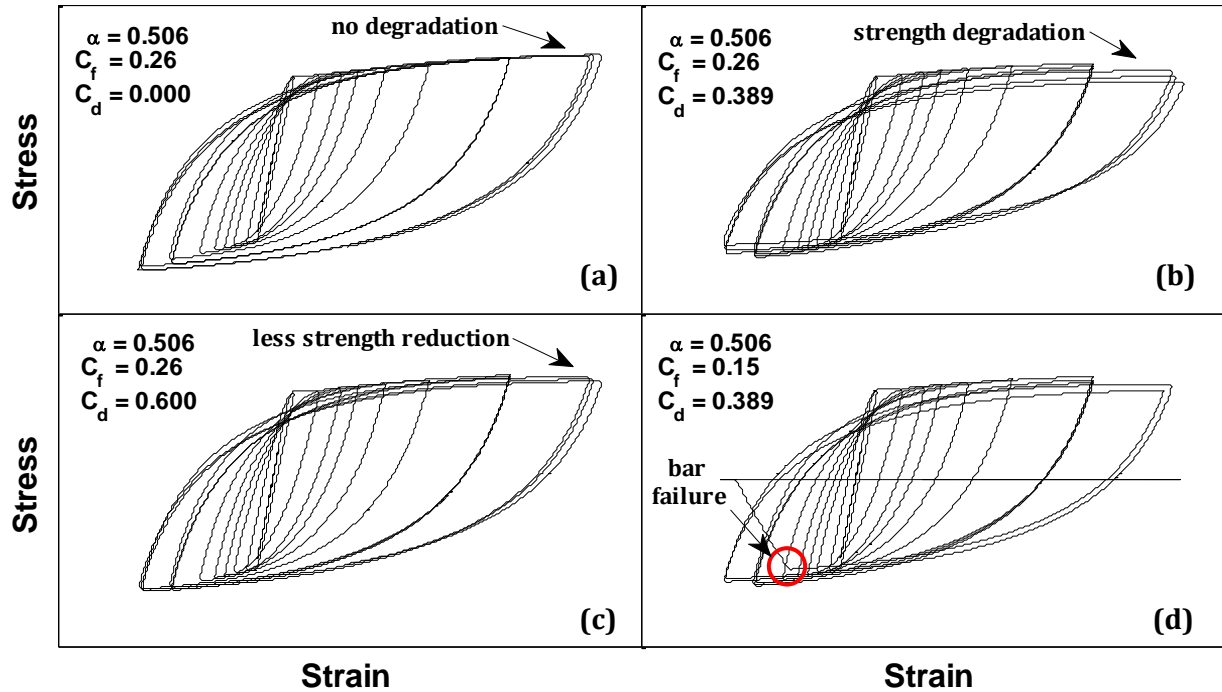


Figure 2-9: Fatigue and degradation parameters example

In Figure 2-9a, the response contains no strength degradation by setting the C_d variable to 0.0. The response in Figure 2-9b shows strength degradation due to the suggested values of C_f , α , and C_d . The response shown on the Figure 2-9c demonstrates the change in the response when the suggested values of C_f and α are used with $C_d = 0.6$. Making the value of C_d larger will result in less strength reduction due to damage. In the response on Figure 2-9d C_f is changed to 0.15. This results in a more rapid accumulation of damage causing the bar to fail sooner.

2.2.2 Sections generation

OpenSees has a diversity of sections representation, but we concentrate on the Aggregator section and the Fiber-based section. These commands are used to create a *SectionForceDeformation* object, which represents force-deformation (or resultant stress-strain) relationships at beam-column (Figure 2-10).

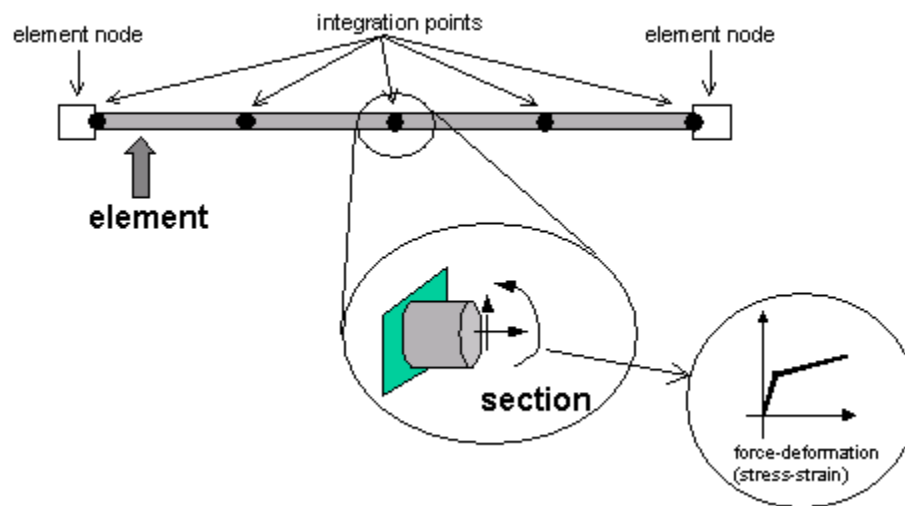


Figure 2-10: Example of OpenSees sections to describe force-deformation relationship (Mazzoni, 2007)

2.2.2.1 Aggregator Section

This section is used to construct a *SectionAggregator* object which groups previously-defined UniaxialMaterial objects into a single force-deformation model. The *aggregator* section is used to merge the corresponding materials previously mentioned to simulate our bilinear and hysteretic models. The parameters for this *aggregator* section are presented in Table 2-6, while Figure 2-11 illustrates a group example of two materials previously-defined (e.g., Steel01) to create a unique section.

Table 2-6: Aggregator Section parameters

section Aggregator \$secTag \$matTag1 \$string1 \$matTag2 \$string2...	
< -section \$sectionTag >	
\$secTag	unique section object integer tag
\$matTag1 \$matTag2...	previously-defined <i>UniaxialMaterial</i>
\$string1 \$string2...	the force-deformation quantities corresponding to each section object. One of the following string is used:
P	Axial force-deformation
Mz	Moment-curvature about section local z-axis
Vy	Shear force-deformation along section local y-axis
My	Moment-curvature about section local y-axis
Vz	Shear force-deformation along section local z-axis
T	Torsion Force-Deformation
<-section \$sectionTag >	specifies a previously-defined Section object (identified by the argument \$sectionTag) to which these <i>UniaxialMaterial</i> objects may be added to recursively define a new Section object

Code developed by Micheal Scott, Oregon State University

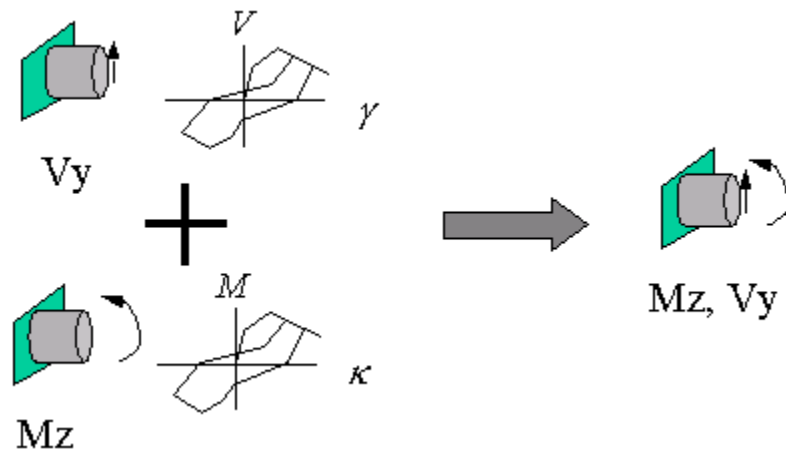


Figure 2-11: Group previously-defined materials to describe stress resultant section behavior

2.2.2.2 Fiber Section

The fiber section has a general geometric configuration formed by subregions of simpler, regular shapes (e.g., quadrilateral, circular and triangular regions) called *patches*. Figure 2-12 shows a simple circular fiber-based section with the materials that describes it. Layers of reinforcement bars also can be specified. The subcommands *patch* and *layer*

(Straight Layer Command, Circular Layer Command) are used to define the discretization of the section into fibers. Table 2-7 summarizes the parameters for fiber section and its subcommands. Individual fibers, however, can also be defined using the fiber command, but in this research it is not used. Obviously, as our columns are circular, the circular layer (Figure 2-13a) and the circular region for the patch will be used (Figure 2-13b).

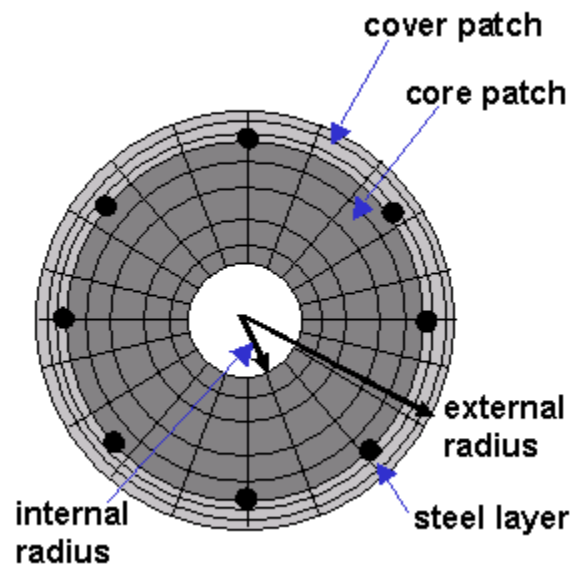


Figure 2-12: Fibers-based section

Table 2-7: Fibers Section Parameters

<pre> section Fiber \$secTag { fiber <fiber arguments> patch <patch arguments> layer <layer arguments> } </pre>	
\$secTag	unique tag among Fiber Sections
fiber...	command to generate a single fiber
patch...	command to generate a number of fibers over a geometric cross-section
layer...	command to generate a row of fibers along a geometric arc

patch circ \$matTag \$numSubdivCirc \$numSubdivRad \$yCenter \$zCenter \$intRad \$extRad <\$startAng \$endAng>	
\$matTag	material integer tag of the previously-defined uniaxialMaterial object used to represent the stress-strain for the area of the fiber
\$numSubdivCirc	number of subdivisions (fibers) in the circumferential direction.
\$numSubdivRad	number of subdivisions (fibers) in the radial direction.
\$yCenter \$zCenter	y & z coordinates of the center of the circle
\$intRad	internal radius
\$extRad	external radius
\$startAng	starting angle (optional, default = 0.0)
\$endAng	ending angle (optional, default = 360.0)
layer circ \$matTag \$numBar \$areaBar \$yCenter \$zCenter \$radius <\$startAng \$endAng>	
\$matTag	material integer tag of the previously-defined <i>UniaxialMaterial</i> object used to represent the stress-strain for the area of the fiber
\$numBar	number of reinforcing bars along layer
\$areaBar	area of individual reinforcing bar
\$yCenter \$zCenter	y & z coordinates of the center of reinforcing layer (local coordinate system)
\$radius	radius of reinforcing layer
\$startAng \$endAng	starting and ending angle of reinforcing layer, respectively. (Optional, Default: a full circle is assumed 0-360)

Code developed by Micheal Scott, Oregon State University

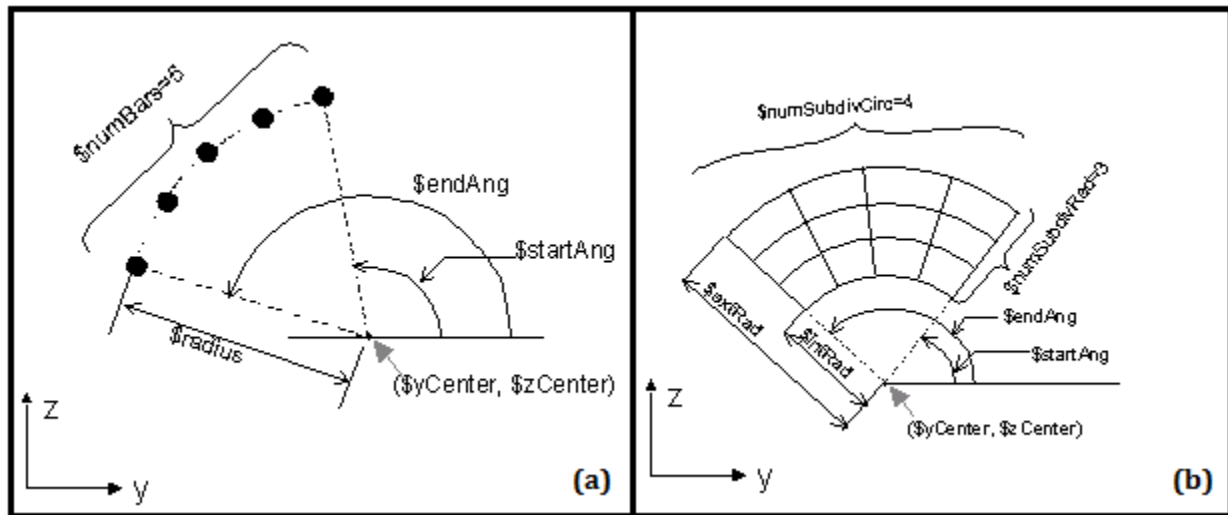


Figure 2-13: (a) Circular layer parameters (b) Circular patch parameters (Mazzoni, 2007)

2.2.3 Elements generation

For the modeling of the RC columns, the Nonlinear Beam-Column elements of OpenSees were used. Basically, OpenSees has two types of Nonlinear Beam-Column applications: the force-based elements and the displacement-based elements. For this research we used the force-based elements. These are the “*nonlinearBeamColumn*” element that represents concentrated plasticity used on the bilinear and hysteretic models, and the “*beamWithHinges*” element that refers to distributed plasticity with elastic interior used on the fibers approach. These two force-based elements are presented next.

2.2.3.1 Nonlinear Beam Column Element

Finite element models for seismic design and assessment traditionally use a concentrated plasticity approach as shown in Figure 2-14. In this model the inelastic deformations are concentrated into rotational springs at the ends of a linear elastic element. This approach provides an efficient way of modeling and controlling plastic hinge formation. The drawback to concentrated plasticity models is that axial force-moment interaction and axial-force stiffness interaction are separate from the element behavior (Scott and Fenves, 2006).

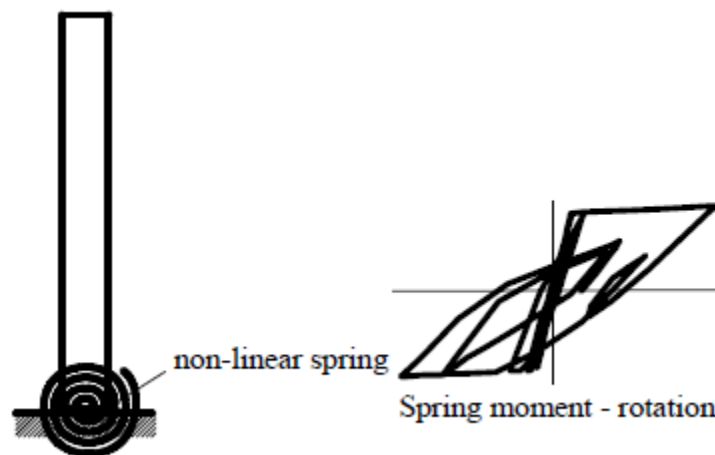


Figure 2-14: Concentrated plasticity model (Montejo, 2008)

An alternative approach is to use the *nonlinearBeamColumn* element object, which is based on the force formulation and considers the spread of plasticity along the element. Table 2-8 shows the *nonlinearBeamColumn* element parameters. The distributed plasticity model as is presented in Figure 2-15, provides general framework for non-linear frame analysis which allow plastic hinges to form at any location and account for axial force-moment interaction by integrating the force-deformation response at sections along the element length (Scott and Fenves, 2006).

Table 2-8: Nonlinear Beam-Column Parameters

element nonlinearBeamColumn \$eleTag \$iNode \$jNode \$numIntgrPts \$secTag \$transfTag < -mass \$massDens> < -iter \$maxIters \$tol>	
\$eleTag	unique element object tag
\$iNode \$jNode	end nodes
\$numIntgrPts	number of integration points along the element
\$secTag	identifier for previously-defined section object
\$transfTag	identifier for previously-defined section coordinate-transformation
\$mass Dens	element mass density (per unit length) from which a lumped-mass matrix is formed (optional, default = 1)
\$maxIters	maximum number of iterations to undertake to satisfy element compatibility (optional, default = 1)
\$tol	tolerance for satisfaction of element compatibility (optional, default = 10 ⁻¹⁶)
Note: The element is prismatic, i.e. the beam is represented by the section model identified by \$secTag at each integration point.	
Code developed by Micheal Scott, Oregon State University	

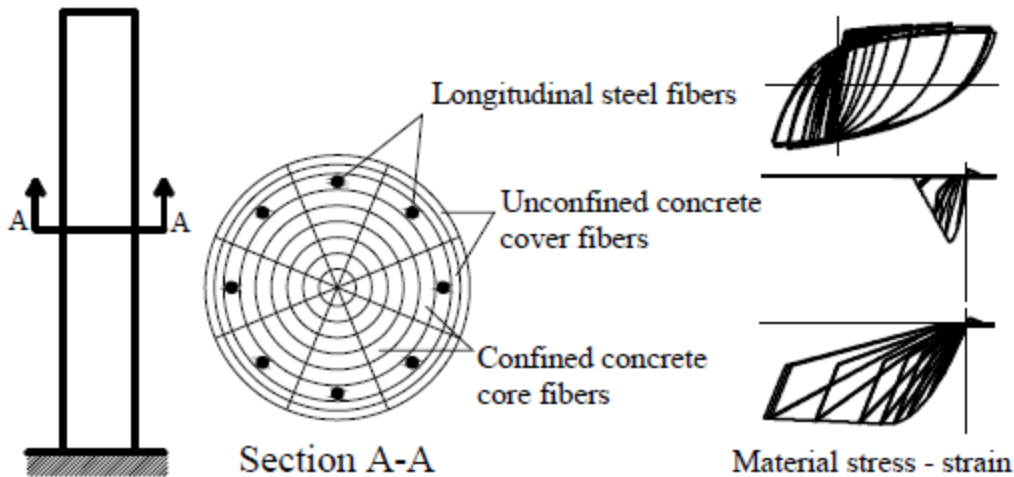


Figure 2-15: Distributed plasticity model (Montejo, 2008)

2.2.3.2 Beam With Hinges Element

This command is used to construct a *beamWithHinges* element object, which is based on the flexibility formulation and considers plasticity to be concentrated over specified hinge lengths at the element ends (Table 2-9).

Table 2-9: Beam With Hinges Parameters

element beamWithHinges \$eleTag \$iNode \$jNode \$secTagI \$Lpi \$secTagJ \$Lpj \$E \$A \$Iz \$transfTag < -mass \$massDens> < -iter \$maxIters \$tol>	
\$eleTag	unique element object tag
\$iNode \$jNode	end nodes
\$secTagI	identifier for previously-defined section object at node \$iNode
\$Lpi	plastic hinge length at end i
\$secTagJ	identifier for previously-defined section object at node \$jNode
\$Lpj	plastic hinge length at end j
\$E	Young modulus elastic portion
\$A	Area for elastic portion
\$Iz	second moment of area for elastic portion about local z
\$transfTag	identifier for previously-defined section coordinate-transformation
\$maxIters	maximum number of iterations to undertake to satisfy element compatibility (optional, default = 1)
\$tol	tolerance for satisfaction of element compatibility (optional, default = 10-16)

Code developed by Micheal Scott, Oregon State University

The *beamWithHinges* element is a *ForceBeamColumn* element. The implementation divides the element in three parts: two hinges at the ends, and a linear-elastic region in the middle (Figure 2-16). The hinges are defined by assigning to each a previously-defined section, e.g., fiber-based approach. The length of the each hinge is also specified by the user.

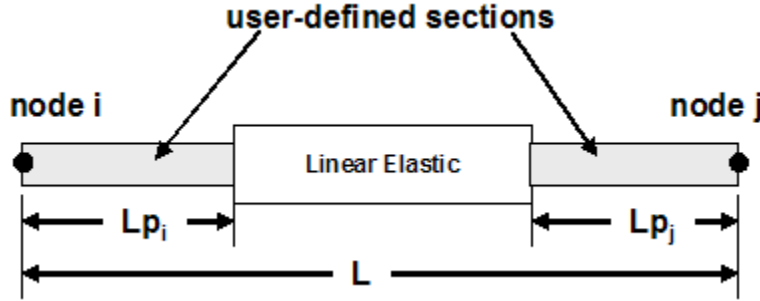


Figure 2-16: Beam With Hinges Element

The value for the plastic hinge length (L_p) was obtained using the approach proposed by Priestley, Seible and Calvi (1996):

$$L_p = kL_c + 0.022 f_s d_{bl} \geq 2 (0.022 f_s d_{bl}) \quad (2-1)$$

where:

$$k : 0.2 \left(\frac{f_{su}}{f_y} - 1 \right) \leq 0.08,$$

L_c : length from the critical section to the point of contraflexure,

f_s : tension stress in the longitudinal bars ($f_s \leq f_y$),

f_y : longitudinal bar yielding stress,

d_{bl} : longitudinal bar diameter, and

f_{su} : longitudinal bar maximum stress.

2.3 Calibration and validation of structural models

This topic covers four column examples. It shows the calibration process in RC structures for the three analytical models. Model calibration is done by direct comparison with the experimental results. Also on this section, the models generation processes are displayed as flowcharts. These figures illustrate the basic process of modeling in OpenSees. Once the

model is built, it begins to be calibrated with different values for the required parameters. In the fiber based approach, for example, parameter calibration includes the longitudinal steel reinforcement parameters (i.e., *CMFatigue* and *MPCurveParams*), especially when rebar fracture is present on the experimental test. For simplification, just the final values (i.e., *CMFatigue* and *MPCurveParams*) used to confirm the validations are presented in each case.

For the first column example (i.e., FL-89A) the experimental response, the theoretical force displacement envelope based on a monotonic moment curvature analysis, and the “OpenSees” predictions for each model are presented. For the remaining three columns, just the fiber-based approach is applied, because as we mentioned earlier, this is the model that will be implemented to validate the damage detection methodologies in reinforced concrete structures.

2.3.1 FL-89A

2.3.1.1 Column Description

FL-89A was a cantilever column built and tested by Montejo (2006) at North Carolina State University, Raleigh, NC. The column was designed with a longitudinal steel ratio of 3% to ensure a flexural failure and it was only exposed to a cyclic pushover test. On the transverse section it has about 1.2% of steel ratio, spirals pitch was 2.33-in. The column and its geometric properties are displayed in Figure 2-17. The reversal cycles for pushover analysis will be explained below.

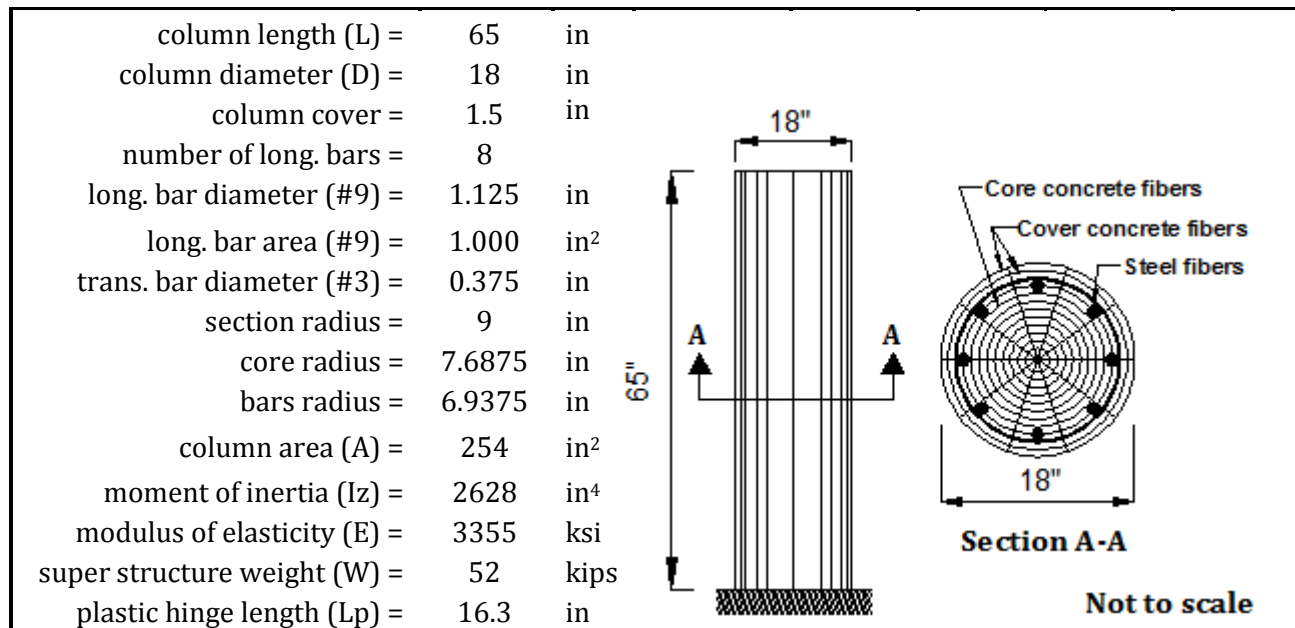


Figure 2-17: FL89A Geometric Properties

The column was tested quasi-statically. The procedure consisted of pushing and pulling the specimen in force control until first yield of the longitudinal reinforcement, and subsequently cycling in displacement control to prescribed ductility levels. The column was tested following the next loading protocol: (1) one cycle up to 0.085in ($\mu = 0.10$); (2) one cycle up to 0.211in ($\mu = 0.25$); (3) one cycle up to 0.423in ($\mu = 0.50$); (4) one cycle up to 0.635in ($\mu = 0.75$); (5) three cycles up to 0.846in ($\mu = 1$); (6) three cycles up to 1.27in ($\mu = 1.5$); (7) three cycles up to 1.70in ($\mu = 2$); (8) three cycles up to 2.12in ($\mu = 2.5$); (9) three cycles up to 2.54in ($\mu = 3$); (10) three cycles up to 3.39in ($\mu = 4$); (11) three cycles up to 5.08in ($\mu = 6$); (12) three cycles up to 5.93in ($\mu = 8$). The loading pattern is shown in Figure 2-18.

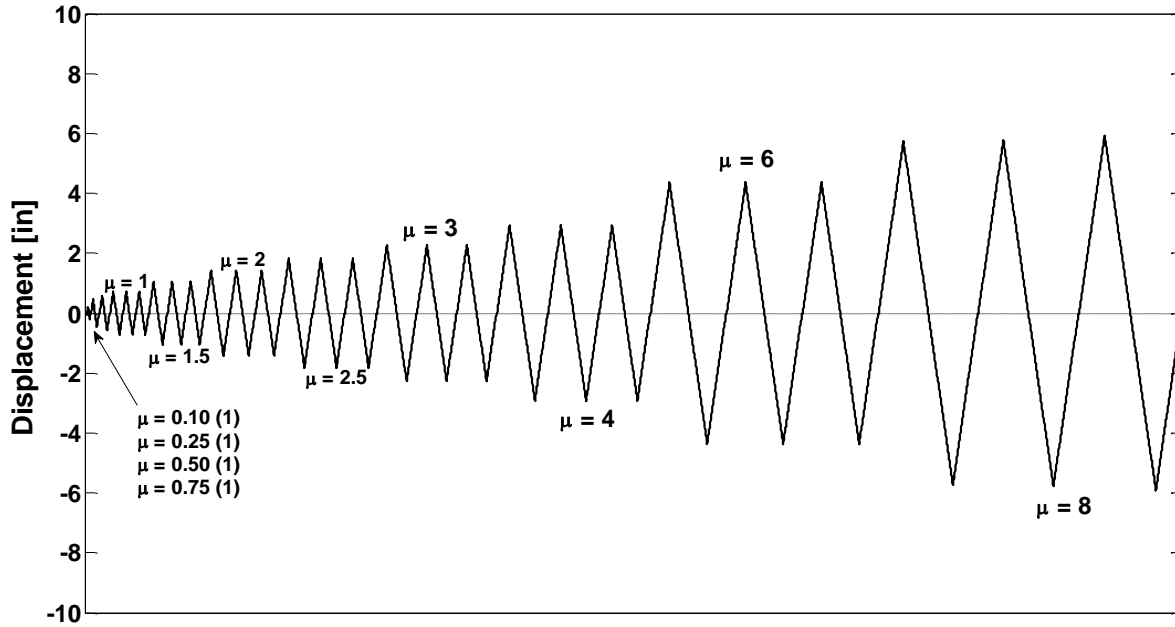


Figure 2-18: Cyclic Test: Displacement Loading History for FL-89A

The bilinear and hysteretic models to represent the column were achieved using the *nonlinearBeamColumn* element. As we mentioned before, the fiber-based approach will be performed using *beamWithHinges* element. The cross-sections of the inelastic elements (i.e. at the column ends) were discretized into 240 fibers, distinguishing between the longitudinal reinforcement bars, the cover concrete and the confined concrete. It may be seen in section A-A of Figure 2-17. However, the three model generations for these columns with all the parameters used are presented next in Figures 2-19, 2-20, and 2-21 (or Appendix A).

Start	
Geometric Properties	
<i>See Figure 2-17</i>	
Stiffness Parameters	
$EI_z = 8816940 \text{ kips-in}^2$ $EA = 852170 \text{ kips}$ $M_v = 4098 \text{ k-in}$ $b = 0.0012$	
Section Generation	
ColSecTag	1
ColMatTagFlex	2
ColMatTagAxial	3
uniaxialMaterial Steel01 \$ColMatTagFlex \$My \$EI \$b; uniaxialMaterial Elastic \$ColMatTagAxial \$EA;	
section Aggregator \$ColSecTag \$ColMatTagAxial P \$ColMatTagFlex Mz;	
Element Generation	
ColTransfTag	1
geomTransf Linear \$ColTransfTag;	
set numIntgrPts	5
element nonlinearBeamColumn 1 1 2 \$numIntgrPts \$ColSecTag \$ColTransfTag;	
Cyclic Pushover Analysis	Dynamic Analysis
End	

Figure 2-19: FL-89A bilinear model generation

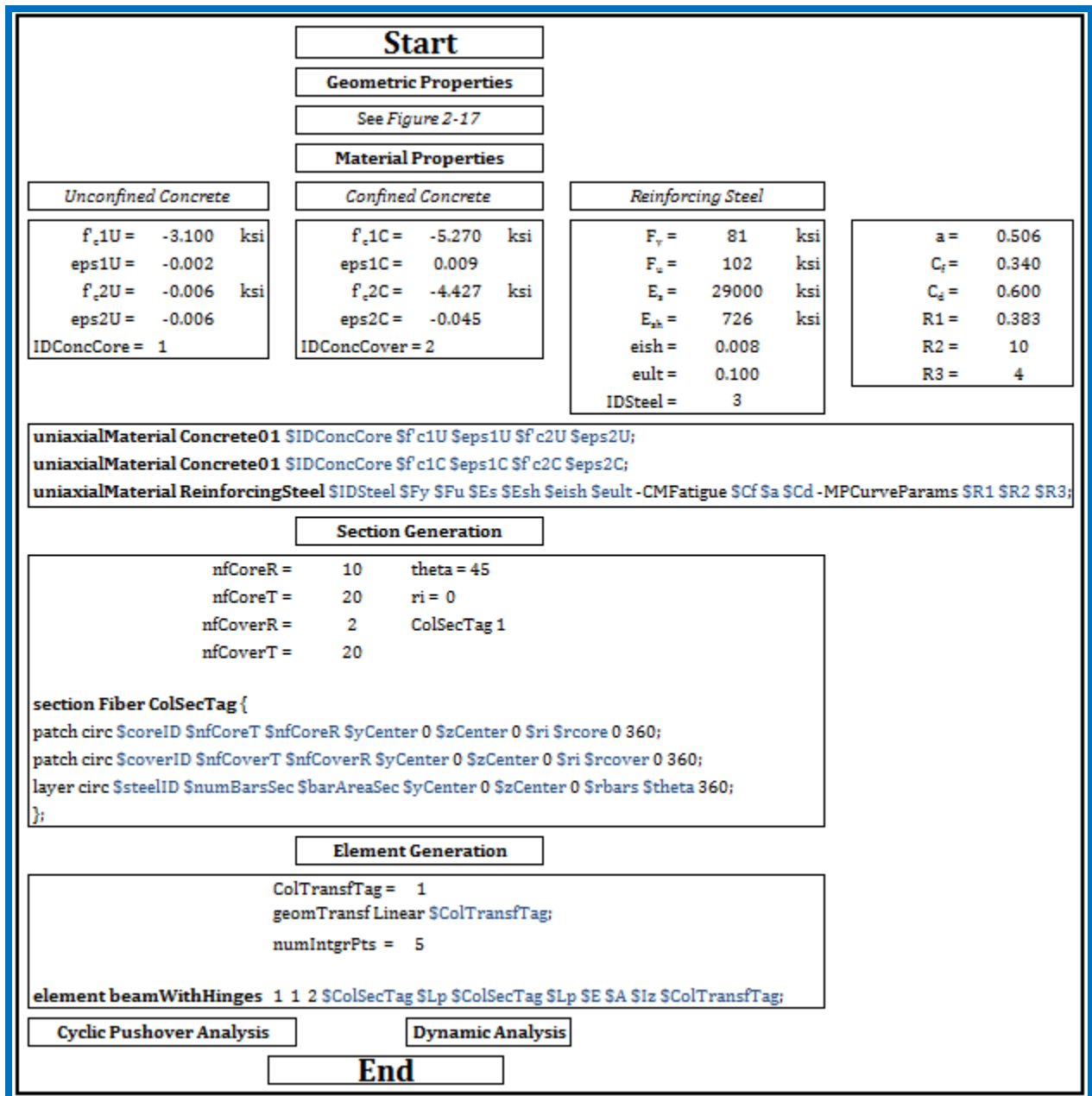


Figure 2-21: FL-89A fiber-based model generation

2.3.1.2 Cyclic Pushover Test Results

The results obtained from the simulations are presented in Figures 2-22 to 2-24. For each unit, the force-displacement was calculated and compared with the theoretical prediction made by CUMBIA and the experimental results. It may be note that an ultimate displacement of 5.93in (corresponding to the ultimate cycle of ductility 8) was reached successfully for the three models. Even though the column had flexural dominated behavior, no rebar fracture occurred.

From the Figures 2-22 (i.e., bilinear model), 2-23 (i.e., hysteretic model) and 2-24 (i.e., fiber-based model), some observations can be made:

- In the case of the bilinear model, it may be noted that the changes in stiffness are much sharper than in the actual column response. This is a serious drawback for this model because it does not represent properly the gradual stiffness degradation proper of well detailed reinforced concrete structures. Moreover, it has no strength degradation during its reversal cycles, which is a typical conduct of RC members, losing strength as they continue receiving cargo. The problem of no strength degradation is represented clearly in Figure 2-22. This implies that column stiffness is intact and ready to receive additional cargo when in reality it does not have it, due to the loss of inertia as a consequence of the reduction in its cross-sectional area.
- In the hysteretic “Takeda like” model, even though it has strength degradation, the problem of sudden (drastic) changes in stiffness continues. Although the stiffness change in this model at the ultimate force point (F_u) of each cycle is lower than in the bilinear model, neither represents the actual inelastic behavior. The stiffness changes of this model are mostly related to the model key points that represent its hysteresis behavior. These points are the yielding point (F_y) and the ultimate point (F_u). An additional change in stiffness of this model is observed when it crosses the zero-force line to begin its next cycle. Therefore, we can say that the hysteretic model is a much more suitable representation than the bilinear model. As such, it has been successfully used for many years by structural engineers for design and assessment purposes.

However, due to the exhibited drastic change in stiffness it is not appropriate for validation of damage detection methodologies.

- Through the use of a more sophisticated approach like the fibers-element model, a better simulation was obtained. There is no doubt that the fiber-based method exhibited the best match with the experimental response in all aspects. Taking a look to the stiffness changes, this method have the finest smooth changes and closely resemble the experimental response. This feat was due to the addition of each constitutive model (i.e., unconfined concrete, confined concrete and steel reinforcement) separately to finally form a single element that picks all properties. Hence, the combination of the constitutive models helps to make the behavior of the stiffness to be smoother and eliminates the abrupt changes shown in the previous models. Based on the results obtained for this first example, only the fiber-based model results are presented for the next 3 examples.

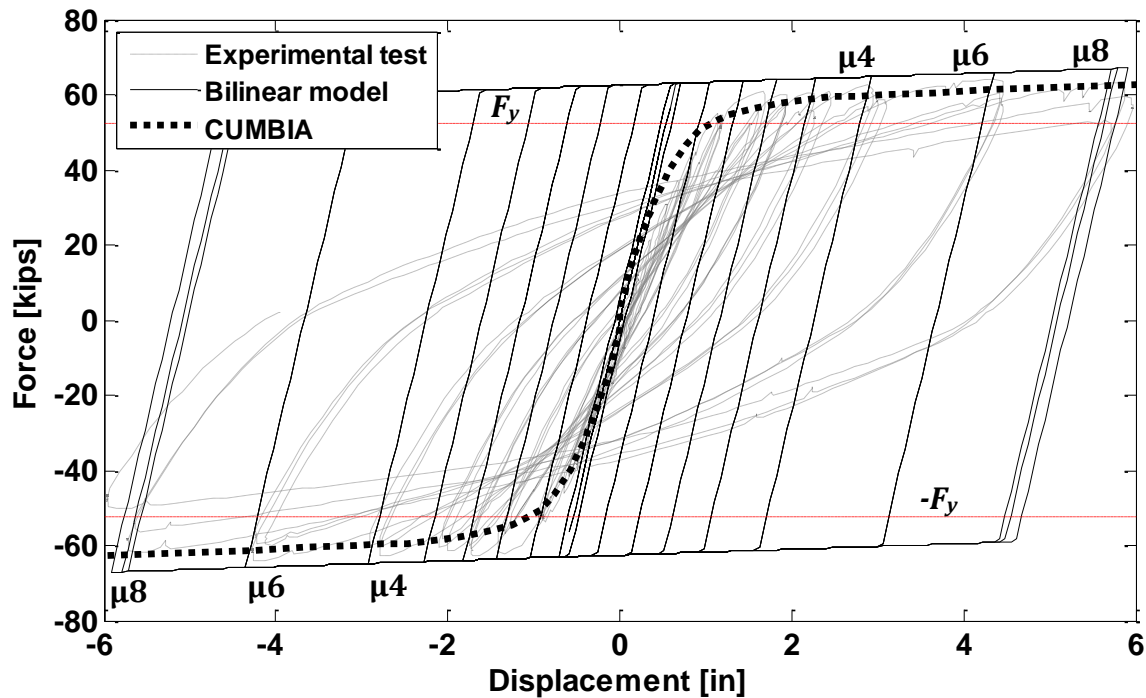


Figure 2-22: Bilinear experimental response and predictions for FL-89A

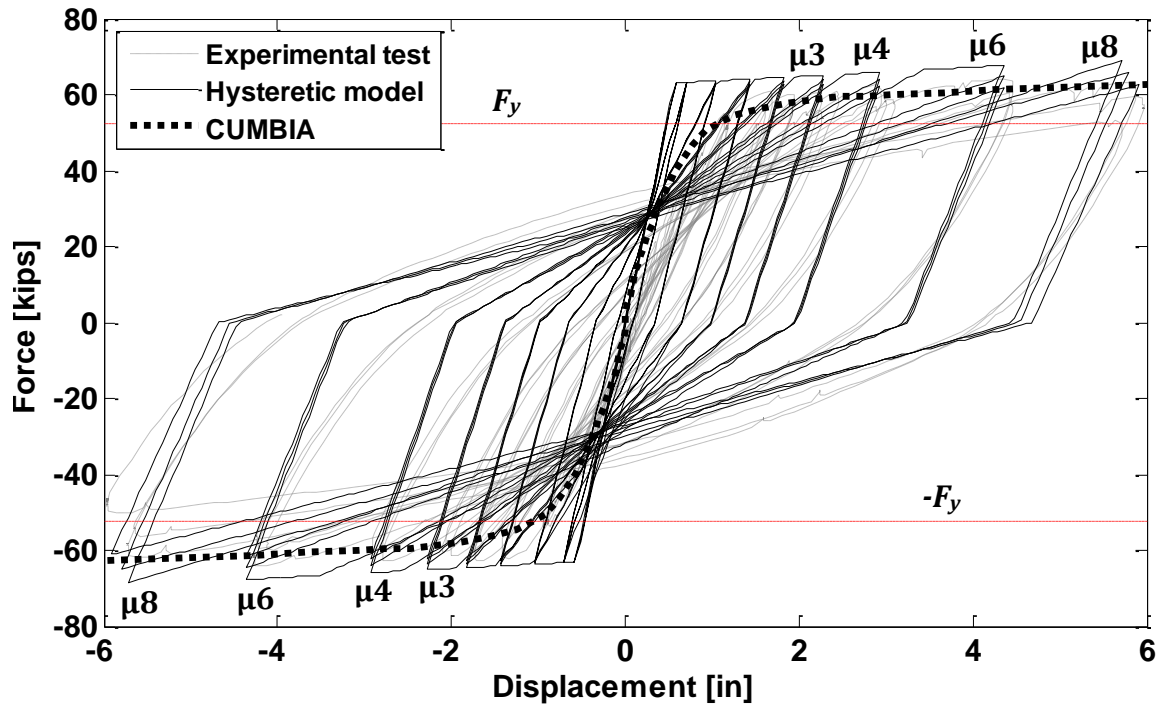


Figure 2-23: Hysteretic experimental response and predictions for FL-89A

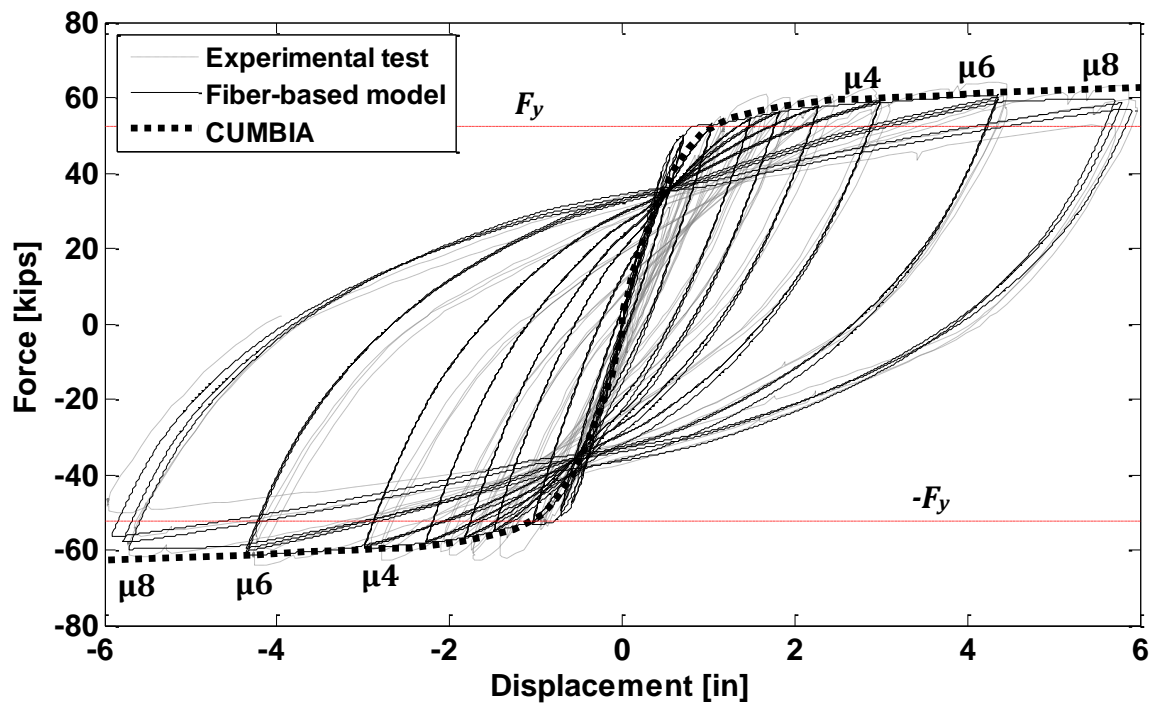


Figure 2-24: Fiber-based experimental response and predictions for FL-89A

2.3.2 SL-P20

2.3.2.1 Column Description

SL-P20 was another column tested by Montejo (2005) at NC State University. This column, as the FL-89A, was subjected to a reversal cyclic pushover. It is very similar to the FL-89A; the main difference is on the steel reinforcement ratio. SL-P20 has less steel reinforcement ratio than the FL-89A column. In particular, SL-P20 has about 1.3% of longitudinal reinforcement. The column, the transversal section and its geometric properties are all shown in Figure 2-25.

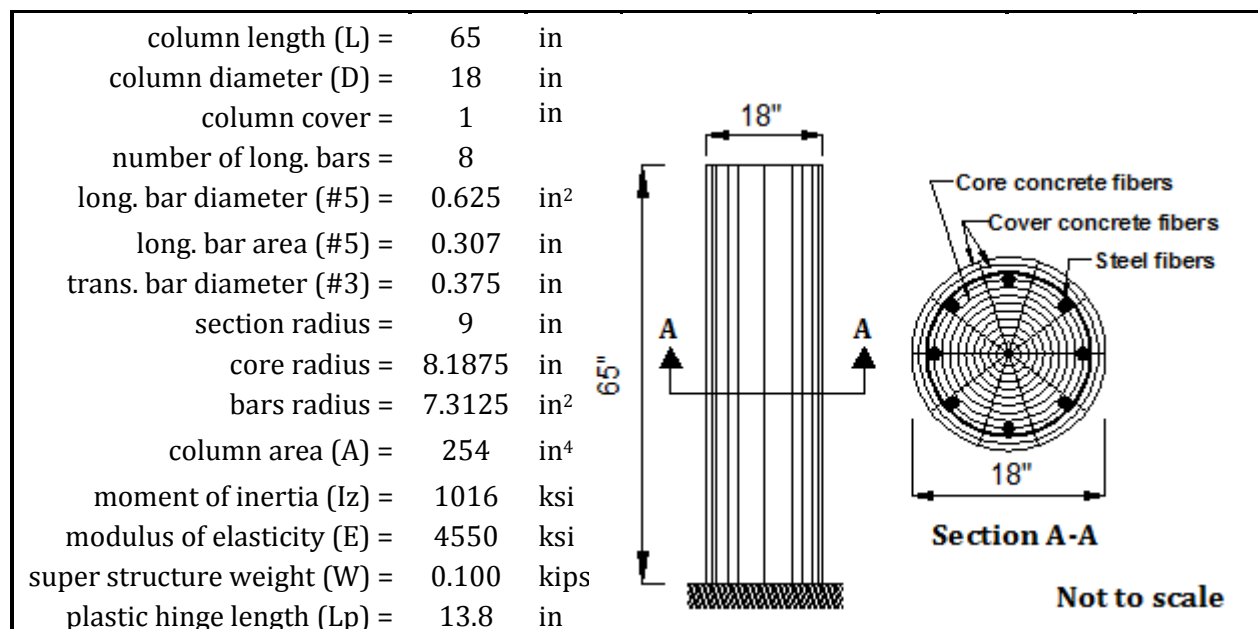


Figure 2-25: SL-P20 geometric properties

For SL-P20, the procedure of cyclic reversal testing was similar to FL-89A. But for this particular case, it was tested up to a displacement that corresponds to ductility 10. The displacement loading history was applied as follow: (1) one cycle up to 0.085in ($\mu = 0.10$); (2) one cycle up to 0.211in ($\mu = 0.25$); (3) one cycle up to 0.423in ($\mu = 0.50$); (4) one cycle up to 0.635in ($\mu = 0.75$); (5) three cycles up to 0.846in ($\mu = 1$); (6) three cycles up to 1.27in ($\mu = 1.5$); (7) three cycles up to 1.70in ($\mu = 2$); (8) three cycles up to 2.12in ($\mu = 2.5$); (9) three cycles up to 2.54in ($\mu = 3$); (10) three cycles up to 3.39in ($\mu = 4$); (11) three cycles up

to 5.08in ($\mu = 6$); (12) three cycles up to 5.93in ($\mu = 8$). The loading pattern is shown in Figure 2-18.

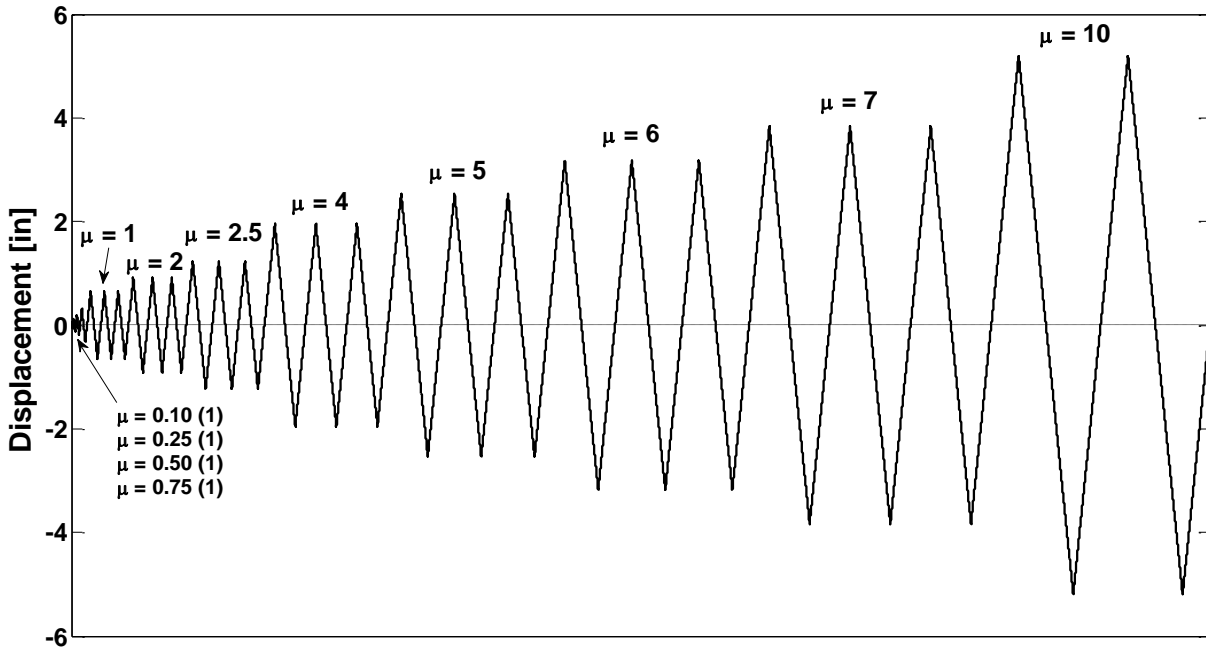


Figure 2-26: Cyclic Test: Displacement Loading History for SL-P20

The fiber-based model generation for this column is demonstrated in Figure 2-27 (or Appendix A). It was performed using *beamWithHinges* element and the cross-sections of the inelastic elements (i.e. at the column ends) were discretized into 240 fibers, distinguishing between the constitutive models illustrated in section A-A of Fig. 2-25.

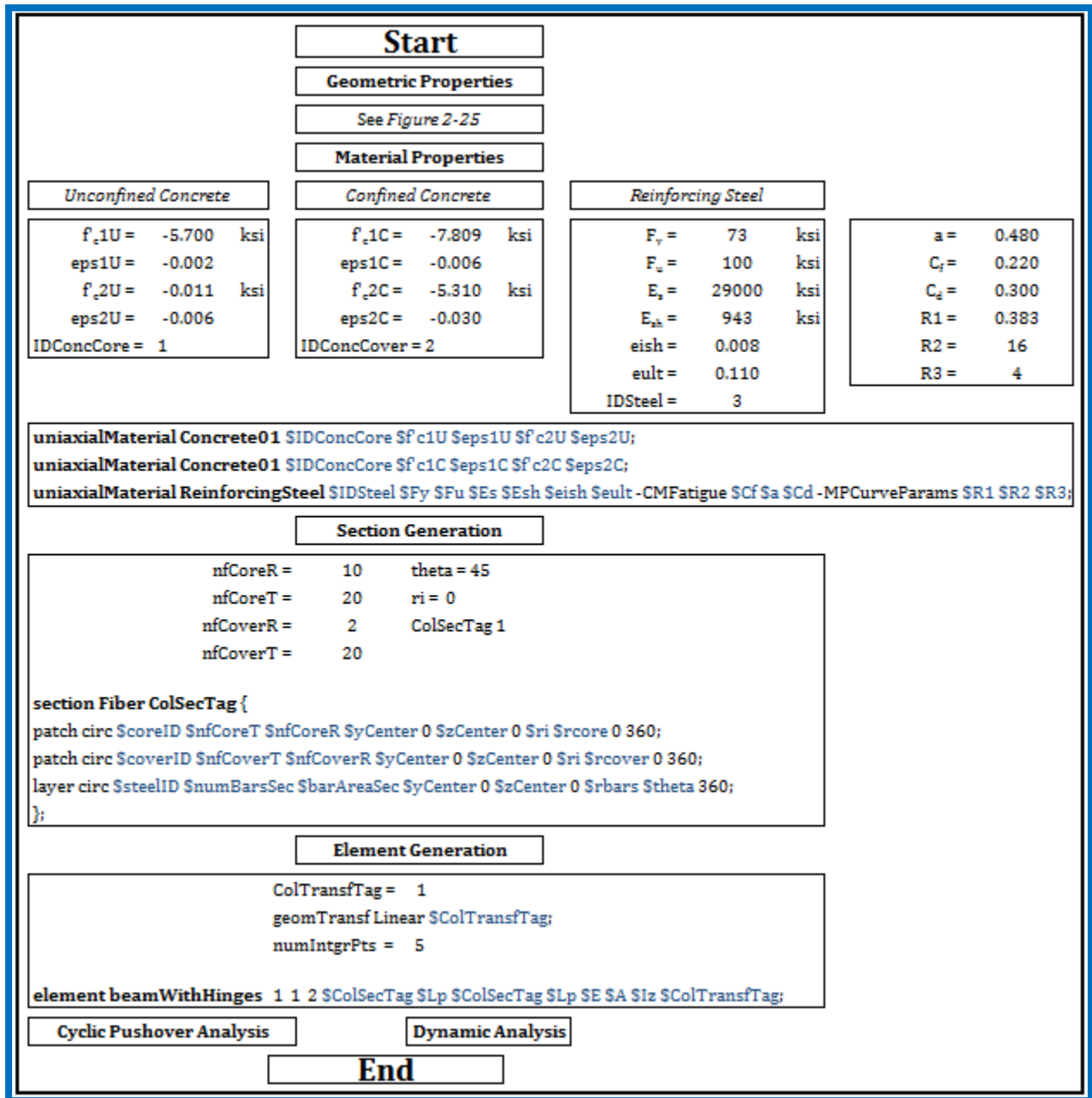


Figure 2-27: SL-P20 fiber-based model generation

2.3.2.2 *Cyclic Pushover Test Results*

The hysteretic force displacement response recorded during the test is displayed in Figure 2-28; this figure also shows the theoretical force displacement envelop of CUMBIA and the OpenSees response. This specimen failed by buckling and then ruptures of the bottom-most bar due to a combination of high axial strain and low cycle fatigue during next half in the pull direction of loading (Montejo, 2008). Figure 2-29a shows the strain when rebar fracture occurs, whereas the displacement corresponding to this strain is presented on Figure 2-29b.

It should be noticed that when the columns are subjected to equal displacements in the two loading directions, the measured lateral force resistance in the push direction is lower than the measured in the pull direction, providing an unsymmetrical response. This difference is the result of different phenomena:

- The steel cages in some of the columns may have been slightly off center (Montejo, 2008).
- When testing the columns in a horizontal position the self-weight of the column and the actuator chair start acting as an additional load in the push direction that is not being recorded (Montejo, 2008).
- Once the concrete in the bottom face of the column crushes it fails from the column due to its own weight, however when the concrete in the top face of the column crushes it stays there providing some strength to the column when the force is applied in the pulling direction (Montejo, 2008).

Nonetheless, the difference is minimal and the measured responses in the two directions can be used to represent the response of the column, and also to validate the fiber-based model.

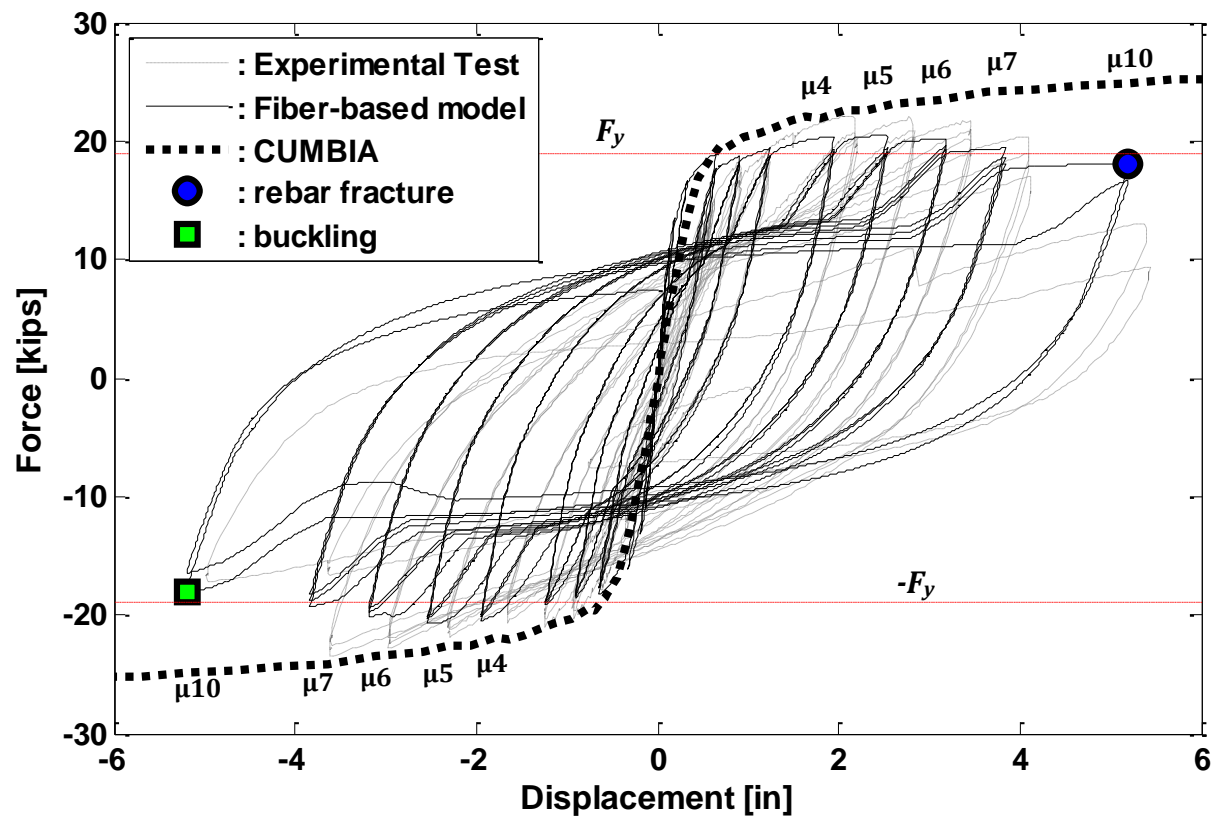


Figure 2-28: Fiber-based experimental response and predictions for SL-P20

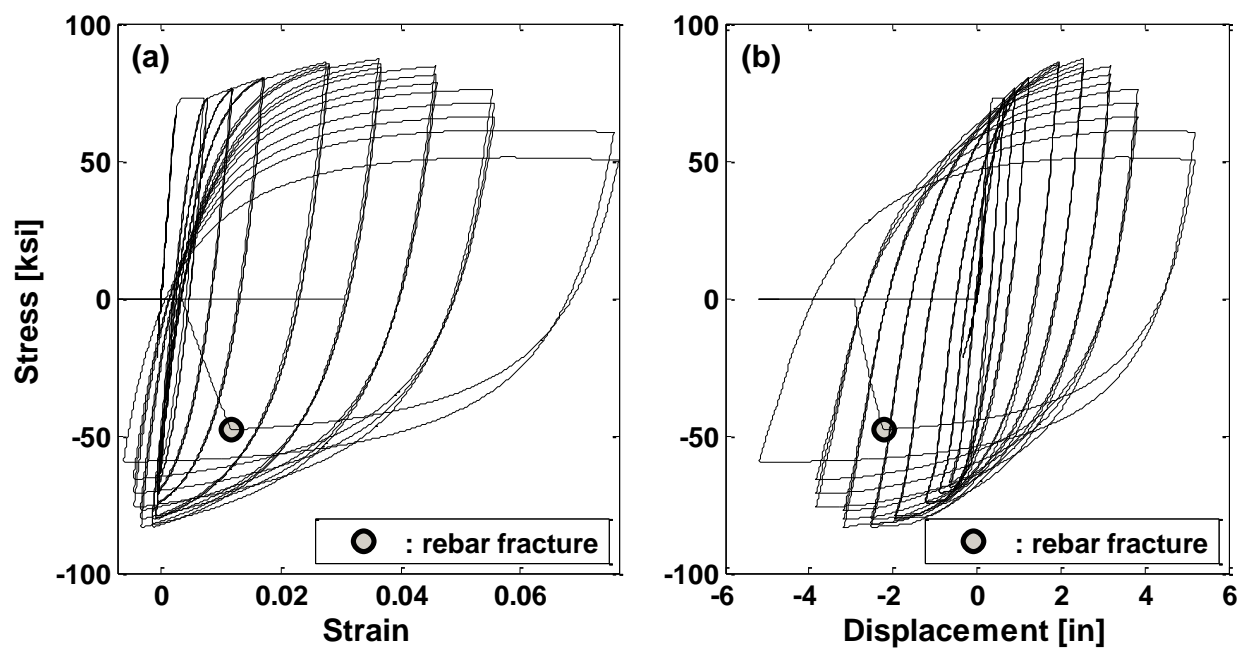


Figure 2-29: (a) Stress-Strain for Reinforcing Steel (b) Stress-Displacement Relationship

2.3.3 EUCENTRE

2.3.3.1 Column Description

EUCENTRE is a bridge pier tested by Petrini *et al.* in 2008. The bridge pier was subjected to a reversal cyclic pushovers of load, but also a dynamic analyzes was performed on another identical bridge pier. The geometric properties (summarized in Fig. 2-30) were chosen considering a full scale standard RC hollow-section cantilever bridge pier and assuming a scaling factor of 4. Concrete and reinforcing steel properties are presented in Figure 2-33. The transversal reinforcement used was a spiral (1.25in \approx 30mm) with the minimum diameter available (0.25in \approx 6mm), it was designed to allow a plastic hinge development and ductile behavior (Petrini *et al.*, 2008).

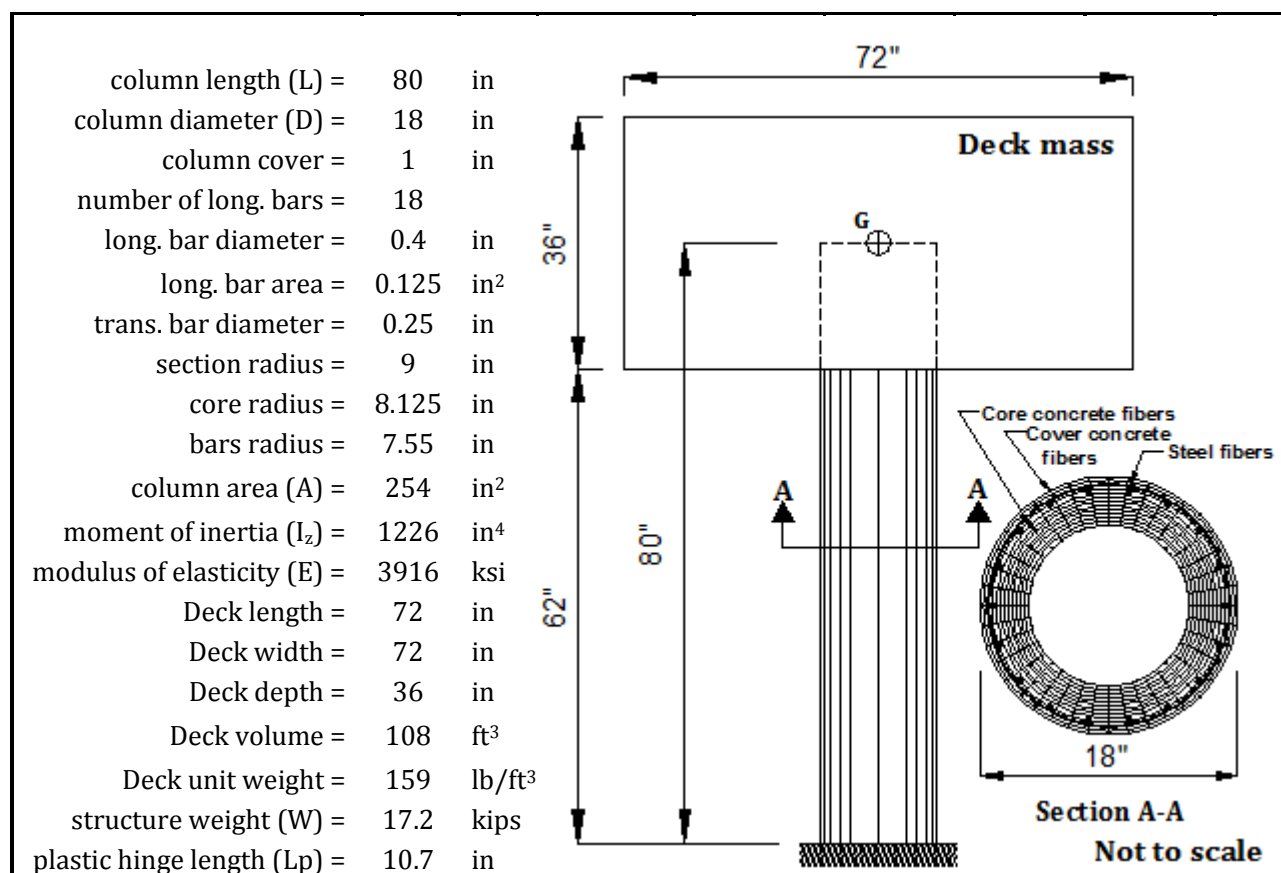


Figure 2-30: EUCENTRE bridge pier geometric properties

The cyclic analysis was performed based on a bi-linear approximation to the moment-curvature diagram of the pier base cross-section. Petrini *et al.* determine a yield displacement of 0.7in and an ultimate displacement of 4.33in, corresponding to a displacement ductility μ of 6, calculated according to approaches presented in Priestly *et al.* (1996).

Taking into account these values, the displacement loading history of the cyclic test was selected (Figure 2-31). The displacement series was divided in eight sequences: (1) 3 cycles up to 0.033in (displacement ductility $\mu = 0.05$); (2) 3 cycles up to 0.067in ($\mu = 0.1$); (3) 3 cycles up to 0.511in ($\mu = 0.75$); (4) 3 cycles up to 1.33in ($\mu = 2$); (5) 1 cycle up to 0.669in ($\mu = 1$); (6) 3 cycles up to 2.67in ($\mu = 4$); (7) 1 cycle up to 0.669in ($\mu = 1$); (8) 3 cycles up to 3.94in ($\mu = 6$).

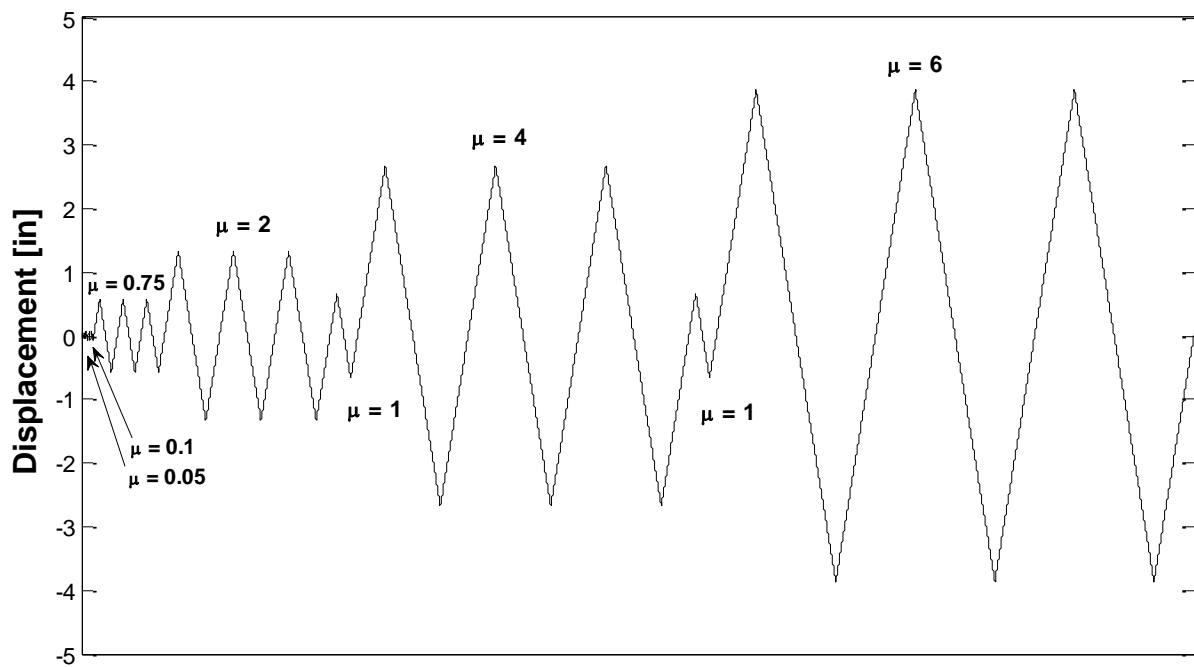


Figure 2-31: EUCENTRE Cyclic Test: Displacement Loading History

On the dynamic analysis, the pier was excited with a scaled recorded accelerogram using the EUCENTRE shaking table. For the selection of the input ground motion, the Pacific Earthquake Engineering Research Center (PEER, 2006) and the Woodward-Clyde Federal Services of Pasadena ground motion database were consulted. After a large amount of

analyzes, the Morgan Hill Earthquake (1984, Halls Valley, $M = 6.2$, $PGA = 0.15g$) scaled to a $1.2g$ of PGA was adopted. This accelerogram was able to induce in the pier several cycles in the plastic range with displacement ductility between 4 and 6 (from the initial analyzes it was determined that a peak displacement corresponding to $\mu = 6$ was the maximum stable displacement response), allowing a more accurate study of the influence of the model parameters on the nonlinear structural response. During the data processing, the registered values were filtered to remove high-frequency noise.

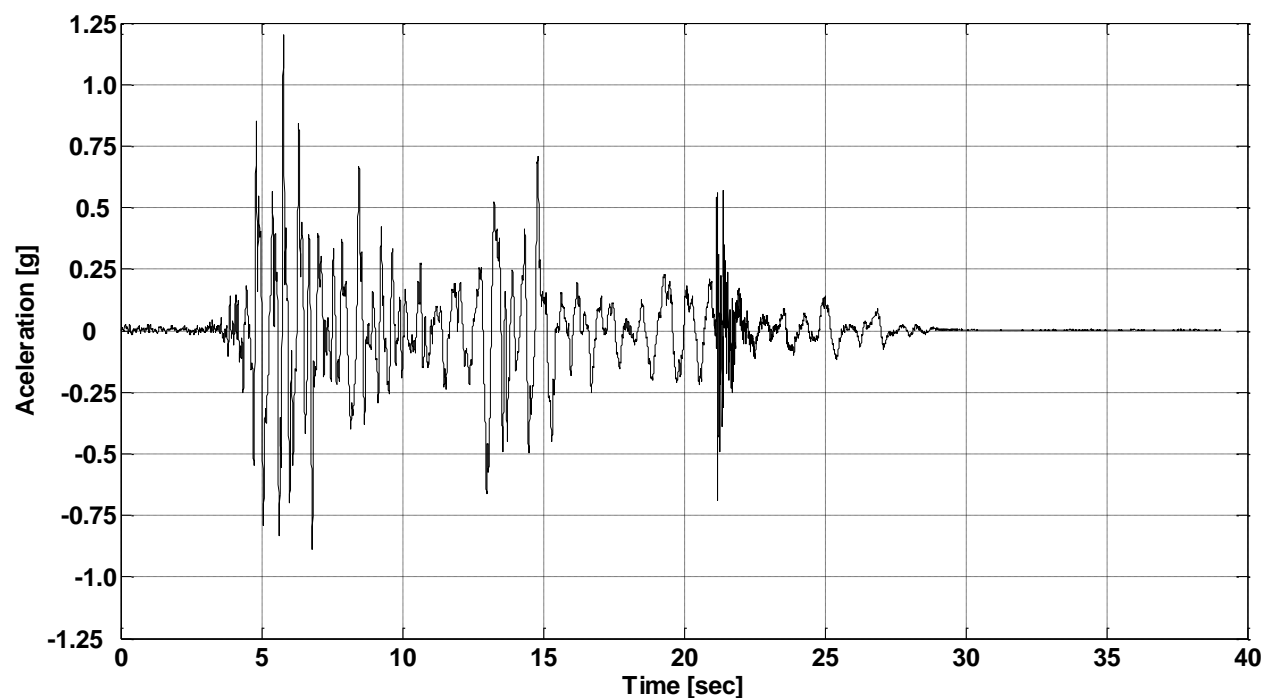


Figure 2-32: Shaking table test: input ground motion (Morgan Hill - 1984 scaled to $1.2g$ PGA)

2.3.3.2 Fiber-based Model

Using the OpenSees *Fiber* section and the *beamWithHinges* element, the EUCENTRE column was modeled with 80 inches from the base to the center of gravity (where its weight -17.2 kips– is concentrated). The cross-sections of the inelastic elements (i.e. at the pier ends) were discretized into 960 fibers, it can be seen in section A-A of Fig. 2-30.

Start			
Geometric Properties			
See Figure 2-30			
Material Properties			
Unconfined Concrete $f_{c1U} = -5.656$ ksi $\epsilon_{s1U} = -0.002$ $f_{c2U} = -0.006$ ksi $\epsilon_{s2U} = -0.006$ IDConcCore = 1	Confined Concrete $f_{c1C} = -7.491$ ksi $\epsilon_{s1C} = -0.005$ $f_{c2C} = -4.467$ ksi $\epsilon_{s2C} = -0.026$ IDConcCover = 2	Reinforcing Steel $F_y = 75$ ksi $F_u = 104.5$ ksi $E_s = 29000$ ksi $E_{sh} = 726$ ksi $\epsilon_{sh} = 0.008$ $\epsilon_{ult} = 0.100$ IDSteel = 3	$a = 0.506$ $C_i = 0.250$ $C_d = 0.500$ $R1 = 0.383$ $R2 = 16$ $R3 = 8$
<pre> uniaxialMaterial Concrete01 \$IDConcCore \$f c1U \$eps1U \$f c2U \$eps2U; uniaxialMaterial Concrete01 \$IDConcCore \$f c1C \$eps1C \$f c2C \$eps2C; uniaxialMaterial ReinforcingSteel \$IDSteel \$Fy \$Fu \$Es \$Esh \$eish \$eult -CMFatigue \$Cf \$a \$Cd -MPCurveParams \$R1 \$R2 \$R3; </pre>			
Section Generation			
<pre> nfCoreR = 20 theta = 20 nfCoreT = 40 ri = 5.5 nfCoverR = 4 ColSecTag 1 nfCoverT = 40 </pre> <pre> section Fiber ColSecTag { patch circ \$coreID \$nfCoreT \$nfCoreR \$yCenter 0 \$zCenter 0 \$ri \$rcore 0 360; patch circ \$coverID \$nfCoverT \$nfCoverR \$yCenter 0 \$zCenter 0 \$ri \$rcore 0 360; layer circ \$steelID \$numBarsSec \$barAreaSec \$yCenter 0 \$zCenter 0 \$rbars \$theta 360; }; </pre>			
Element Generation			
<pre> ColTransfTag = 1 geomTransf Linear \$ColTransfTag; numIntgrPts = 5 </pre> <pre> element beamWithHinges 1 1 2 \$ColSecTag \$Lp \$ColSecTag \$Lp \$E \$A \$Iz \$ColTransfTag; </pre>			
Cyclic Pushover Analysis		Dynamic Analysis	
End			

Figure 2-33: EUCENTRE Fiber-based model generation

2.3.3.3 Cyclic Pushover Test Results

The results of the cycle test performed at the EUCENTRE of Pavia, Italy were used to calibrate and validate the analytical fiber-based model. In addition, the analytical prediction from the monotonic moment-curvature analysis was also used to compare with the fibers approach. With the results of the cycle test analysis, the hysteresis curve (shown in Fig. 2-34) was obtained.

Comparing the force-displacement response of the fiber-based model prediction with the experimental specimen, it was noted that the computational results underestimated the pier strength, even though the strength hardening was alike. Note that initial peak force levels at $\mu = 2$ and 4 in the positive quadrant exceeded the predicted values by about 15%, but in the reversed direction (negative quadrant) and in subsequent cycles to a given ductility level the correlation was excellent. In the case of the monotonic moment-curvature prediction, it compares very well with the response of the fiber-based model, but it equals the same behavior of the fibers simulation when it is compared with the experimental test.

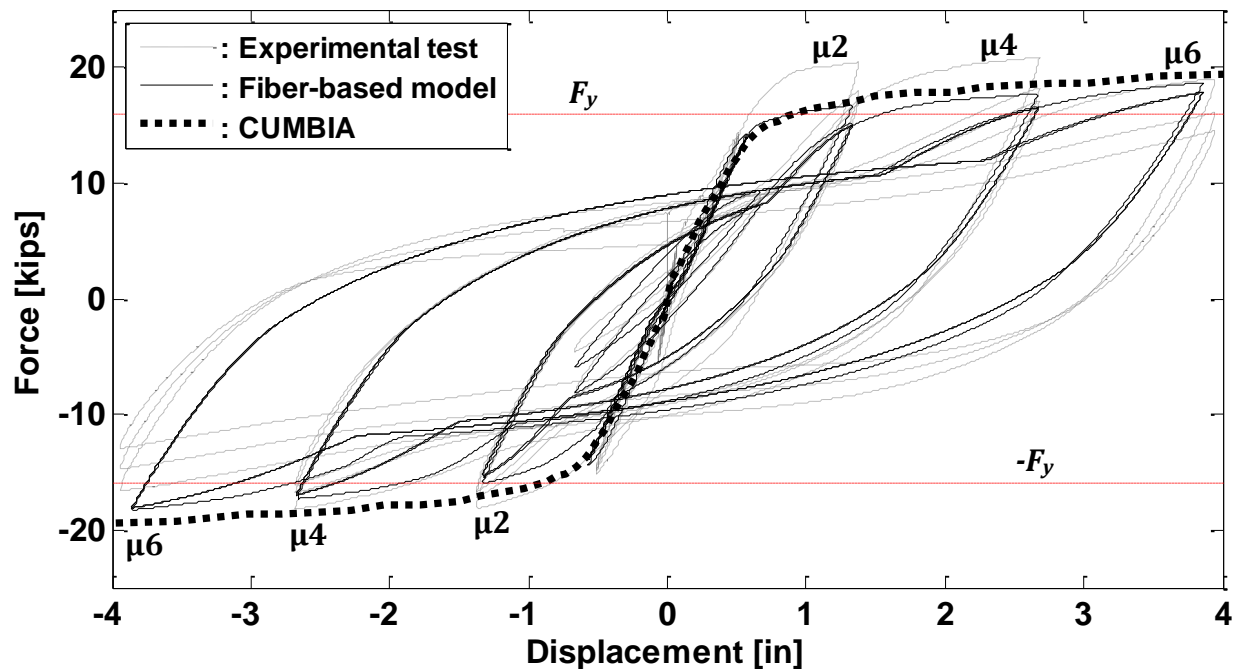


Figure 2-34: Fiber-based response and predictions for EUCENTRE

2.3.3.4 Dynamic Analysis Test Results

Figure 2-35 compares the results obtained with the fiber model with the experimental dynamic test obtained from the EUCENTRE shake table. Considering first the experimental response, it is seen that the peak displacement is reached at 3.5 seconds to about 4-in, the value corresponding to $\mu = 6$. This corresponds to the peak displacement capacity from the static test. In the following cycles, strength degradation was significant (Petrini *et al.* 2008). Between 10 and 10.4 seconds, another large displacement pulse takes place, reaching a negative displacement of 6.5-in, corresponding to a displacement ductility factor of $\mu = 10$. It induced severe strength degradation and it was eventually accompanied by fracture of all flexural reinforcement at the column base, causing catastrophic failure of the column (Petrini *et al.* 2008). For that reason, it may be noted that the displacement time-histories is presented up to 12.5 seconds of analysis (time in where the fracture occurs) in comparison of approximately 40 seconds of earthquake duration.

The fiber-based model prediction provided good representation of the experimental response. Around 10 seconds the strength degradation resulting from fracture of the flexural reinforcement was captured and the displacement were in close agreement. It may be noted that the maximum displacement (in absolute value) for the experimental test is 8.5-in, while the fiber model is 8.1-in, meaning a decent prediction of the fiber model simulation. The maximum values for each direction are shown in Table 2-10.

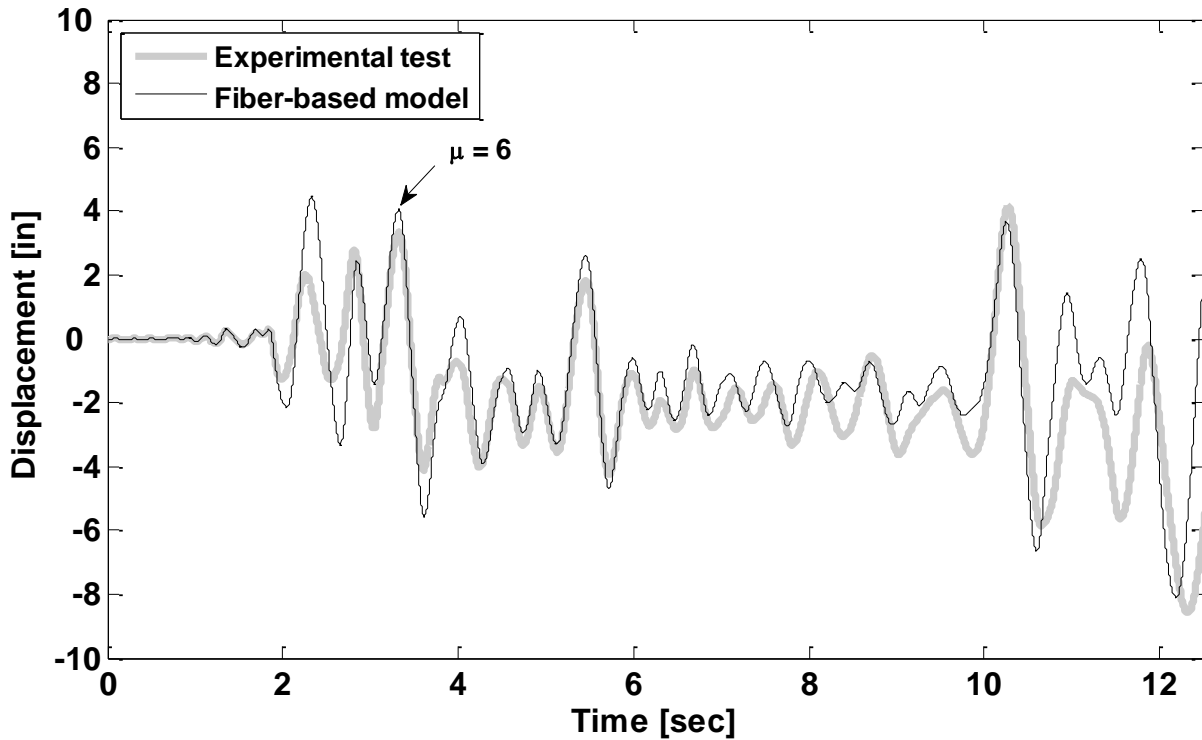


Figure 2-35: Experimental response and predicted displacement time-histories for dynamic test

Table 2-10: Numerical vs Experimental positive and negative peak displacements

	Max Displacement [in]	Min Displacement [in]
Experimental test	4.18	-8.56
Fiber-based model	4.44	-8.11

2.3.4 UCSD

2.3.4.1 Column Description

UCSD is a bridge pier built and tested by University of California at San Diego for a Blind Prediction Contest in 2010. The geometric dimensions (summarized in Fig. 2-36) were chosen considering a full-scale reinforced concrete bridge pier tested on the NEES Large High-Performance Outdoor Shake Table located at *UCSD's Englekirk Structural Engineering Center*.

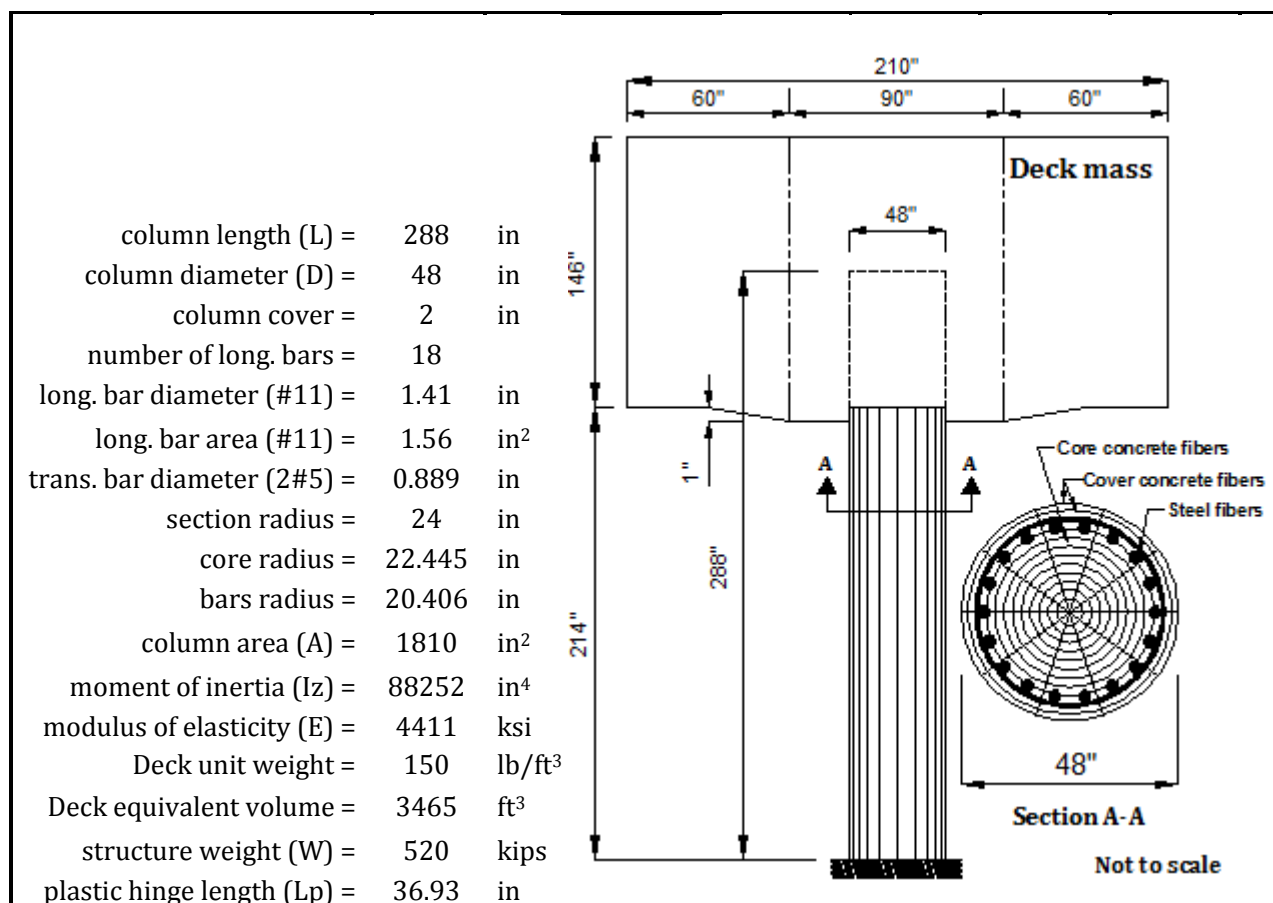


Figure 2-36: UCSD Geometric Properties

In particular, for this column, the experimental test for cyclic analysis was not performed. However, its cyclic pushover simulation was performed and compared with the prediction of CUMBIA. This was done to partially validate the model before proceeding to the dynamic analysis. In both analyzes, a P- Δ effect was considered due to the large mass at the top of the pier and the pier length. Figure 2-37 presents the displacement time-history at which the column was subjected. The test protocol was based in a moment-curvature analysis from CUMBIA.

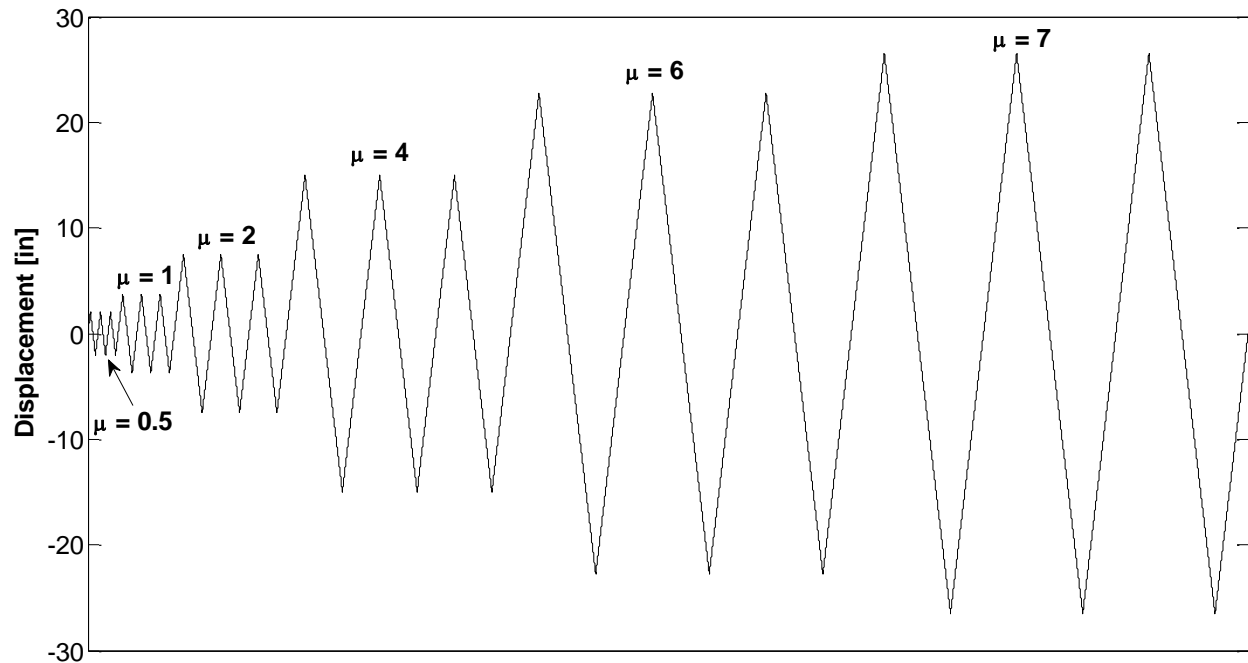


Figure 2-37: UCSD Cyclic Test: Displacement Loading History

On the dynamic analysis, the bridge pier was subjected to an increasing intensity of uniaxial earthquake ground motions starting with low-intensity shaking and bringing the column progressively to near-collapse conditions. The test protocol included white-noises excitations, to identify the dynamic properties of the system, as well as historical earthquake records reproduced with the 25-ft x 40-ft uniaxial shake table (Figure 2-38).



Figure 2-38: UCSD Shake Table

The earthquakes (summarized in Table 2-11) used for the contest were *Loma Prieta* (at different stations) from October 17, 1989 and *Kobe* from January 16, 1995. Corralitos and LGPC stations from Loma Prieta earthquake were repeated for a total of six earthquakes. Figure 2-39 shows the acceleration time-history applied to the bent.

Table 2-11: Ground motions induced to the UCSD bridge pier

TEST	Earthquake	Station Name	PEER ID	Magnitude	Duration*
EQ1	Loma Prieta	AGNEWS STATE HOSPITAL	AGW090.AT2	6.9	70
EQ2	Loma Prieta	CORRALITOS	CLS090.AT2	6.9	70
EQ3	Loma Prieta	LGPC	LGP000.AT2	6.9	55
EQ4	Loma Prieta	CORRALITOS	CLS090.AT2	6.9	70
EQ5	Kobe	TAKATORI	TAK000.AT2	6.9	71
EQ6	Loma Prieta	LGPC	LGP000.AT2	6.9	55

* unit: seconds

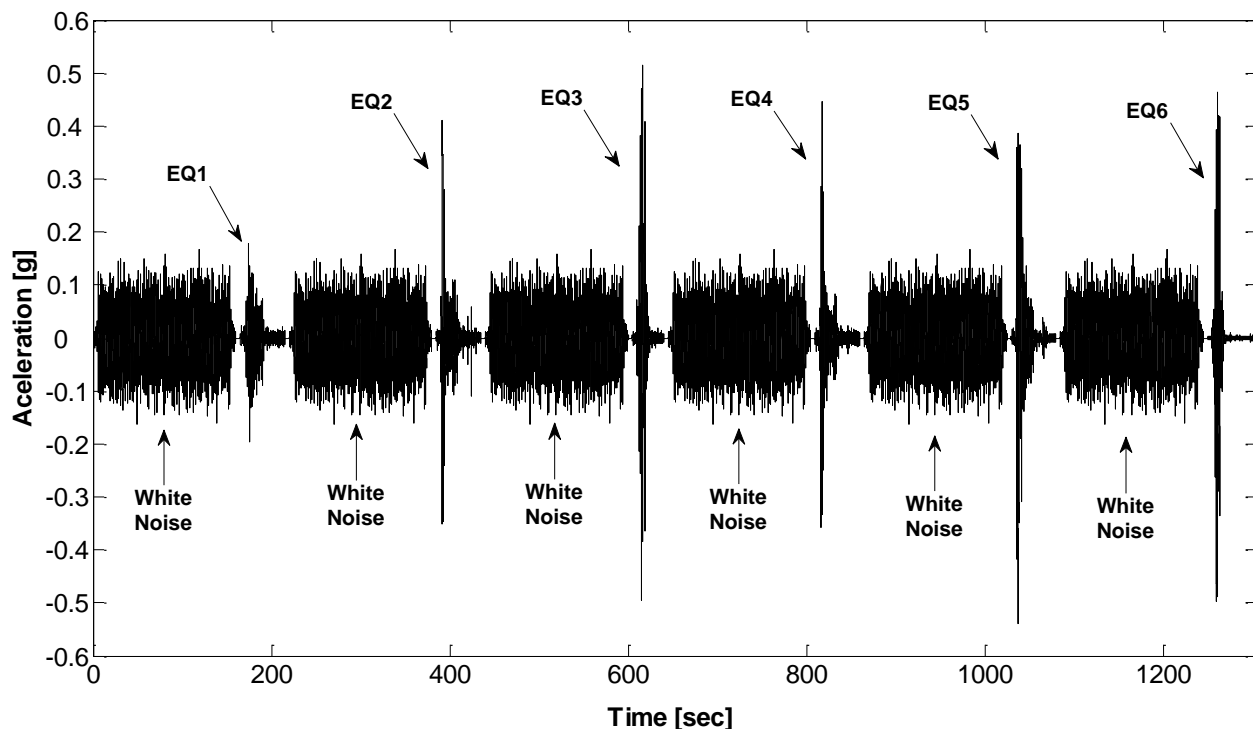


Figure 2-39: UCSD Dynamic test: Acceleration time-history

The essential properties for the model generation in OpenSees are presented in Figure 2-40. As the EUCENTRE pier member, the fibers discretization carried out on this model was 960, distributed between the longitudinal reinforcement bars, the cover concrete and the confined concrete, as shown in section A-A of Figure 2-36. In addition, the model includes the P- Δ effects (marks with a red circle in the figure) that was previously

mentioned. This effect is related to the magnitude of the axial load, stiffness of the structure as a whole and the slenderness of individual elements. For this cantilever column with a 24-ft of height and 4-ft of diameter, the slenderness ratio is 12 (kL/d ; $k = 2$ for *free-fixed ends*).

Start			
Geometric Properties			
See Figure 2-33			
Material Properties			
<i>Unconfined Concrete</i>	<i>Confined Concrete</i>	<i>Reinforcing Steel</i>	
$f_{c1U} = -5.366$ ksi $\epsilon_{s1U} = -0.002$ $f_{c2U} = -0.145$ ksi $\epsilon_{s2U} = -0.006$ IDConcCore = 1	$f_{c1C} = -6.984$ ksi $\epsilon_{s1C} = -0.005$ $f_{c2C} = -4.562$ ksi $\epsilon_{s2C} = -0.026$ IDConcCover = 2	$F_y = 75.2$ ksi $F_u = 102.4$ ksi $E_s = 29000$ ksi $E_{sh} = 726$ ksi $\epsilon_{sh} = 0.008$ $\epsilon_{ult} = 0.100$ IDSteel = 3	$a = 0.506$ $C_i = 0.300$ $C_d = 0.600$ $R1 = 0.383$ $R2 = 16$ $R3 = 8$
<pre> uniaxialMaterial Concrete01 \$IDConcCore \$f_c1U \$eps1U \$f_c2U \$eps2U; uniaxialMaterial Concrete01 \$IDConcCore \$f_c1C \$eps1C \$f_c2C \$eps2C; uniaxialMaterial ReinforcingSteel \$IDSteel \$F_y \$F_u \$E_s \$E_{sh} \$Se_{sh} \$e_{ult} -CMFatigue \$C_f \$a \$C_d -MPCurveParams \$R1 \$R2 \$R3; </pre>			
Section Generation			
<pre> nfCoreR = 20 theta = 20 nfCoreT = 40 ri = 0 nfCoverR = 4 ColSecTag 1 nfCoverT = 40 </pre> <pre> section Fiber ColSecTag { patch circ \$coreID \$nfCoreT \$nfCoreR \$yCenter 0 \$zCenter 0 \$ri \$rcore 0 360; patch circ \$coverID \$nfCoverT \$nfCoverR \$yCenter 0 \$zCenter 0 \$ri \$rcore 0 360; layer circ \$steelID \$numBarsSec \$barAreaSec \$yCenter 0 \$zCenter 0 \$rbars \$theta 360; }; </pre>			
Element Generation			
<pre> ColTransfTag = 1 geomTransf(PDelta) \$ColTransfTag; numIntgrPts = 5 </pre> <pre> element beamWithHinges 1 1 2 \$ColSecTag \$Lp \$ColSecTag \$Lp \$E \$A \$Iz \$ColTransfTag; </pre>			
Cyclic Pushover Analysis		Dynamic Analysis	
End			

Figure 2-40: UCSD Fiber-based Model Generation

2.3.4.2 Cyclic Pushover Test Results

Based on the results obtained from the prediction of CUMBIA and the model simulation, the comparison of both predictions are shown in Figure 2-41. At first glance, it may be note the great difference existing in the level forces once both leave the elastic range. The force prediction made by CUMBIA tends to keep increasing whereas the OpenSees simulation tends to decreases. This force level decay for the simulation is basically due to the P- Δ effect. The P- Δ effect tends to decrease the level force when large displacements are achieved. It is due because P- Δ effect take into account a destabilizing force resulting from very high structures (that is relative to its thickness) and it is added to the moment on the base. As the result of these combinations, the column reaches a maximum level force of ~ 150 kips at ductility 2 and then it reduces down to 125 kips at ductility 7.

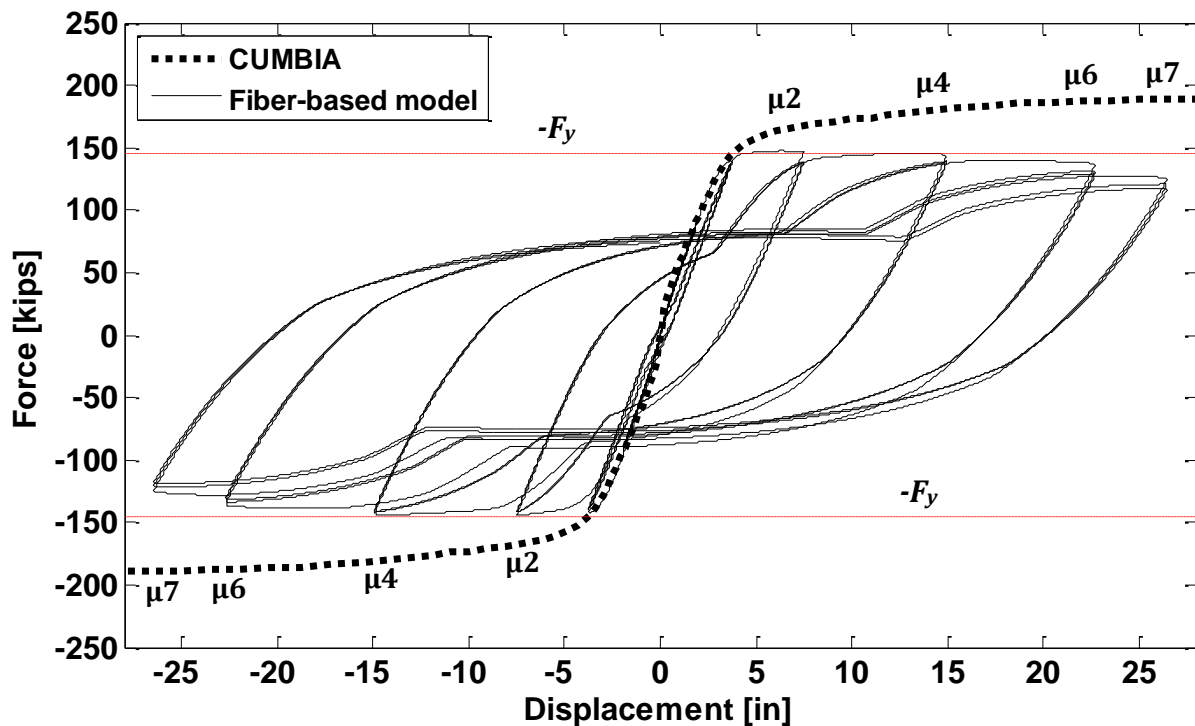


Figure 2-41: Fiber-based simulation and CUMBIA prediction for UCSD

2.3.4.3 *Dynamic Analysis Test Results*

Experimental results were obtained from the UCSD shaking table test. Comparison of the horizontal relative displacements and total accelerations from the test response and predictions are presented next in Figures 2-42 to 2-47. There are several observations that should be made from the results presented on these figures:

- The results presented are not calibrated. We participated of the blind prediction contest and the results presented here are those obtained from our blind prediction without any correction.
- It may be note that the accelerations of the experimental results are smooth, unlike the obtained from our numerical model. The reason is that accelerations measured during the test were filtered to take-off the high frequencies of the response before they were provided to the general public.
- At the figures 2-45 to 2-47, we can appreciate that the horizontal relative displacements do not start from zero-displacement. This is because the earthquakes were applied one behind the other separated by a white noise. When it occurs, the following earthquakes begin at the level of displacement in where the previous earthquake ended. These relative displacements are present in EQ4, EQ5 and EQ6.
- The time duration for each earthquake not coincides with the time duration from Table 2-11. Only the results for the strong motion part are presented to allow a better comparison of the relative displacements and total accelerations.

Tables 2-12 and 2-13 summarize the maximum positives and the maximum negatives values for the horizontal relative displacements and accelerations registered during the shaking table test and those calculates by the fiber-based model simulation. It is seen that the maximum values are in close agreement.

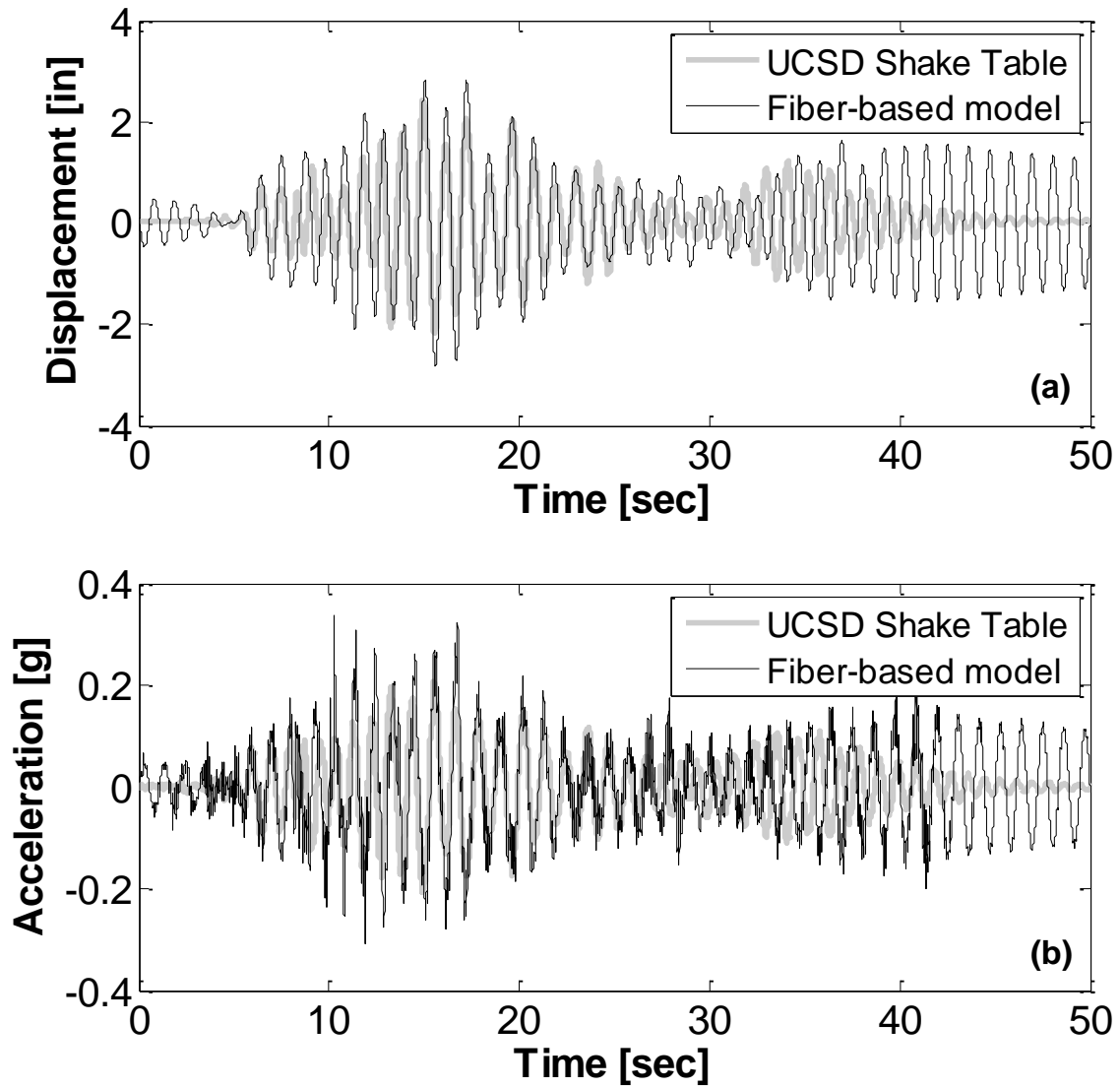


Figure 2-42: (a) Displacement time-histories for EQ1, (b) Acceleration time-histories for EQ1

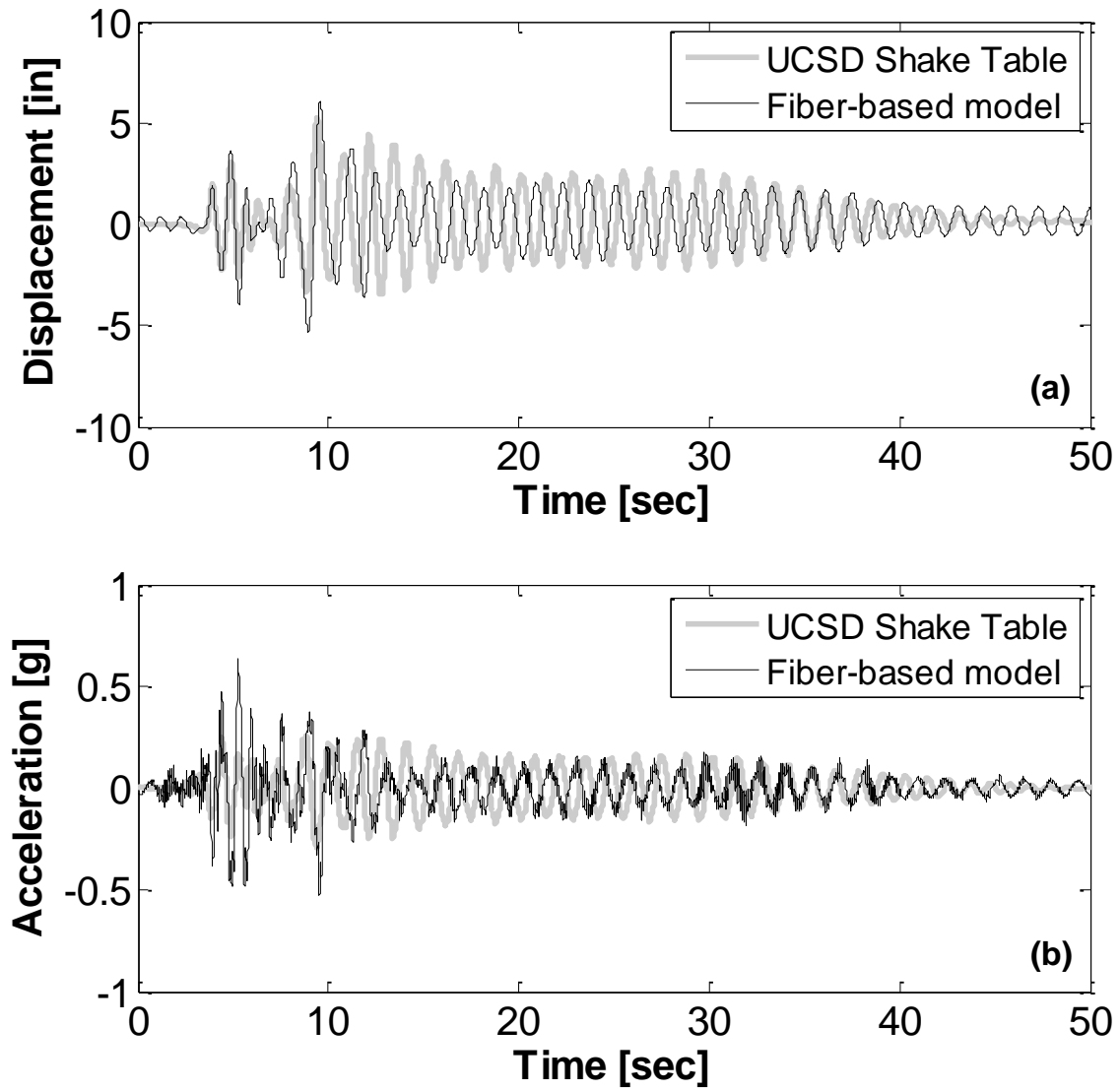


Figure 2-43: (a) Displacement time-histories for EQ2, (b) Acceleration time-histories for EQ2

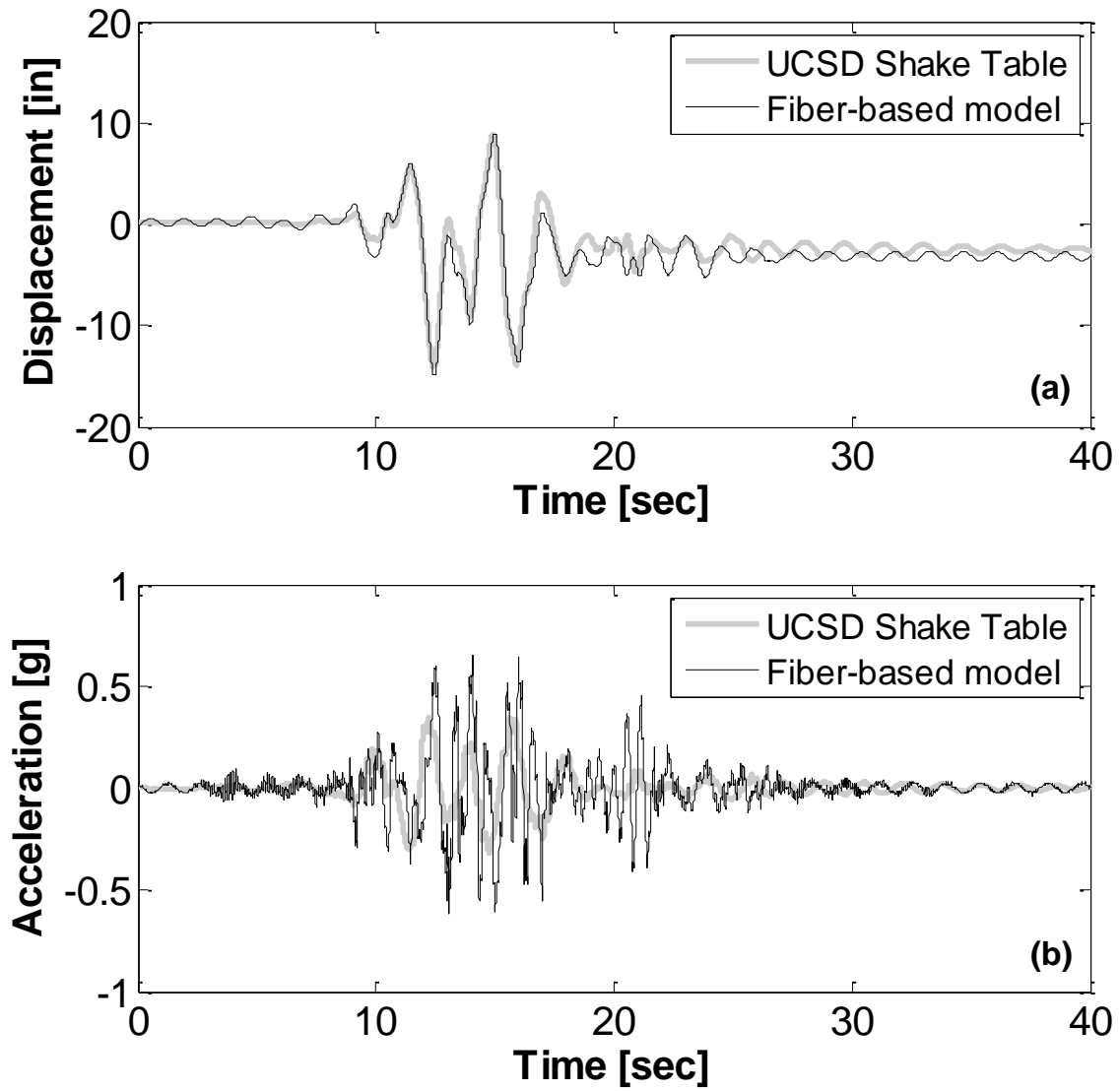


Figure 2-44: (a) Displacement time-histories for EQ3, (b) Acceleration time-histories for EQ3

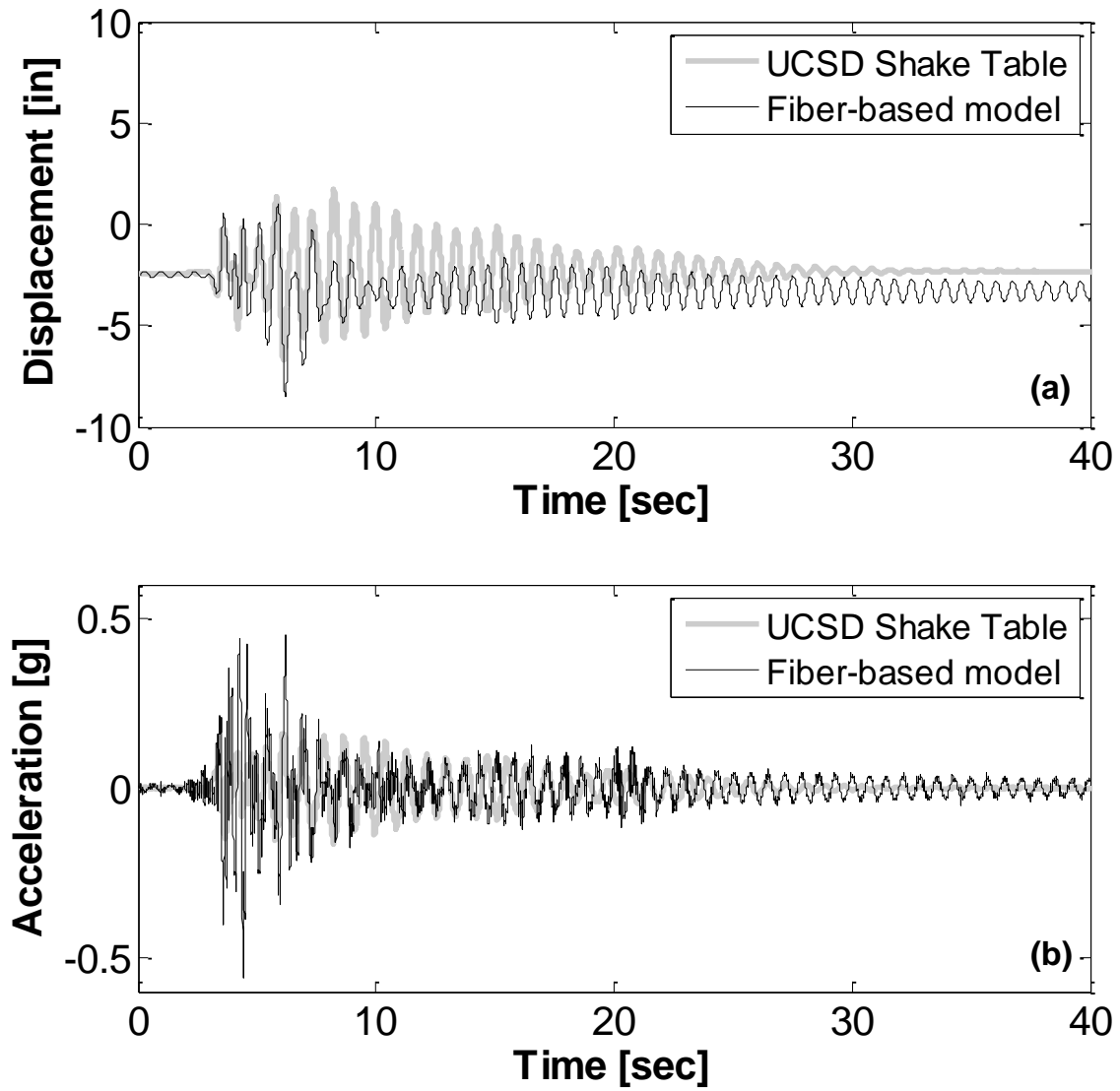


Figure 2-45: (a) Displacement time-histories for EQ4, (b) Acceleration time-histories for EQ4

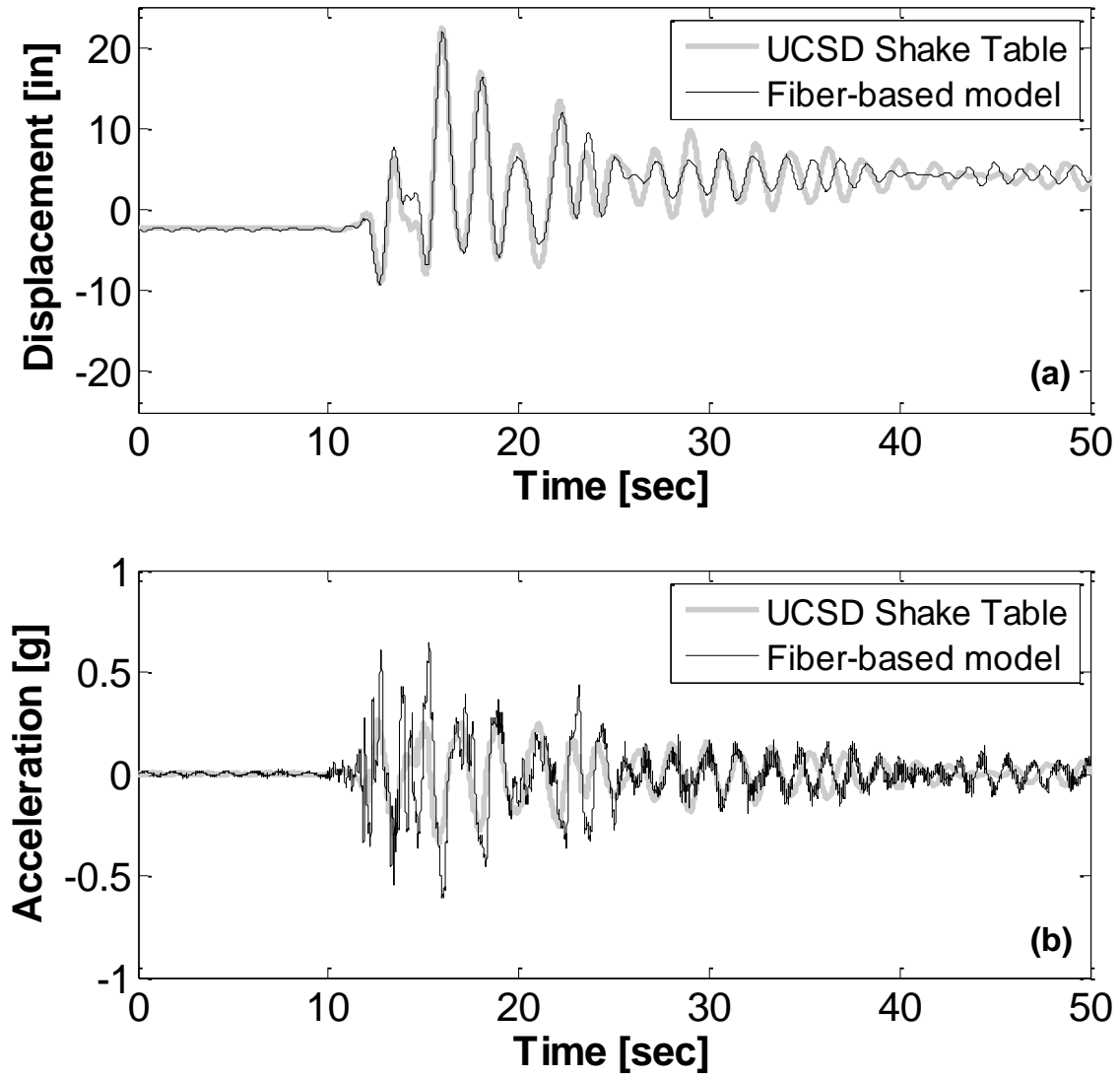


Figure 2-46: (a) Displacement time-histories for EQ5, (b) Acceleration time-histories for EQ5

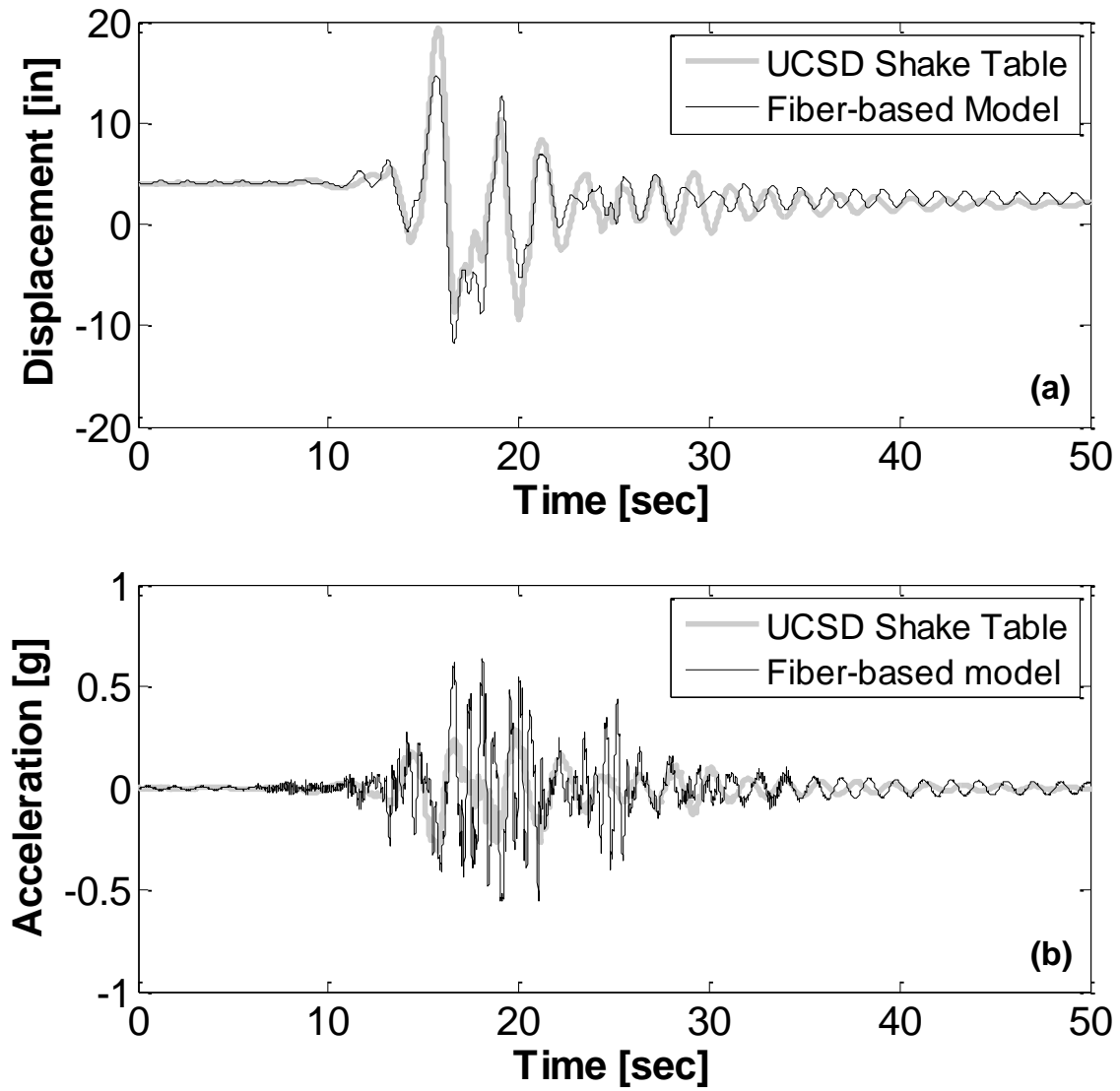


Figure 2-47: (a) Displacement time-histories for EQ6, (b) Acceleration time-histories for EQ6

Table 2-12: Numerical vs Experimental positives and negatives peak displacements

Test	Max. Positive Displacement [in]		Max. negative Displacement [in]	
	Fibers model	UCSD	Fiber model	UCSD
EQ1	2.81	2.19	-2.83	-2.43
EQ2	6.06	5.24	-5.33	-3.56
EQ3	9.10	8.94	-14.95	-14.20
EQ4	0.40	1.69	-9.12	-6.71
EQ5	20.42	22.40	-10.76	-9.12
EQ6	13.39	19.28	-13.02	-9.34

Table 2-13: Numerical vs Experimental positives and negatives peak ground accelerations

Test	Max. Positive Acceleration [g]		Max. Negative Acceleration [g]	
	Fibers model	UCSD	Fiber model	UCSD
EQ1	0.337	0.207	-0.307	-0.206
EQ2	0.632	0.295	-0.525	-0.261
EQ3	0.658	0.348	-0.620	-0.317
EQ4	0.452	0.162	-0.560	-0.163
EQ5	0.643	0.335	-0.611	-0.262
EQ6	0.638	0.310	-0.559	-0.297

2.4 Conclusions

Since the modeling approach plays an important role on the RC member representation, several examples were evaluated in order to develop and validate the three structural model approaches presented on Chapter I. Based on the results, we can conclude that each analytical model evaluated was capable to somehow represent the actual response of the RC member with the simulations performed. However, the results presented by the bilinear and hysteretic “Takeda” models do not represent the actual response of the RC column because of the sudden changes in stiffness. Moreover, as was expected, the fiber-based model showed the best representation in comparison with the actual response of the columns.

In general, this chapter presented the effectiveness of the fiber-based approach by showing the closest prediction for a RC member representation. This is very important since we needed a realistic RC member representation to validate and calibrate the damage identification technique in civil structures presented on the next chapters. Nevertheless,

the three modeling approaches will be used on Chapter IV to test the damage detection algorithms at different levels of model complexity.

2.5 References

Kent D.C., Park R. and Scott B.D. *"Concrete01. OpenSees User's Manual"*, <http://opensees.berkeley.edu>

Mazzoni S., McKenna, F., Scott M.H., Fenves, G.L. *et al.* (2007). *"The OpenSees command language manual"*, Pacific Earthquake Engineering Research Center, University of California at Berkeley.

McKenna, F., Fenves, G.L., Scott, M.H. and Jeremic, B. (2000). *"Open System for Earthquake Engineering Simulation – OpenSees"*, <http://opensees.berkeley.edu>

Mohle J. and Kunnath S. (2007). *"Reinforcing Steel. OpenSees User's Manual"*, <http://opensees.berkeley.edu>

Montejo, L. A. (2008). *"Seismic Behavior of Reinforced Concrete Bridge Columns at Sub-Freezing Temperatures"*, PhD dissertation, North Carolina State University.

Montejo, L.A and Kowalsky, M.J. (2007). *"CUMBIA – Set of Codes for the Analysis of Reinforced Concrete Members"*, CFL Technical Report No. IS-07-01, Department of Civil, Construction and Environmental Engineering, North Carolina State University, Raleigh.

Pacific Earthquake Engineering Research Center PEER, (2006). Ground Motions NGA database, <http://peer.berkeley.edu/nga/index.html>

Petrini L., Maggi C., Nigel Priestly M. J. and Calvi G. M. (2008). *"Experimental Verification of Viscous Damping Modeling for Inelastic Time History Analyzes"*, Journal of Earthquake Engineering, Vol. 12, No. 1, pages 125 – 145.

Raynor D.J., Lehman D.L. and Stanton J.F. (2002). *"Bond Slip Response o Reinforced Bars Grouted in Ducts"*. ACI Structural Journal, Vol. 99, No. 5.

Scott, M.H. and Fenves, G.L. (2006). *"Plastic Hinge Integration Methods for Force-Based Beam-Column Elements"*, ASCE Journal of Structural Engineering, Vol. 132, No. 2, pages 244-252.

CHAPTER III

EVALUATION AND CALIBRATION OF WAVELET PARAMETERS

3.1 Introduction

Wavelet analysis is a convenient tool for solving many practical problems. It is primarily applied to analyze and process signals and functions that vary in time or are heterogeneous in space for detecting not only the general frequency pattern of a signal (distribution of signal energy by frequency components), but also information on certain local coordinates on which certain groups of frequency components appear or frequency components of a signal change rapidly (Misrikhanov, 2006). Wavelet analysis is thus capable of revealing some hidden aspects of the data that other signal analysis techniques fail to detect. This property is particularly important for damage detection applications (Ovanesova and Suárez, 2004).

In this chapter we will present some important details about wavelets, such as its characteristics and how to make use of them. It includes a description of different kinds of wavelets such as Haar, Daubechies, Complex Morlet and Bior6.8. The two different types of transform are evaluated, the Continuous Wavelet Transform (CWT) and the Discrete Wavelet Transform (DWT). For each type of transform, a wavelet is selected to develop the damage detection technique that will be presented in Chapters IV and V. Some numerical examples will be included taking into account the wavelet parameters (e.g., bandwidth and center frequency). The principal objective of this chapter is the evaluation and calibration of the wavelet parameters based on the capacity to detect natural frequencies and discontinuities on the signal. Once the more appropriate wavelets and their parameters are established, this configuration will be used in the next chapters to develop algorithms capable of identifying damage on civil structures subjected to seismic loads.

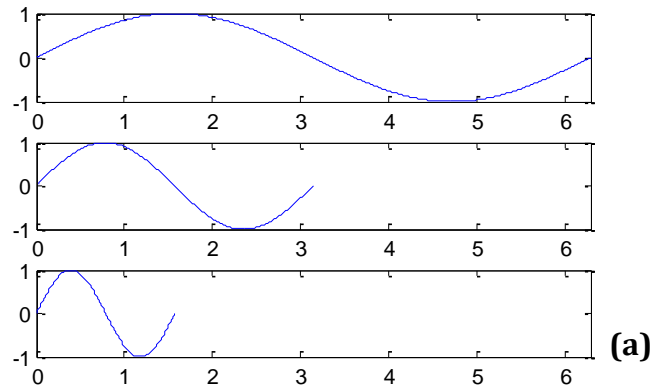
3.2 Continuous Wavelet Transform (CWT)

Continuous transformation is preferable for signal analysis, determination of characteristic properties, and detection problems. The CWT properties as the frequency analysis and its characteristics (such as the scaling and shifting) are discussed in detail below.

3.2.1 Scaling

We already alluded in Chapter I (section 1.3.3) to the fact that wavelet analysis produces a time-scale view of a signal, and now here we discuss the scaling of wavelets. Scaling a wavelet simply means stretching or compressing it.

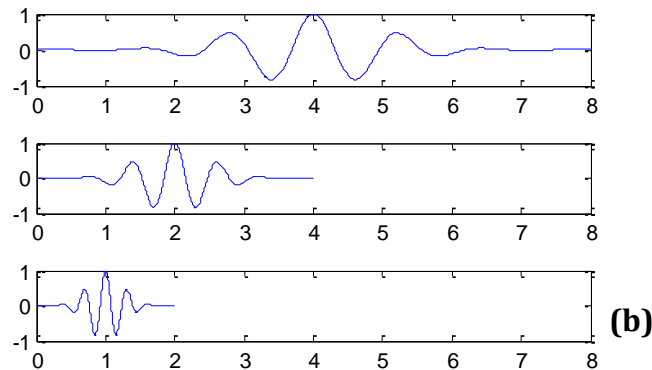
"Stretching" is performed by means of the *scale factor*, often denoted by the letter ***a***. If we are talking about sinusoids, the effect of the scale factor is very easy to see (Figure 3-1a). In wavelets, the scale factor works exactly the same. The smaller the scale factor, the more "compressed" the wavelet (Figure 3-2b).



$$f(t) = \sin(t) ; \quad a = 1$$

$$f(t) = \sin(2t) ; \quad a = 1/2$$

$$f(t) = \sin(4t) ; \quad a = 1/4$$



$$f(t) = \psi(t) ; \quad a = 1$$

$$f(t) = \psi(2t) ; \quad a = 1/2$$

$$f(t) = \psi(4t) ; \quad a = 1/4$$

Figure 3-1: (a) Sinusoid scaling factor, (b) Wavelet scaling factor

It is clear from the diagrams that, for a sinusoid $\sin(\omega t)$, the scale factor a is related (inversely) to the circular frequency ω . Similarly, with wavelet analysis, the scale is related to the frequency of the signal.

3.2.2 Shifting

Shifting a wavelet simply means delaying (or hastening) its onset (Figure 3-2). Mathematically, delaying a function $f(t)$ by k is represented by $f(t - k)$:

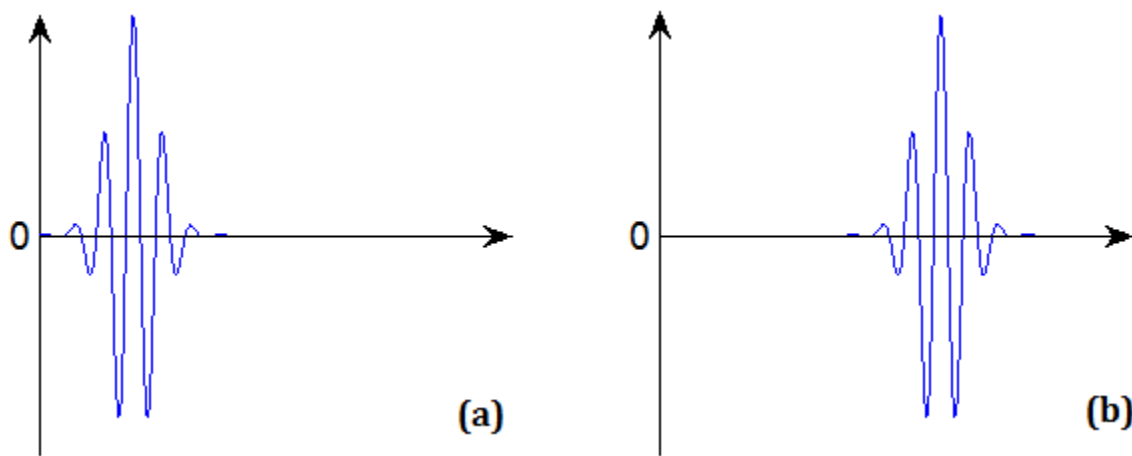


Figure 3-2: (a) Wavelet function $\psi(t)$, (b) Shifted Wavelet function $\psi(t-k)$

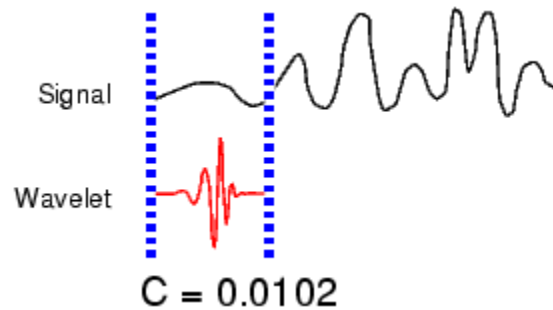
3.2.3 Continuous Wavelet Transform Calculation

The continuous wavelet transform is the sum over all time of the signal multiplied by scaled, shifted versions of the wavelet (eq. 1-2). This process produces wavelet coefficients that are a function of scale and position.

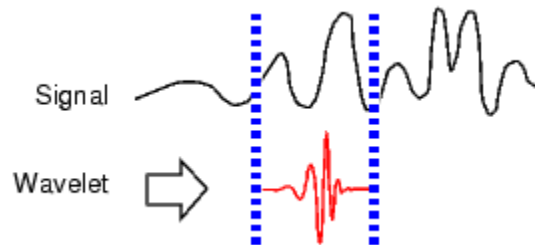
A simple process to create the CWT is summarized next in 5 simple steps:

1. Take a wavelet and compare it to a section at the start of the original signal (Misiti *et al.* 2000).
2. Calculate a number, C , that represents how closely correlated the wavelet is with this section of the signal. The higher C is, the more the similarity. More precisely, if the signal energy and the wavelet energy are equal to one, C may be interpreted as a correlation coefficient (Misiti *et al.* 2000).

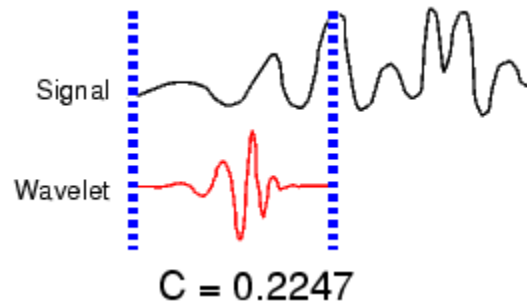
Note that the results will depend on the shape of the wavelet one chooses.



3. Shift the wavelet to the right and repeat steps 1 and 2 until you've covered the whole signal (Misiti *et al.* 2000).



4. Scale (stretch) the wavelet and repeat steps 1 through 3 (Misiti *et al.* 2000).



5. Repeat steps 1 through 4 for all scales (Misiti *et al.* 2000).

When the process is finished, one will have all the coefficients produced at different scales by different sections of the signal. The coefficients constitute the results of a regression of the original signal performed on the wavelets (Misiti *et al.* 2000).

The function that generates the CWT coefficients in Matlab is defined as:

$$C = \text{cwt}(S, a, 'wname') \quad (3-1)$$

where:

C : matrix coefficients for CWT,

S : signal to analyze,

a : scales for the wavelet, and

wname : name of the wavelet.

Figures 3-3 and 3-4 display an illustration of the CWT using the example presented in Chapter I (i.e., the signal with two different frequencies of 1-Hz from 0-5s and the 2Hz from 5-10s – having a discontinuity at 5 seconds).

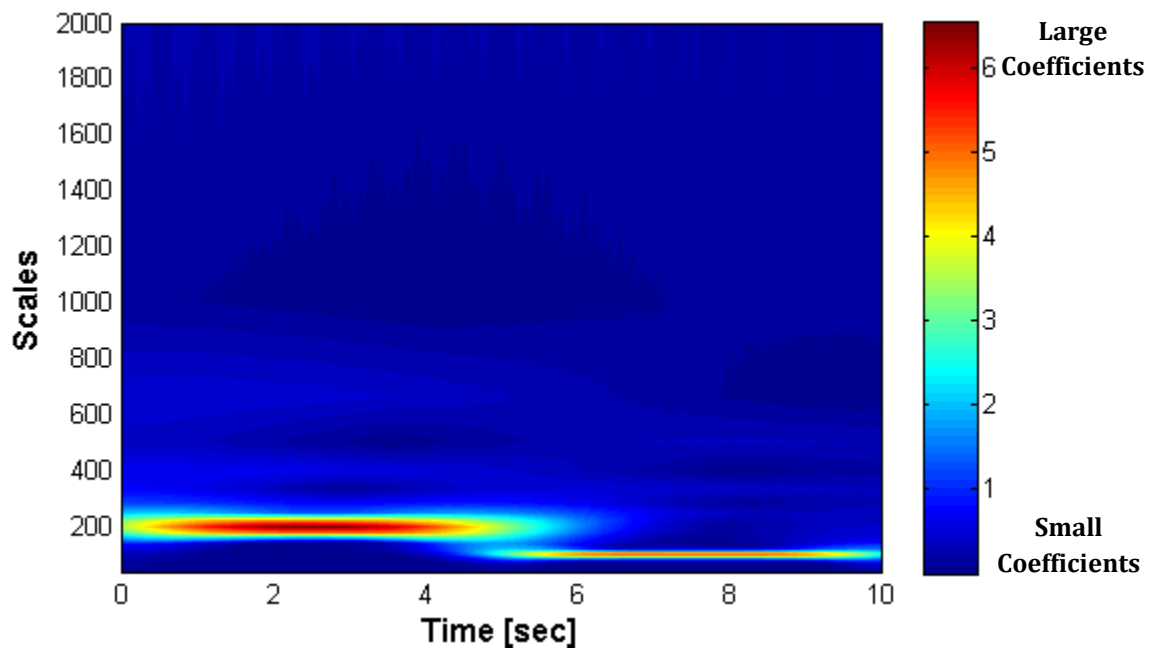


Figure 3-3: CWT Wavelet Map

These coefficient plots resemble a surface seen from above (top view). Also we could look at the same surface from an “isometric” view, as shown in Figure 3-4.

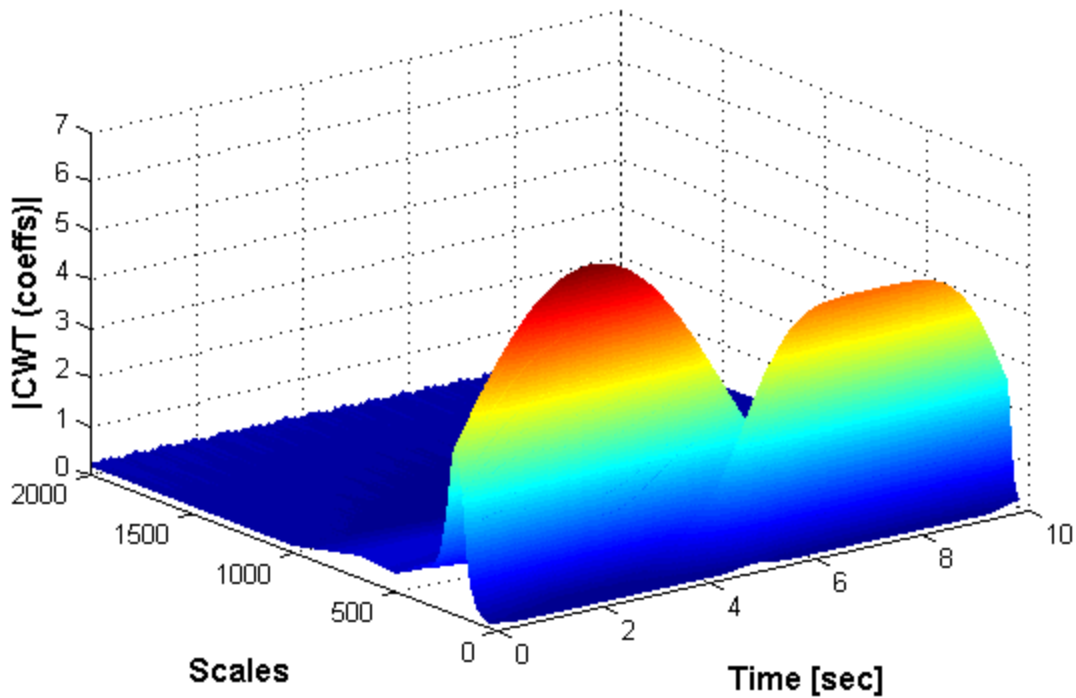


Figure 3-4: 3D plot of the CWT

The continuous wavelet transform coefficient plots of Figures 3-3 and 3-4 are precisely the time-scale view of the signal we referred to earlier. It is a different view of signal data from the time-frequency Fourier view, but it is not unrelated.

3.2.4 Scale and Frequency relationship

Note that the scales in the coefficients plot from Figure 3-4 run from 1 to 2000. Remember that the higher scales correspond to the most "stretched" wavelets. The more stretched the wavelet, the longer the portion of the signal with which it is being compared, and thus the coarser the signal features being measured by the wavelet coefficients.



Figure 3-5: CWT - Low and High scales comparison (Misiti *et al.* 2000)

Thus, there is a correspondence between wavelet scales and frequency as revealed by wavelet analysis:

- High scale $a \rightarrow$ Stretched wavelet \rightarrow Slowly changing details \rightarrow Low Frequency ω
- Low scale $a \rightarrow$ Compressed wavelet \rightarrow Rapidly changing details \rightarrow High Frequency ω

The relationship between scales and frequencies is expressed as:

$$a = \frac{f_c}{f_a * dt} \quad (3-2)$$

where:

a : scales for the wavelet,

f_c : center frequency for the wavelet,

f_a : range of frequencies to analyze, and

dt : time interval of the signal.

For the results displayed in Figures 3-6 and 3-7, the center frequency and the time interval of the signal were taken as 1 and 0.005, respectively, and the range of frequencies was taken from 0.1Hz up to 10Hz, with a frequency-interval of 0.1Hz. It is seen how an analysis at high scales (low frequencies) allow us to identify the evolution of the frequency content on the signal. On the other hand, an analysis at low scales (high frequencies) allows the detection of the time instant where the discontinuity occurred.

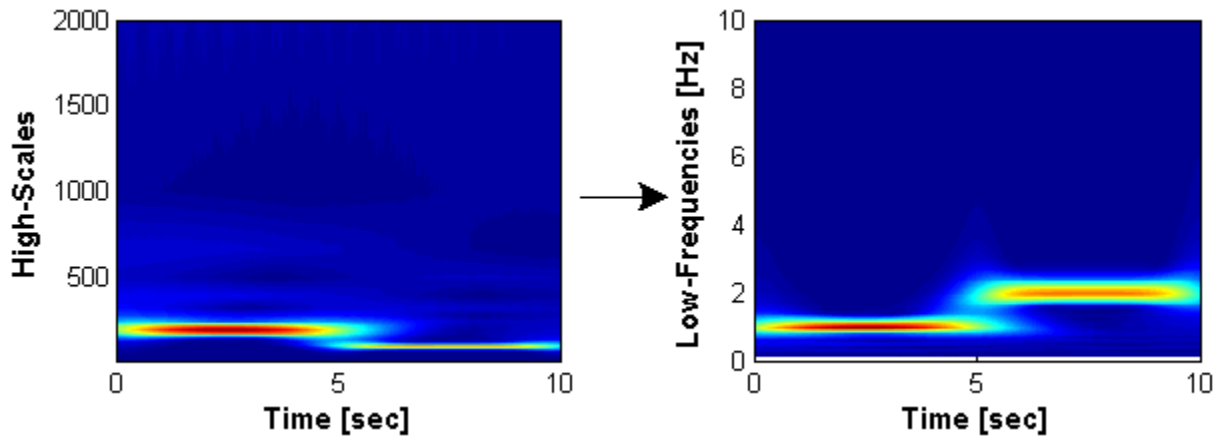


Figure 3-6: Representation of CWT High-scales to get CWT Low-Frequencies

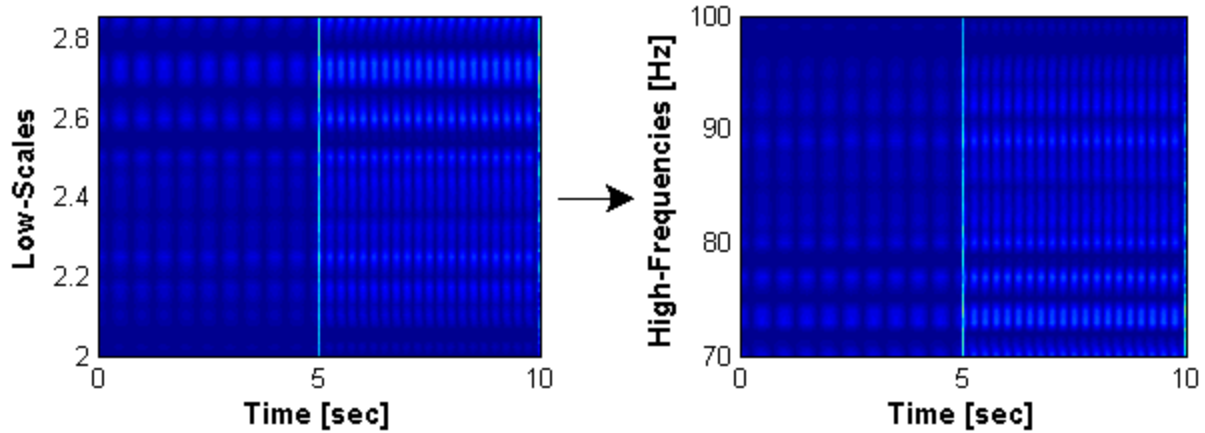


Figure 3-7: Representation of CWT Low-Scales to get CWT High-Frequencies

3.3 Discrete Wavelet Transform (DWT)

Calculating the wavelet coefficients in all possible scales demands a lot of computational time and generates a large amount of data. In the DWT, a subset of stretching and translations is selected to make the calculations. It serves to streamline the process without requiring much memory and the efficiency can be maintained by using dyadic scales (i.e., scales and positions in powers of 2 as was discussed in section 1.3.4).

3.3.1 Decomposition and reconstruction of wavelets

Mallat (1989) developed a fast wavelet decomposition and reconstruction algorithm for the DWT using a two-channel sub-band coder. Using this algorithm, a signal can be represented by its approximations (A) and details (D) at different levels of decomposition (j) as shown in Figure 3-8. This process can be applied for different levels of decomposition as needed. DWT analysis has three ways for signal decomposition such as the One-Level filtering, the Multiple-Level Decomposition and the Wavelet Packet Analysis (WPA). The One-Level filtering and the WPA are discussed here since they will be used in the DWT analyses implemented in this work.

3.3.1.1 One-level filtering: Approximation and Details

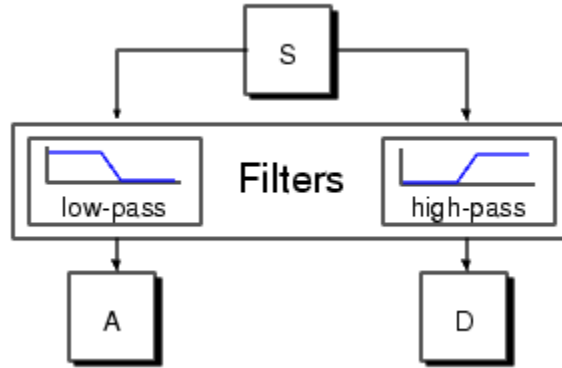


Figure 3-8: DWT decomposition for level 1 (Misiti *et al.* 2000)

The signal, S , is passed through two filters (Figure 3-8) to get two new signals: the approximation signal (from the approximation coefficients, cA) and the detail signal (from the detail coefficients, cD). The detail coefficients cD consists mainly of the signal high frequency components whereas the coefficient cA contains the low frequency component of the original signal. The Matlab function used to generate the decomposition of the original signal into approximation coefficients (cA) and detail coefficients (cD) is presented next.

$$[cA, cD] = wavedec(S, L, 'wname') \quad (3-3)$$

where:

S : signal to analyze,
 L : level number for decomposition, and
 $wname$: name of the wavelet (e.g., morl, bior6.8, haar, etc.).

Once the signal was decomposed into cA and cD coefficients, the details and approximation are obtained by using the following Matlab functions:

$$A = wrcoef('a', cA, cD, 'wname', N) \quad (3-4a)$$

$$D = wrcoef('d', cA, cD, 'wname', N) \quad (3-4b)$$

Equation 3-4a reconstructs the approximation coefficients while the equation 3-4b reconstructs the detail coefficients. Notice that for these equations the user has to specify the coefficients that wants to reconstruct, with the letter **a** for the approximations and

letter ***d*** for the details. There are different ways in where you can decompose the signal entirely without specify anything. The reason why is the signal decomposed individually is that the chapter objective is to detect natural frequencies and discontinuities, and the detail (*D*) is the part of the DWT features used to detect discontinuities.

To gain a better appreciation of this process, a one-stage discrete wavelet transform of a signal was performed in Figure 3-9. The signal is a pure sinusoid with white noise added to it. The figure also presents the Fourier transform for each signal. Note that Fourier spectrum for the detail coefficients has frequencies between ~50Hz up to 100Hz. This upper limit is due to the Nyquist frequency (f_{ny}), where for the interval time (dt) of 0.005 seconds is the maximum frequency that can be analyzed. The Nyquist frequency is defined as

$$f_{ny} = \frac{1}{2 * dt} \quad (3-5)$$

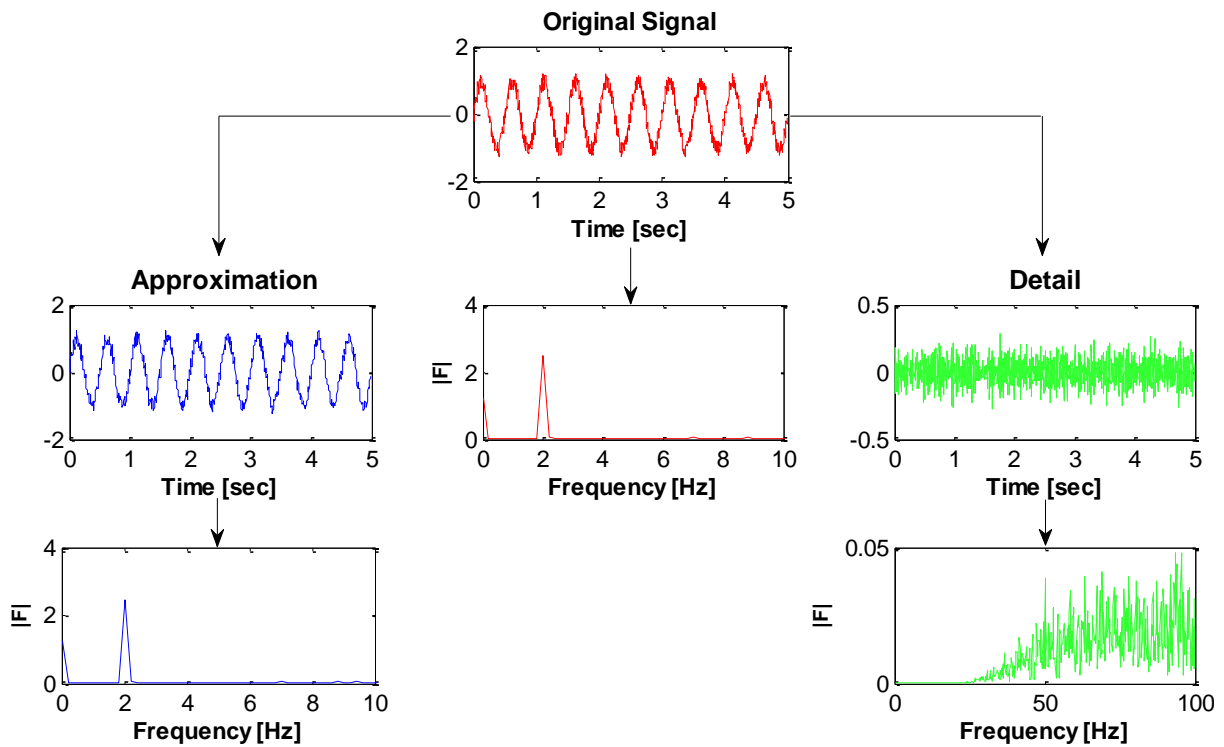


Figure 3-9: Schematic diagram for DWT single-decomposition

3.3.1.2 Wavelet Packet Analysis

In the discrete wavelet analysis, a signal is decomposed into an approximation and a detail. These are first class, but the signal-class approach can also be decomposed into an approximation and detail signals, but are now second level. If we repeat the process on the signals, we get n-levels decomposition. This is called the *wavelet packet decomposition tree*. It is the richest analysis: the complete binary tree is produced as shown in Figure 3-10.

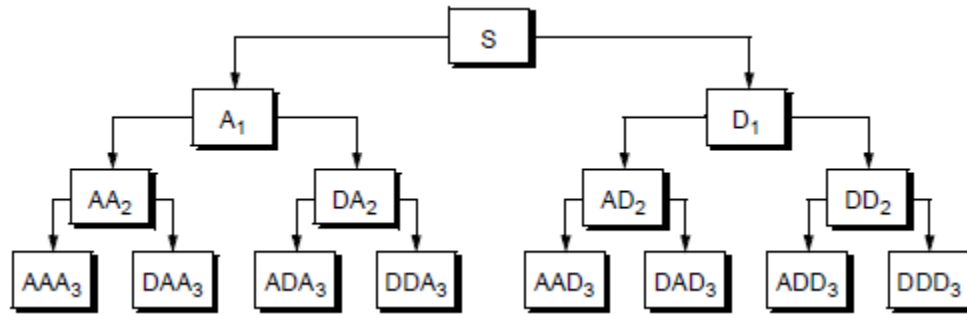


Figure 3-10: Wavelet packet decomposition tree at level 3 (Misiti *et al.* 2000)

The function used in Matlab to generate the wavelet packet tree is

$$wpt = wpdec(S, N, 'wname') \quad (3-6)$$

where:

wpt : wavelet packet tree,
 S : signal to analyze,
 N : level number for decomposition, and
 wname : name of the wavelet (e.g., morl, bior6.8, haar, etc.).

Now we have to reconstruct the wavelet packet decomposition tree to obtain the coefficients. This is done by taking the Wavelet Packet and organizing each packet decomposed as presented in Figure 3-11.

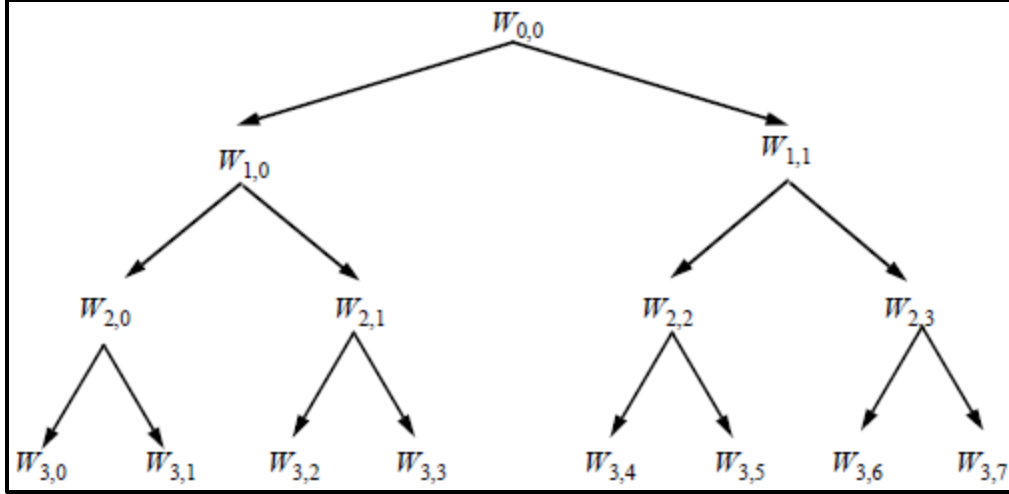


Figure 3-11: Wavelet Packet Tree organized at level 3 (Misiti *et al.* 2000)

The function that produces the coefficients for a Wavelet Packet Tree is

$$W_{j,n} = wprcoef(wpt, [j \ n]) \quad (3-7)$$

where:

$W_{j,n}$: packet node,

wpt : wavelet packet tree from where we get the coefficients, and

$[j \ n]$: j = level of decomposition in where the packet is located, and n = node position.

If we take a look at the subscript (n) of the packets, the even numbers match with the coefficients of approximation while the odd numbers correspond to the coefficients of detail. To reconstruct some particular decomposed packet it is important to know the position where it is. For example, if we take the first decomposed packet from the second-level decomposition, the node position would be $[2 \ 0]$; these values are the letters j and n .

Continuing with the same example used for the one-level decomposition now we used it to apply the WPA; the results are displayed in Figure 3-12. The WPA was performed up to the third-level of decomposition for both DWT coefficients (the approximations and details). After the signal decomposition, the Fourier spectrum is presented for the second-level of decomposition (Figure 3-13). Note that when the process of decomposition is repeated, the frequency content is reduced by half. For the one-level decomposition (D_1) we appreciate in Figure 3-9 that the frequency content was from 50 to 100 Hz, now (for DD_2) it is from

~75 to 100Hz, and if we perform the Fourier analysis for the detail of the third-level of decomposition (DDD_3) we would notice that the frequencies will be from ~87.5 to 100Hz.

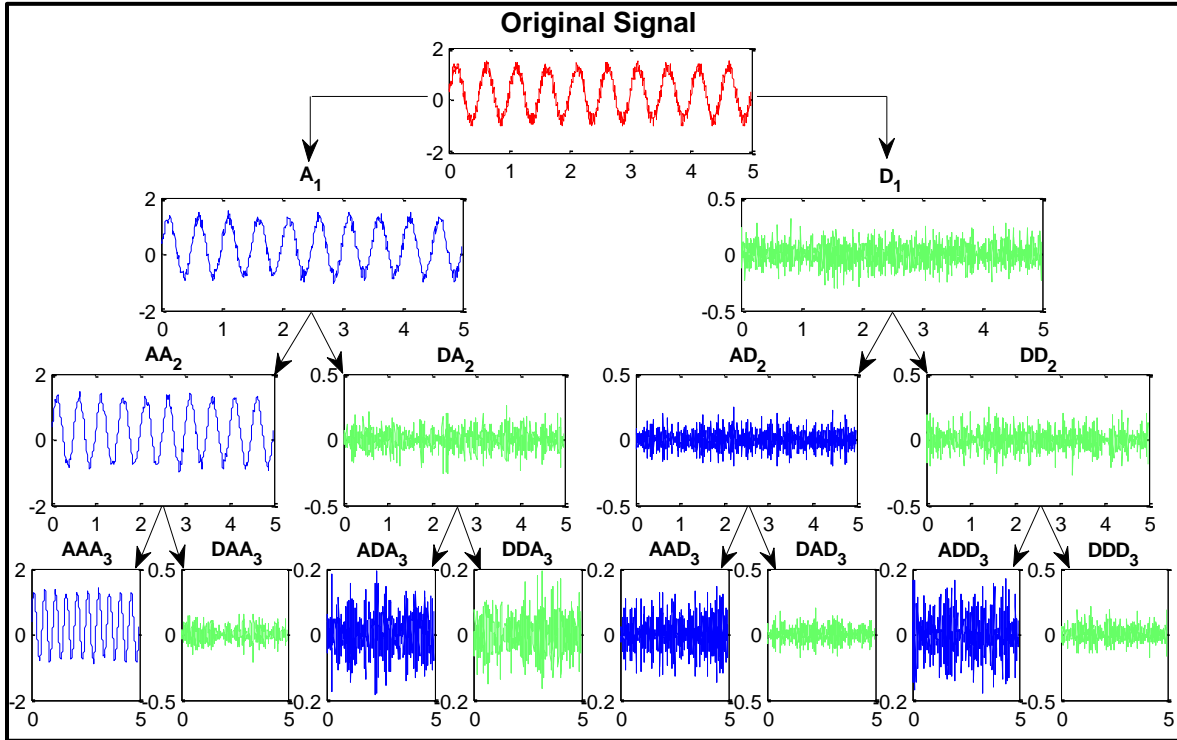


Figure 3-12: Wavelet Packet Tree (WPT)

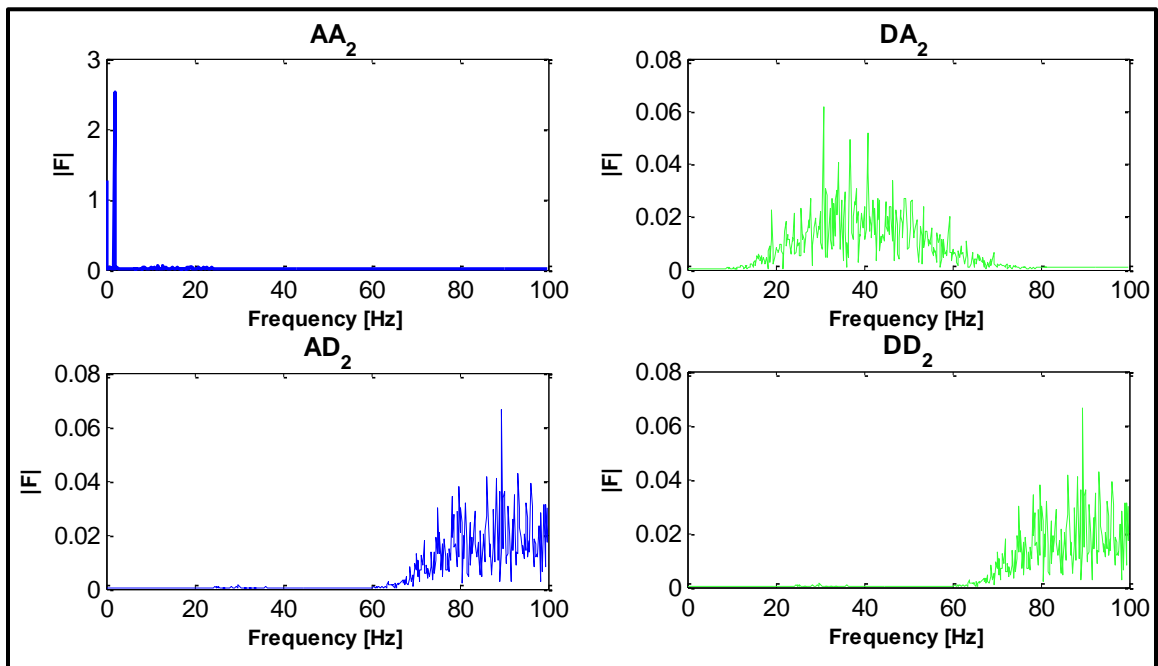


Figure 3-13: Fourier Spectrum for second-level decomposition of the WPT

3.4 Mother wavelets used in the research

The wavelet base of the signal space is constructed from finite functions belonging to this space and tending to zero at infinity. The faster the functions tend to zero, the more the suitable their use as a base for wavelet transformation in the analysis of real signals. Table 3-1 presents a summary of the wavelets that were evaluated in this research.

Table 3-1: Summary of the Wavelets and Associated Parameters

Wavelet Family Name Wavelet Family Short Name	Haar (haar)	Daubechies (dbN ¹)	BiorSplines (biorNr ² .Nd ³)	Mexican Hat (mexh)	Complex Morlet (cmor)
Symmetry	•		•	•	•
Exact Reconstruction	•	•	•	•	•
Continuous Transform	•	•	•	•	•
Discrete Transform	•	•	•		
Fast Algorithm	•	•	•		

In the case of the complex Morlet wavelet two different approaches were used to perform the CWT. One was using the function available in the Matlab Toolbox, in which the complex Morlet is expressed as

$$\psi(t) = \frac{1}{\sqrt{\pi f_b}} e^{2i\pi f_c t} e^{-\frac{t^2}{f_b}} \quad (3-8)$$

depending on two parameters:

- f_b : bandwidth parameter, and
 f_c : wavelet center frequency.

In this approach the CWT is calculated on the frequency domain via the Fast Fourier Transform. The second approach is the one used in Montejo (2010), with the complex Morlet wavelet defined as shown in Equation 3-9. In this approach the CWT is performed in the time domain, and as a result it takes considerable more time than the first approach. However, the results are expected to be cleaner as the steps of going back and forward from the frequency domain are avoided. For the sake of brevity and since the results

¹ Determines the filter order

² Denotes the order of the reconstruction filter

³ Denotes the order of the decomposition filter

obtained were slightly better, only the results obtained using the second approach are presented here. For all the other wavelets evaluated the transform was performed using the commands and functions predefined in the Matlab Toolbox

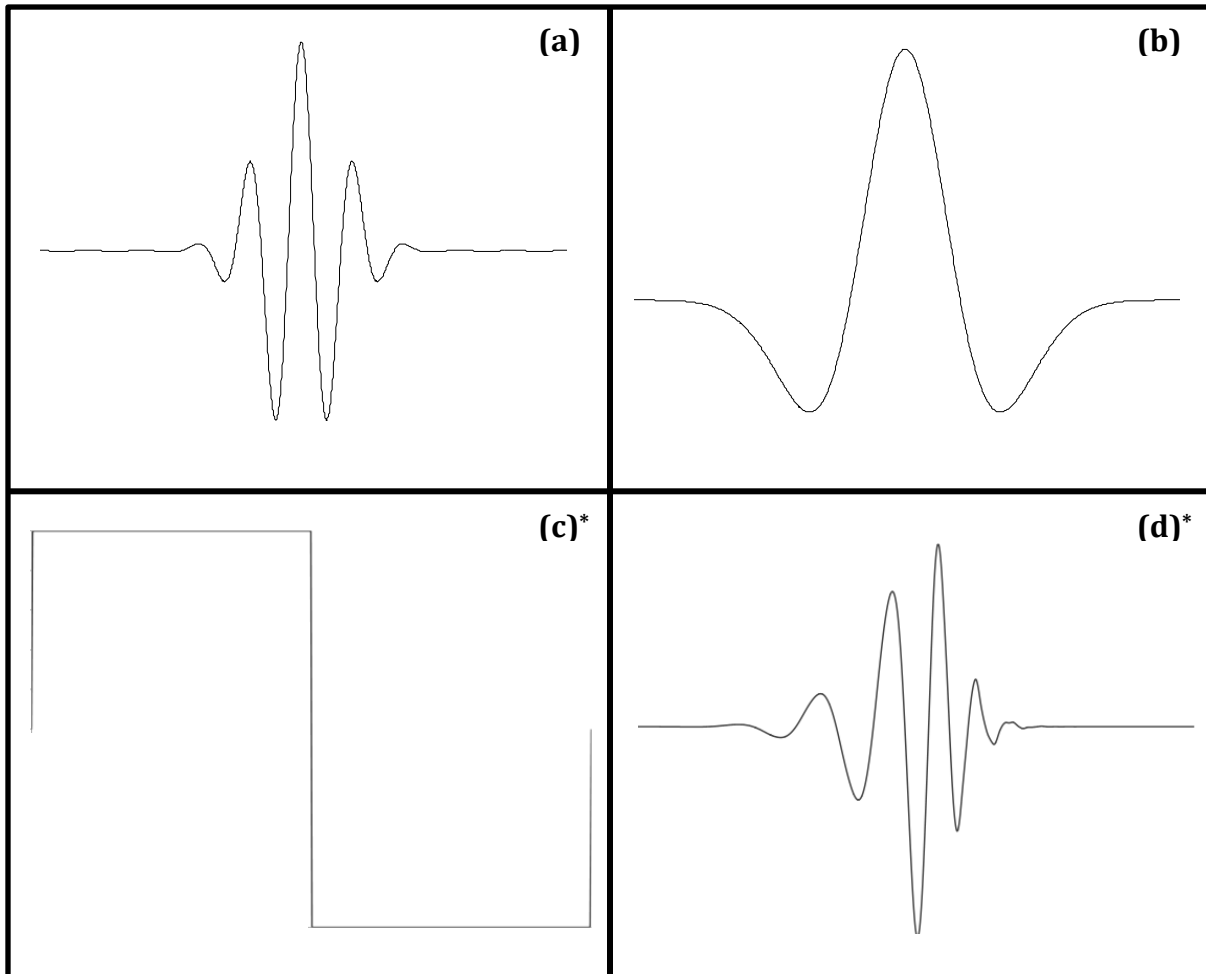
$$\psi(t) = e^{2i\pi f_0 t} e^{-\frac{t^2}{2p^2}} \quad (3-9)$$

where:

f_0 : natural frequency, and

p : bandwidth parameter.

A representation of the mother wavelets summarized in Table 3.1 is displayed in Figure 3-14 a to d.



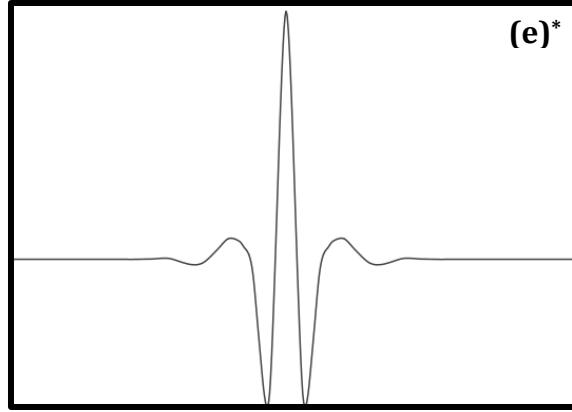


Figure 3-14: Mother Wavelets: (a) Complex Morlet, (b) Mexican Hat, (c) Haar, (d) db8, (e) Bior6.8 (PyWavelet, 2006)*

3.5 Evaluation and Calibration of the CWT

In order to validate the CWT, two numerical examples will be presented next. The signal for the first example was artificially generated by adding a 6Hz sinusoid to a chirp that goes down from 3Hz to 1Hz with total duration of 10 seconds (Figure 3-15). The main objective of this example is to see if the CWT is capable to detect the sinusoidal frequency and the frequency evolution in the chirp. The analysis will be performed only in the low frequency range, and it will be from 0.1Hz to 10Hz in order to detect the frequencies induced on the signal. On this example three wavelets will be evaluated to calculate the CWT coefficients. They are the Mexican Hat, the Bior6.8, and the complex Morlet (using the time domain approach, eq. 3-9). For the complex Morlet wavelet parameters several combinations were used, the best results were obtained by using 1 and 2 for the bandwidth (p) and center frequency (f_0), respectively.

The results obtained using the three wavelets are presented on Figures 3-16 to 3-18. For all figures we first present the real part of the CWT coefficients in a 3D plot. Then we show the Wavelet Map (a 2D top view of the coefficients absolute values) from the coefficients previously mentioned. And finally the instantaneous frequencies of the wavelet ridges extracted from the Wavelet Map are shown. By looking at the Mexican Hat wavelet results, we can noticed that it partially identifies the change in frequency for the chirp, but it practically mixes the results for the 6Hz sinusoidal frequency with the frequency change of

the chirp. It was not able to identify the frequency of 6Hz coming from the sinusoid accurately (Figure 3-16). From the results of the Bior6.8 it can be noted that the results are slightly improved when compared to the Mexican Hat, but it still has the drawback of the frequency mix (Figure 3-17). Viewing the wavelet ridges, it is noticed that a clear identification of the instant frequencies is not possible. Practically, both wavelets show similar results. Finally, the complex Morlet was able to successfully identify both, the frequency change of the chirp and the sinusoidal frequency of 6Hz (Figure 3-18).

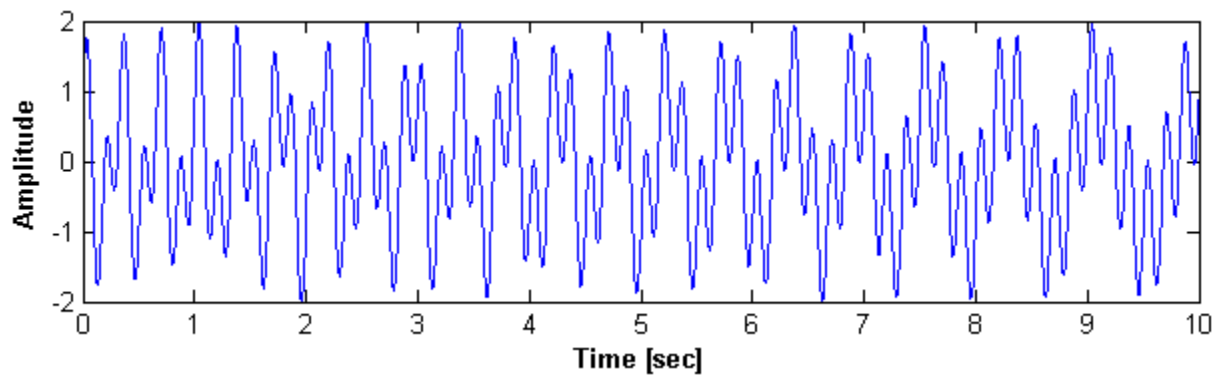


Figure 3-15: 6Hz Sinusoid + Chirp (3Hz to 1Hz)

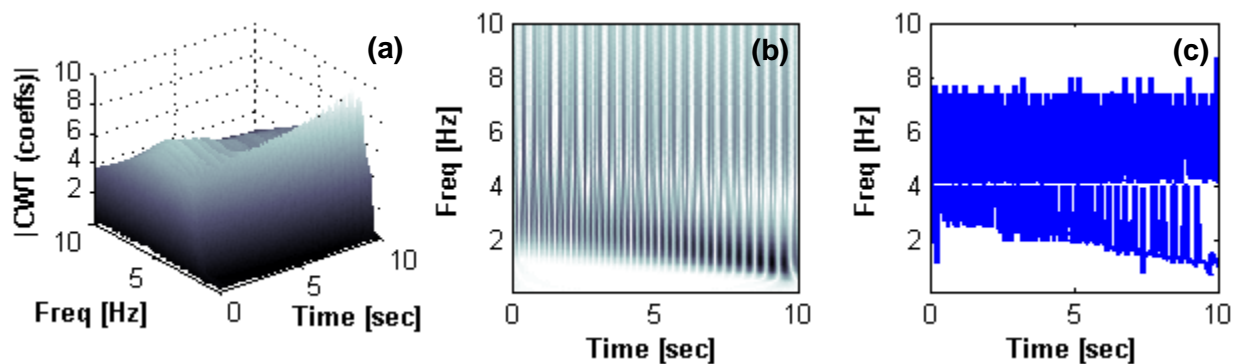


Figure 3-16: Mexican Hat Wavelet: (a) 3D plot, (b) CWT Wavelet Map, (c) IF from wavelet ridges

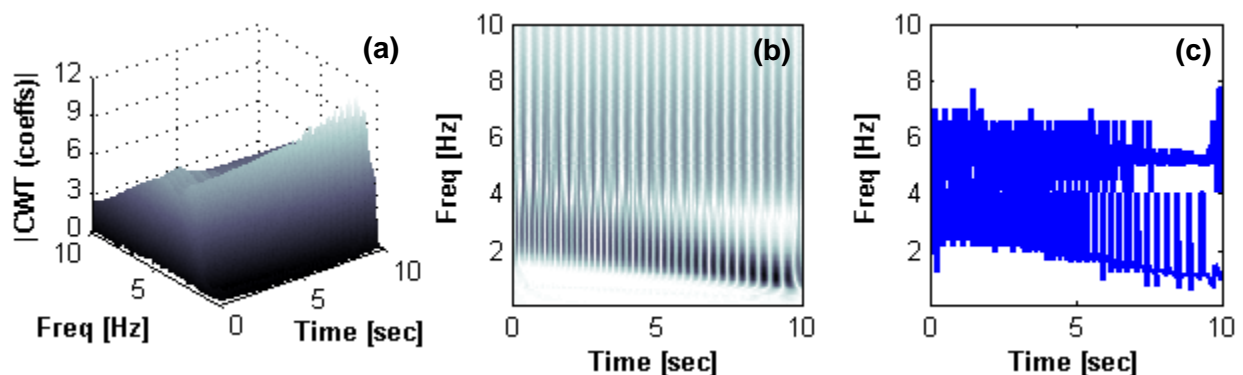


Figure 3-17: Bior6.8 Wavelet: (a) 3D plot, (b) CWT Wavelet Map, (c) IF from wavelet ridges

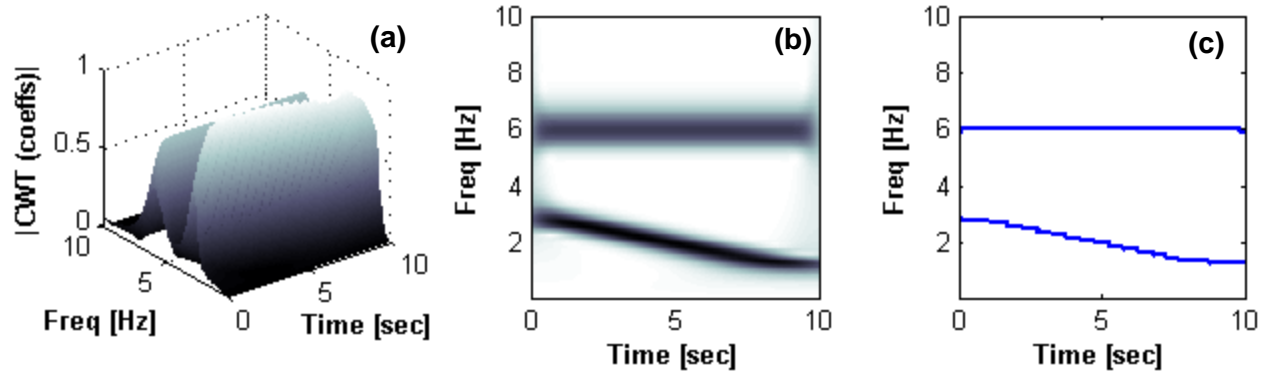


Figure 3-18: Complex Morlet Wavelet: (a) 3D plot, (b) CWT Wavelet Map, (c) IF from wavelet ridges

The next example consists of three signals that were artificially generated with 10 seconds of duration and a discontinuity added at the time 4.75 seconds. The signal is a pure sinusoid with a frequency of 1Hz plus a percentage of discontinuity, i.e., 10%, 1%, 0.1%. The principal objective of using different percentages of discontinuity is to see if the high frequencies analysis of the CWT can detect those different levels of discontinuity.

For this example the low frequency analysis and high frequency analysis were performed. The wavelet parameters for the low frequency analysis were the same used in the previous example. This analysis was performed from 0.1Hz to 4Hz frequency content at an interval of 0.1Hz. For the high frequency analysis, the bandwidth (p) and center frequency (f_0) parameters were 0.5 and 6, respectively. Several combinations were evaluated and the best results were obtained by using these values. The frequency content for this analysis was from 70-100Hz. We continue using the same three mother wavelets as in the previous example. The results for the low and high frequencies analyzes are presented in Figures 3-19 to 3-21 for the three wavelets evaluated.

In Figure 3-19 we can observe the results when the percentage of discontinuity was 10%, the higher discontinuity induced. This particular discontinuity can be seen with the naked eye in the first plot. For both frequency analyses, it can be seen that the complex Morlet presents better results than the other two wavelets since it was able to identify the 1Hz frequency on the signal, and also it detected exactly the time instant (i.e., 4.75s) where the 10% of discontinuity was induced.

Now if we look at the results for the last two cases (when the percentages of discontinuity are equal to 1% and 0.1%) shown in Figures 3-20 and 3-21, again the complex Morlet yields better results. If we take a look at the high frequencies we can recognize that when the discontinuity is lower, the results of the Mexican Hat and the Bior6.8 are a little more difficult to identify the time instant. Therefore, the wavelet chosen to be used in the next chapters will be the complex Morlet with the parameters used here.

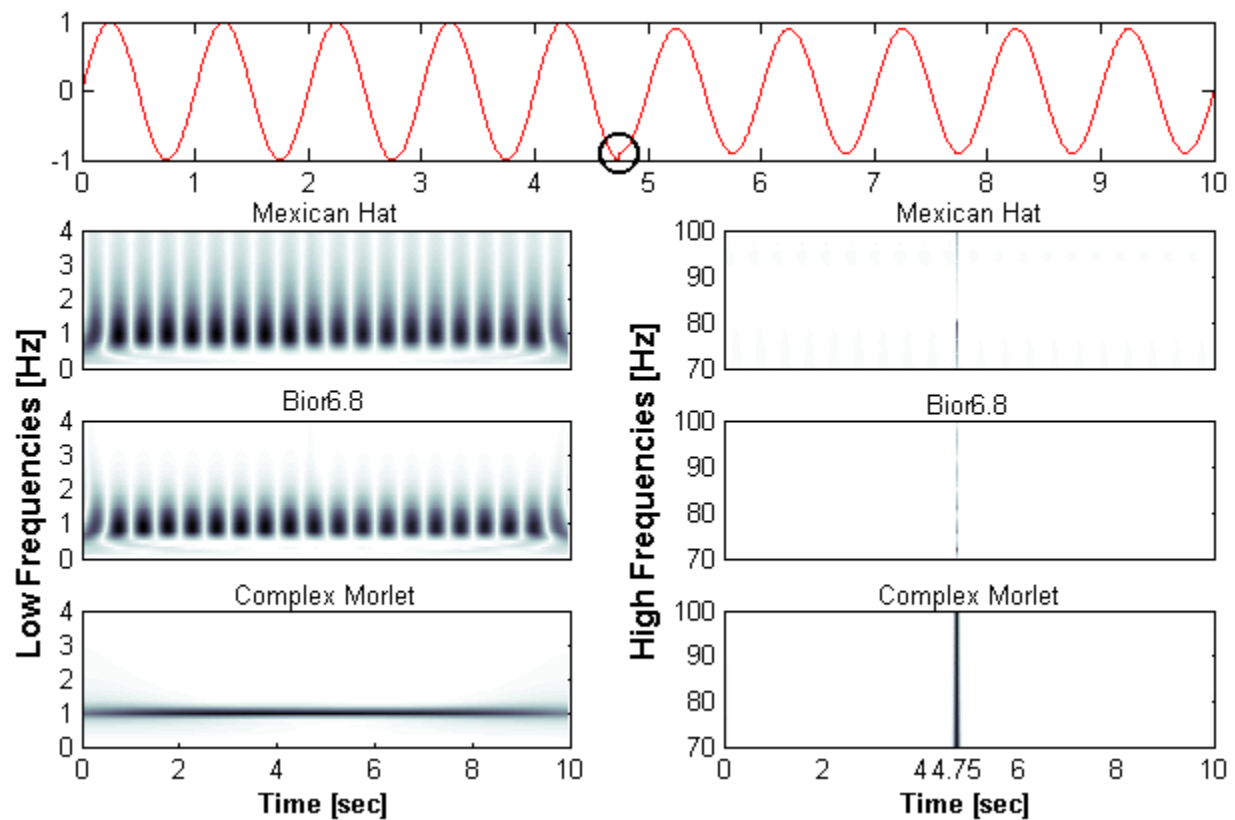


Figure 3-19: 1Hz sinusoidal signal + 10% discontinuity at 4.75s

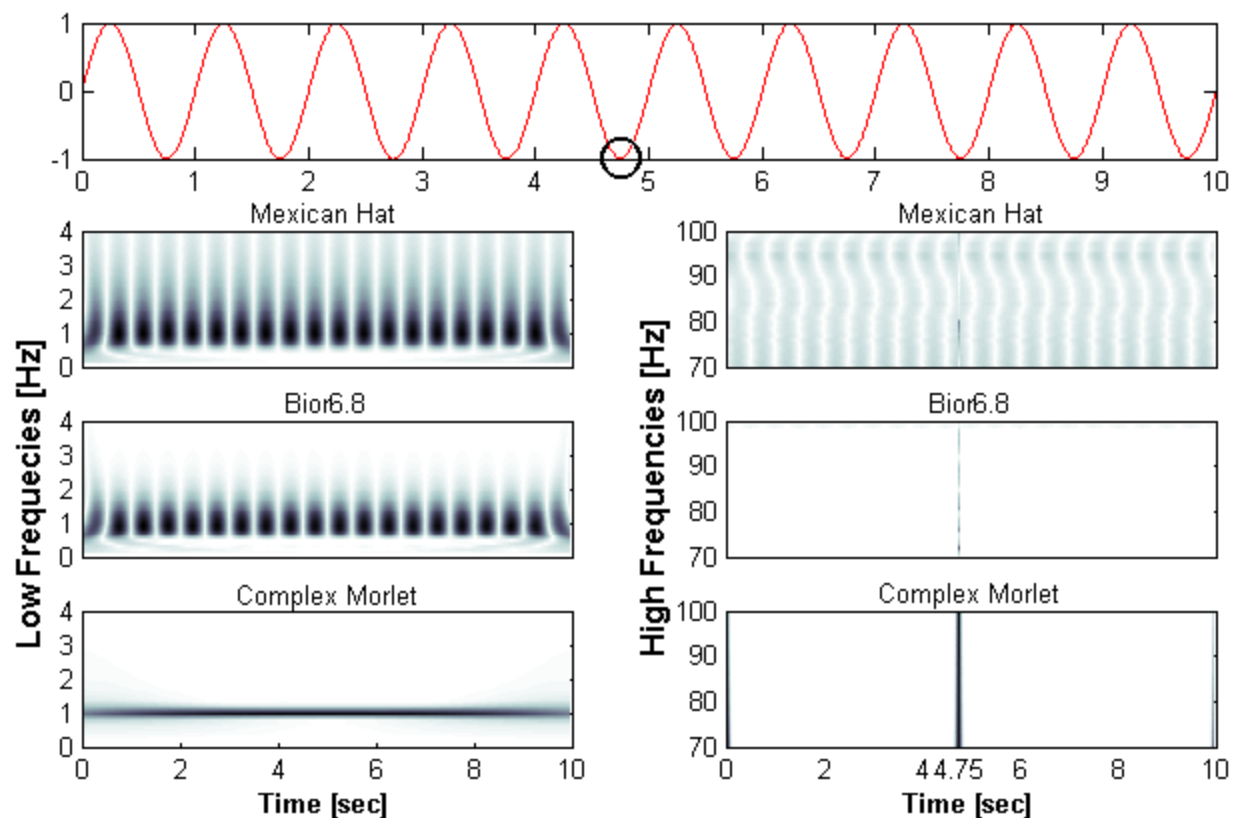


Figure 3-20: 1Hz sinusoidal signal + 1% discontinuity at 4.75s

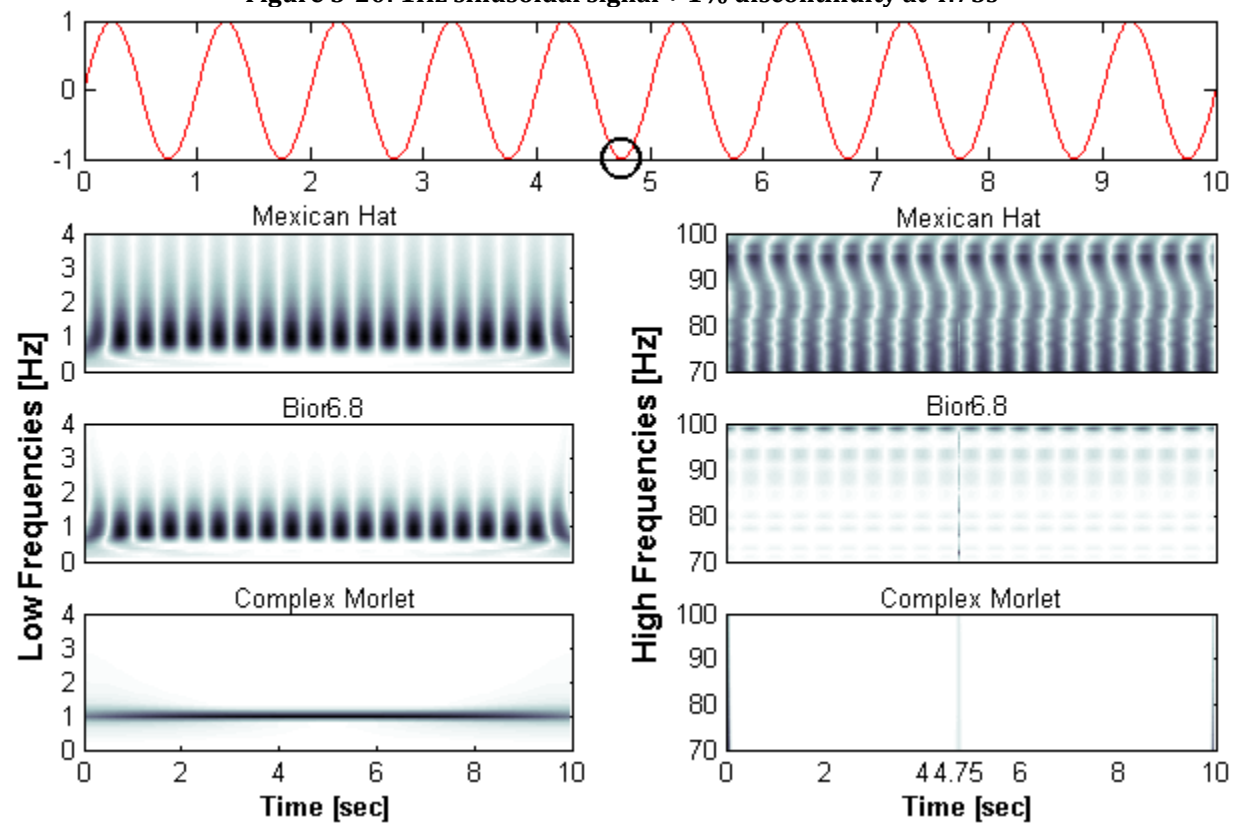


Figure 3-21: 1Hz sinusoidal signal + 0.1% discontinuity at 4.75s

3.6 Evaluation and Calibration of the DWT

In order to evaluate the DWT, two numerical examples are presented next. They will be evaluated with different mother wavelets. These wavelets are the Haar, Bior6.8 and Daubechies (db8). These three wavelets will be compared to finally choose the one that will be used in the wavelet based damage detection methodology for nonlinear structures presented on Chapters IV and V. The first example is the same used on the first chapter, i.e., two sinusoids with frequencies of 1Hz and 2Hz (with a discontinuity at 5 s). The second example is that previously presented to evaluate the CWT, but now it will be used to evaluate the DWT. It is the sinusoid signals with different levels of discontinuity induced at time 4.75 seconds.

The results for the two examples are presented in Figures 3-22 to 3-25. For the sake of brevity, we are just showing the DWT detail (D) since it is the part that identity the singularities on the signal e.g., discontinuity. Looking at the Figure 3-22, we can notice that for Haar, the change in frequencies from 1Hz to 2Hz is reflected clearly on the detail (D) with a change in its amplitude. However, if we are analyzing a nonlinear structure we cannot simply associate this variation with damage. We need a better illustration on the detail coefficients that can related with damage. Now by looking the results of the Bior6.8 and Daubechies (db8), a better-more clear representation of the discontinuity emerges. It can be seen that a spike appears at the time when the discontinuity occurs.

Looking at the results for the second example displayed on Figures 3-23 to 3-25 we can see that the bior 6.8 and db8 wavelets were able to detect all three levels of discontinuity, while the Haar failed. Hence, the Haar wavelet is excluded for the DWT analysis of the next chapters. Now by comparing the two remaining wavelets, the Bior6.8 shows a slightly sharper spike where the discontinuity took place. If we look carefully, we can notice that both wavelets present two spikes closely spaced, but this phenomenon is more evident on the db8 results. As we decrease the percentage of discontinuity, one peak becomes to vanish, allowing the peak that corresponds to the discontinuity to stand out. The additional peak can be misleading with another discontinuity when it really does not. Therefore,

Bior6.8 was selected as the wavelet used to perform the DWT in the next chapters. Notice that in addition to detect the time instant where the discontinuity took place, the magnitude of the emerging spikes can be related to the level of the discontinuity induced.

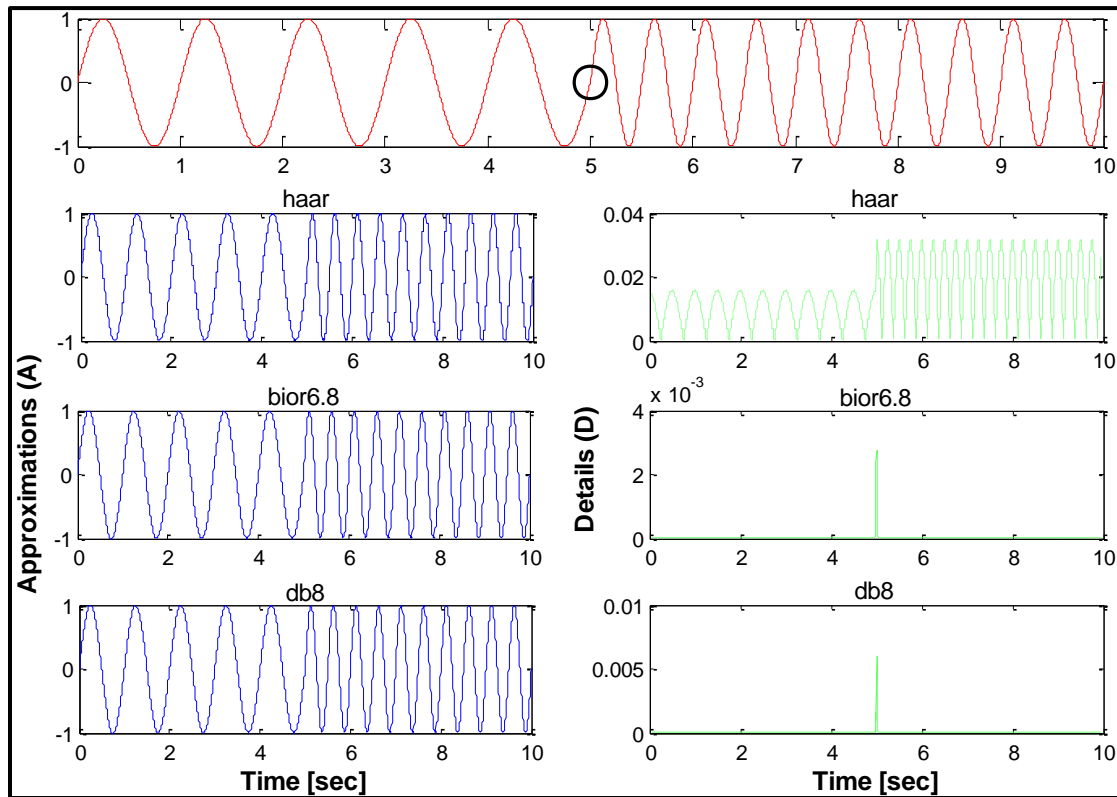


Figure 3-22: Sinusoidal with a change in frequency from 1Hz to 2Hz at $t = 5$ sec

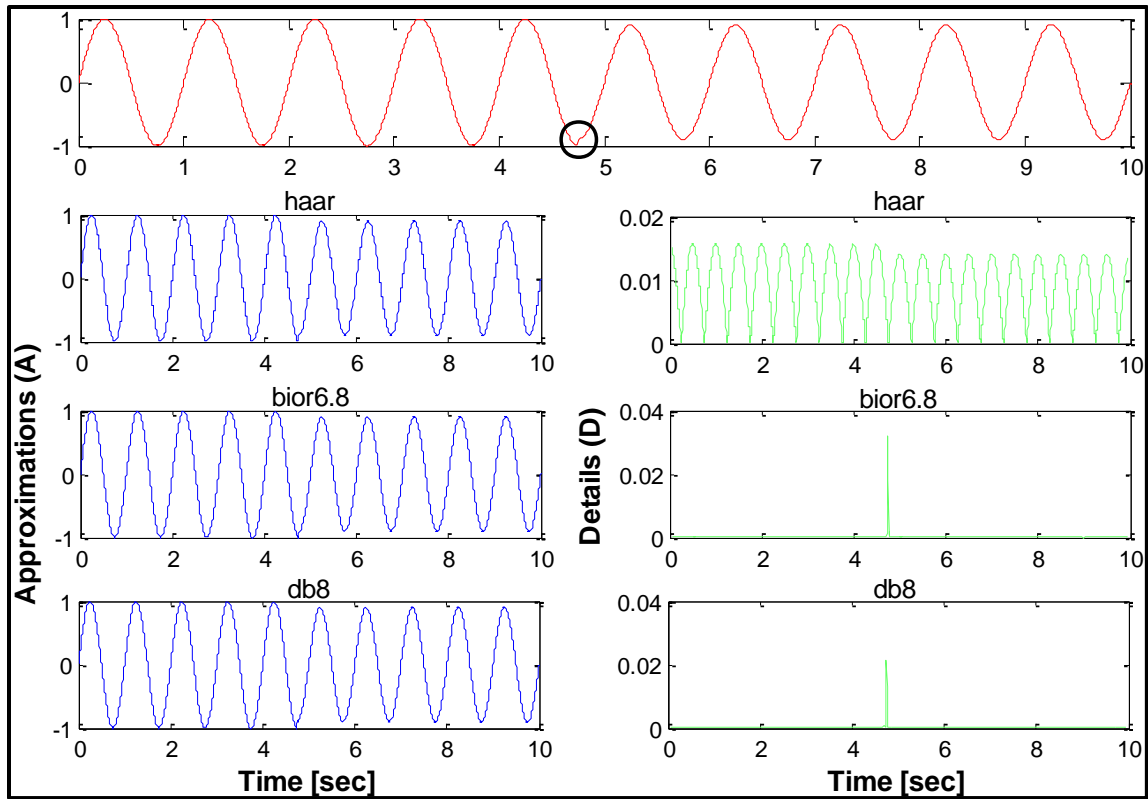


Figure 3-23: Signal with a discontinuity of 10% at $t = 4.75$ sec

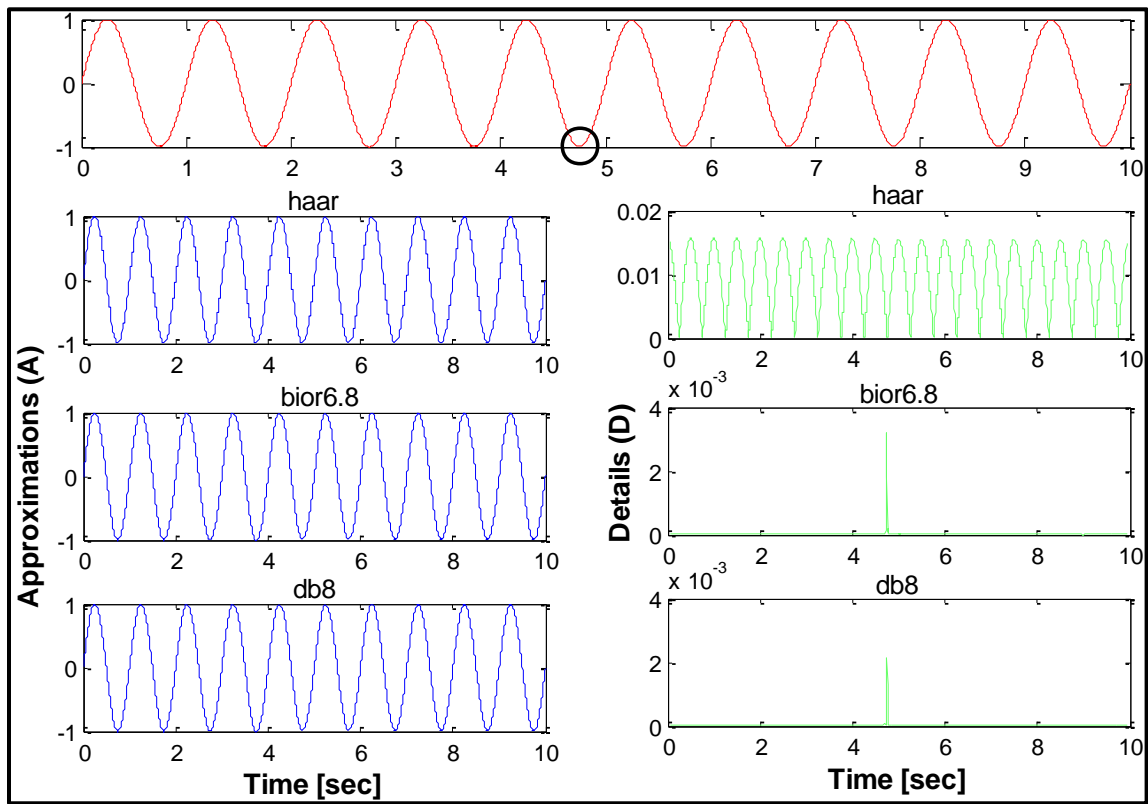


Figure 3-24: Signal with a discontinuity of 1% at $t = 4.75$ sec

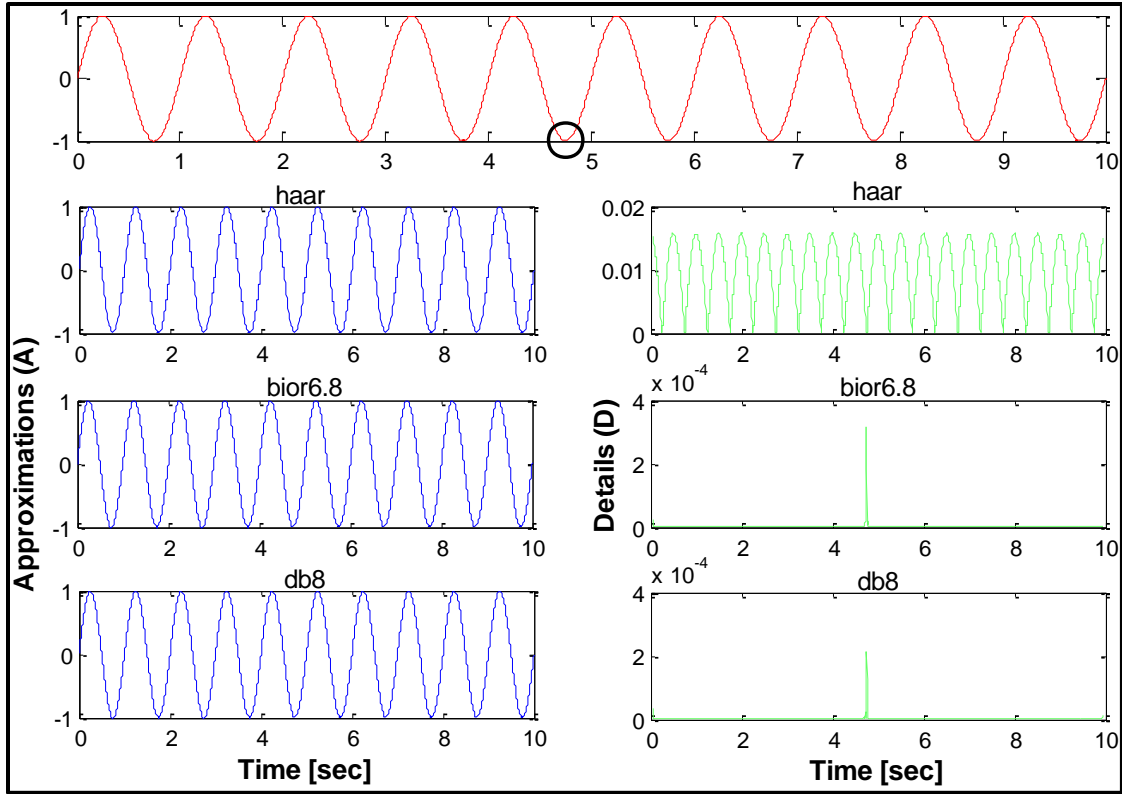


Figure 3-25: Signal with a discontinuity of 0.1% at $t = 4.75$ sec

3.7 Conclusions

In order to evaluate and calibrate the CWT and the DWT some numerical examples were presented. We could clearly appreciate that wavelet analyses were able to detect the frequencies of the signals, but particularly the discontinuities that were induced on it. In the case of the CWT, it detects without any difficulty the natural frequencies of the signal from the low-frequency analysis whereas the discontinuities were identified from the high-frequency analysis. Moreover, the DWT presents good results when different percentages of discontinuities (i.e., ranging from an discontinuity that could hardly be seen at a glance, to one that could be seen to simple sight) were induced on the signal. It was capable to successfully identify the time instance (for the three cases) in which the discontinuity was applied no matter how small it was. Furthermore, the magnitude of the spikes appearing in the detail functions seems to be related with the level of discontinuity induced in the signal being analyzed.

For each type of transform (CWT and DWT) a wavelet function was selected. In the case of the Continuous Wavelet Transform, the complex Morlet was chosen while for the Discrete Wavelet Transform, the wavelet selected was the Bior6.8. The use of these two mother wavelets does not mean that they are better than other wavelets; the use of a particular wavelet depends on the signal that will be evaluated. These two wavelets are the ones that will be initially used on the damage identification technique to the civil structures subjected to seismic loads in Chapters IV and V.

3.8 References

Misiti, M., Misiti, Y., Oppenheim, G. and Poggi, J. M. (2000). "Wavelet toolbox user's guide". The Math Works Inc., Natick, Massachusetts.

Misrikhanov, A. M. (2006). "*Wavelet Transform Methods: Application in Electroenergetics*". Automation and Remote Control, Ivanovo State Power Institute, Ivanovo, Russia, Vol. 67, No. 5, pages 682 – 697.

Montejo, L. A. (2010). "*Signal Processing Based Damage Detection in Structures Subjected to Random Excitations*". Structural Engineering and Mechanics, submitted for publication.

Ovanesova, A. and Suárez, L. E. (2004). "*Applications of Wavelet Transforms to Damage Detection in Frame Structures*", Engineering Structures, Vol. 26, No. 1, pages 39 – 49.

PyWavelet (2006). "*Documentation – Discrete Wavelet Transform in Python*", <http://wavelets.pybytes.com/>

CHAPTER IV

WAVELET BASED DAMAGE DETECTION METHODOLOGY APPLIED TO CIVIL STRUCTURES

4.1 Introduction

This chapter describes the evaluation of the Continuous Wavelet Transform (CWT) and the Discrete Wavelet Transform (DWT) for damage detection in civil structures. This analysis consists of the use of low and high frequencies decomposition to identify the occurrence of structural damage (inelastic action) using distinct modeling approaches and dynamic load excitations. The modeling approaches used are these described in Chapter II. The dynamic excitation loads are separated in two: artificially generated signals and dynamic loads registered from real earthquake excitations. As was determined in Chapter III, the wavelets use in this chapter will be the Complex Morlet (for the CWT analysis) and the Bior6.8 (for the DWT analysis). The wavelet parameters will be these determined in Chapter III. The low frequencies analyses are used to track changes in the natural frequencies of vibration of the structure, while the high frequencies analyses allow us to identify the instant when the structure suffers a sudden change in stiffness. Since a sudden change in stiffness introduces a discontinuity in the acceleration response, as is shown formally later, the problem of identifying the instant of damage is then one of identifying and localizing such sudden changes, or singularities, in the measured acceleration response (Bisht and Singh, 2011).

4.2 Description of the Dynamic Load Excitations

Different dynamic load excitations were generated/selected to study the influence of different frequency contents and non-stationary characteristics in the results of the detection methodologies. The artificially generated signals are a 5Hz tapered sinusoidal and two white noises with limited frequency contents (i.e. [0-20Hz] and [0-40Hz]). The earthquakes used

are those that occurred in Round Valley and Loma Prieta. All the excitation loads have a sampling time dt equal to 0.005 seconds. Beginning with the tapered sinusoidal, it was generated with two transient of 5 seconds duration each one (for a total of 10s) and a frequency of 5Hz (Figure 4-1). The second and third signals are the white noises with frequency content up to 20Hz and 40Hz respectively (Figures 4-2 and 4-3). The peak amplitude for these three artificially generated excitations was normalized to 1 and each have time duration of 10 seconds. The earthquakes loads are presented in Figures 4-4 and 4-5, they are the Round Valley earthquake of November 23, 1984 from the McGee Creek Surface Station with 0.14 of PGA (which can be considered as a wide-band record) and the Loma Prieta earthquake of October 17, 1989 from the Treasure Island Station with 0.1 of PGA (which can be considered as a narrow-band record). Both earthquakes were obtained from the PEER strong motion database (2010). The Loma Prieta earthquake was edited in order to be applied to the RC member. It was cut to 25 second compared with the original of ~40 seconds (Figure 4-5). The Fourier Spectrum for each dynamic excitation is also shown. A summary of these earthquakes is displayed in Table 4-1.

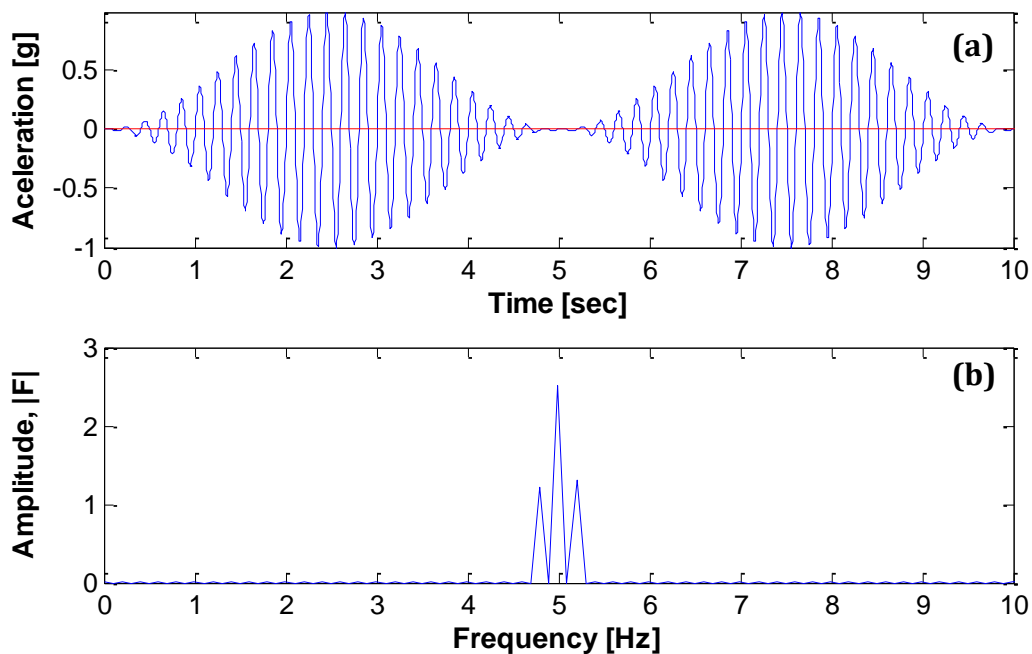


Figure 4-1: (a) 5Hz Tapered Sinusoid, (b) Fourier Spectrum

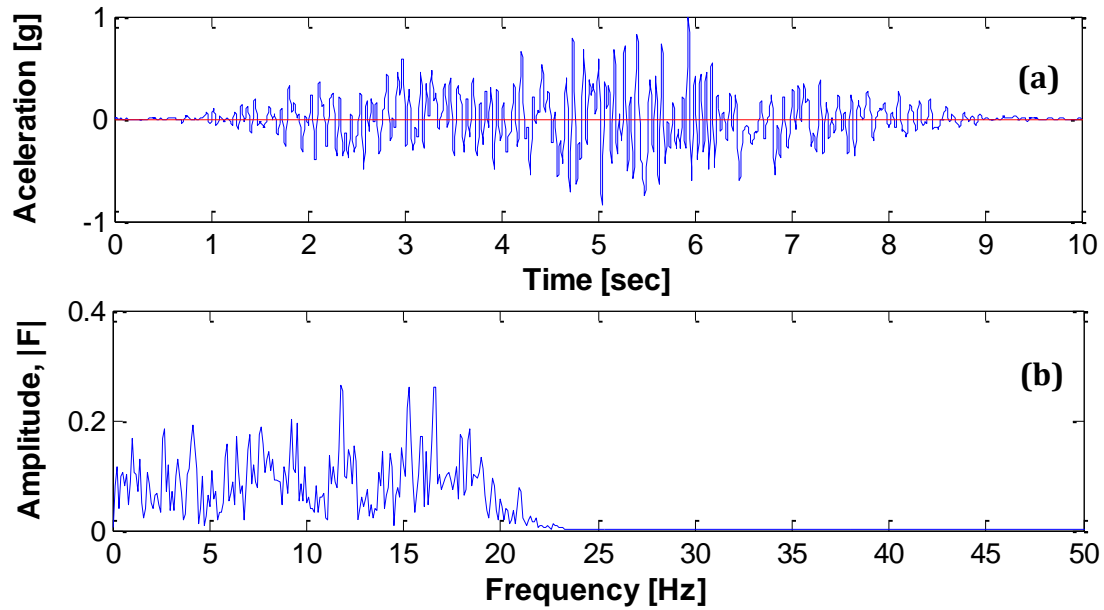


Figure 4-2: (a) White Noise with frequency content of 20Hz, (b) Fourier Spectrum

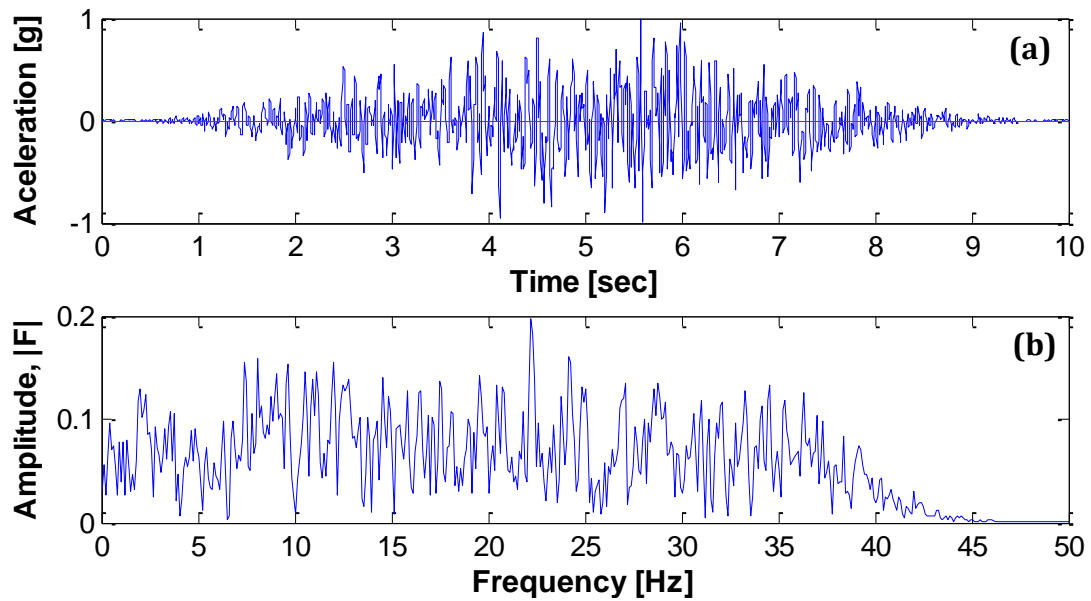


Figure 4-3: (a) White Noise with a frequency content of 40Hz, (b) Fourier Spectrum

Table 4-1: Ground Motions

Earthquake	Station Name	Magnitude	Total Duration [sec]
Round Valley	McGee Creek Surface	5.8	6.85
Loma Prieta	Treasure Island	6.9	39.95

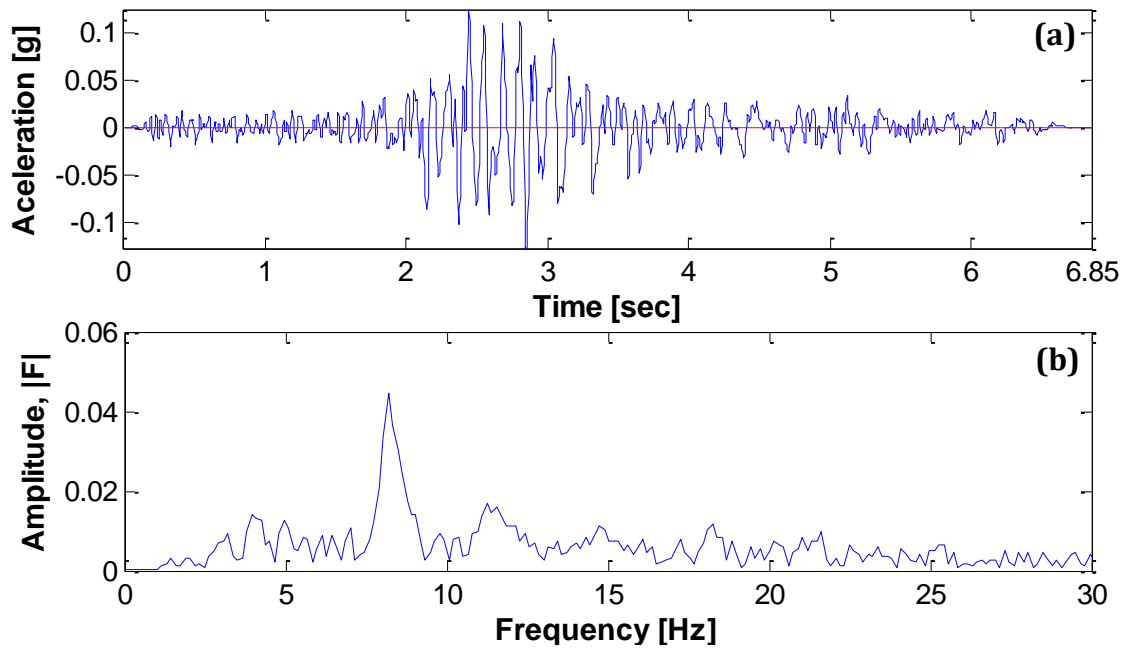


Figure 4-4: (a) Round Valley earthquake from McGee Creek Surface Station - 11/23/1984, (b) Fourier Spectrum

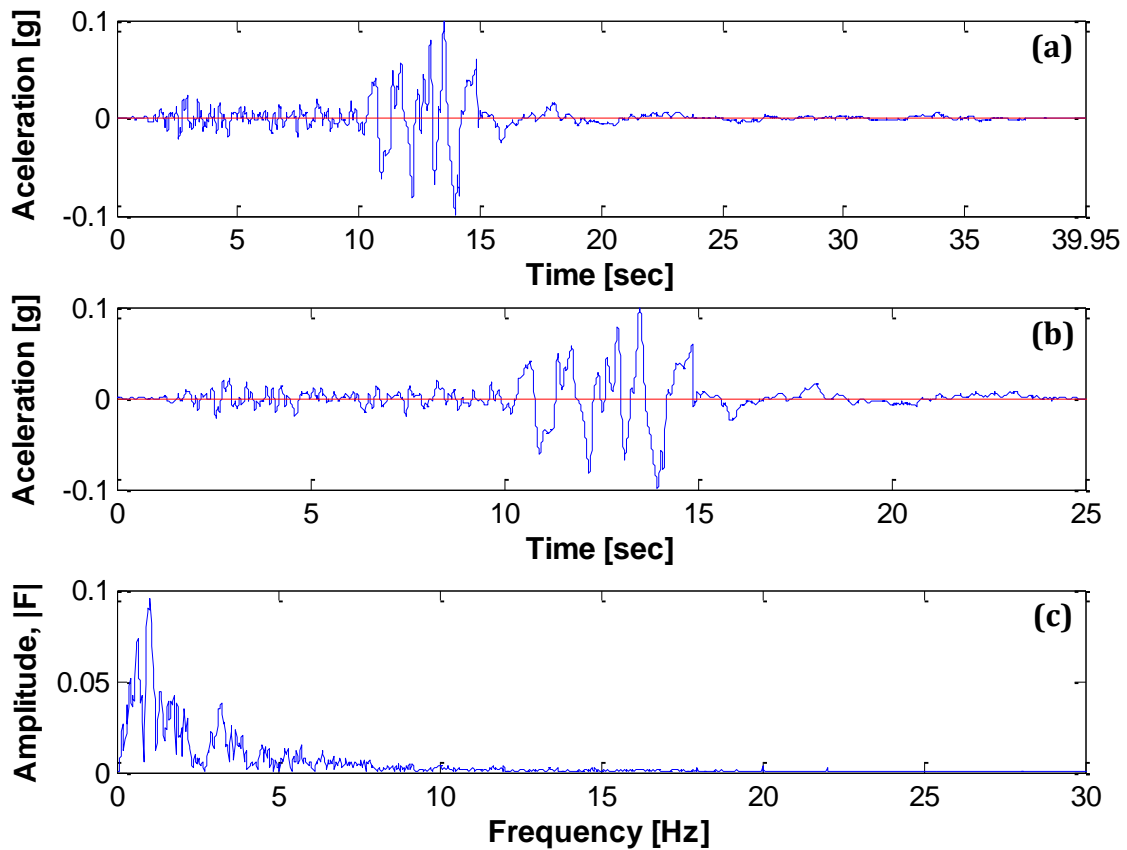


Figure 4-5: Loma Prieta earthquake from Treasure Island Station - 10/17/1989: (a) Original, (b) Edited to 25 s, (c) Fourier Spectrum

4.3 Acceleration and Force-Displacement Responses

Figures 4-6 to 4-8 present the acceleration response for the five dynamic excitation loads at the top of the column (left) with its respective force-displacement response (right) for the three model approaches (bilinear, Takeda and fiber-based). The purpose of showing the acceleration responses is because it is what we are analyzing and just by looking at these we cannot say that damage is present. Now, the force-displacement response is shown to verify that indeed inelastic action is present in the column. The five dynamic load responses illustrated in each figure have the following sequence: tapered sinusoid, white noise 20Hz, white noise 40Hz, Round Valley earthquake, and Loma Prieta earthquake.

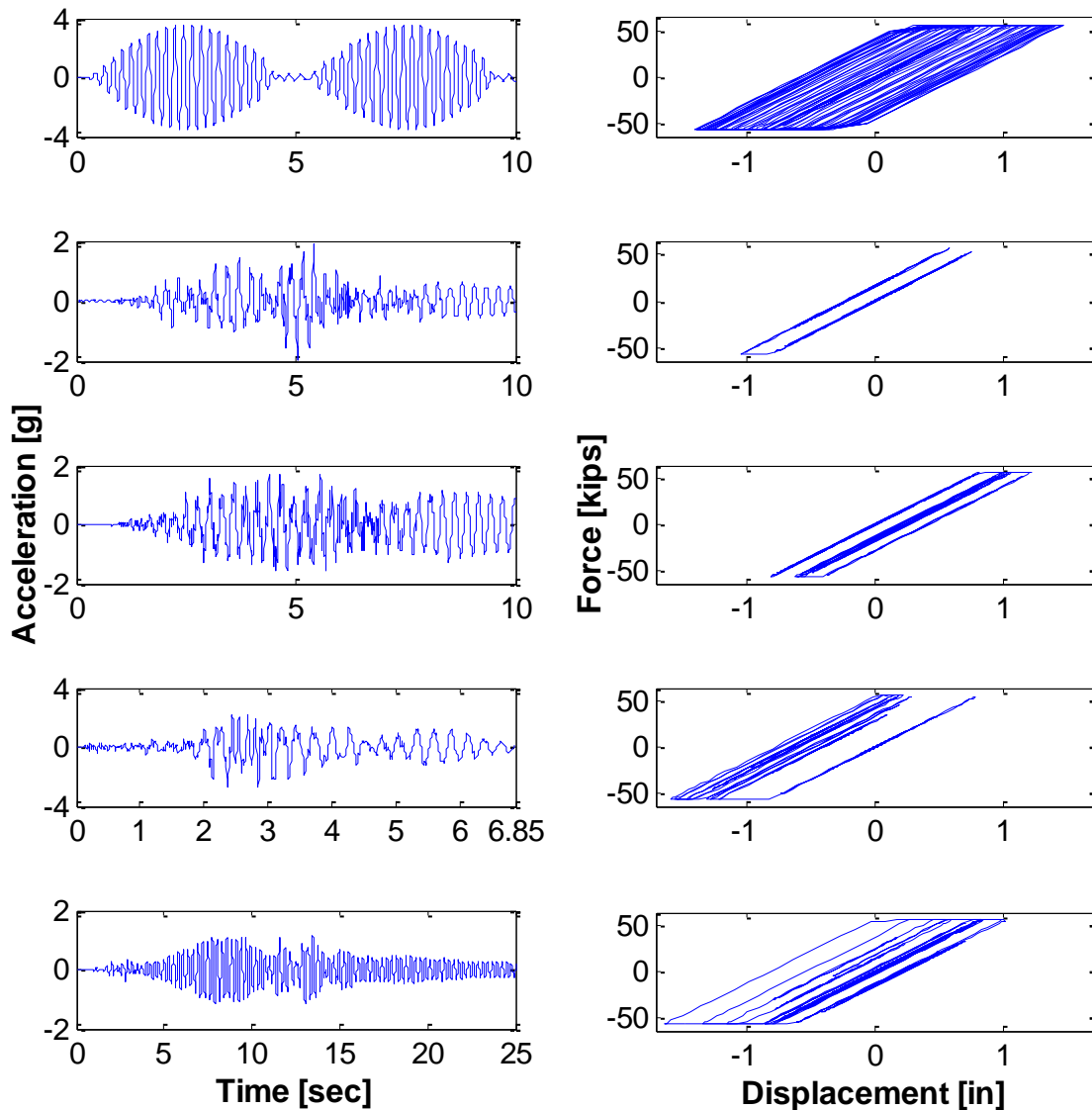


Figure 4-6: Bilinear: Top Acceleration Responses (left) and the Force-Displacement Responses (Right)

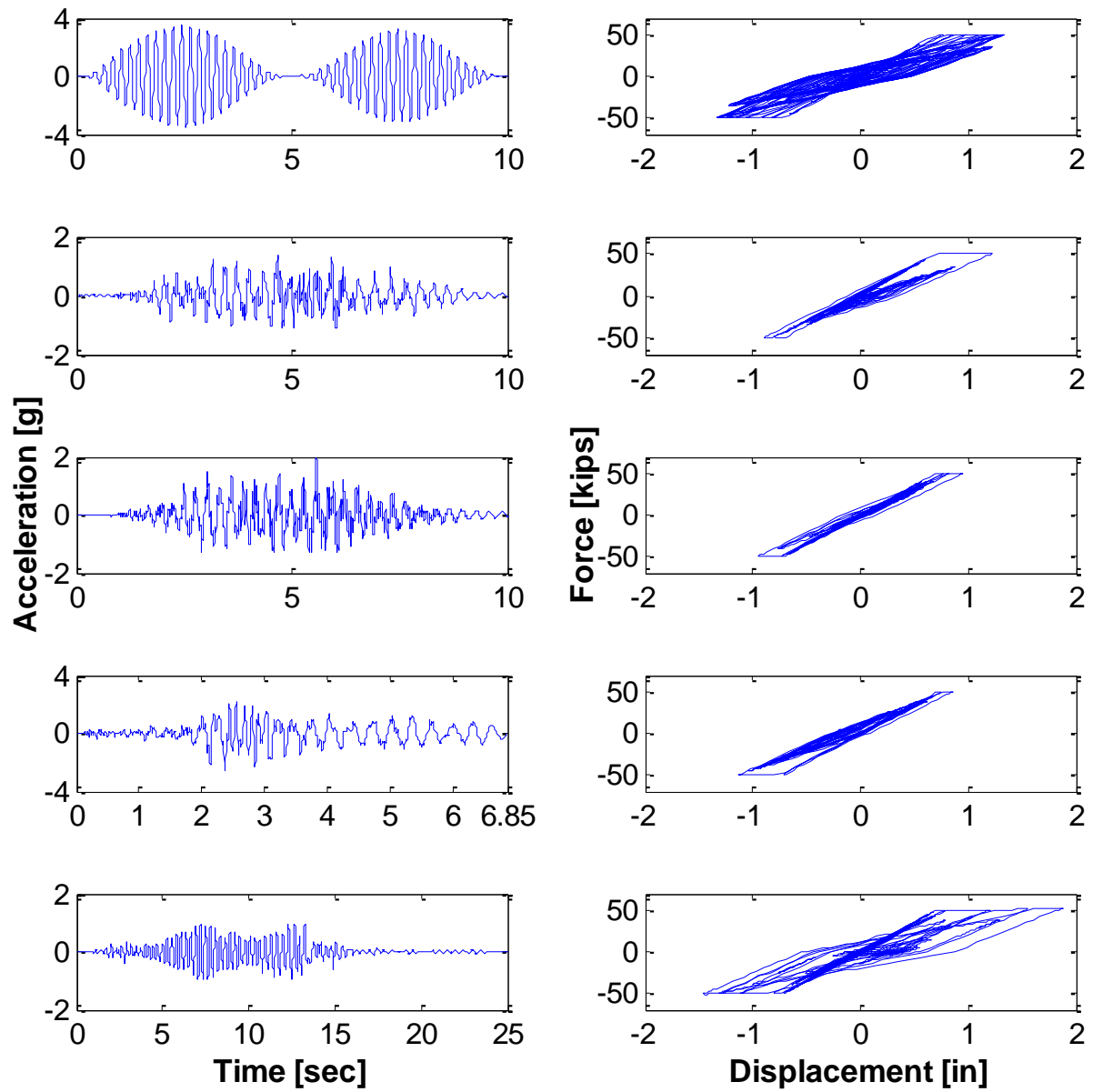


Figure 4-7: Takeda: Top Acceleration Responses (left) and the Force-Displacement Responses (Right)

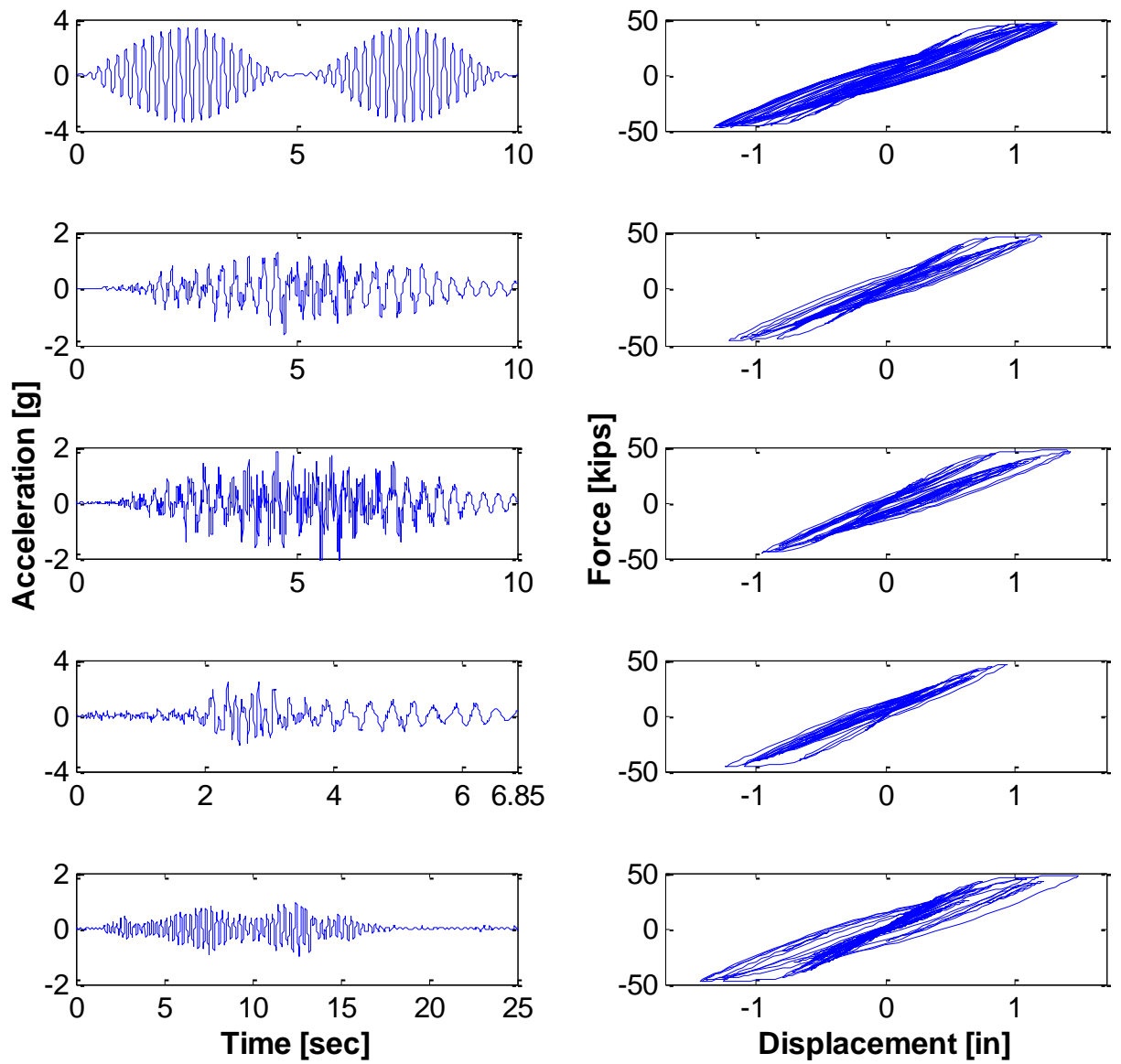


Figure 4-8: Fibers: Top Acceleration Responses (left) and the Force-Displacement Responses (Right)

4.4 Evaluation of the CWT Applied to Civil Structures

The FL-89A column model presented on Chapter II will be used to evaluate the capabilities of the CWT for damage detection in civil structures. The results presented correspond to the low and high frequency analyzes for the three modeling approaches (bilinear, Takeda and fiber-based). For each combination of modeling approach and type of excitation load, four plots are presented. The first plot for each model is the force response in the time domain, the horizontal lines represent the yielding force obtained from a moment-curvature analysis performed in CUMBIA. Each time that the force response cross this line, it represent damage (or a yield episode). These are the time instants that we would capture on the CWT high frequency analysis (and/or DWT detail analysis showed later). The next plot shows the absolute tangent stiffness (K_{tan}) calculated as

$$K_{tan} = abs\left(\frac{F_{i+1} - F_i}{D_{i+1} - D_i}\right) \quad (4-1)$$

where:

F_i and F_{i+1} : column force at time instant i and $i+1$, and

D_i and D_{i+1} : column displacement at time instant i and $i+1$.

The tangent stiffness is calculated to keep track of any sudden change in the structure stiffness. As mentioned earlier, the high frequency analyzes are performed to detect this type of singularities. However, it will be shown later in this chapter that, depending on the modeling approach that a change in stiffness cannot always be related to damage (inelastic action). The third figure presents the CWT application in order to identify the natural frequencies or the singularities of the signal depending on the frequency analysis carried out (low or high frequency). Finally, if the low-frequency analysis is performed, the instantaneous frequency from the wavelet ridges extracted from the Wavelet Map is presented for a better understanding of the frequency changes. In this figure, we plot two lines: a dashed line and a dash-dotted line. The dashed line represents the natural frequency of the column before any excitation was applied and the dash-dotted line represents the final frequency after the excitation. The corresponding values for the frequencies before and after the excitation is applied are summarized in Table 4-2, these values were obtained from eigenvalues analyzes performed to the structure before and

after the load was applied. Finally, when a high-frequency analysis is performed, the CWT coefficients for a frequency equal to 80Hz is presented in the last plot.

Table 4-2: Frequencies in Hz after the dynamic load excitation was applied

Signal	bilinear	hysteretic	fibers
Before load application	3.66	3.65	4.37
Tapered Sinusoid	3.66	1.73	2.83
White Noise <20Hz	3.66	2.90	2.98
White Noise <40Hz	3.66	3.04	3.01
Round Valley	3.66	2.50	3.01
Loma Prieta	3.66	1.57	2.83

4.4.1 5Hz Tapered Sinusoid low-frequency results

The results corresponding to this signal for the low-frequency analysis are presented in Figures 4-9 to 4-11. It can be noted that the low-frequency analysis identified the frequency of the input excitation (5Hz) in all the three model approaches and not the evolution in the frequency of vibration of the structure. This was expected because for this type of excitation (persistent), after several cycles the system will respond only at the frequency of the external forcing.

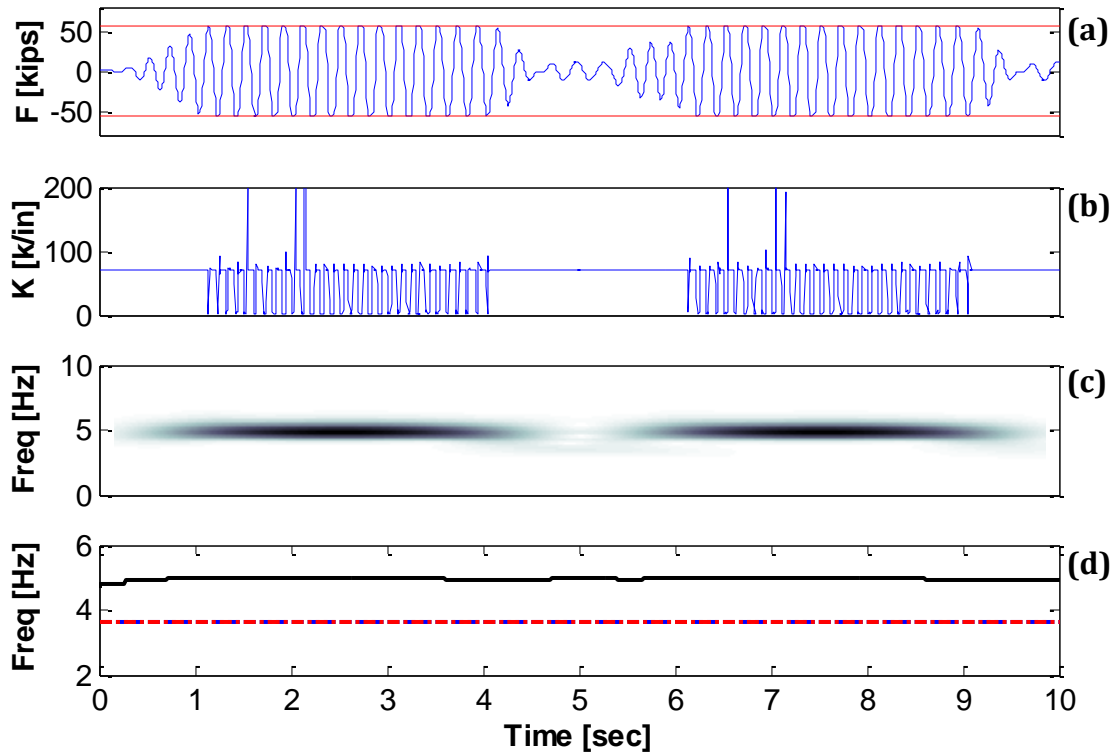


Figure 4-9: Bilinear model: (a) Force Response, (b) Stiffness, (c) Low-Frequency Analysis, (d) IF from wavelet ridges

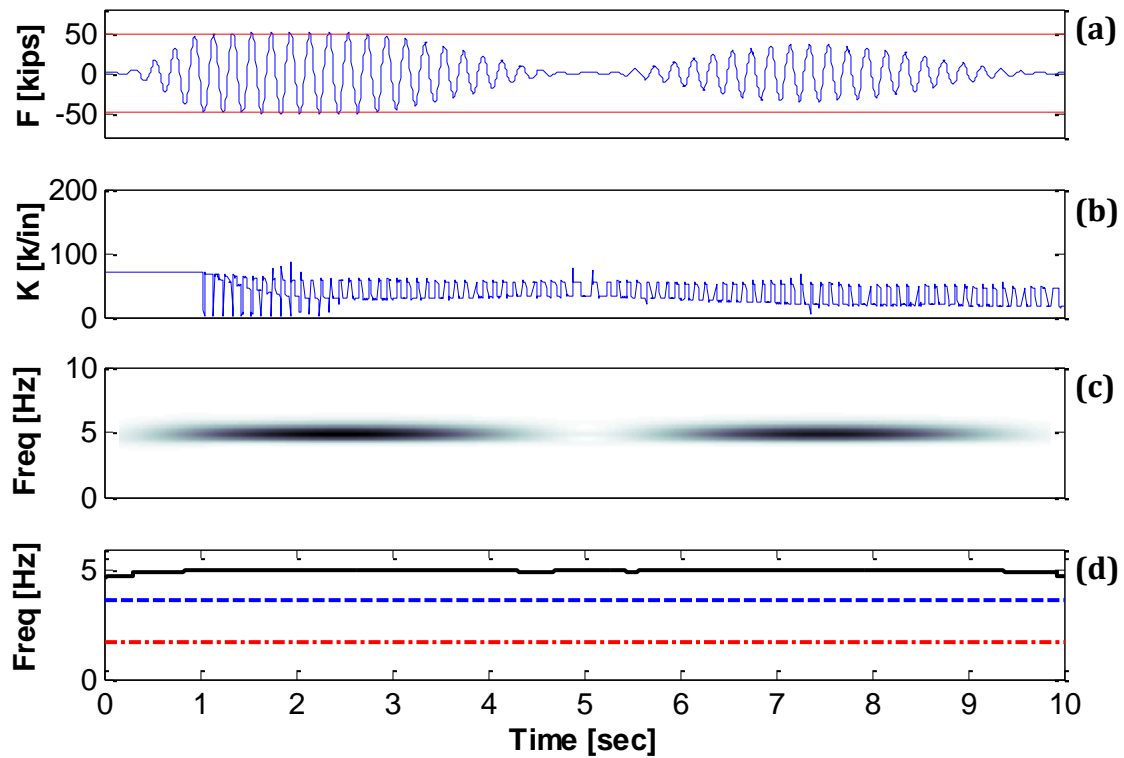


Figure 4-10: Hysteretic model: (a) Force Response, (b) Stiffness, (c) Low-Frequency Analysis, (d) IF from wavelet ridges

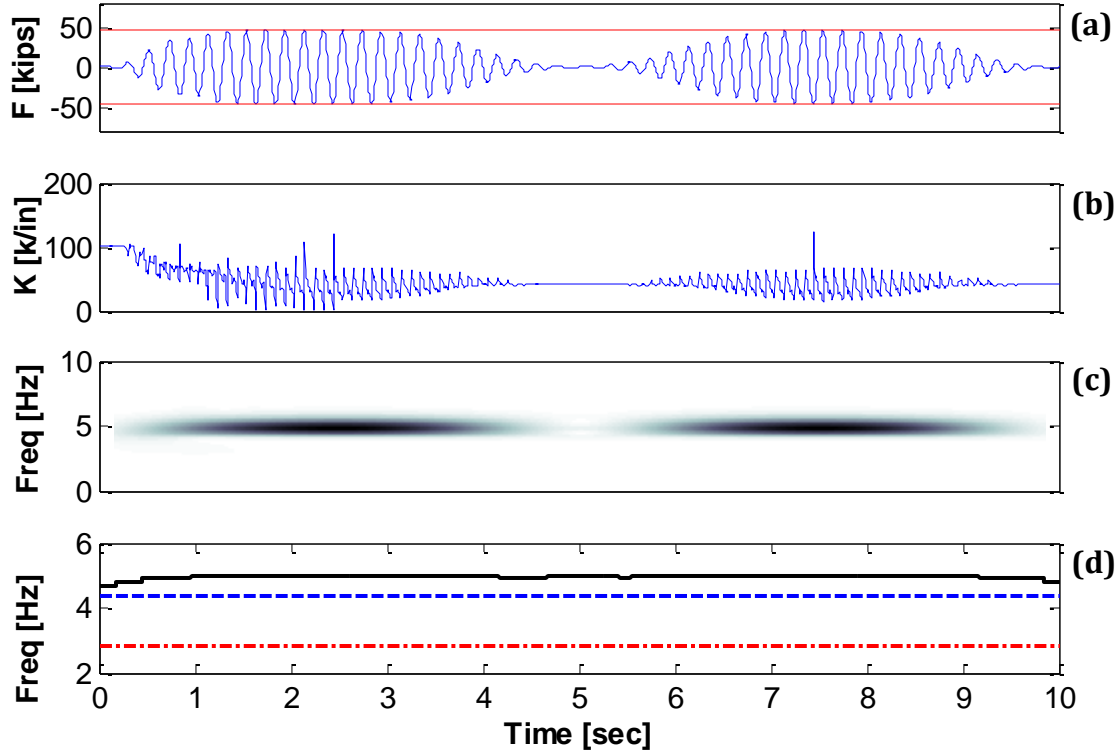


Figure 4-11: Fibers model: (a) Force Response, (b) Stiffness, (c) Low-Frequency Analysis, (d) IF from wavelet ridges

4.4.2 5Hz Tapped Sinusoid high-frequency results

The high-frequency results for the Tapped Sinusoid are presented next in Figures 4-12 to 4-14. If we look at the tangent stiffness plot, it can be noticed that the changes can be related to yield episodes especially for the bilinear model and partially for the fiber-based model. However, in the case of the hysteretic “Takeda” model, these changes does not exactly correlate with yield episodes. For example, in the last 5 seconds (Figure 4-13b), several drastic changes in stiffness are identified while the structure did not yield during this time (Figure 4-13a). These additional change in stiffness occur when the force in the columns pass through zero and are inherent to the modeling approach rather than to the actual occurrence of damage. The wavelet maps at high frequencies (Figures 4.12c, 4.13c and 4.14c) successfully identified the occurrence of discontinuities in the response (dark vertical trends). However, as explained earlier, not all of these discontinuities can be related to damage. The wavelet coefficients for a given high frequency (in this case 80 Hz, Figures 4.12d, 4.13d and 4.14d) are a more time-efficient approach than the highly

redundant wavelet map (though it may be less robust). It is seen that the spikes that appear in these plots can be related to a change in stiffness in the structure.

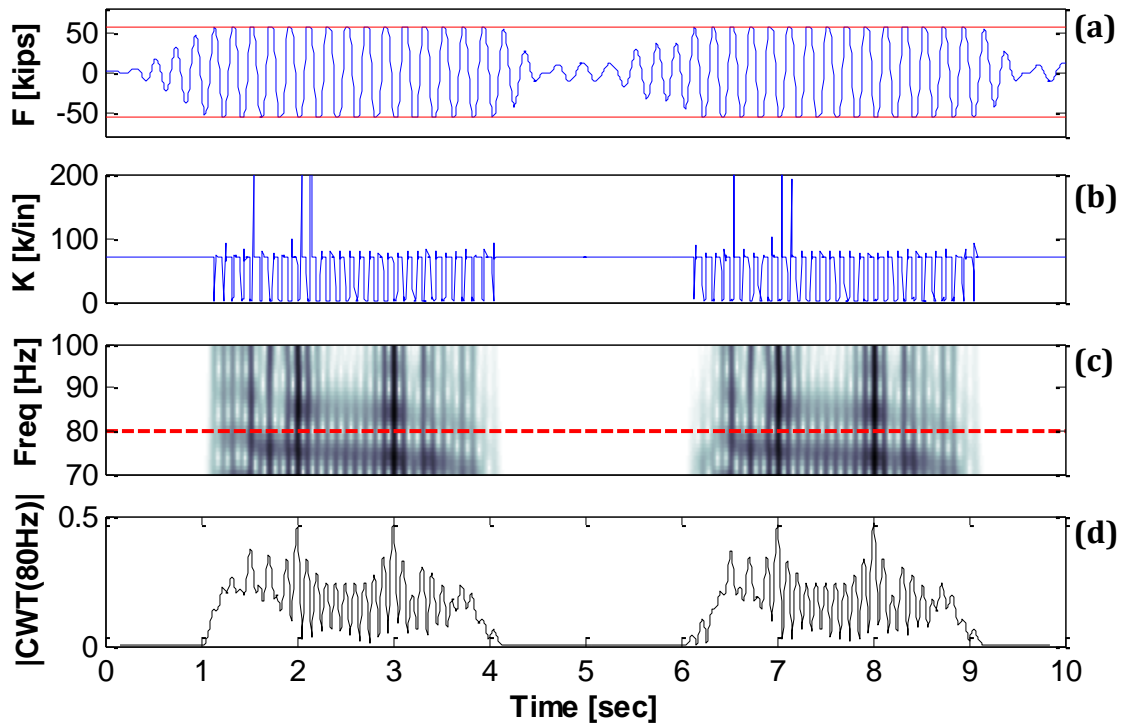


Figure 4-12: Bilinear model: (a) Force Response, (b) Stiffness, (c) High-Frequency Analysis, (d) Coefficients for 80Hz frequency

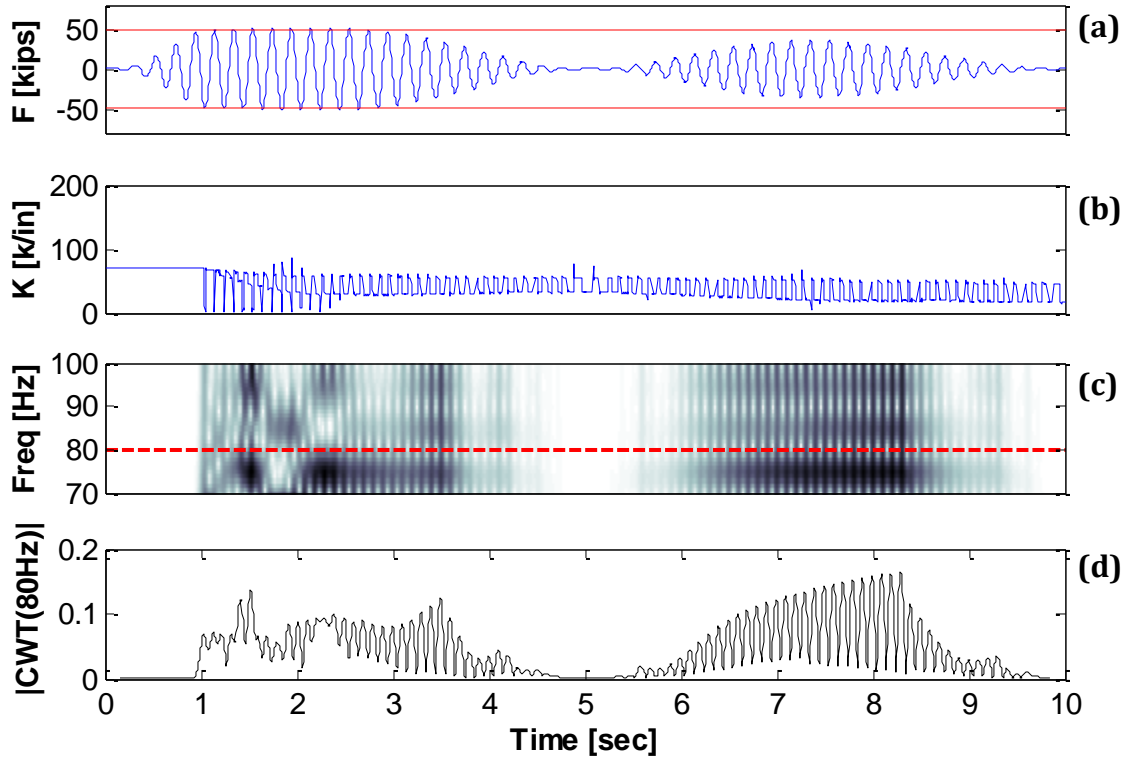


Figure 4-13: Hysteretic model: (a) Force Response, (b) Stiffness, (c) High-Frequency Analysis, (d) Coefficients for 80Hz frequency

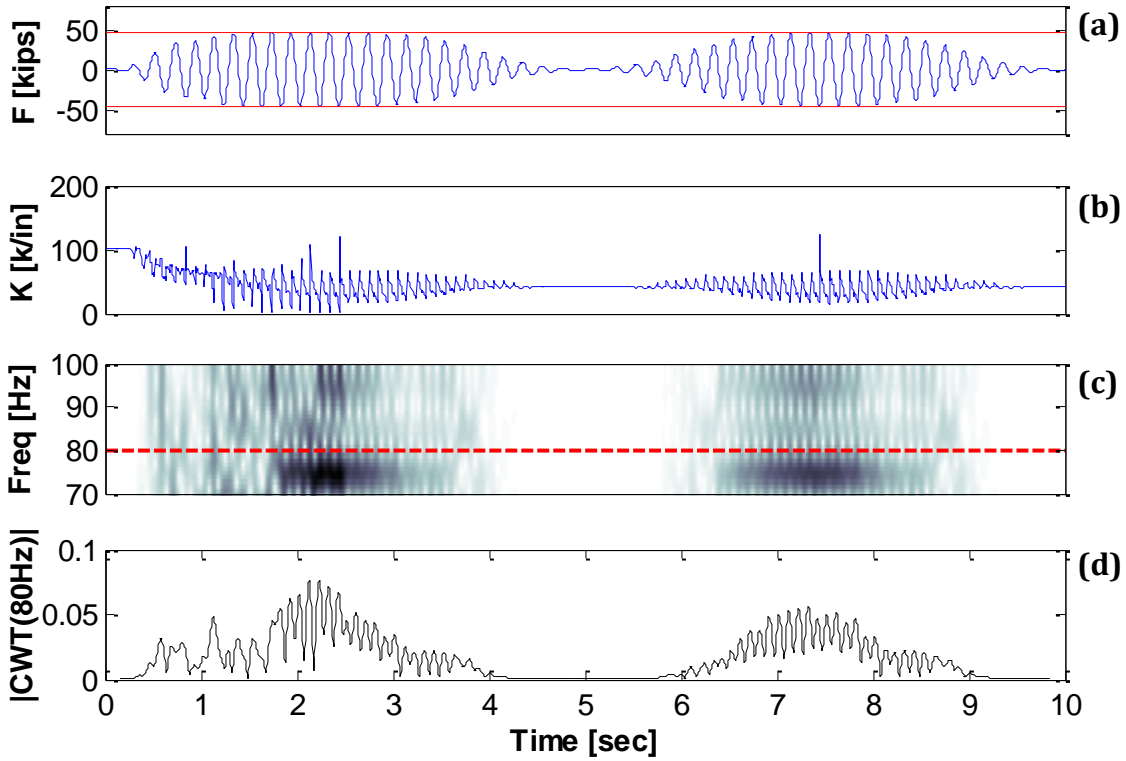


Figure 4-14: Fibers model: (a) Force Response, (b) Stiffness, (c) High-Frequency Analysis, (d) Coefficients for 80Hz frequency

4.4.3 White Noise <20Hz low-frequency results

The low-frequency analysis results for the white noise with a frequency content of 20Hz are presented in Figure 4-15 to 4-17. Looking at the Wavelet Maps and the extracted ridges (Figures c and d) it is noticed that the change in the natural frequency of the structure due to the application of the dynamic excitation was captured for all the three models.

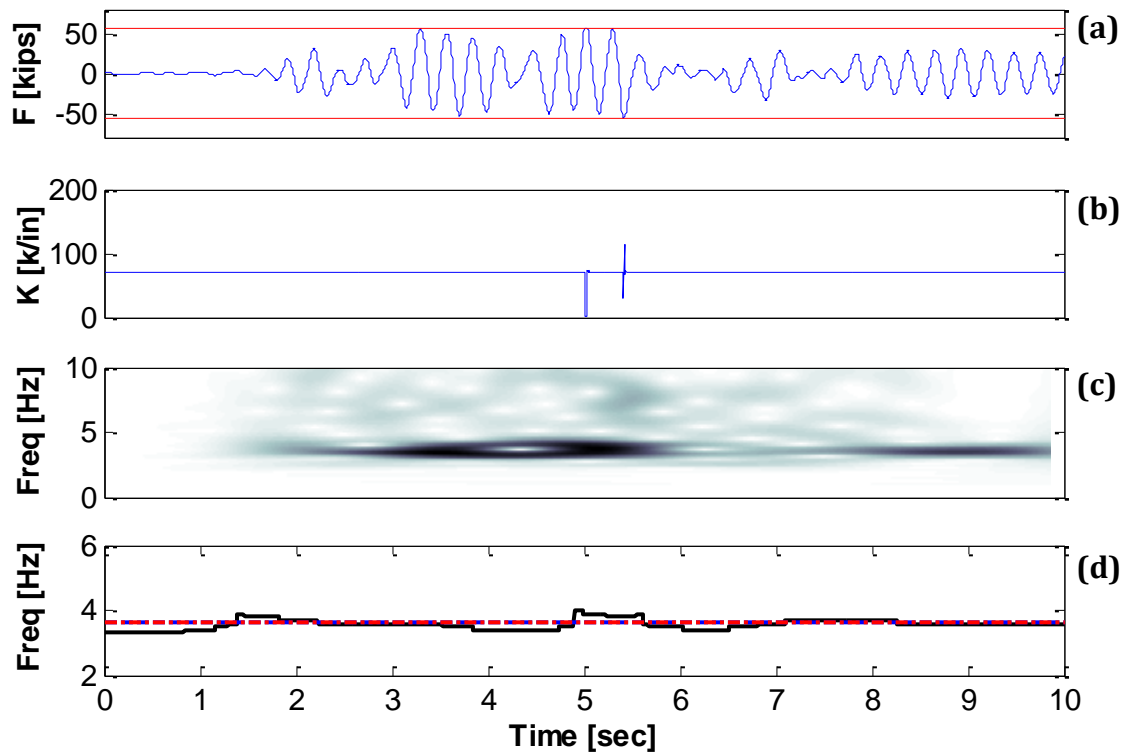


Figure 4-15: Bilinear model: (a) Force Response, (b) Stiffness, (c) Low-Frequency Analysis, (d) IF from wavelet ridges

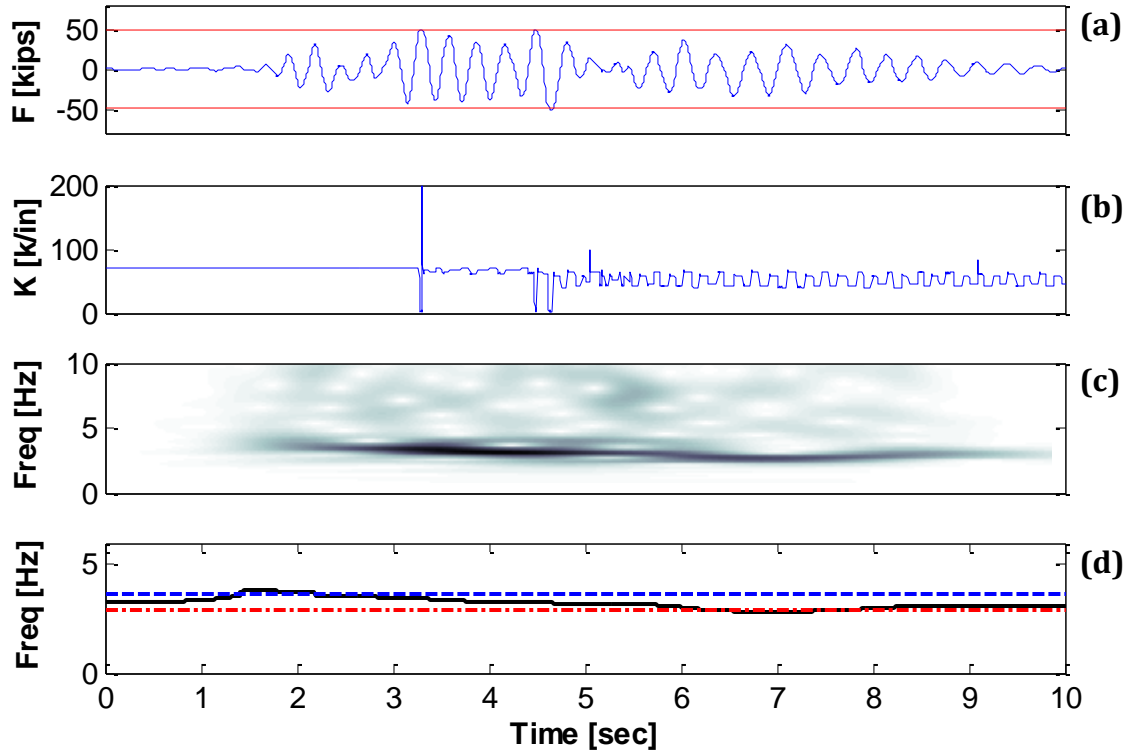


Figure 4-16: Hysteretic model: (a) Force Response, (b) Stiffness, (c) Low-Frequency Analysis, (d) IF from wavelet ridges

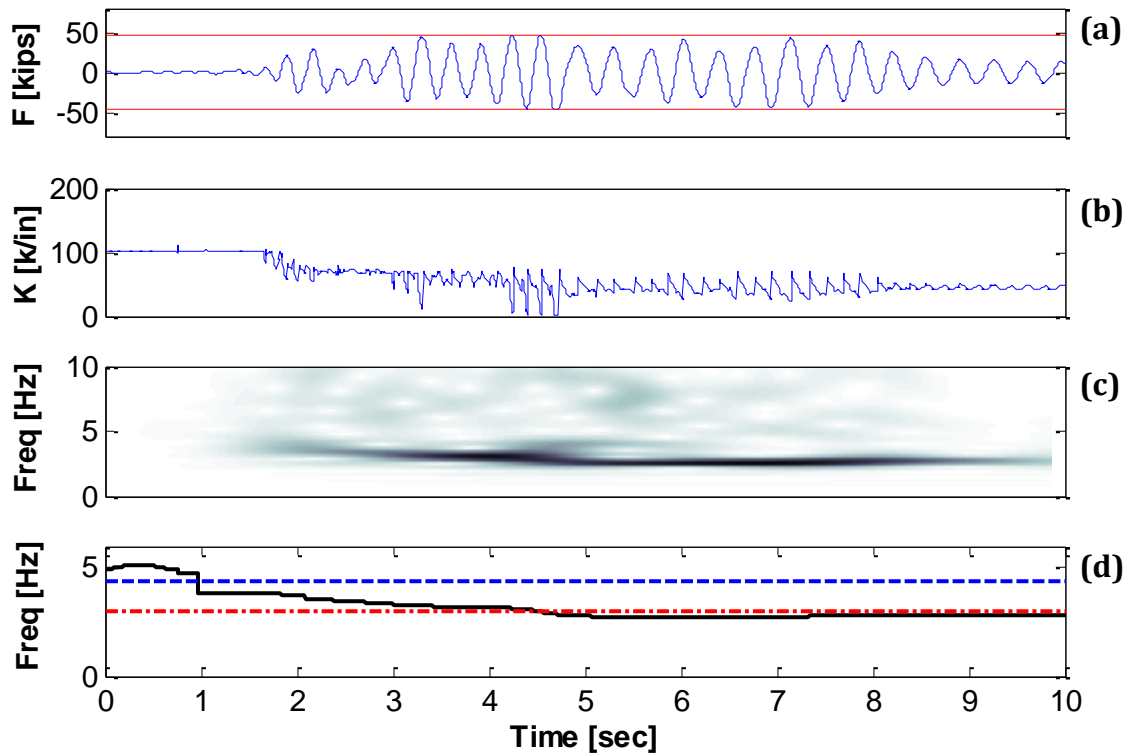


Figure 4-17: Fibers model: (a) Force Response, (b) Stiffness, (c) Low-Frequency Analysis, (d) IF from wavelet ridges

4.4.4 White Noise <20Hz high-frequency results

The high frequency results are presented in Figures 4-18 to 4-20. By looking at the force response we can distinguish (black circles) two yield episodes on the bilinear model occuring at 5 and 5.5 s, three yield episodes in the hysteretic model occuring at 3.2, 4.7 and 4.9 s approximately, and approximately 5 yield episodes in the fiber-based model occurring at 3.2, 4.2, 4.4, 4.6, and 4.7 seconds. Looking at the high frequencies Wavelet Maps and the coefficients at 80 Hz, it can be said that this approach was: (1) Completely succesful for the bilinear model as the two yield episodes were clearly identified; (2) Partially succesfull for the Takeda model because although the three yield episodes were identified, some other minor trends/peaks appear that were not related with yield; (3) Not succesfull for the fiber-based approach as large amount of important trends/peaks that cannot be related with yield episodes appear (see for example the dark trend or peak around 2 seconds, Figures 4-20 c and d).

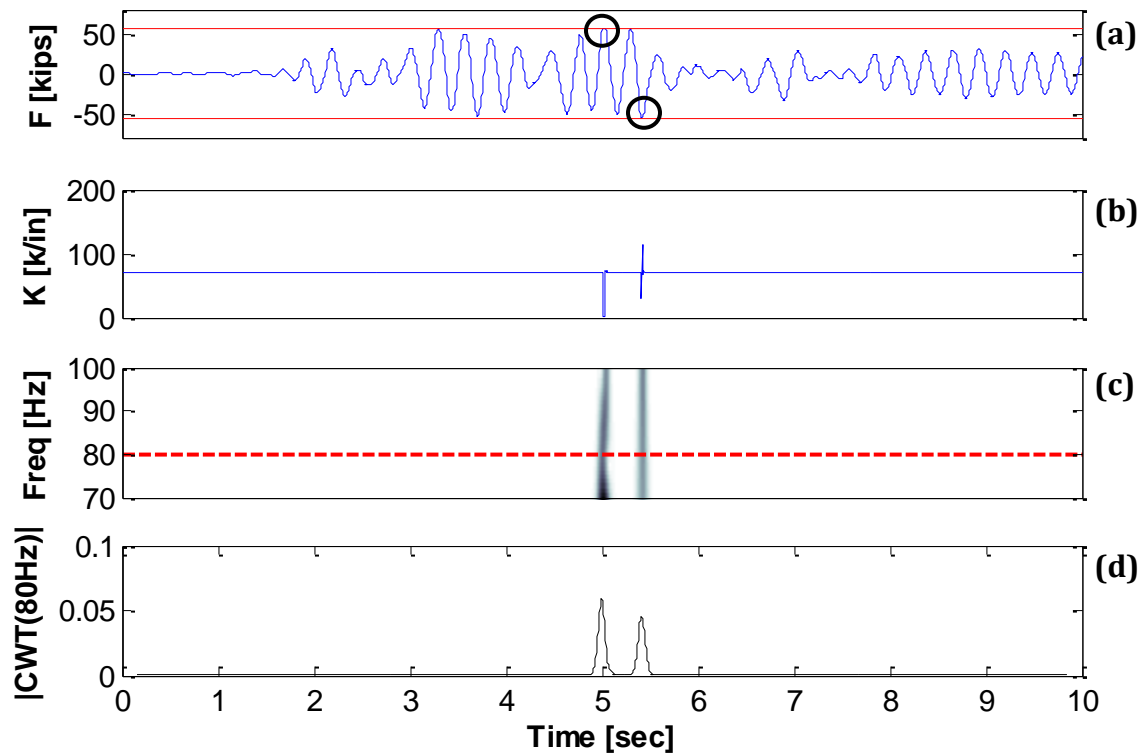


Figure 4-18: Bilinear model: (a) Force Response, (b) Stiffness, (c) High-Frequency Analysis, (d) Coefficients for 80Hz frequency

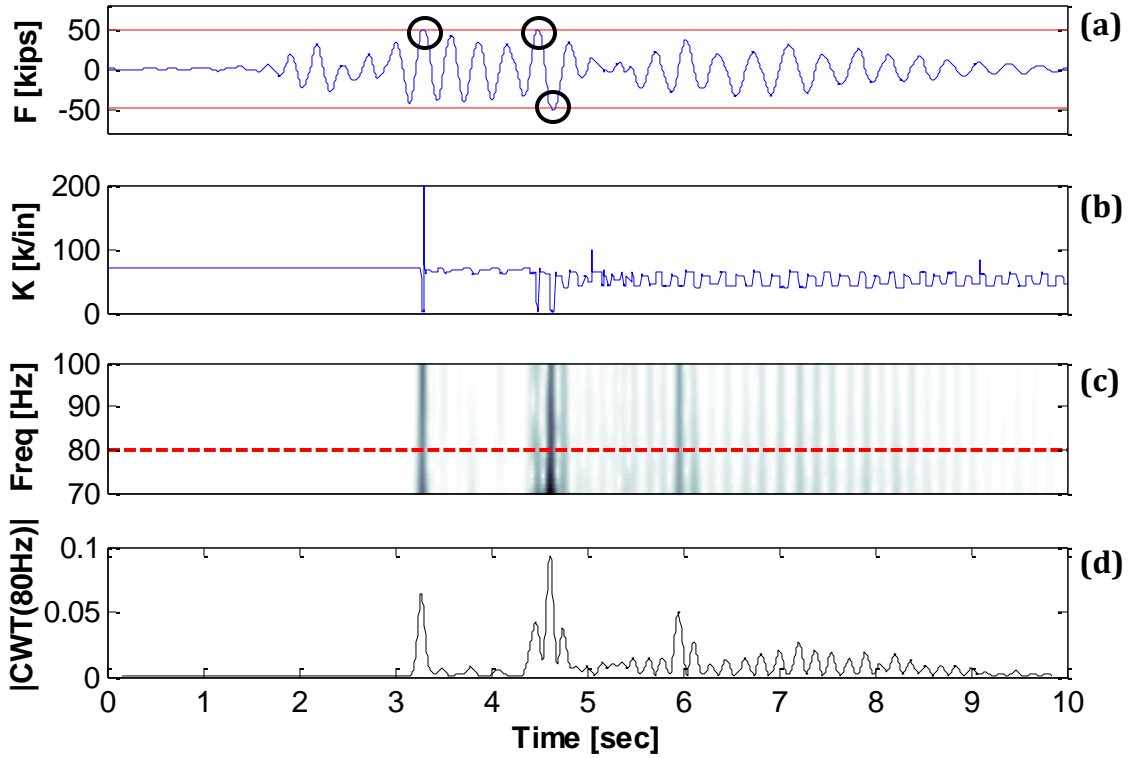


Figure 4-19: Hysteretic model: (a) Force Response, (b) Stiffness, (c) High-Frequency Analysis, (d) Coefficients for 80Hz frequency

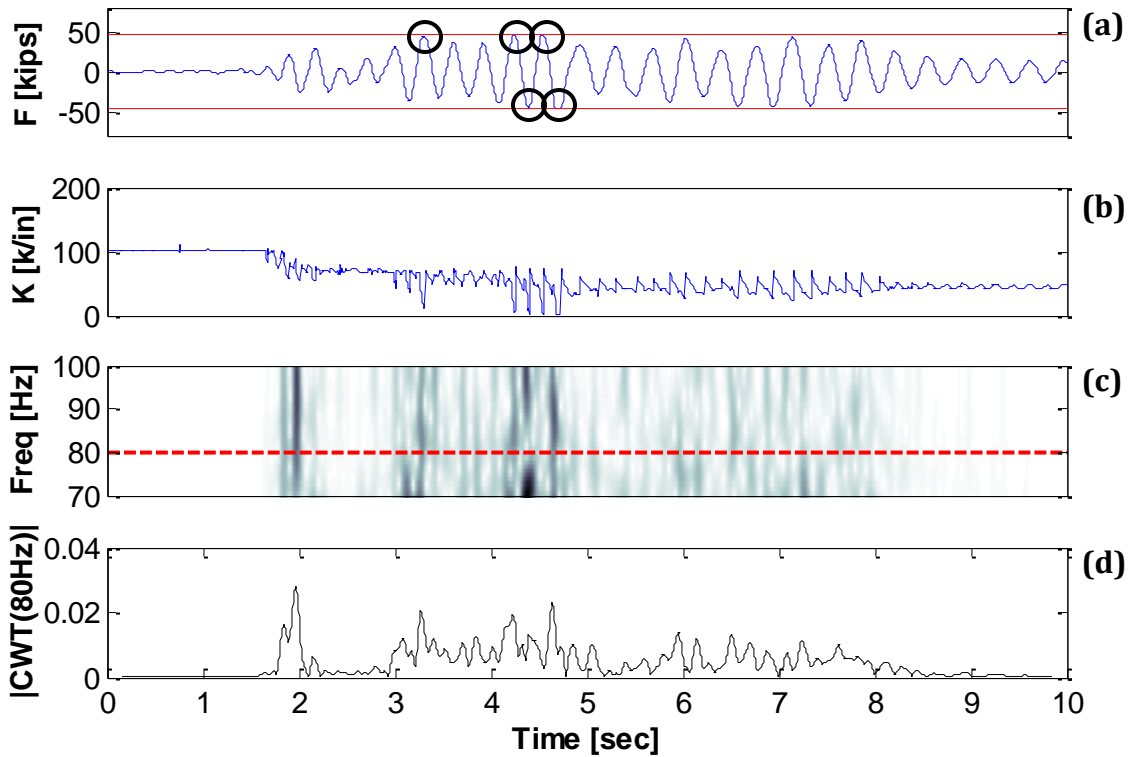


Figure 4-20: Fibers model: (a) Force Response, (b) Stiffness, (c) High-Frequency Analysis, (d) Coefficients for 80Hz frequency

4.4.5 White Noise <40Hz low-frequency results

Figures 4-21 to 4-23 show the low frequency results for the 40Hz white noise excitation. Looking at the Wavelet Maps and the extracted ridges (Figures c and d) it is noticed that the change in the natural frequency of the structure due to the application of the dynamic excitation was capture for all the three models.

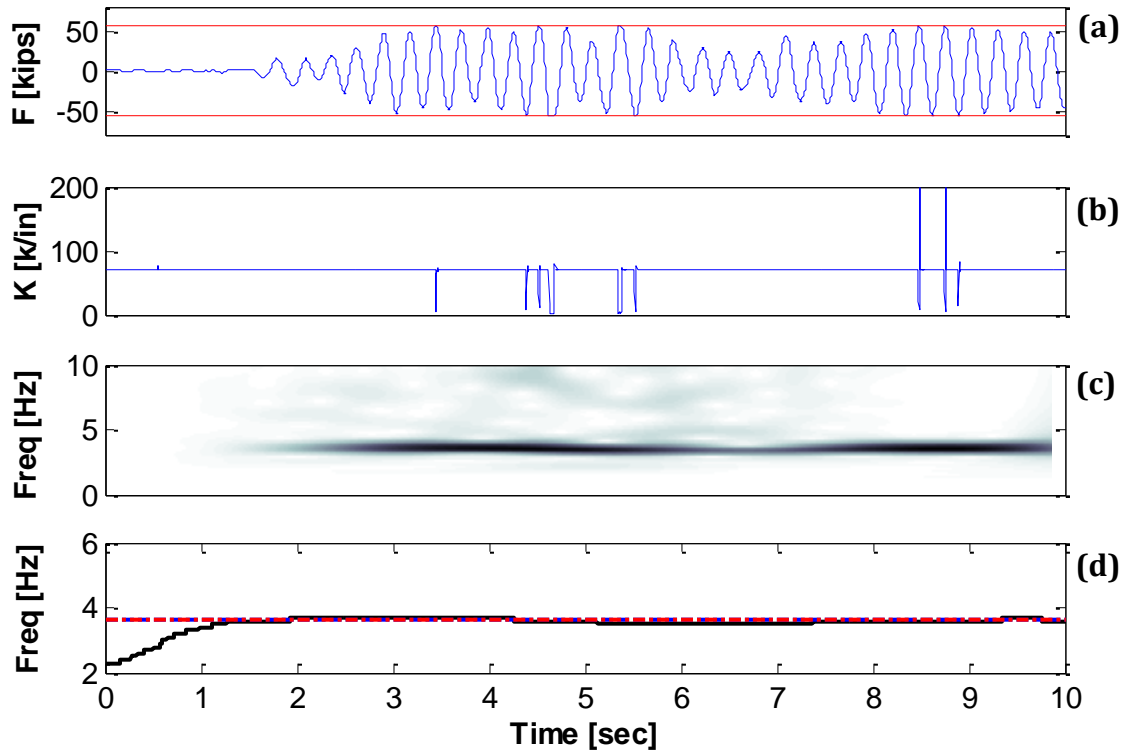


Figure 4-21: Bilinear model: (a) Force Response, (b) Stiffness, (c) Low-Frequency Analysis, (d) IF from wavelet ridges

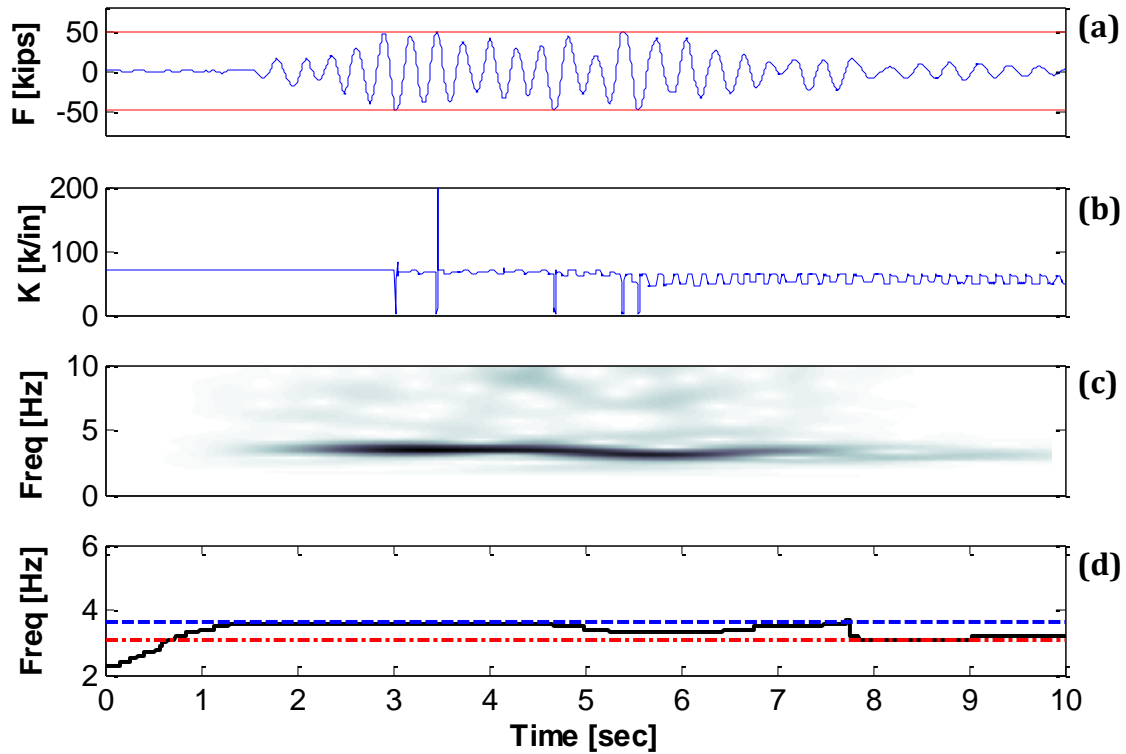


Figure 4-22: Hysteretic model: (a) Force Response, (b) Stiffness, (c) Low-Frequency Analysis, (d) IF from wavelet ridges

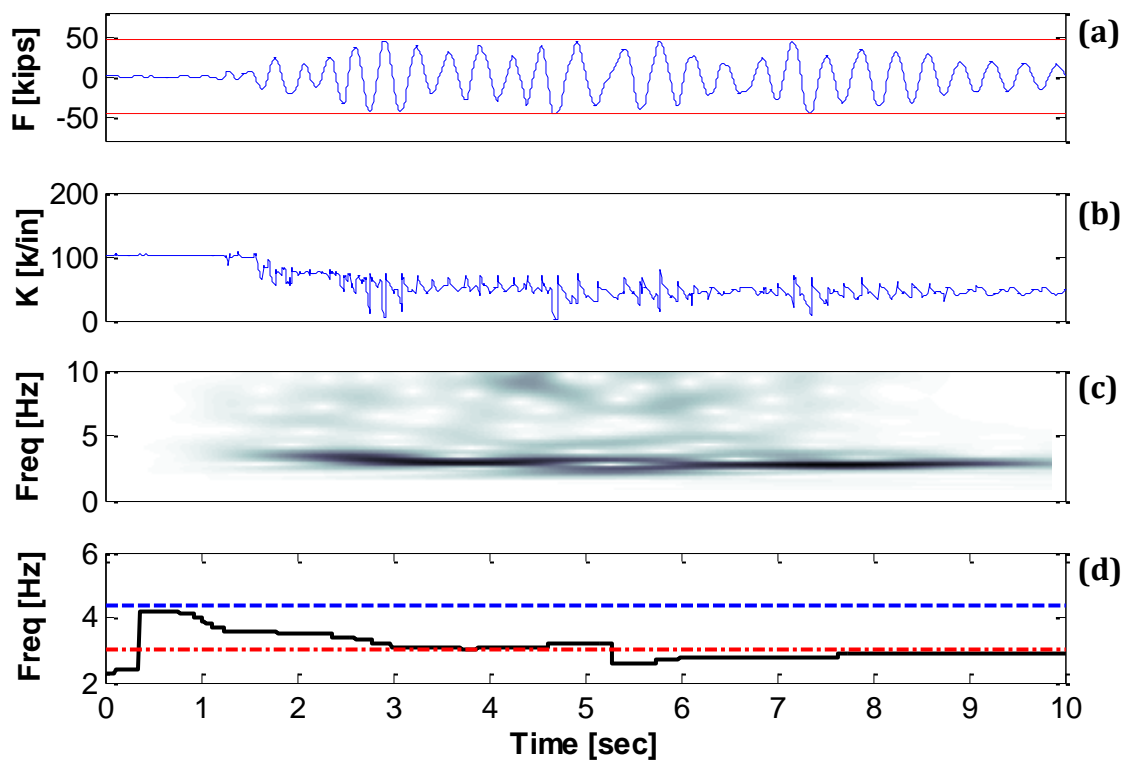


Figure 4-23: Fibers model: (a) Force Response, (b) Stiffness, (c) Low-Frequency Analysis, (d) IF from wavelet ridges

4.4.6 White Noise <40Hz high-frequency results

The high frequency results for the 40Hz white noise are shown in Figures 4-24 to 4-26. For the bilinear model (Figure 4-24) we can observe that nine yield episodes can be identified from the force history and the tangent stiffness plot. These sudden changes in stiffness compare very well with the high frequency analysis showed on the wavelet map. By plotting the coefficients for 80Hz we can observe better when the yield events occurs. For the hysteretic “Takeda” model (Figure 4-25) 5 yield episodes are identified from the force history and corroborated from the tangent stiffness plot. If we look closely at the wavelet map, we can see that the darker colors correspond to those changes in stiffness and they match with the peaks amplitude. The fiber-based model results (Figure 4-26) hardly display drastic changes in the stiffness, many of them are related to other effects that are not yield episodes. However, at the time of 4.7s there is a dominant trend that can be successfully related to a yield episode and it is best represented on the coefficients plot (the highest peak).

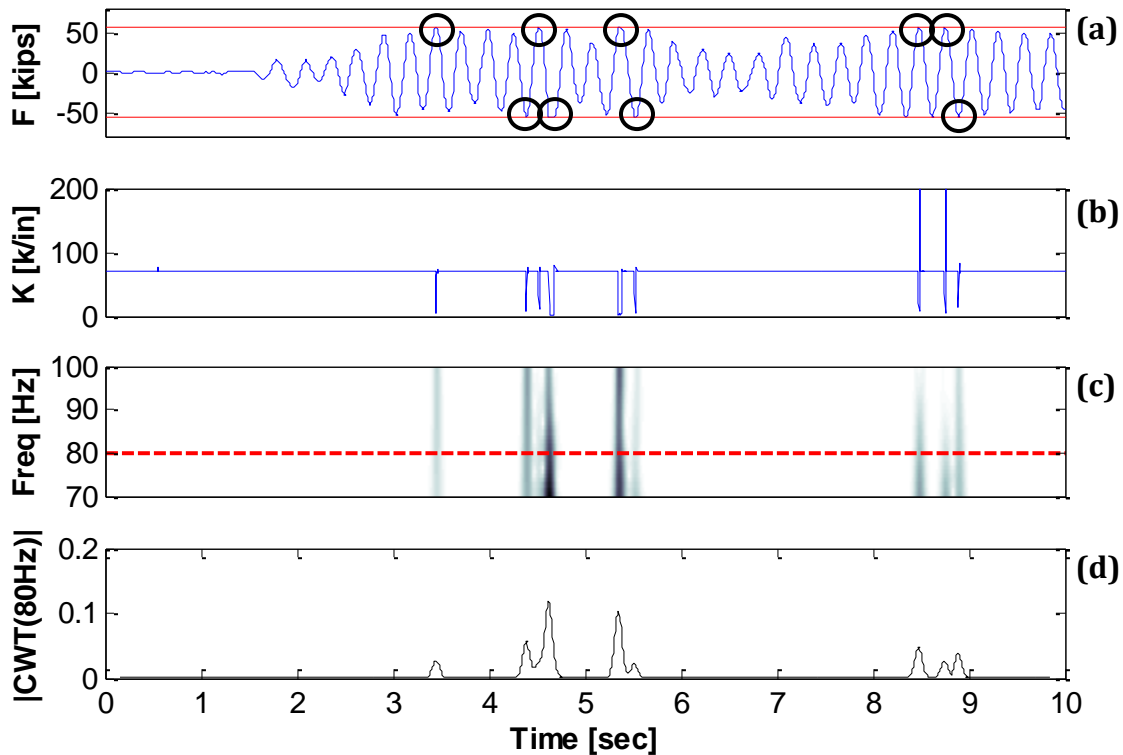


Figure 4-24: Bilinear model: (a) Force Response, (b) Stiffness, (c) High-Frequency Analysis, (d) Coefficients for 80Hz frequency

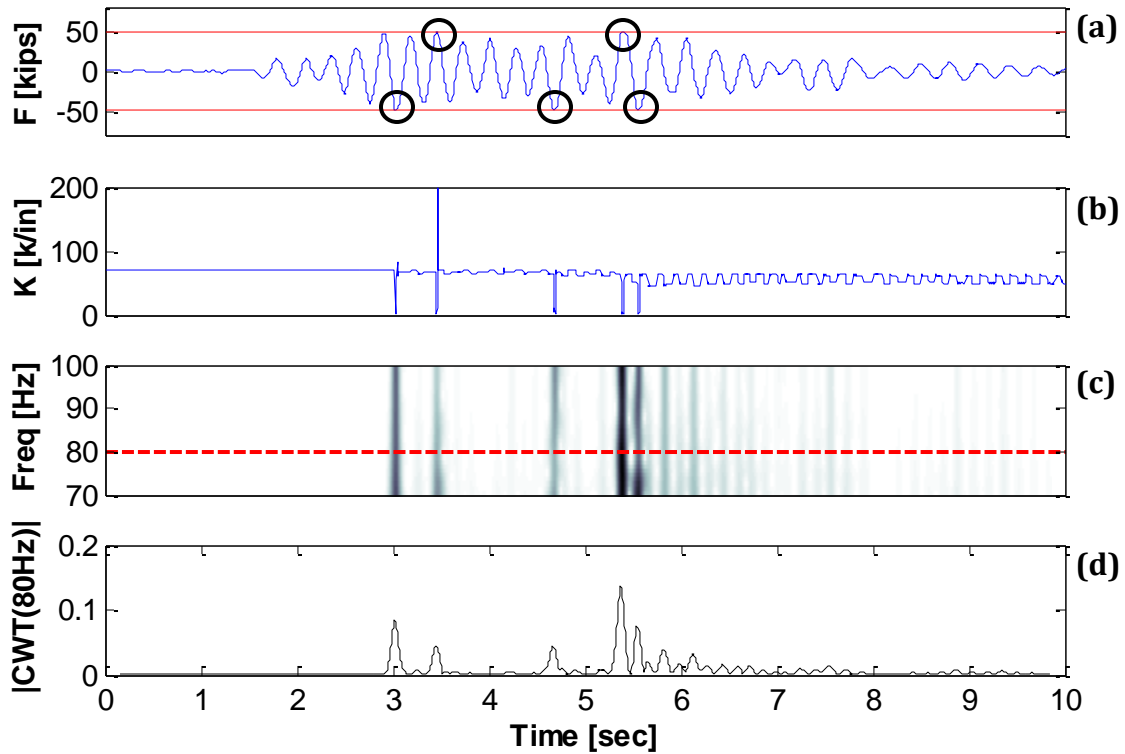


Figure 4-25: Hysteretic model: (a) Force Response, (b) Stiffness, (c) High-Frequency Analysis, (d) Coefficients for 80Hz frequency

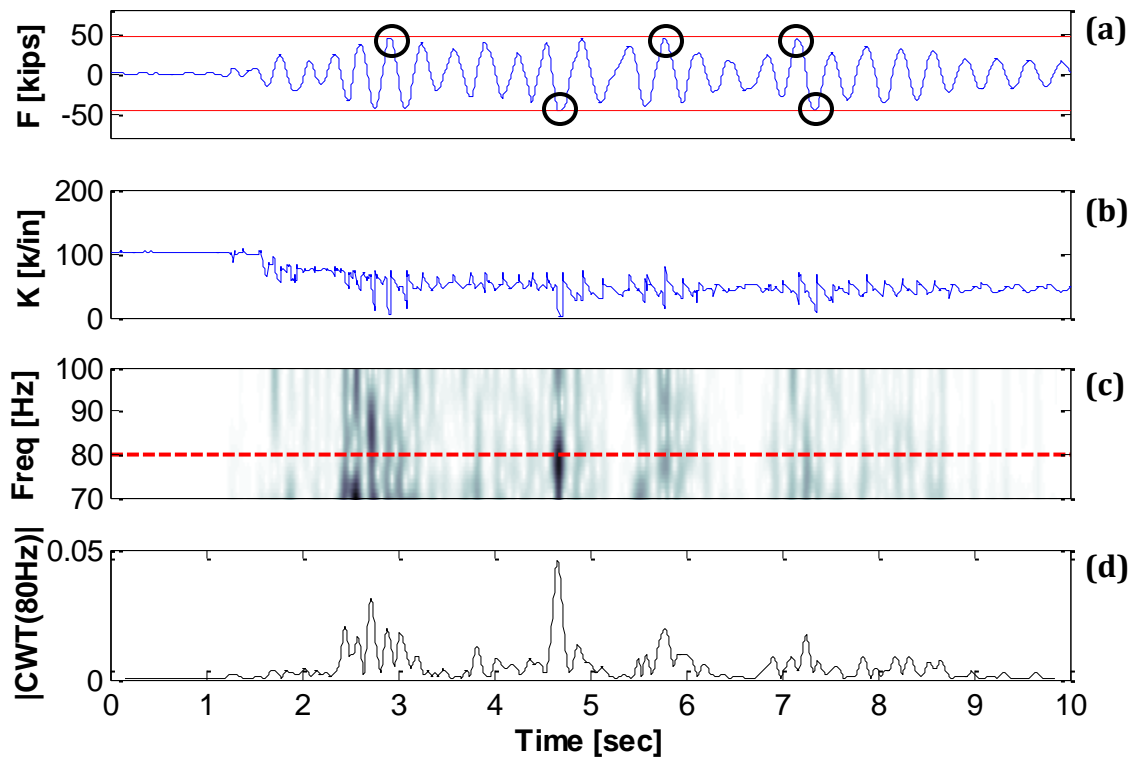


Figure 4-26: Fibers model: (a) Force Response, (b) Stiffness, (c) High-Frequency Analysis, (d) Coefficients for 80Hz frequency

4.4.7 Round Valley earthquake low-frequency results

Beginning with the earthquake loads, our first case is the Round Valley earthquake from McGee Creek Surface Station with a magnitude of 5.8. The low frequency results for this excitation are displayed in Figures 4-27 to 4-29. From the wavelet map for the three model approaches, we can observe that two dominant frequencies are identified. These frequencies are around 3.9Hz and 8Hz. From the Fourier Spectrum shown in Figure 4-4b, it can be noticed that a dominant frequency of 8Hz is present on this earthquake, meaning that the wavelet analysis performed at low frequencies was able to detect the frequency coming from the earthquake and the time instant where it occurs i.e., between 2 and 3 seconds. Similarly, it successfully detected the evolution of the natural frequency of the RC structure as the earthquake excitation was applied in all three cases.

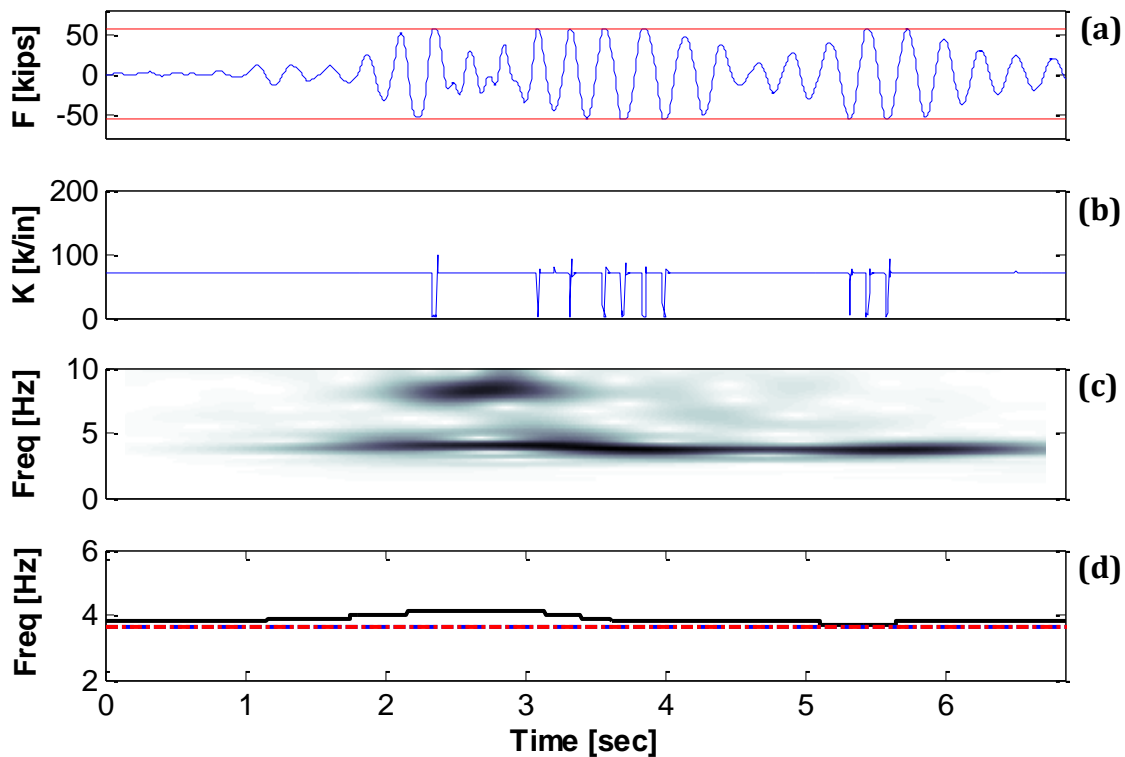


Figure 4-27: Bilinear model: (a) Force Response, (b) Stiffness, (c) Low-Frequency Analysis, (d) IF from wavelet ridges

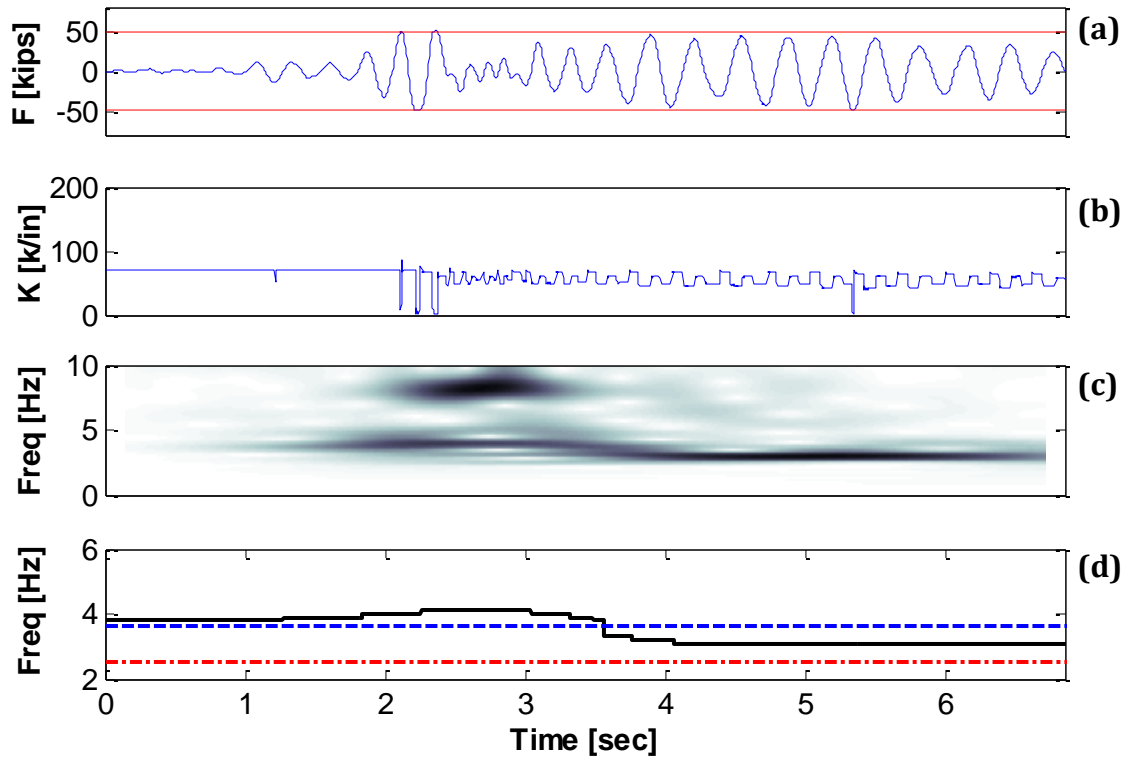


Figure 4-28: Hysteretic model: (a) Force Response, (b) Stiffness, (c) Low-Frequency Analysis, (d) IF from wavelet ridges

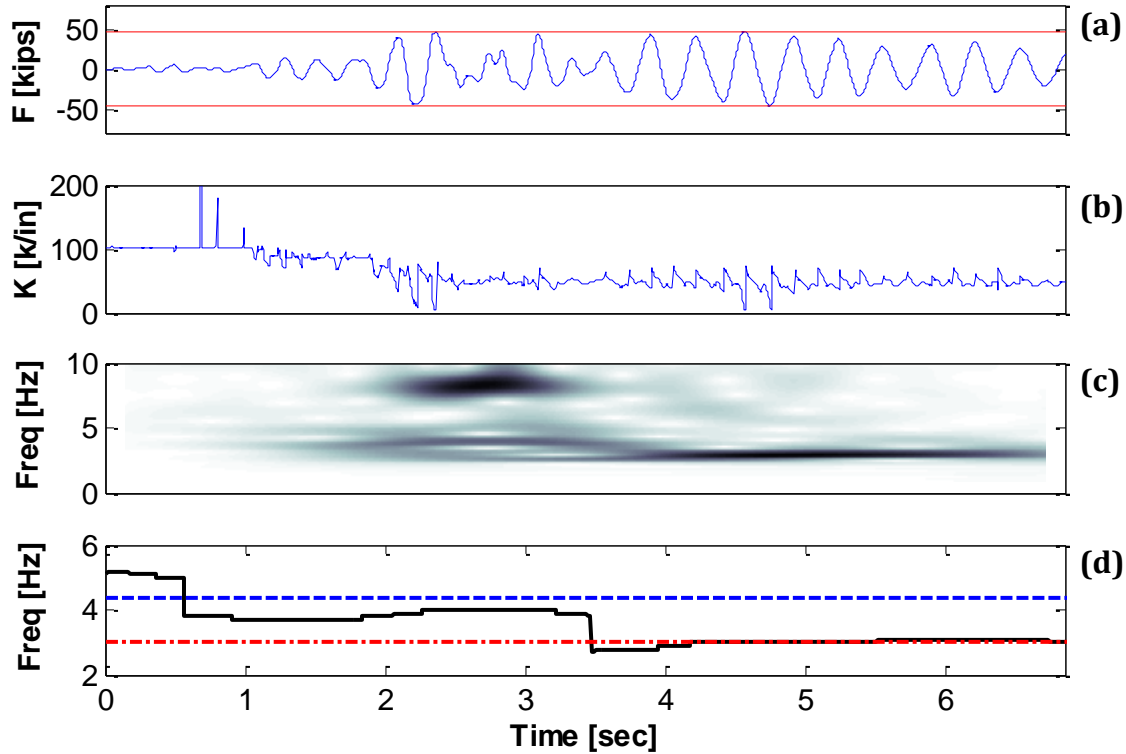


Figure 4-29: Fibers model: (a) Force Response, (b) Stiffness, (c) Low-Frequency Analysis, (d) IF from wavelet ridges

4.4.8 Round Valley earthquake high-frequency results

Figures 4-30 to 4-32 present the results of the high frequency analysis carried out for the Round Valley earthquake. From the tangent stiffness plots for the bilinear model (Figure 4-30) and the hysteretic “Takeda” model (Figure 4-31) we can appreciate that the largest sudden changes are related to the yield episodes of the force response (marked with black circles). Such correlation is not observed in the fibers model (Figure 4-32). The high frequency results presented on the wavelet maps and coefficients plot are not satisfactory, since the darker colors (that correspond to the higher peaks) do not match with the yield episodes identified on the force response for any of the three model approaches. It is noticed that the three high frequency wavelet maps and coefficients plots for the different models are quite similar and that most of the dark trends (highest coefficients peaks) occur between 2 and 3 seconds (time that coincides with the strong motion part of the accelerogram and not necessarily with the occurrence of yield in the structure). So it is more likely that the discontinuities detected arrived directly from the seismic excitation rather than be related to inelastic action in the structure.

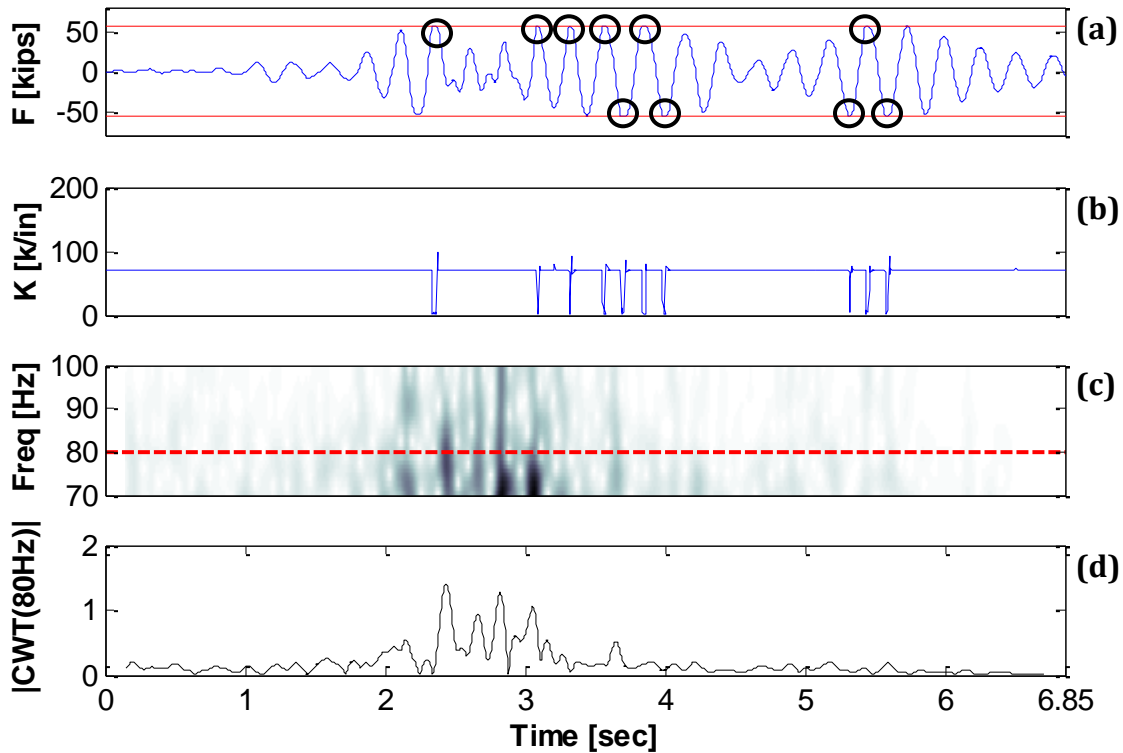


Figure 4-30: Bilinear model: (a) Force Response, (b) Stiffness, (c) High-Frequency Analysis, (d) Coefficients for 80Hz frequency

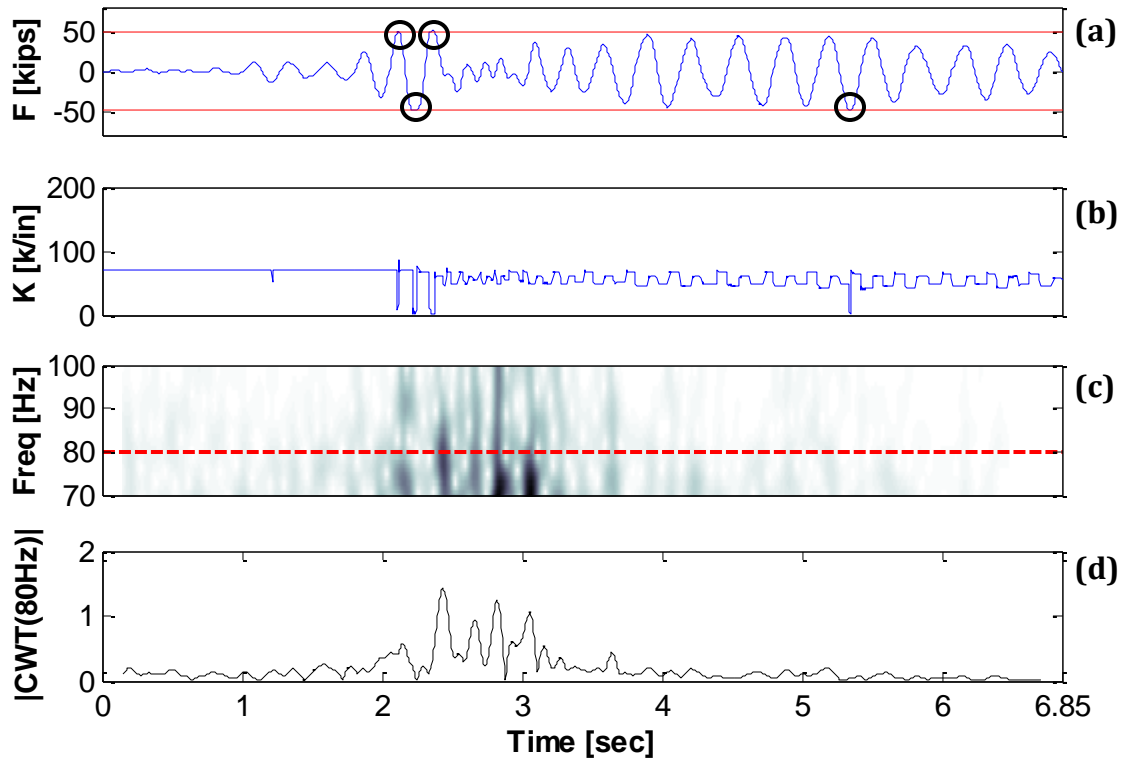


Figure 4-31: Hysteretic model: (a) Force Response, (b) Stiffness, (c) High-Frequency Analysis, (d) Coefficients for 80Hz frequency

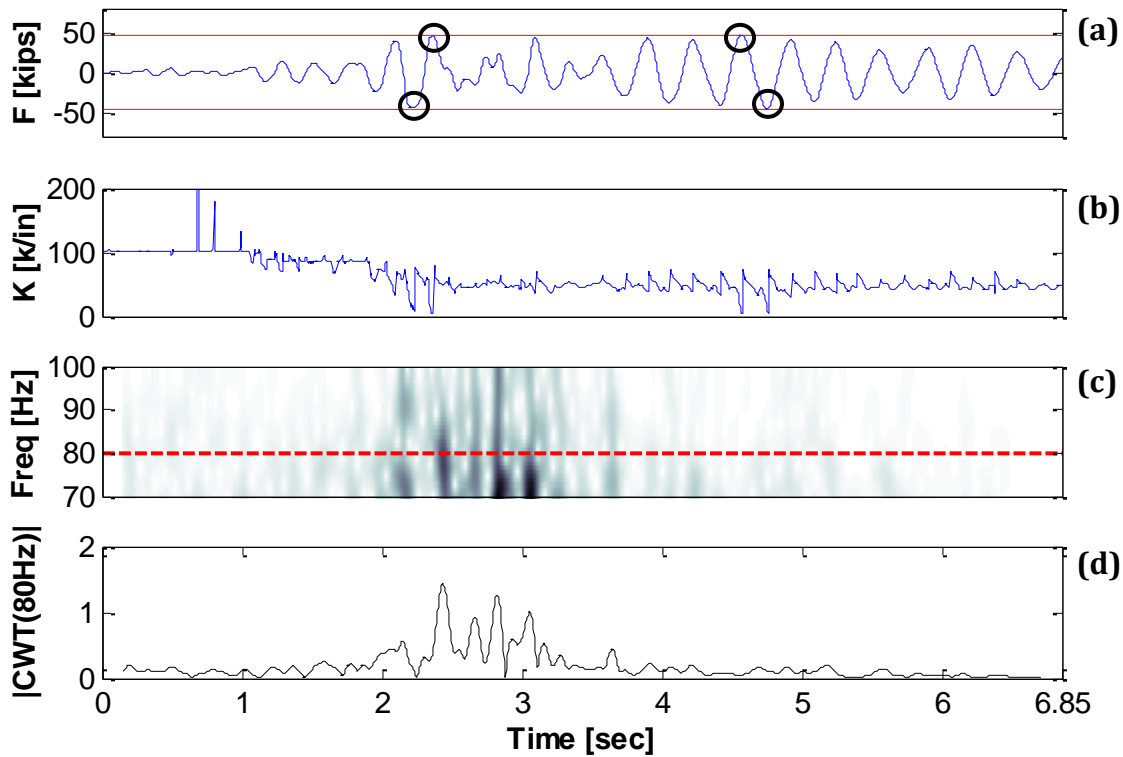


Figure 4-32: Fibers model: (a) Force Response, (b) Stiffness, (c) High-Frequency Analysis, (d) Coefficients for 80Hz frequency

4.4.9 Loma Prieta earthquake low-frequency results

The second seismic analysis is the Loma Prieta earthquake from the Treasure Island Station with a magnitude of 6.9. Figures 4-33 to 4-35 present the results for the low-frequency analysis. Looking at the Wavelet Maps and the extracted ridges (Figures c and d) it is noticed that the change in the natural frequency of the structure due to the application of the dynamic excitation was capture for all the three models.

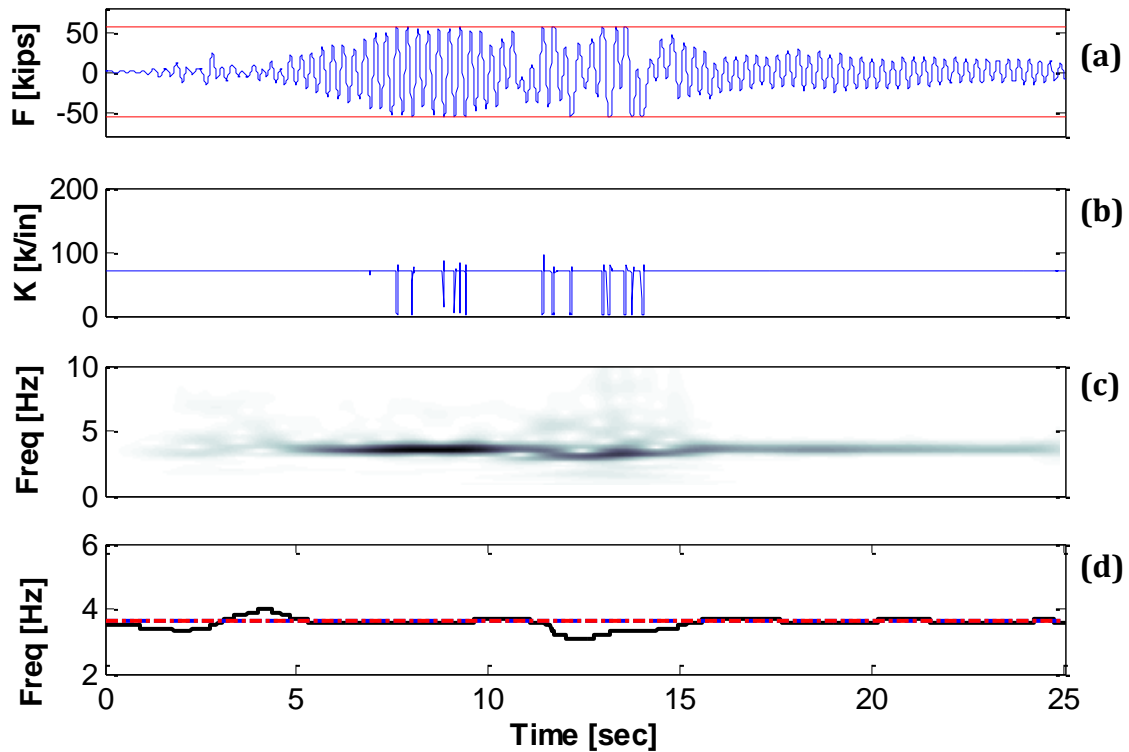


Figure 4-33: Bilinear model: (a) Force Response, (b) Stiffness, (c) Low-Frequency Analysis, (d) IF from wavelet ridges

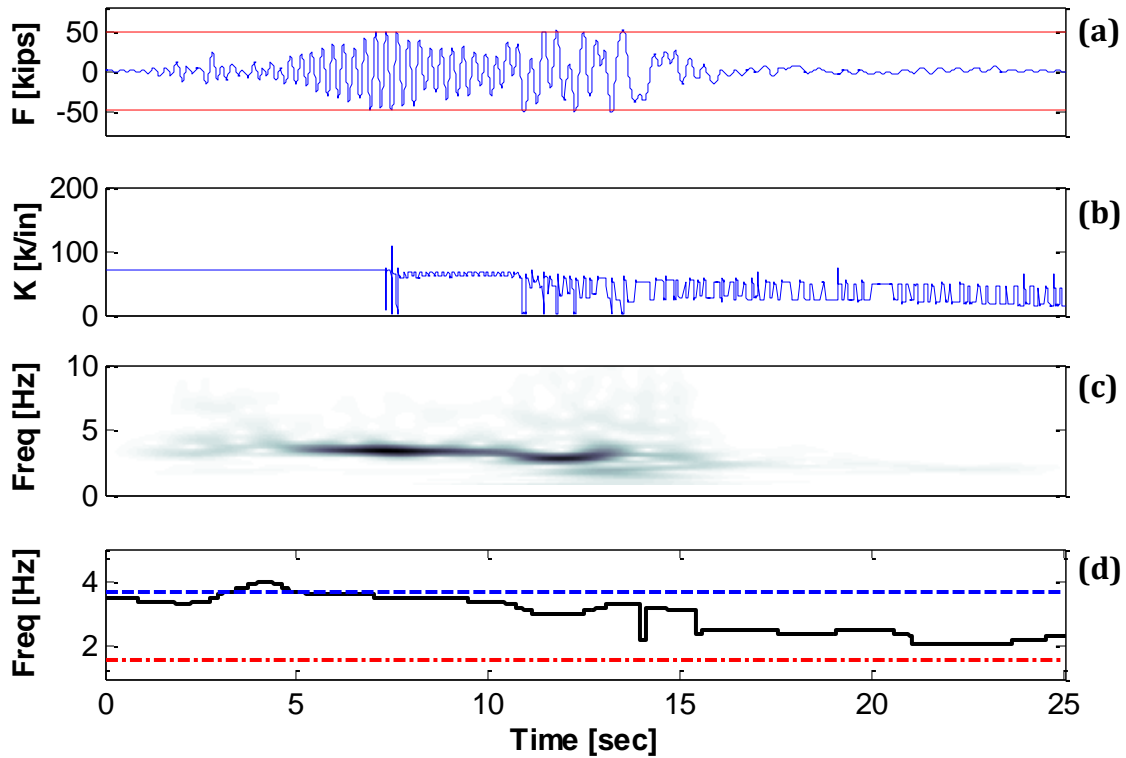


Figure 4-34: Hysteretic model: (a) Force Response, (b) Stiffness, (c) Low-Frequency Analysis, (d) IF from wavelet ridges

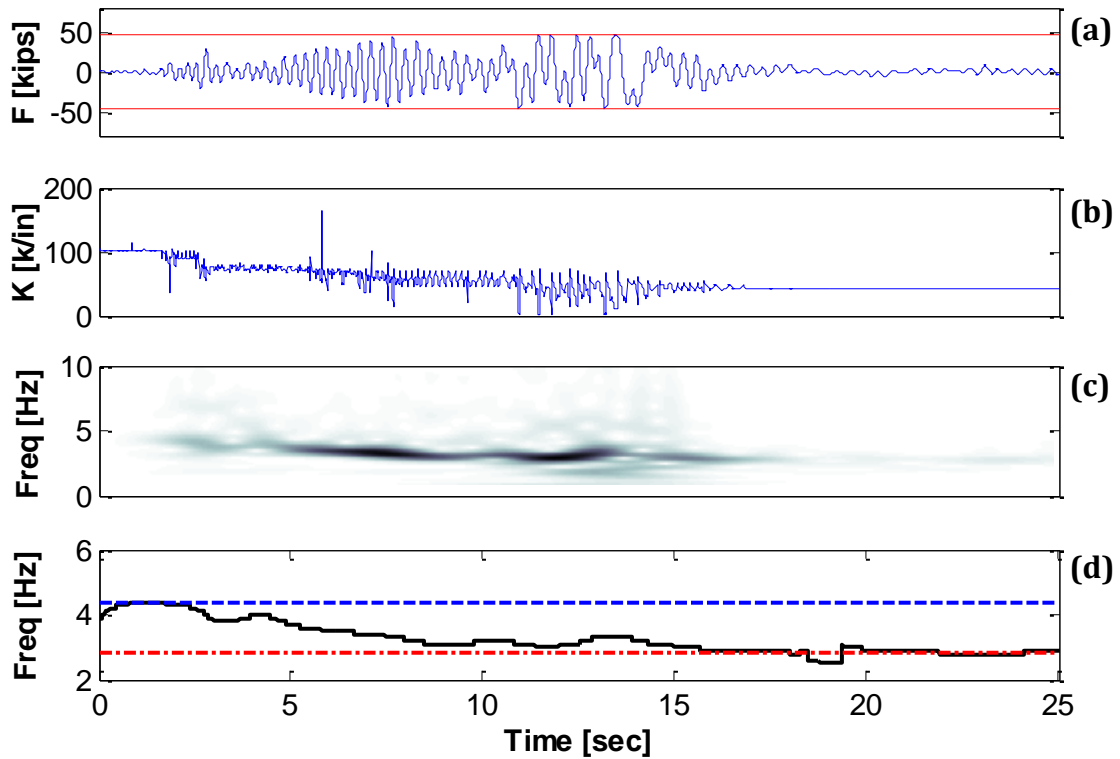


Figure 4-35: Fibers model: (a) Force Response, (b) Stiffness, (c) Low-Frequency Analysis, (d) IF from wavelet ridges

4.4.10 Loma Prieta earthquake high-frequency results

Figures 4-36 to 4-38 present the high-frequency results for the second earthquake analyzed. It is seen that the high frequency CWT approach successfully identified the yield episodes when the structure is modeled using the bilinear and Takeda approaches (Figures 4-36 and 4-37). However, problems arise when a more realistic modeling approach (i.e. the fiber-based approach) is implemented. In this case (Figure 4-38) a large number of trends/peaks appear that are not related with inelastic action in the column.

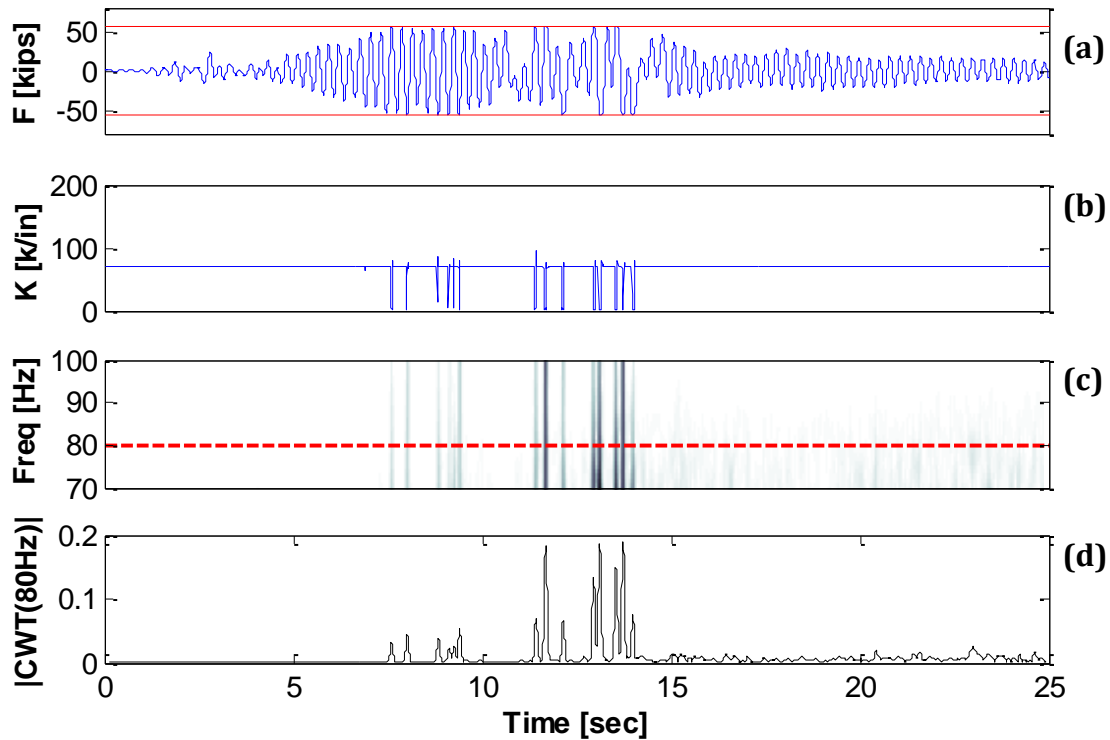


Figure 4-36: Bilinear model: (a) Force Response, (b) Stiffness, (c) High-Frequency Analysis, (d) Coefficients for 80Hz frequency

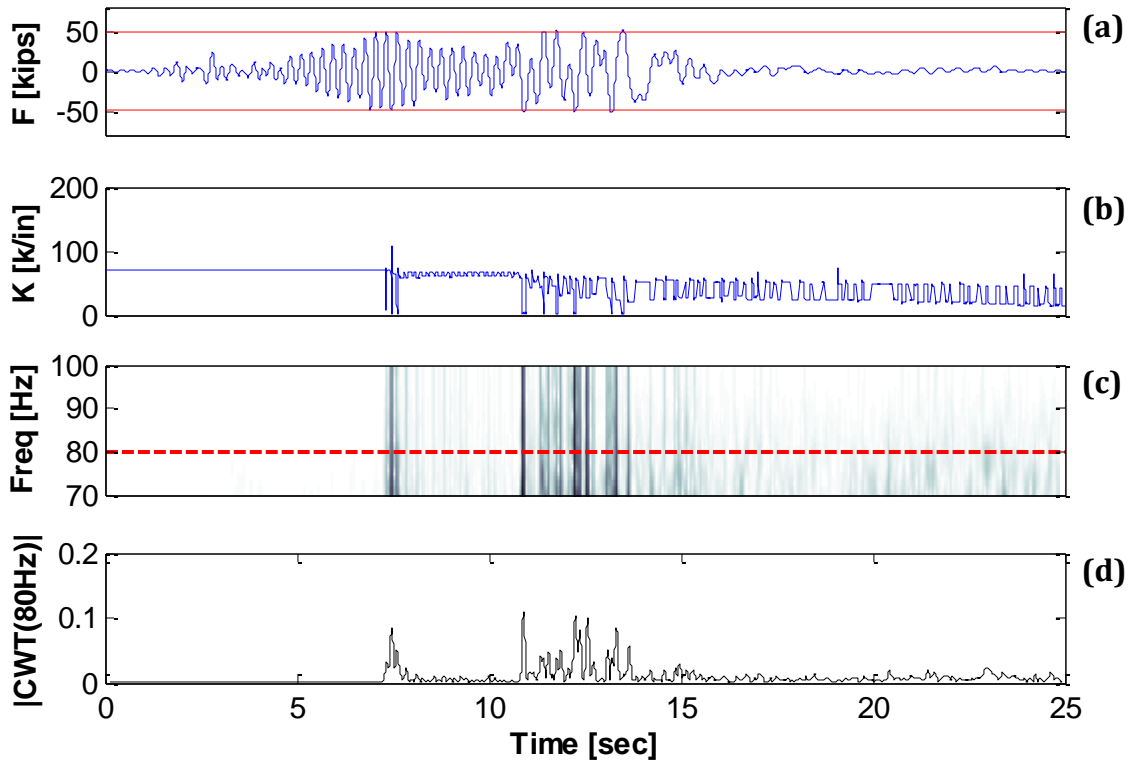


Figure 4-37: Hysteretic model: (a) Force Response, (b) Stiffness, (c) High-Frequency Analysis, (d) Coefficients for 80Hz frequency

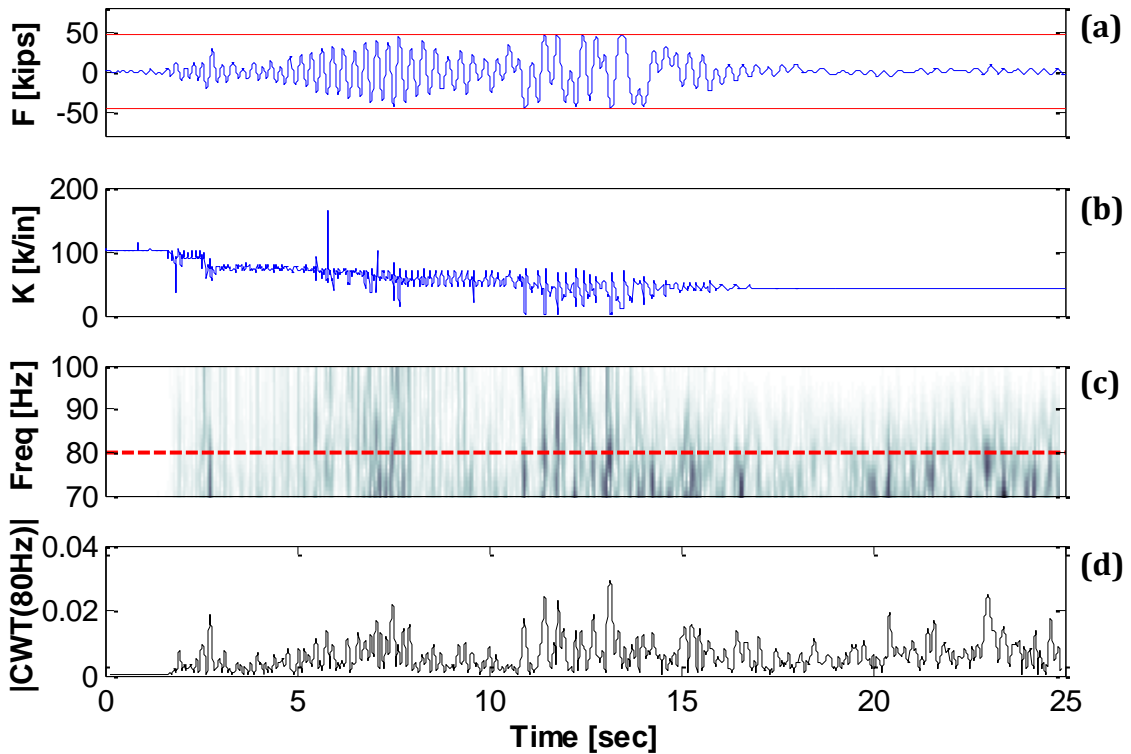


Figure 4-38: Fibers model: (a) Force Response, (b) Stiffness, (c) High-Frequency Analysis, (d) Coefficients for 80Hz frequency

4.5 Evaluation of the DWT Applied to Civil Structures

The same structure and dynamic loads used to evaluate the capabilities of the CWT for damage detection are used now to evaluate the Discrete Wavelet Transform (DWT). As presented earlier in Chapter II, the DWT analysis for damage detection is based on the identification of spikes in the detail function (i.e. the high frequencies component of the signals). The first plot for each model is the force response in which the horizontal lines represent the yielding force obtained from the moment-curvature analysis. The following plot shows the absolute tangent stiffness (equation 4-1). These two previous plots are the same plots presented previously on the CWT analysis. Lastly, the DWT detail functions are presented showing its absolute values. Below are the results obtained for the five dynamic excitation loads.

4.5.1 5Hz Tapered Sinusoid DWT detail analysis

Figures 4-39, 4-40, and 4-41 show the results obtained via DWT detail analysis. From the bilinear model results (Figure 4-39) we can see that the analysis works successfully by detecting all the yield episodes. The hysteretic “Takeda” model (Figure 4-40) presents yield episodes just on the first “transient” of the sinusoid. However, the results of the detail analysis indicate yield events occurring on the second “transient” of the tapered sinusoid (between 6 and 9 seconds). This same phenomenon occurred when applying the CWT at high frequencies, the analysis not only detected discontinuities in the response caused by yielding in the structure – but any “fictitious” discontinuity induced by abrupt changes in stiffness proper of any multilinear hysteretic model. Finally, for the fiber-based (Figure 4-41), the larger spikes appearing in the detail functions can be related to the yield episodes, but some minor spurious spikes also appear.

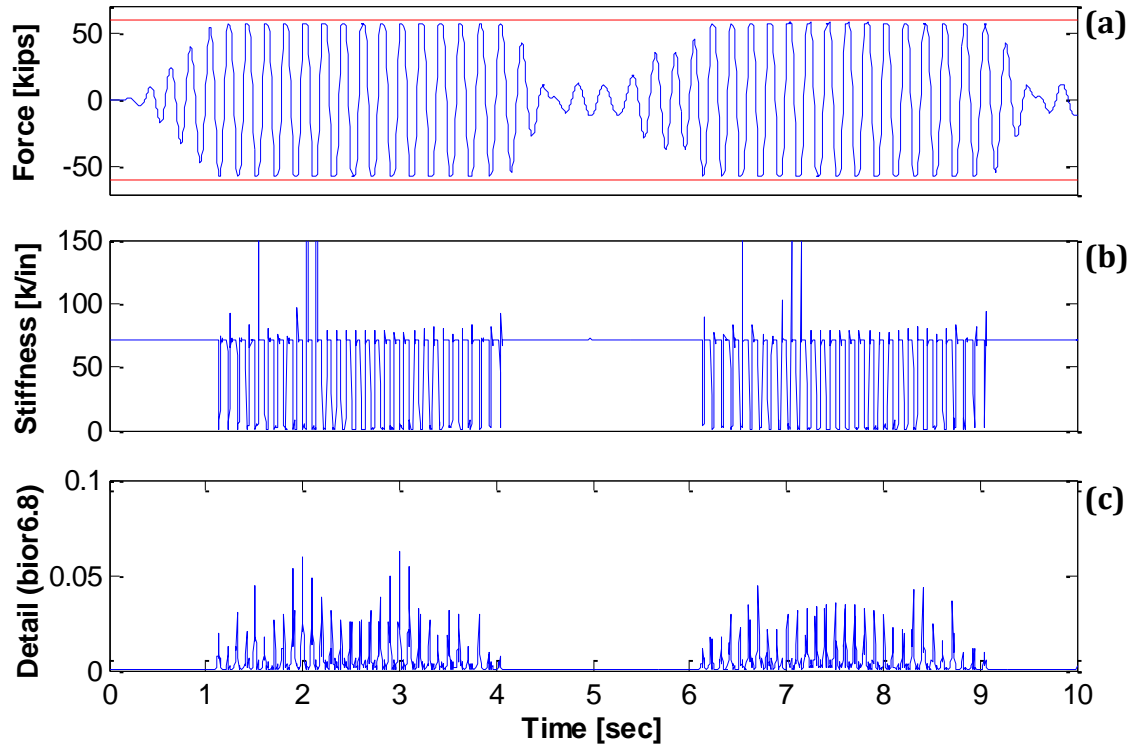


Figure 4-39: Bilinear model: (a) Force Response, (b) Stiffness, (c) DWT Detail analysis

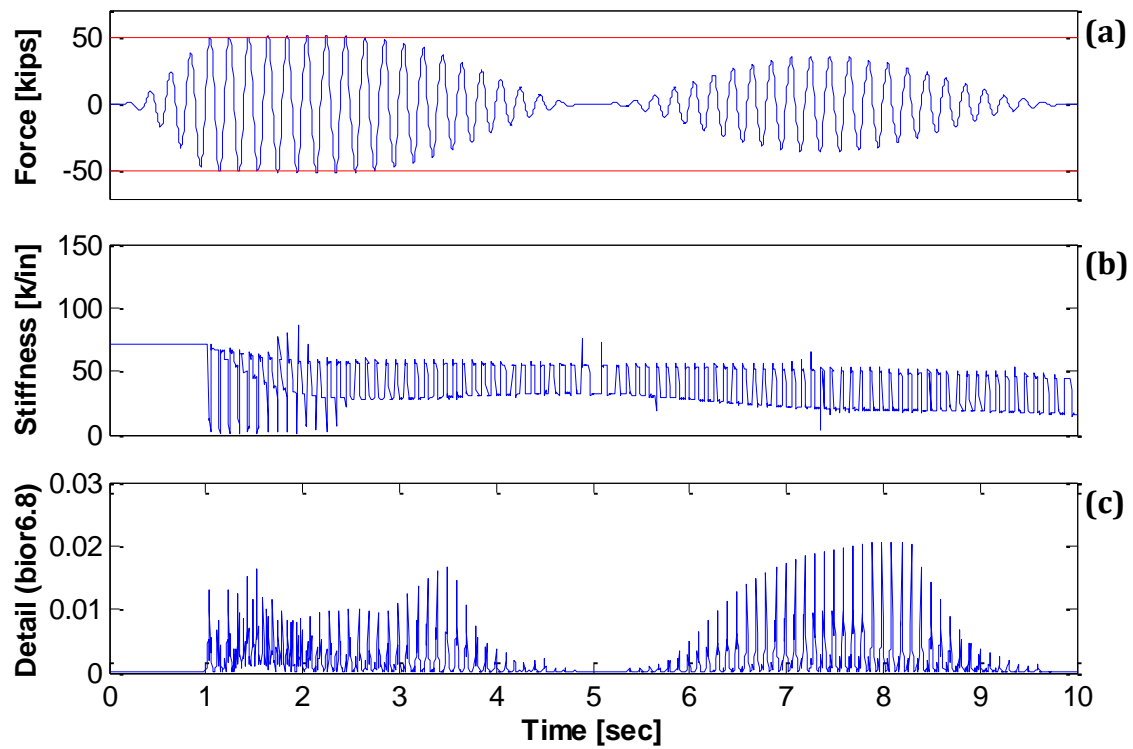


Figure 4-40: Hysteretic "Takeda" model: (a) Force Response, (b) Stiffness, (c) Detail DWT analysis

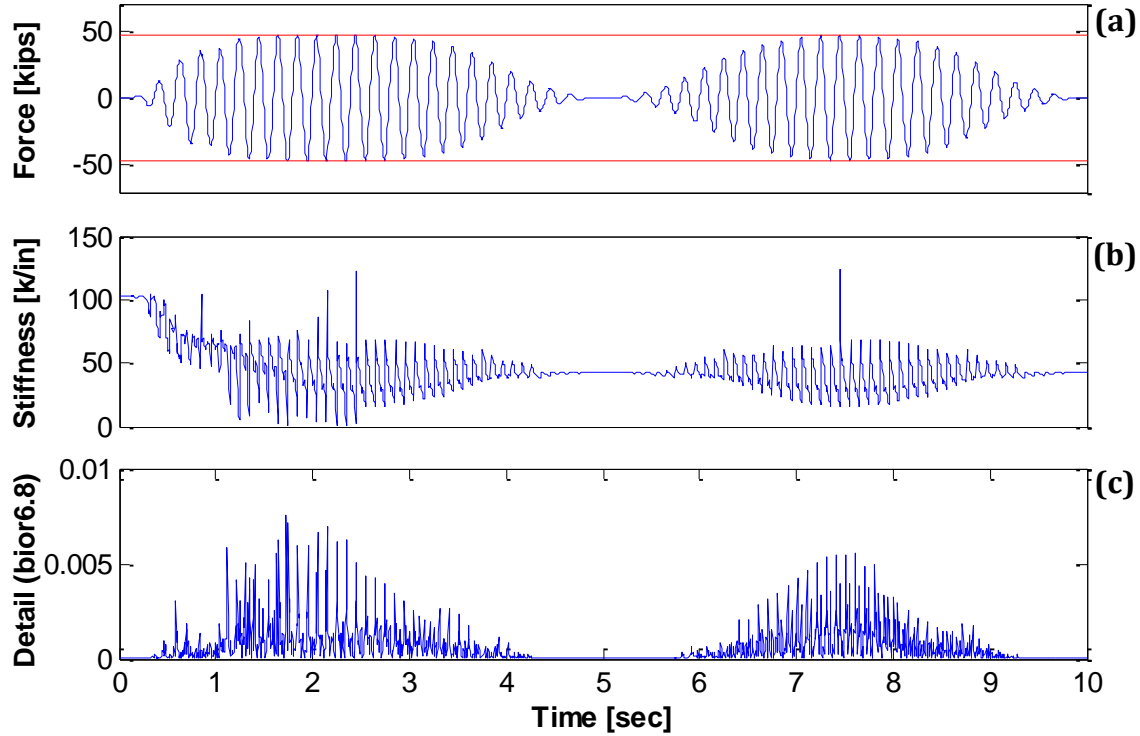


Figure 4-41: Fibers model: (a) Force Response, (b) Stiffness, (c) DWT Detail analysis

4.5.2 White Noise <20Hz DWT detail analysis

The detail analysis results for the 20Hz white noise are presented in Figures 4-42 to 4-44. For this analysis two yield episodes (at 5 and 5.4 seconds approximately) occurred on the bilinear model (Figure 4-42) and it were identified with black circles. The DWT details analysis was capable to clearly identify only the first yield episode. Although a spike also appear at the time instant corresponding to the second yield, other spikes of similar amplitude and no related with yielding make difficult an unambiguous identification. Now seeing at the hysteretic “Takeda” model results (Figure 4-43), it shows three times where yielding occurs. These instants were at 3.3, 4.5 and 4.6 seconds and can be identified from the force response plot and the tangent stiffness plot. From the DWT detail analysis only the yield occuring at the time of 4.5 seconds can be clearly identified. There are spikes at the other two yield instants, but there are other peaks within the same magnitude that can be confounded with yield episodes when in reality they are not. Lastly, on the fibers model (Figure 4-44) four yield events occurred (between 4 and 5 seconds), but none of them can

be clearly identified from the DWT analysis as a large amount of spikes not related to yielding appear in the detail function.

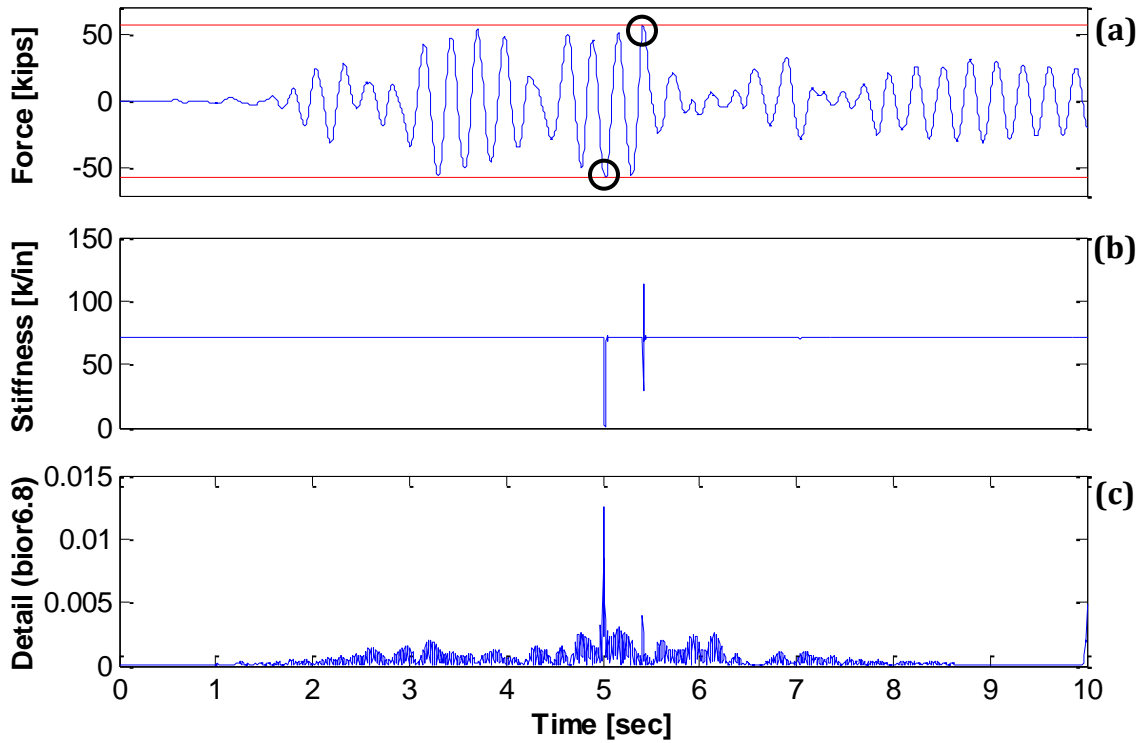


Figure 4-42: Bilinear model: (a) Force Response, (b) Stiffness, (c) DWT Detail analysis

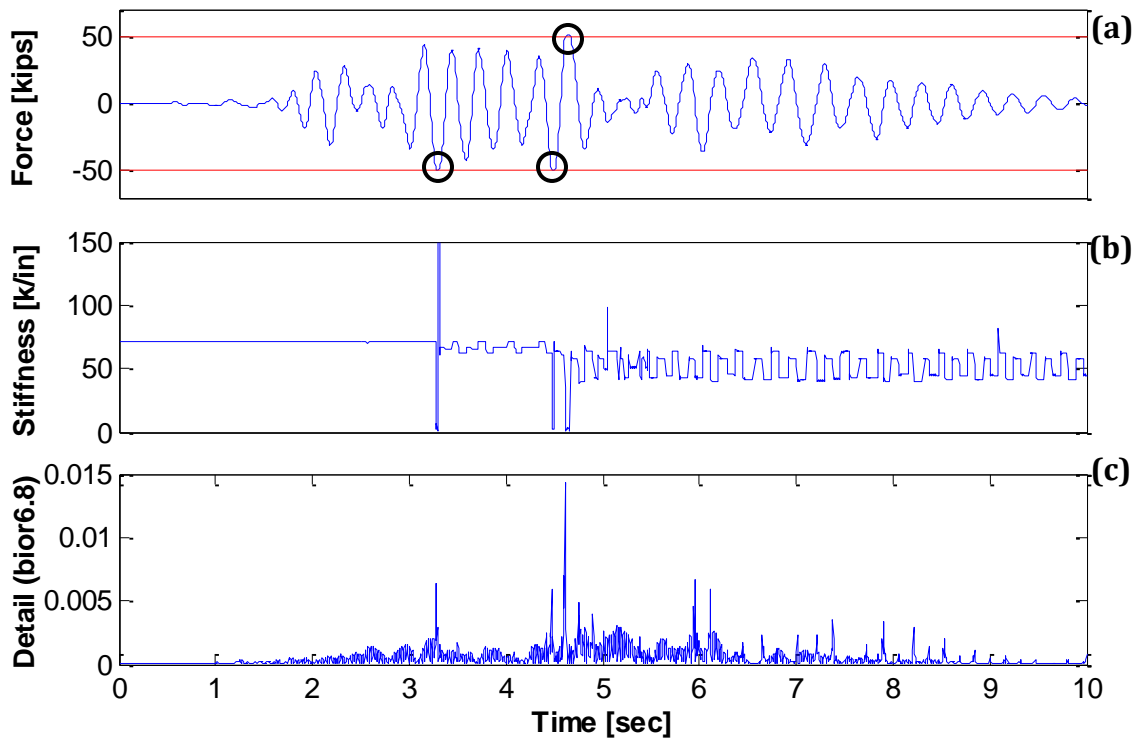


Figure 4-43: Hysteretic "Takeda" model: (a) Force Response, (b) Stiffness, (c) DWT Detail analysis

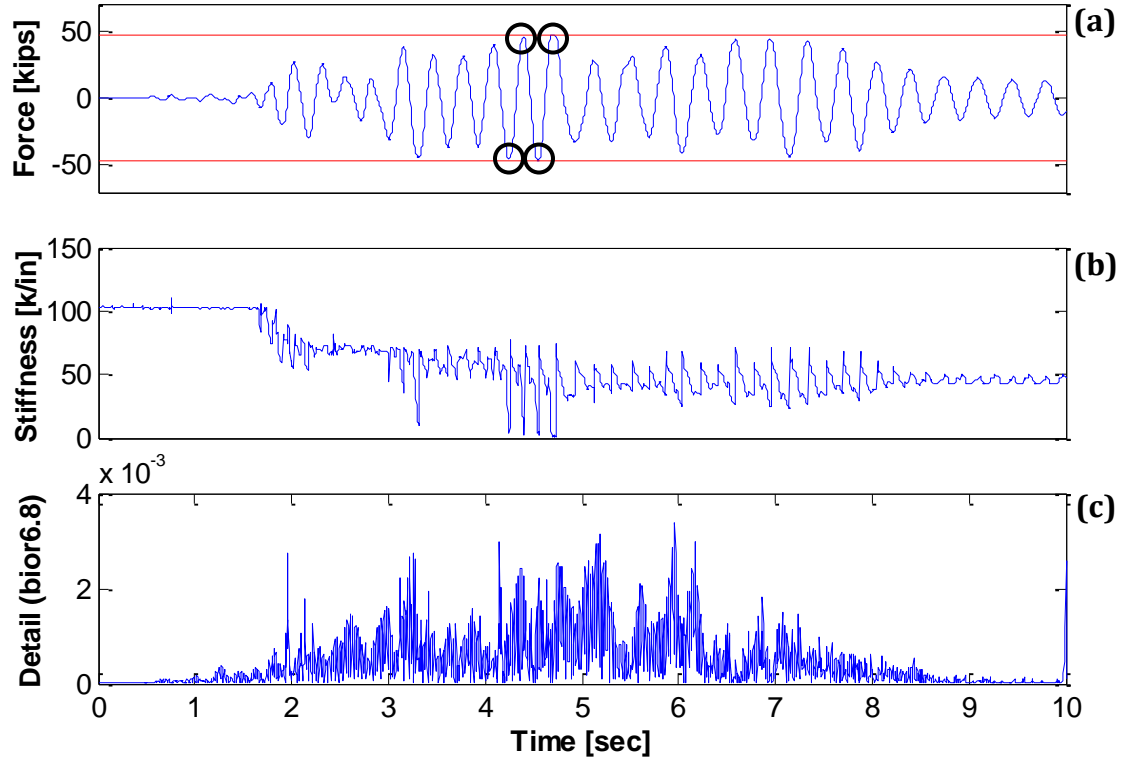


Figure 4-44: Fibers model: (a) Force Response, (b) Stiffness, (c) DWT Detail analysis

4.5.3 White Noise <40Hz DWT detail analysis

The results for this excitation are displayed in Figures 4-45 to 4-47. It is seen that for all three cases, the DWT analysis failed to detect the yield episodes. As we can observe, in comparison with the previous excitation (i.e. the white noise with frequency content up to 20Hz), the larger the high frequency content of the excitation, the less reliable are the results for the DWT detail analysis.

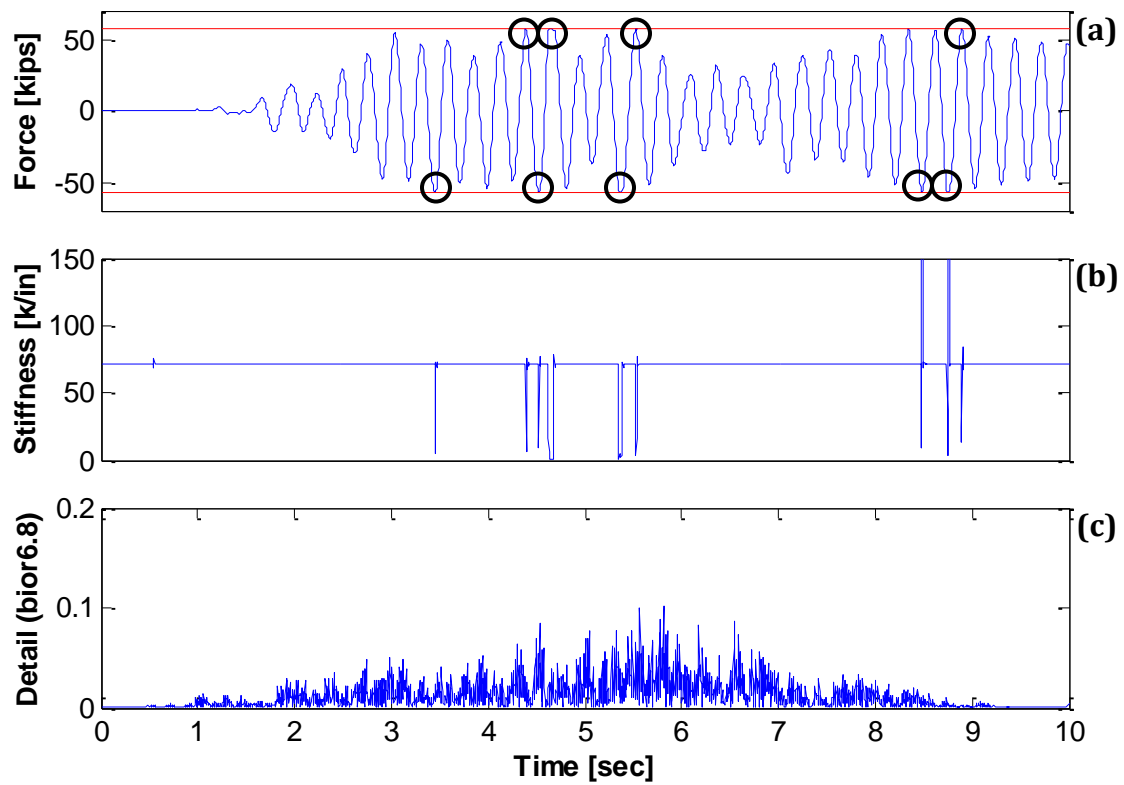


Figure 4-45: Bilinear model: (a) Force Response, (b) Stiffness, (c) DWT Detail analysis

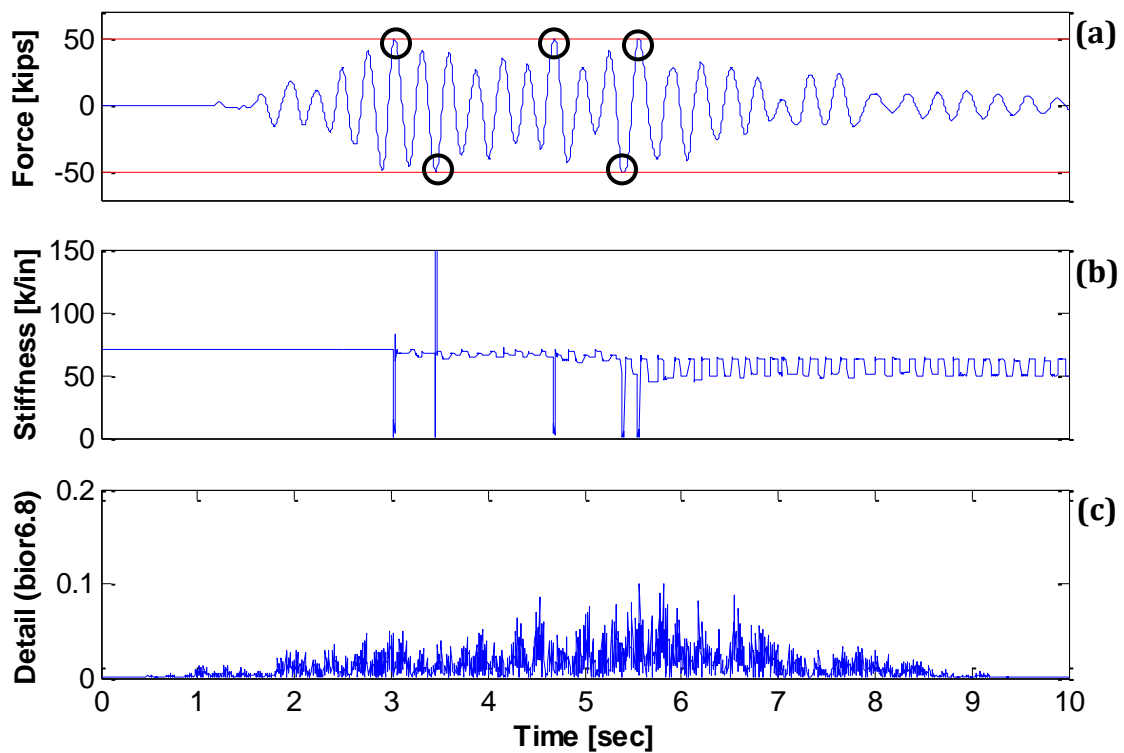


Figure 4-46: Hysteretic "Takeda" model: (a) Force Response, (b) Stiffness, (c) DWT Detail analysis

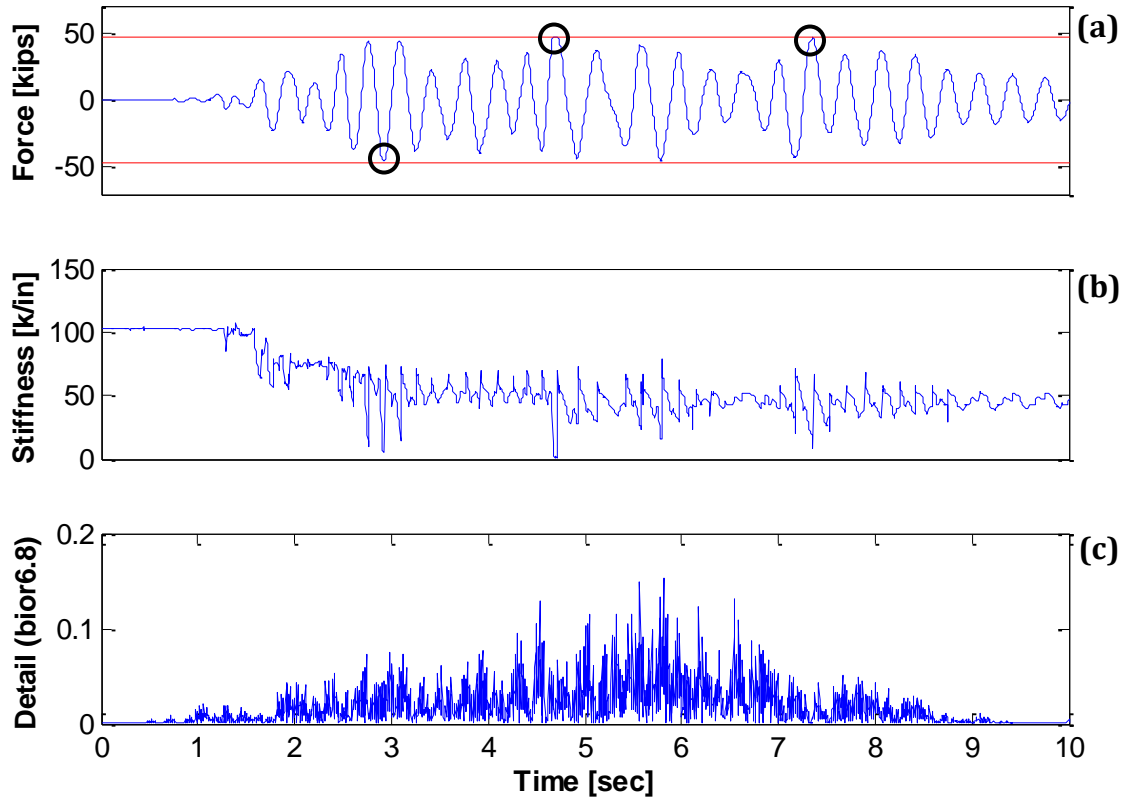


Figure 4-47: Fibers model: (a) Force Response, (b) Stiffness, (c) DWT Detail analysis

4.5.4 Round Valley earthquake DWT detail analysis

The DWT detail analysis results for the three model approaches are illustrated on the Figures 4-48, 4-49, and 4-50. It is noticed that the results obtained applying the DWT detail analysis for this dynamic excitation are no satisfactory for any of the three model approaches.

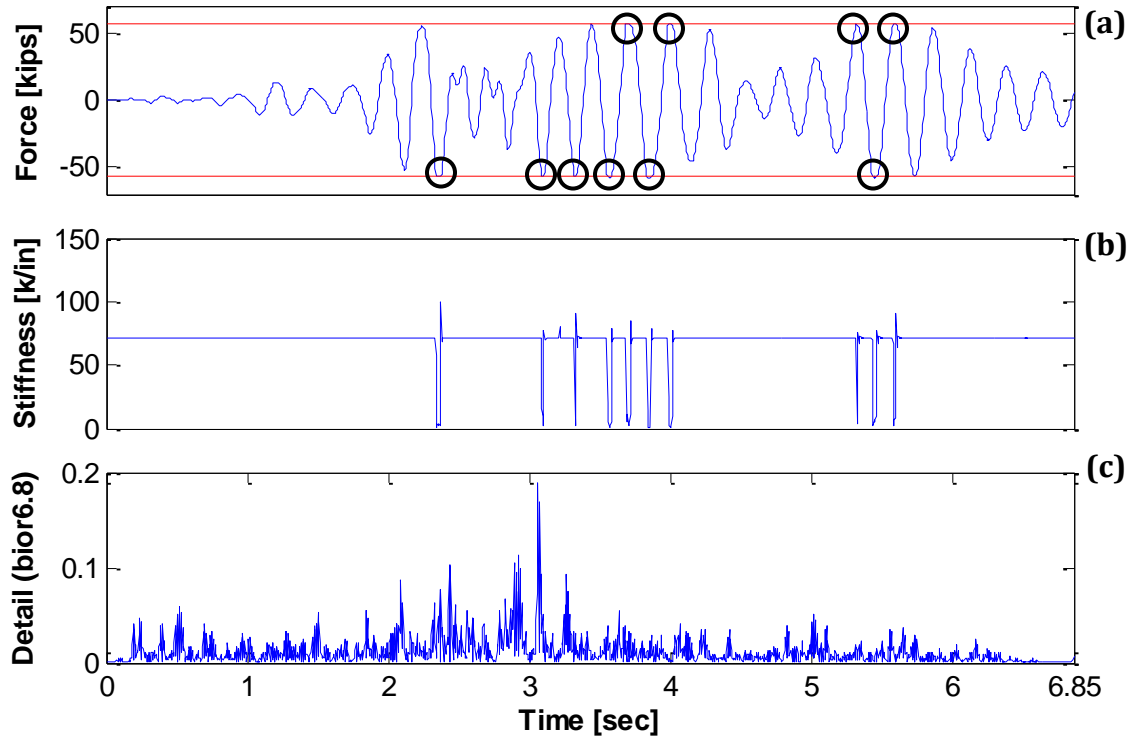


Figure 4-48: Bilinear model: (a) Force Response, (b) Stiffness, (c) DWT Detail analysis

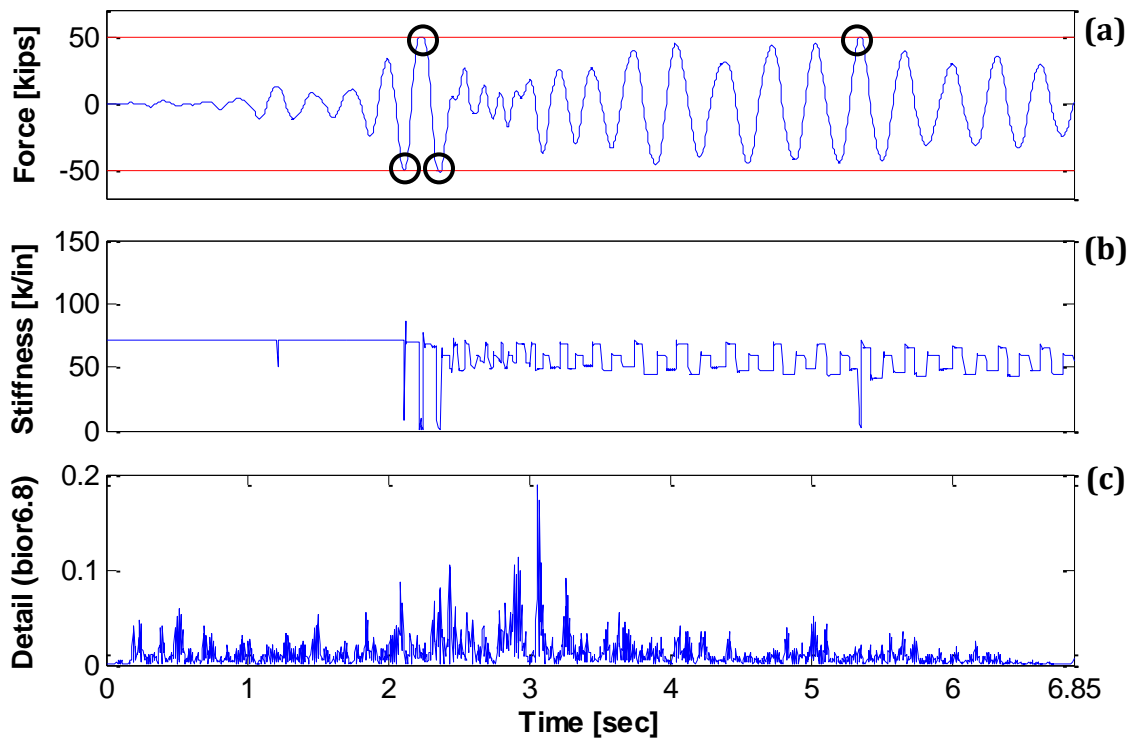


Figure 4-49: Hysteretic "Takeda" model: (a) Force Response, (b) Stiffness, (c) DWT Detail analysis

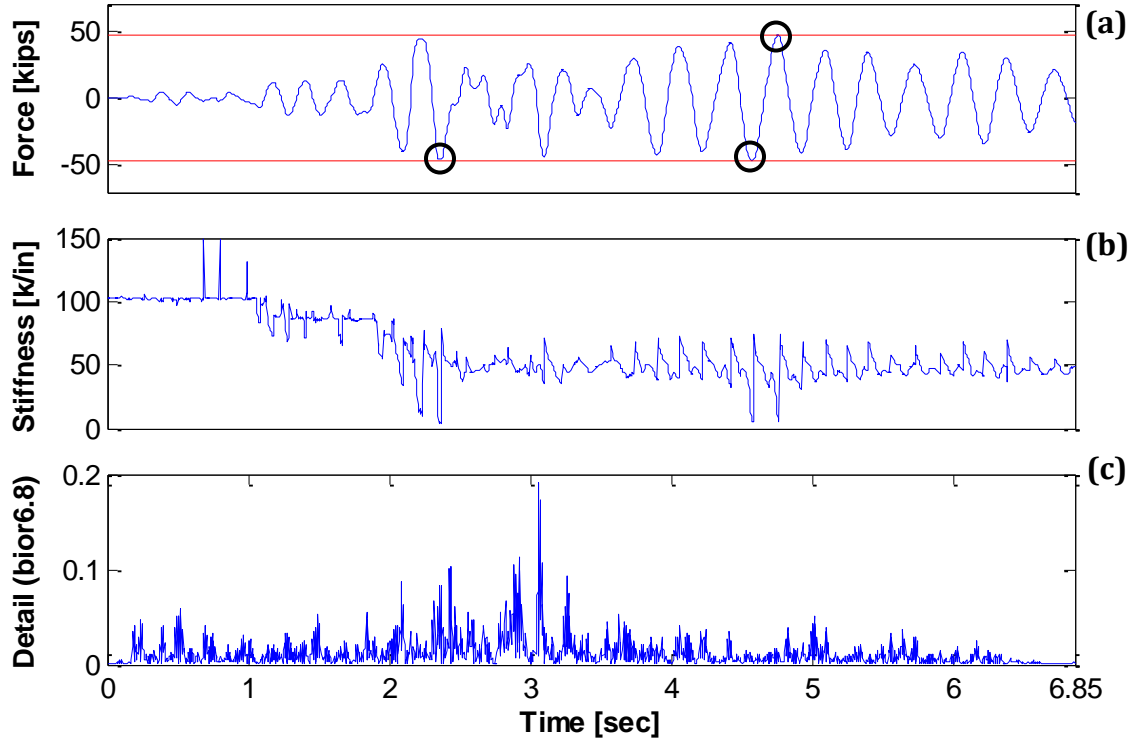


Figure 4-50: Fibers model: (a) Force Response, (b) Stiffness, (c) DWT Detail analysis

4.5.5 Loma Prieta earthquake DWT detail analysis

The Loma Prieta earthquake DWT detail analysis results are illustrated on the Figures 4-51, 4-52, and 4-53. If we look closely on the bilinear model each yield event was captured on the detail function. Furthermore, each peak amplitude seems to be related to the magnitude of the yield episode, this is of large motivation for this method since it open a possibility to identify not only the times at which yield occurs, but also the magnitud of the damage induced. The results obtained for the Takeda case were also very decent, as most of the spikes that appeared in the detail function can be related to yield episodes. Finally, in the fiber-based model the method failed as too many spikes/peaks emerged in the detail function and most of them are not related to the occurance of damage.

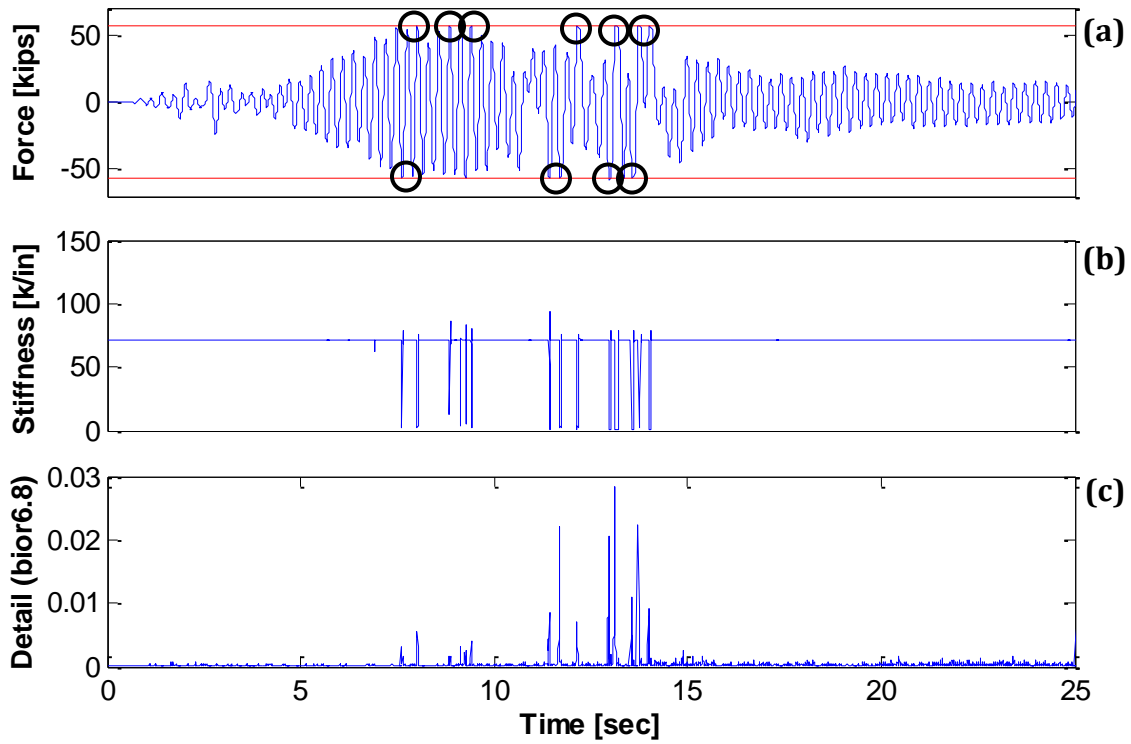


Figure 4-51: Bilinear model: (a) Force Response, (b) Stiffness, (c) DWT Detail analysis

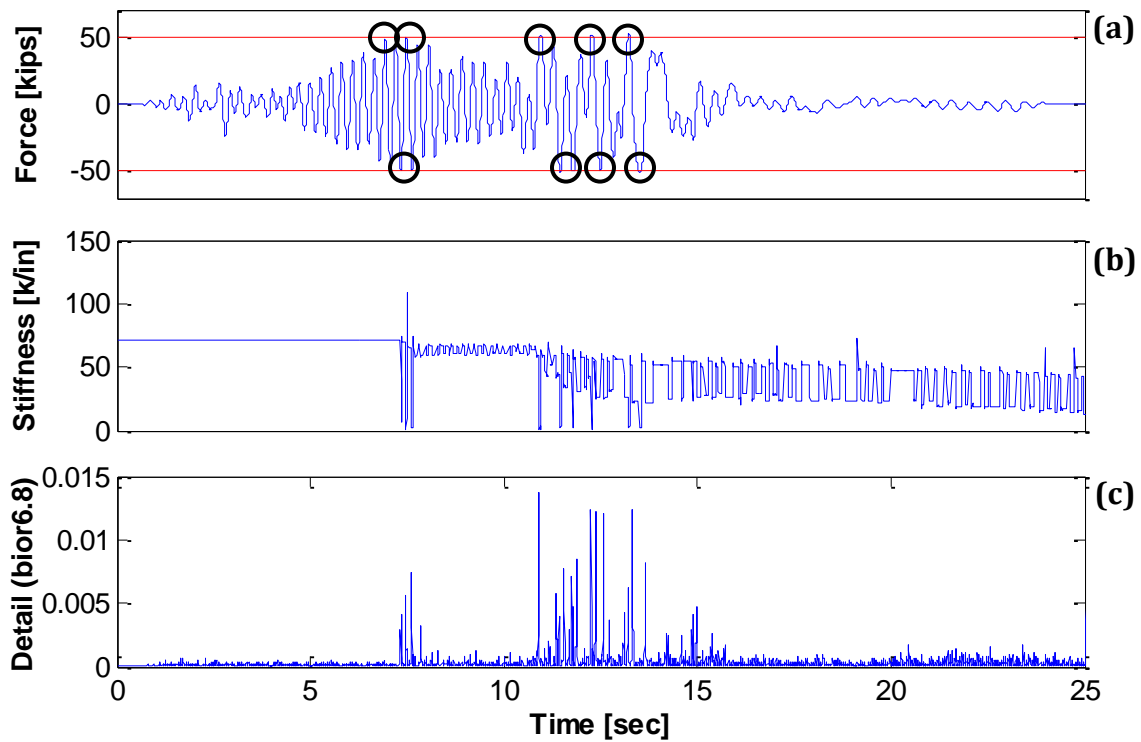


Figure 4-52: Hysteretic "Takeda" model: (a) Force Response, (b) Stiffness, (c) DWT Detail analysis

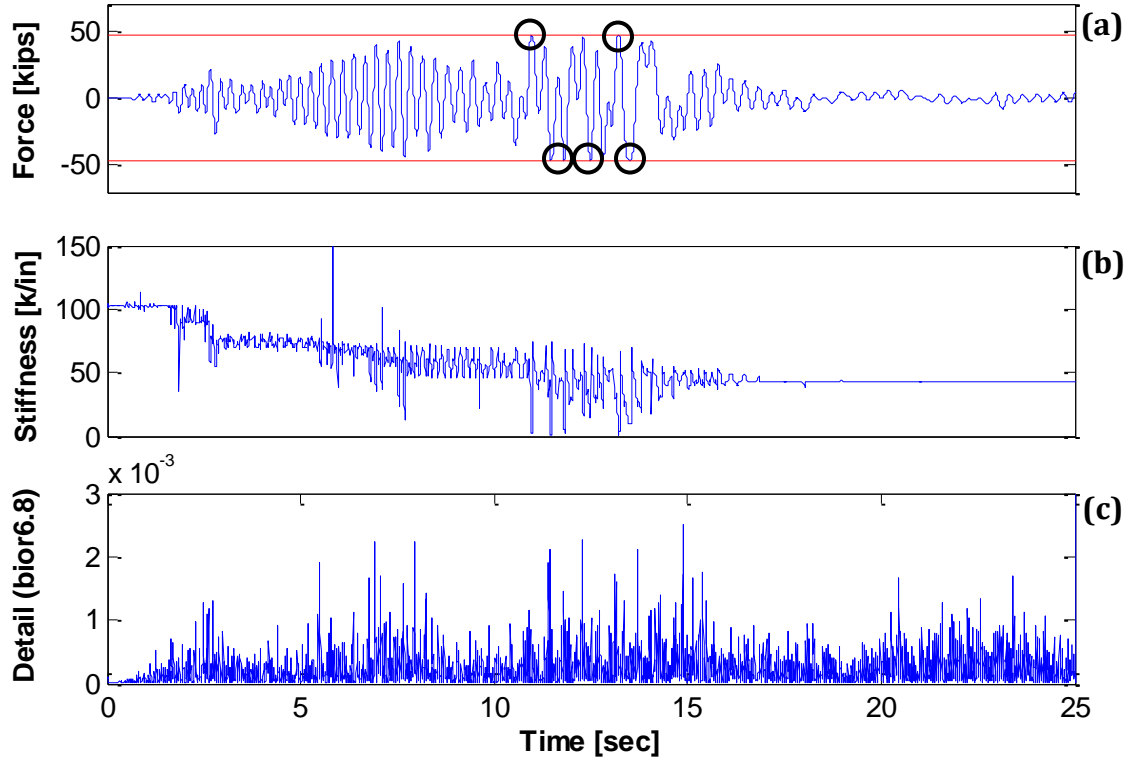


Figure 4-53: Fibers model: (a) Force Response, (b) Stiffness, (c) DWT Detail analysis

4.6 Summary of the results obtained

A summary of the results obtained for the damage identification techniques here presented is displayed in Tables 4-3, 4-4, and 4-5. In this chapter we examined the dynamic response (accelerations) of a RC column subjected to different types of excitation. The yield episodes were identified by looking at the force response of the column and pointing out the instants at which the yield force was reached. Additionally, plots of the tangent stiffness of the column at each time instant were generated to detect any abrupt changes in stiffness. Only the accelerations at the top of the column were analyzed using both, the CWT and the DWT.

In the case of the CWT two analyzes were performed, one at low frequencies and the other at high frequencies. With the CWT analysis at low frequencies we were able to detect the evolution of the natural frequency of vibration of the column as the base accelerations were applied and the column undergo stiffness degradation (Table 4-3). The CWT analysis at high frequencies (Table 4-4) and DWT analysis (Table 4-5) were used to detect any

singularities in the high frequency acceleration response of the structure and check if such discontinuities can be related to damage (yield episodes). The results presented in this chapter show that sudden changes in the system stiffness introduces discontinuities in the acceleration response, however such discontinuities are not always related to yield episodes as some of them are just direct consequence of the multilinear nature of the model (which differs from the actual structure behavior) or the dynamic excitation load.

For the high frequency analyses (both, CWT and DWT approaches) it can be said that better results are obtained for systems (or structures) modeled with a simplified hysteretic behavior (i.e. bilinear or Takeda) and excited with dynamic loads of limited high frequency content. As the high frequency content of the excitation increase and a more realistic modeling approach is used (i.e. fiber-based models), the efficiency of the evaluated methodologies decrease. Though more computationally expensive, the results obtained via CWT were more robust.

Table 4-3: Summary of the CWT Low Frequencies analysis results for each model

Excitation	Results	Bilinear	Takeda	Fibers
Tapered Sinusoid	good			
	partially good			
	poor	●	●	●
White Noise <20Hz	good	●	●	●
	partially good			
	poor			
White Noise <40Hz	good	●	●	●
	partially good			
	poor			
Round Valley Earthquake	good	●	●	●
	partially good			
	poor			
Loma Prieta Earthquake	good	●	●	●
	partially good			
	poor			

Table 4-4: Summary of the CWT High Frequencies analysis results for each model

Excitation	Results	Bilinear	Takeda	Fibers
Tapped Sinusoid	good	●	●	
	partially good			●
	poor			
White Noise <20Hz	good	●	●	
	partially good			●
	poor			
White Noise <40Hz	good	●		
	partially good		●	
	poor			●
Round Valley Earthquake	good			
	partially good	●	●	
	poor			●
Loma Prieta Earthquake	good	●	●	
	partially good			
	poor			●

Table 4-5: Summary of the DWT detail analysis results for each model

Excitation	Results	Bilinear	Takeda	Fibers
Tapped Sinusoid	good	●	●	
	partially good			●
	poor			
White Noise <20Hz	good			
	partially good	●	●	
	poor			●
White Noise <40Hz	good			
	partially good	●		
	poor		●	●
Round Valley Earthquake	good			
	partially good			
	poor	●	●	●
Loma Prieta Earthquake	good			
	partially good	●	●	
	poor			●

4.7 Conclusions

Besides the recent advances and promising capabilities of wavelet based methods for damage detection, in this chapter we have identified two important challenges that such techniques have to overcome before they can be successfully implemented for structural health monitoring of civil structures:

1. Since the detection of damage is based on the premise that its occurrence will be reflected in the high frequency component of the structural response, application of the available methodologies is limited by the frequency content of the load excitation. If the frequency content of the excitation spans over the frequency range where damage is reflected, the results obtained after a high frequency analysis may include not only spikes due to structural damage but also spikes proper of the excitation. For example, it was shown in this chapter how the results obtained when the structure is excited by a narrow band earthquake (i.e. the Loma Prieta record) are much better than those obtained when the structure is subjected to a wide band earthquake (i.e. the Round Valley record). Figures 4-54 and 4-55 present this drawback by showing the responses (CWT high frequency and DWT detail analyzes) obtained for the Round Valley record and also each model approach.
2. Most of the wavelet approaches have been validated in the past (Sone *et al.* 1995, Al-Khalidy *et al.* 1997, Hou and Noori 1995) through numerical simulations where the characteristic hysteretic and non-linear behavior of the elements of a civil structure is misrepresented by assuming linear or multi-linear behavior at most. The gradual occurrence of damage proper of modern detailed structures is also misrepresented when the damage is introduced as a suddenly lost of stiffness in one of the elements or levels of the structure. It was shown in this chapter that when a more realistic modeling approach (i.e. the fiber-based approach) is used to generate the structural model, the efficiency of the detection technique largely diminishes.

The next chapter will present further developments aimed at ameliorating the aforementioned problems. As such, in the next chapter only fiber-based models and non-stationary excitations will be used for evaluation purposes.

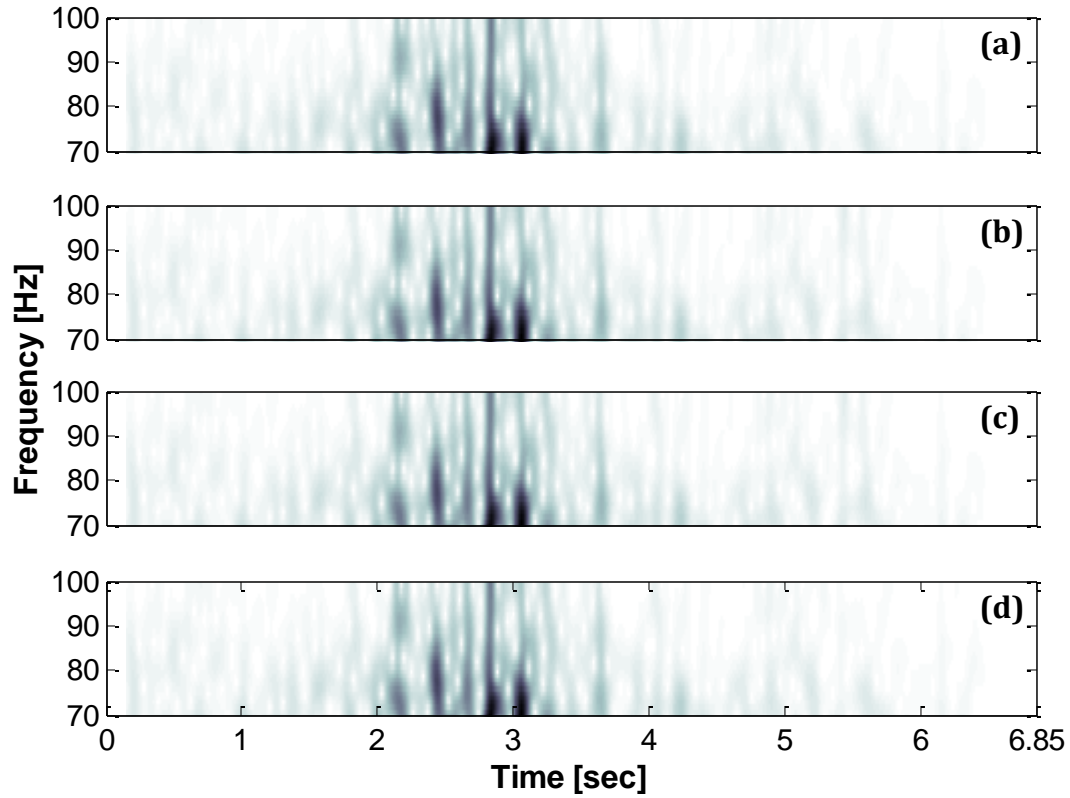


Figure 4-54: (a) Round Valley earthquake, (b) Bilinear model, (c) Takeda model, (d) Fibers model

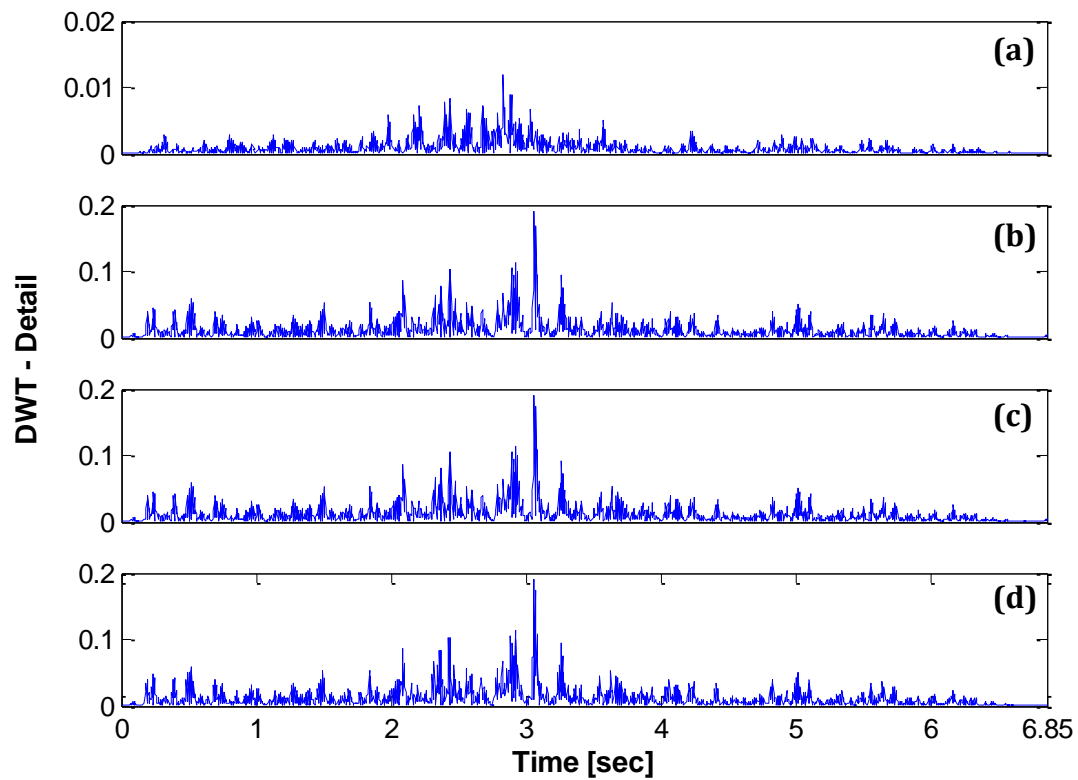


Figure 4-55: (a) Round Valley earthquake, (b) Bilinear model, (c) Takeda model, (d) Fibers model

4.8 References

Al-Khalidy, A., Noori, M., Hou, Z., Yamamoto, S., Masuda, A. and Sone, A. (1997). "*Health monitoring systems of linear structures using wavelet analysis.*" Proceeding of the 1st International Workshop on Structural Health Monitoring, Stanford, CA, pages 164-174.

Bisht, S.S. and Singh, M.P. (2011). "*Detecting sudden changes in stiffness using high-pass filters.*" Structural Control and Health Monitoring, John Wiley & Sons, Ltd.

Hou, Z. and Noori, M. (1999). "*Application of wavelet analysis for structural health monitoring.*" Proceedings 2nd International Workshop on Structural Health Monitoring, Stanford, CA, pages 946-955.

PEER Pacific Earthquake Engineering Research Center (2010), Next Generation Attenuation of Ground Motions NGA database <http://peer.berkeley.edu/nga/index.html>

Sone, A., Yamamoto, S., Nakaoka, A., Masuda, A. (1995). "*Health monitoring system of structures based on orthonormal wavelet transform.*" Proceedings of the ASME Pressure Vessels and Piping Conference, pages 161–167.

CHAPTER V

FURTHER REFINEMENTS FOR DAMAGE DETECTION IN REINFORCED CONCRETE STRUCTURES SUBJECTED TO EARTHQUAKE LOADS

5.1 Introduction

Based on the results obtained from the evaluation performed in Chapter IV, methodology refinements will be developed aiming to specifically tackle the damage identification problem in RC structures subjected to seismic loads. In order to carry out this methodology we will only focus in the fiber-based modeling approach. Four dynamic load excitations will be applied and the RC member that will be used is the FL-89A column. Some changes will be made to this column to examine the effect of different types of failure and levels of inelastic action.

This chapter consists of two parts. First, an Incremental Dynamic Analysis (IDA) will be performed. IDA is the application of a specific dynamic excitation load at different intensities of peak ground acceleration (PGA). The principal objective in the utilization of this method is to induce different levels of damage on the column until get rebar fracture. Then, we apply the CWT and DWT transforms to verify the capability of identifying the damage (or yield episodes) of both transforms. The second part involves taking the accelerations from the IDA and apply the new refinements (that will be explained later) in order to eliminate (or reduce) some peaks that correspond to the higher frequencies coming from the base excitation and are no related to damage.

Finally, the level of induced damage is compared with the peaks amplitude of the CWT high frequency and DWT detail analyzes to see if there is any kind of relationship.

5.2 FL-89A modification

Some changes were made to the FL-89A RC column to ensure that the column suffer considerable damage at large levels of ductility demand. Among these changes, we increased the spiral spacing until the limit required for shear capacity. Another change was to modify the reinforcing steel degradation parameters to ensure rebar fracture. Other changes are presented in *bold* and *italic* numbers in Figure 5-1.

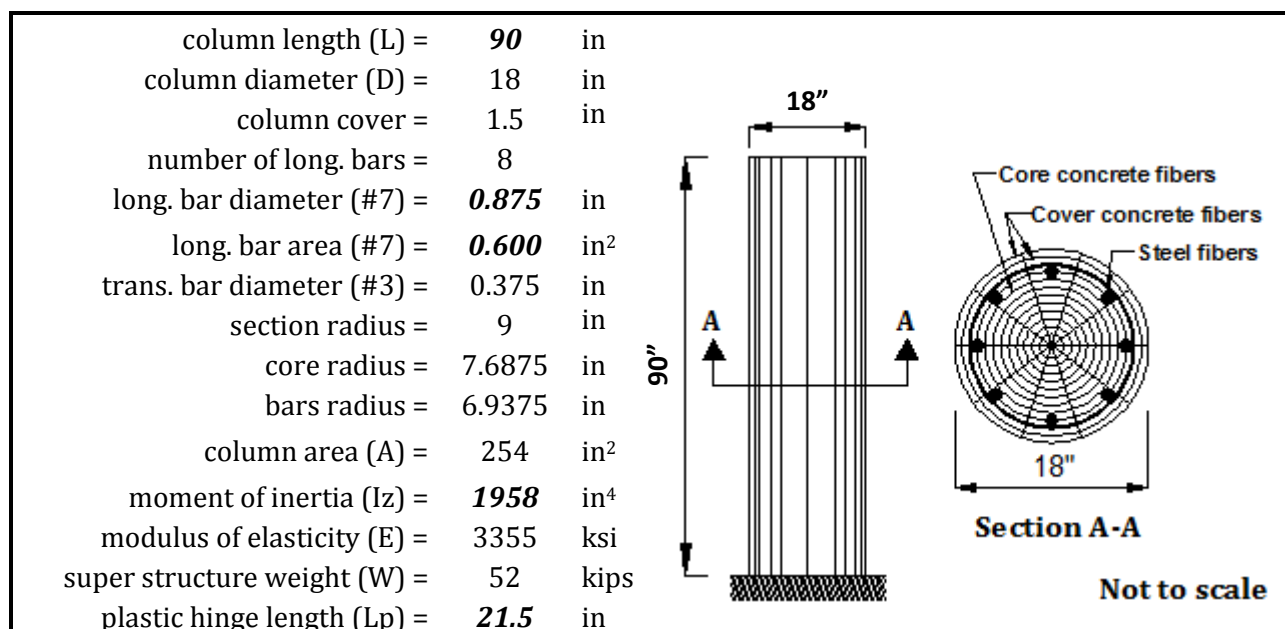


Figure 5-1: FL-89A - geometric properties modification

5.3 Dynamic Excitation Loads

The dynamic excitation loads for this chapter will be two white noises and two earthquakes (wn20, wn40, EQ1, EQ2). The white noises (Figures 5-2 and 5-3) are similar to those used in Chapter IV with the only difference that now they have 20 seconds of time duration. The earthquakes loads (Figures 5-4 and 5-5) are the Loma Prieta earthquake ($M = 6.9$, $PGA = 0.14$) from Treasure Island Station (also used in the previous chapter) and the Whittier Narrows ($M = 6.0$, $PGA = 0.14$) of October 1, 1987 from LA Baldwin Hills Station. This last earthquake was modified. The strong motion part (identified with dashed semicircles in Figure 5-5) was duplicated to induce more damage to the RC column in order to achieve the rebar fracture. Notice that the frequency content of the Whittier Narrows (EQ2) record

is much wider than the frequency content of the Loma Prieta record (EQ1), which can be considered as a narrow band record. Both records were obtained from the NGA database (PEER, 2010). All four acceleration histories have a sampling rate of 200 Hz and were normalized to a maximum acceleration of 1g.

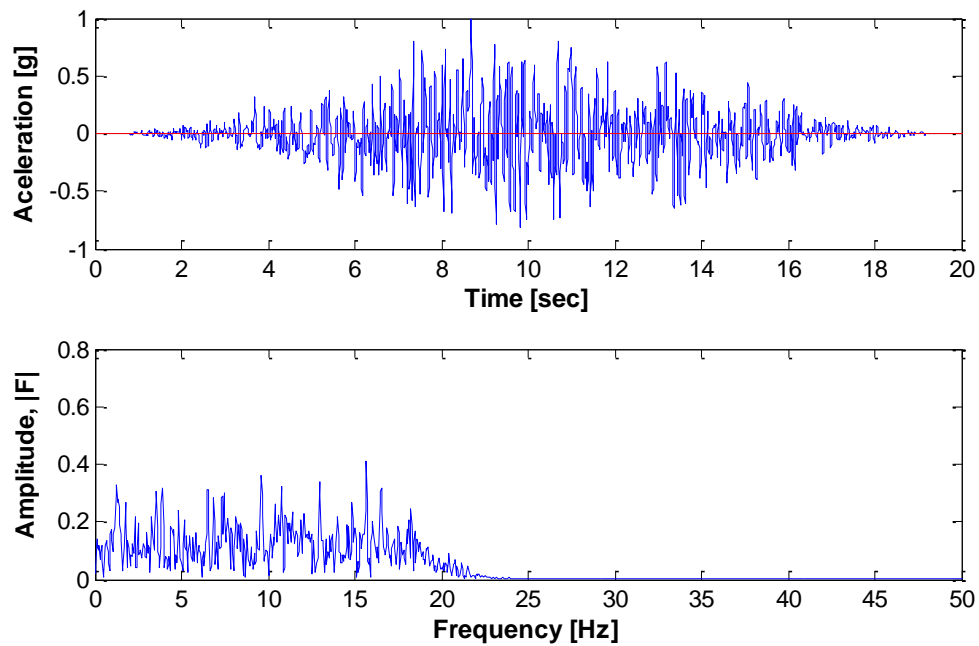


Figure 5-2: (a) White Noise with frequency content of 20Hz, (b) Fourier Spectrum

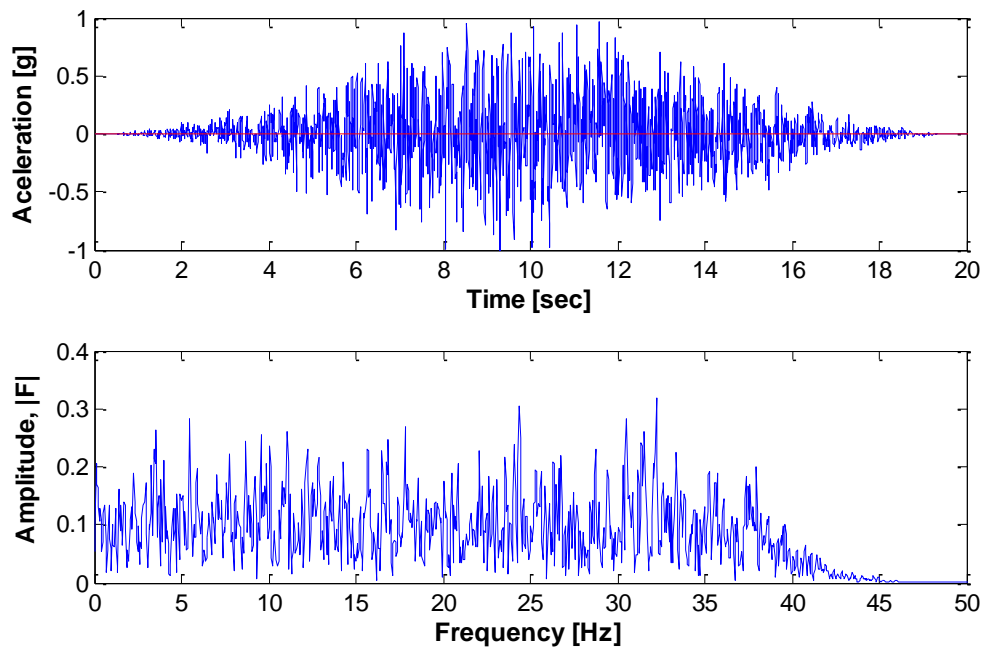


Figure 5-3: (a) White Noise with frequency content of 40Hz, (b) Fourier Spectrum

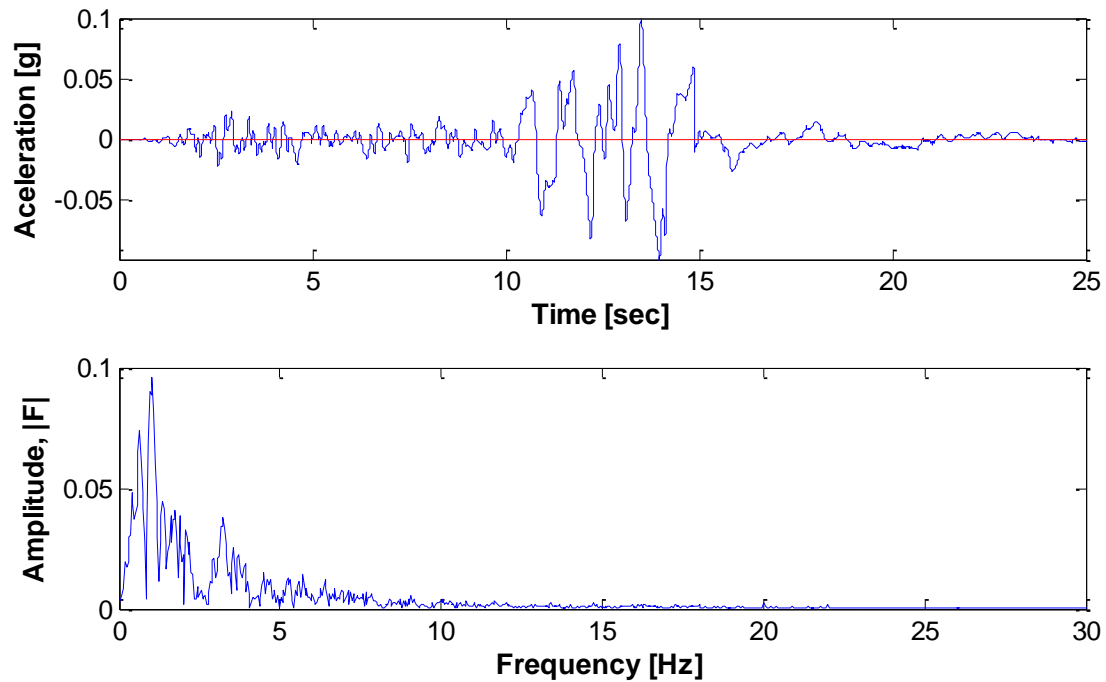


Figure 5-4: (a) Loma Prieta earthquake from Treasure Island - 10/17/89, (b) Fourier Spectrum

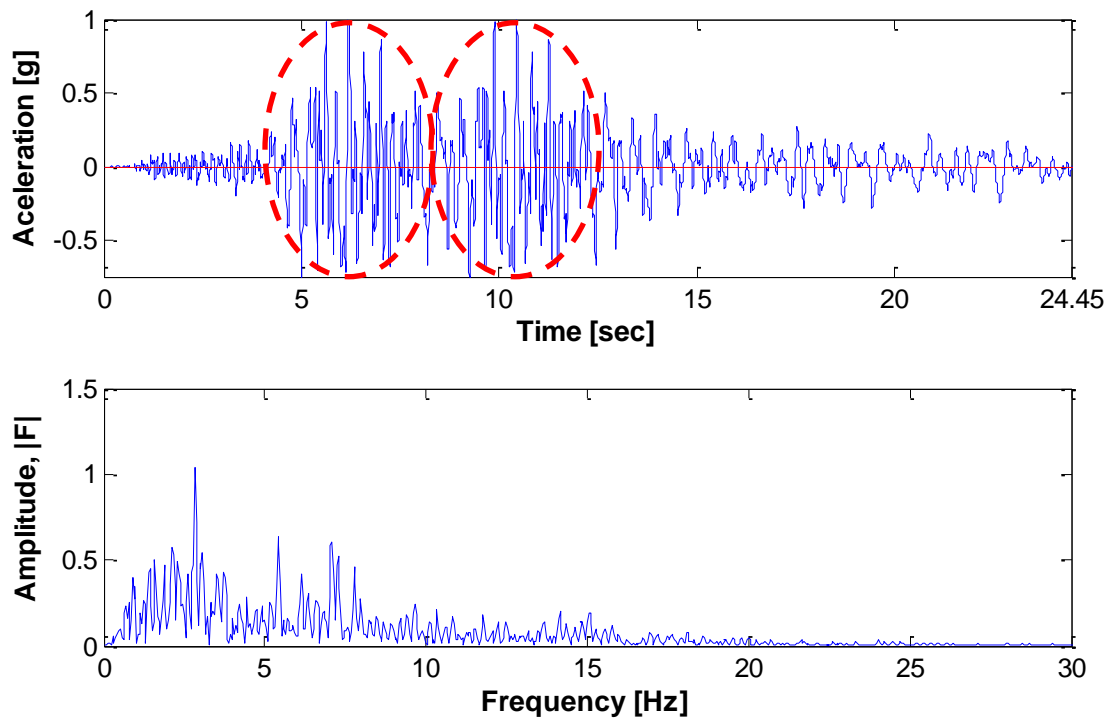


Figure 5-5: (a) Whittier Narrows from LA Baldwin Hills Station - 10/1/87, (b) Fourier Spectrum

5.4 Incremental Dynamic Analysis (IDA)

The implementation of the incremental dynamic analysis for the excitation loads presented on the previous topic is summarized below:

- Run the dynamic analysis for each of the four excitations loads (wn20, wn40, EQ1, EQ2) and find a factor (f_1) for which each excitation has to be multiplied to get a ductility ~ 1 .
- Run the dynamic analysis for each of the four excitations loads (wn20, wn40, EQ1, EQ2) and find a factor (f_2) for which each excitation has to be multiplied to get rebar fracture.
- Run the analysis using amplification factors (which in this case is the same that PGA since the signals were normalized to 1g) as follow: $0.5f_1$, f_1 , f_2 , and the obtained from equation 5-1.

$$f_k = f_1 + k * (f_2 - f_1) \quad (5-1)$$

where,

$k = 0.2, 0.4, 0.6, 0.8$

Therefore, a total of 7 amplification factors will be obtained for each excitation load (Table 5-1). Once the amplification factors are obtained, we proceed to applying it to each dynamic excitation. After obtain the 7 structural responses for each excitation load, the two wavelet transforms (CWT and DWT) are applied.

Table 5-1: PGA for each dynamic excitation load

Amplification Factor	white noise <20Hz	white noise <40Hz	Loma Prieta Earthquake	Whittier Narrows Earthquake
$0.5 f_1$	0.23	0.25	0.11	0.12
f_1	0.45	0.50	0.22	0.23
$f_{k=0.2}$	0.97	1.15	0.33	0.68
$f_{k=0.4}$	1.49	1.80	0.45	1.14
$f_{k=0.6}$	2.01	2.45	0.56	1.60
$f_{k=0.8}$	2.53	3.10	0.68	2.05
f_2	3.05	3.75	0.80	2.50

5.5 CWT analysis – Low and High Frequency analyzes

This section presents the results for the incremental dynamic analysis for all the four dynamic excitation loads previously described. The resulting acceleration responses are analyzed through CWT low and high frequency analyzes. Displacement, force and acceleration time histories are also presented.

5.5.1 White Noise <20Hz

The results obtained for the first dynamic load are presented in Figures 5-6 to 5-13. Figure 5-6 present the displacement histories at the top of the column. The horizontal lines represent the displacement for ductility 1. Also, we can notice that a vertical line is present in the last plot. It is the time instant when rebar fracture occurs (we will explained later how it was captured). In Figure 5-7, the results for the incremental dynamic analysis were plotted. Ductility values were obtained by taking the maximum peak from each displacement history shown in Figure 5-6 and divide it between the displacement corresponding to ductility 1 (i.e., 1.27 in). Figures 5-8 a and b show the rebar stress-strain relationship and the stress as function of time. From these plots we can identify the time instant when rebar fracture occurred (which are identified with a circle). Figure 5-9 illustrates the force (at left) and acceleration (at right) time histories for the different levels of ground motion intensities calculated in the previous section. In the force plots, we can see two horizontal lines in each plot. They represent the yield force, f_y , which is 21.38 kips; each time that the responses cross these lines it represents a yield episode. Figures 5-10 and 5-11 present the results obtained for the low and high frequency analyzes respectively. We can appreciate from the low frequency analysis that each plot was able to detect the change in frequency due to the application of different PGA. The high frequency analysis (from 70-100Hz) only partially identified the yield episodes. There are some trends that cannot be associated with yielding, as those appearing in the first graph were the level of ductility demand is below 1. Figure 5-12 displays the results for the 80Hz coefficients; the maximum spike is identified in each plot. Looking at the last plot, it is note that the maximum spike coincides very well with the time instant when rebar fracture occurs, i.e. 13.3 seconds. The principal reason of identify the maximum spike for each plot is because

we want to verify if there is a relationship between the amplitude of those spikes and the levels of induced damage (Figure 5-13). At first glance, it can be note that it seems like if there is relationship, but there is a peak that corresponds to a $PGA = 2.53$ ($\mu = 9.88$) that do not follow the pattern. Therefore, we cannot relate the level of damage (inelastic action) with the spikes amplitude.

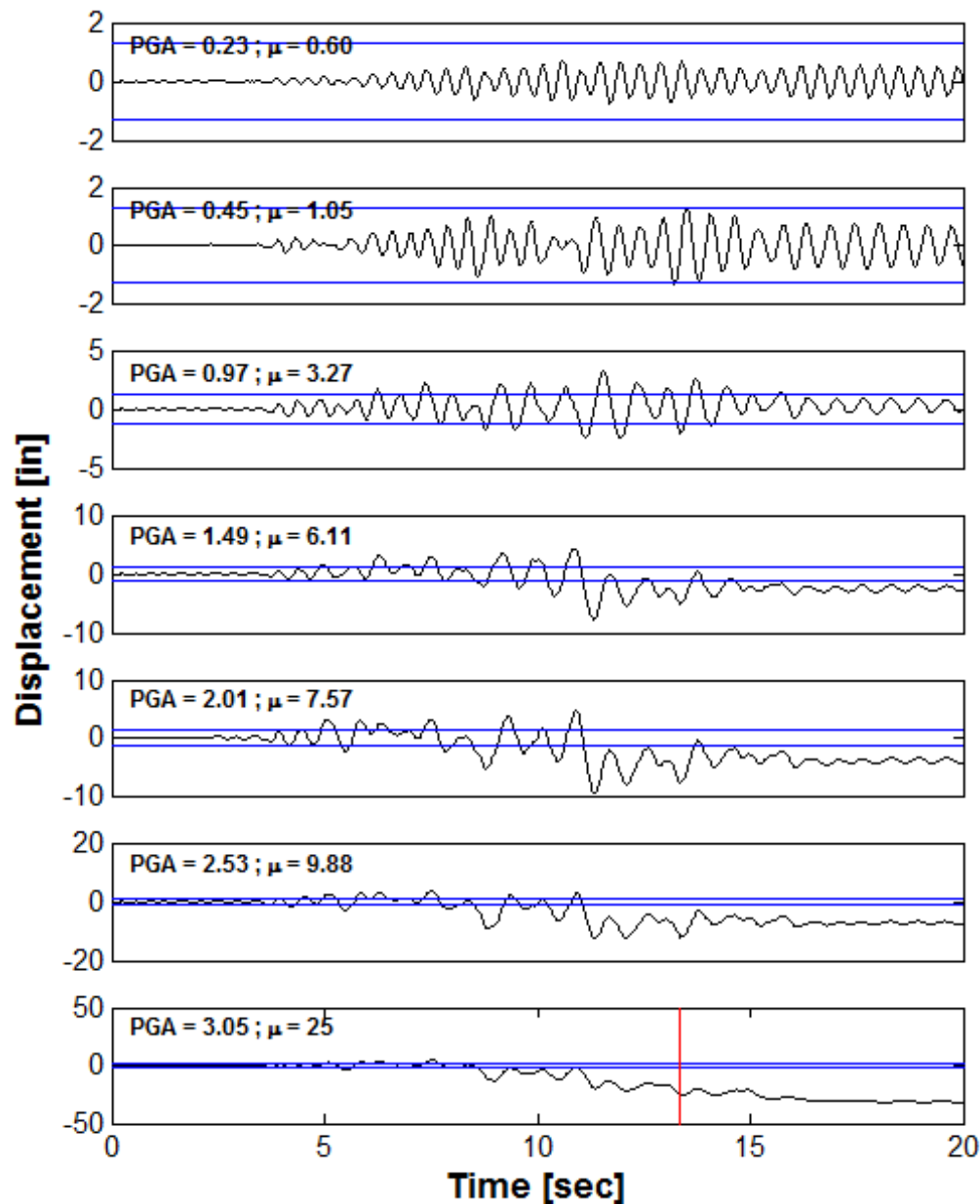


Figure 5-6: Displacement histories for different levels of ground motion intensities

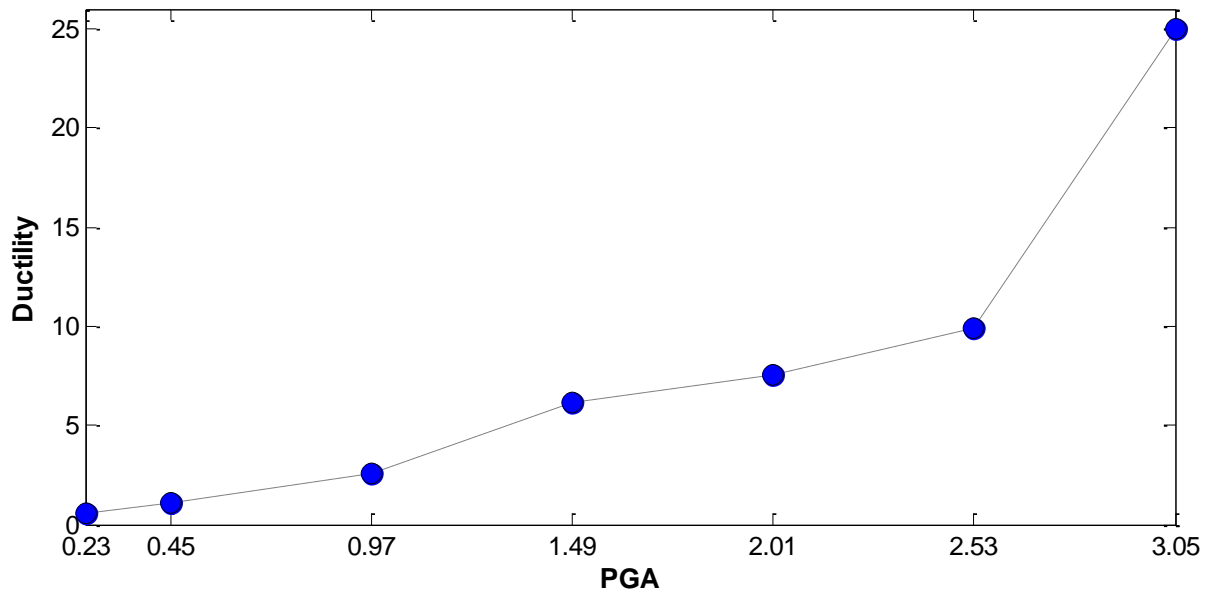


Figure 5-7: White Noise 20Hz - Incremental Dynamic Analysis (IDA Curve)

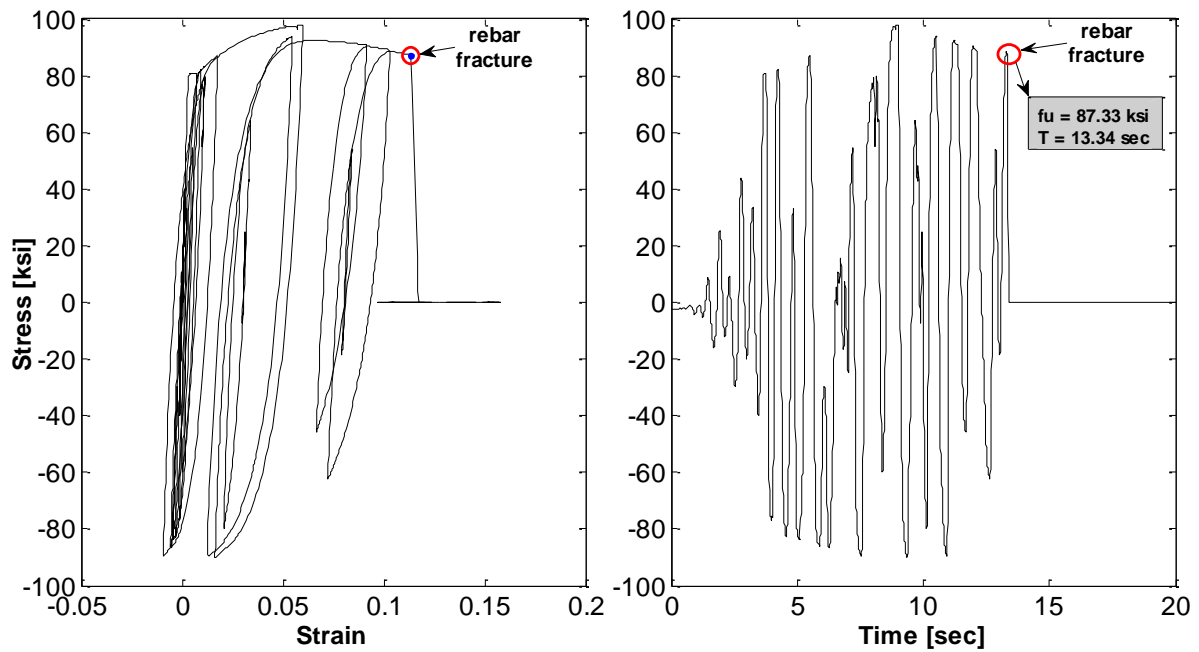


Figure 5-8: (a) Stress - Strain Relationship, (b) Stress-Time Relation

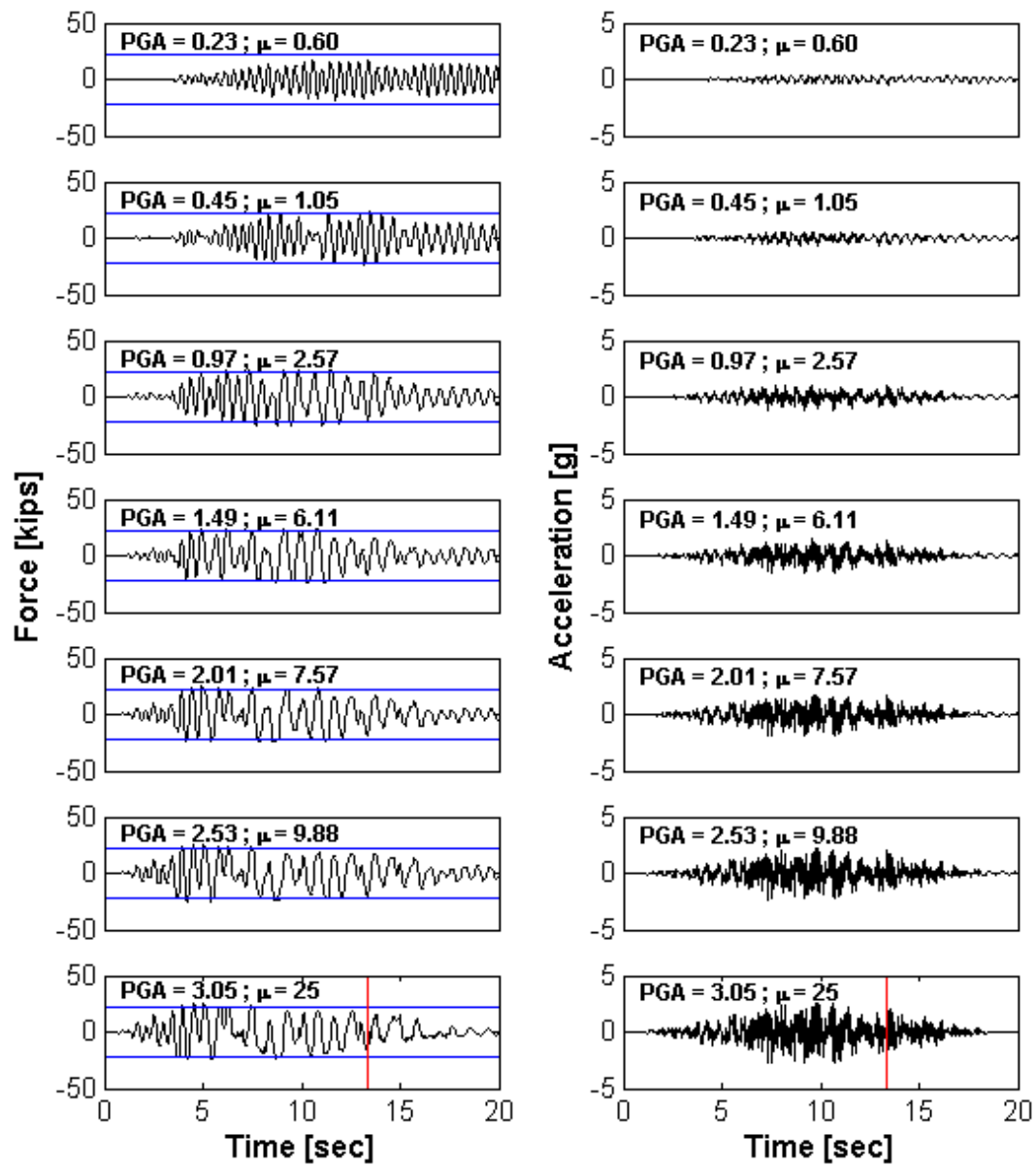


Figure 5-9: Force (left) and Acceleration (right) histories for different PGA

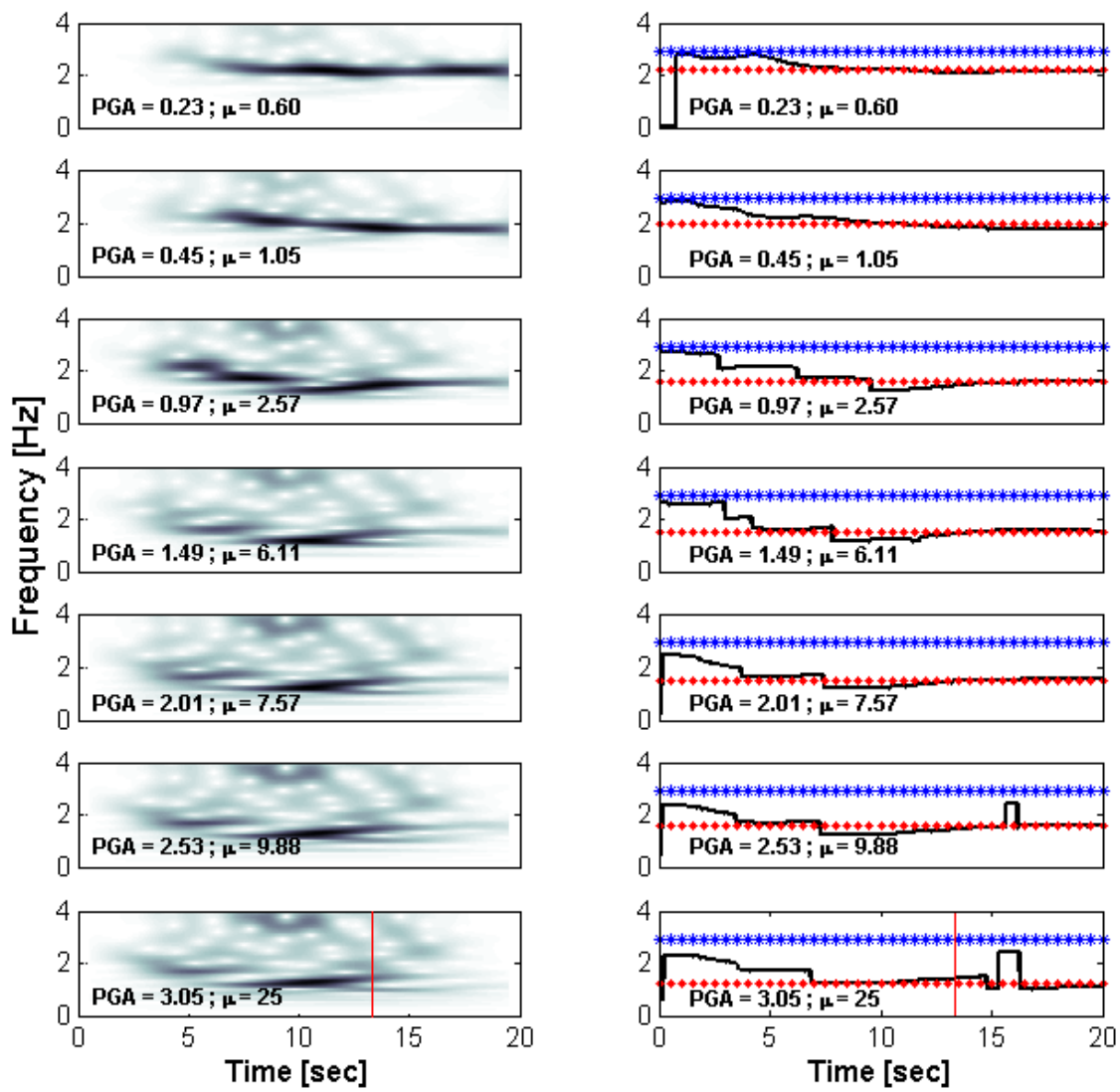


Figure 5-10: CWT - Low Frequency analysis

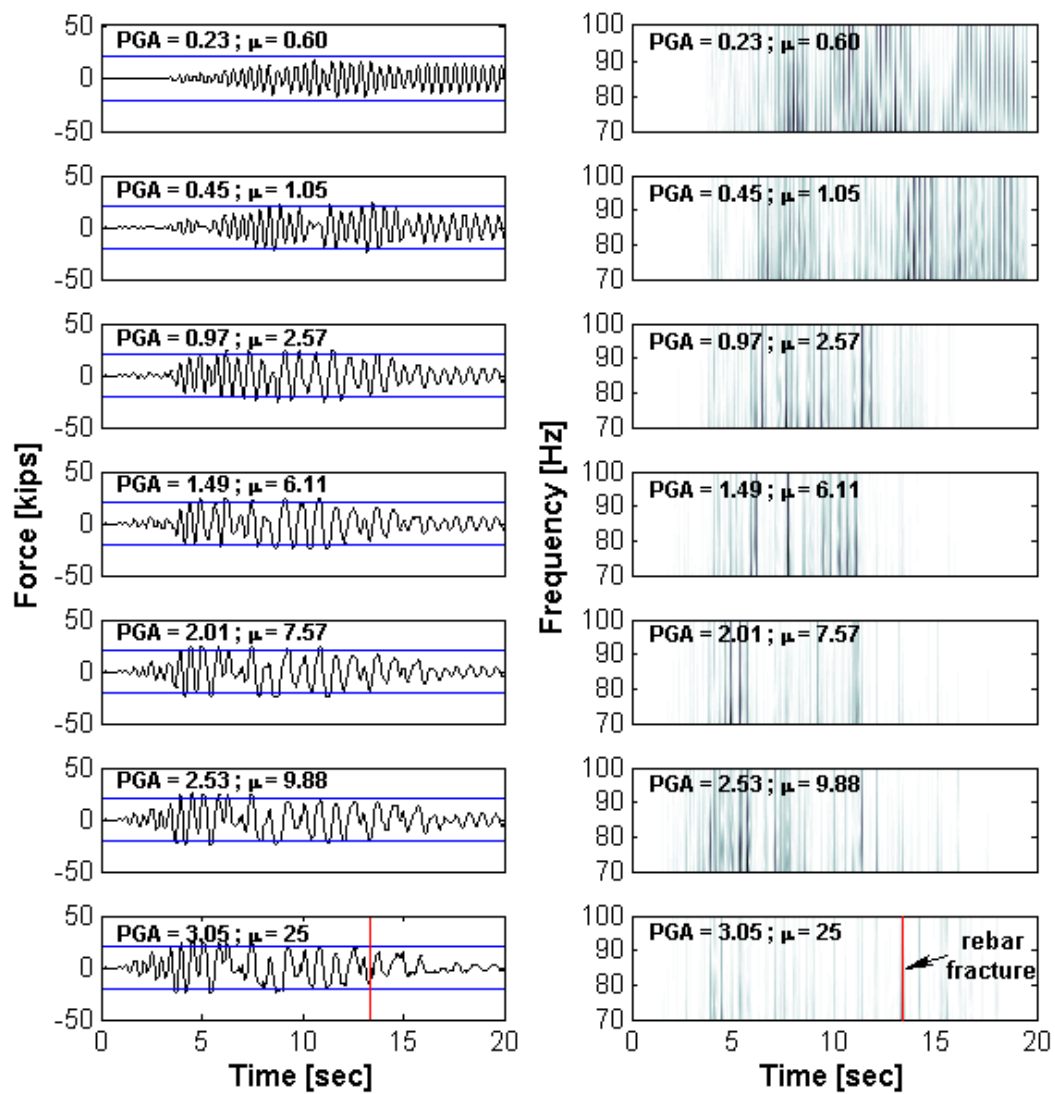


Figure 5-11: CWT - High Frequency analysis

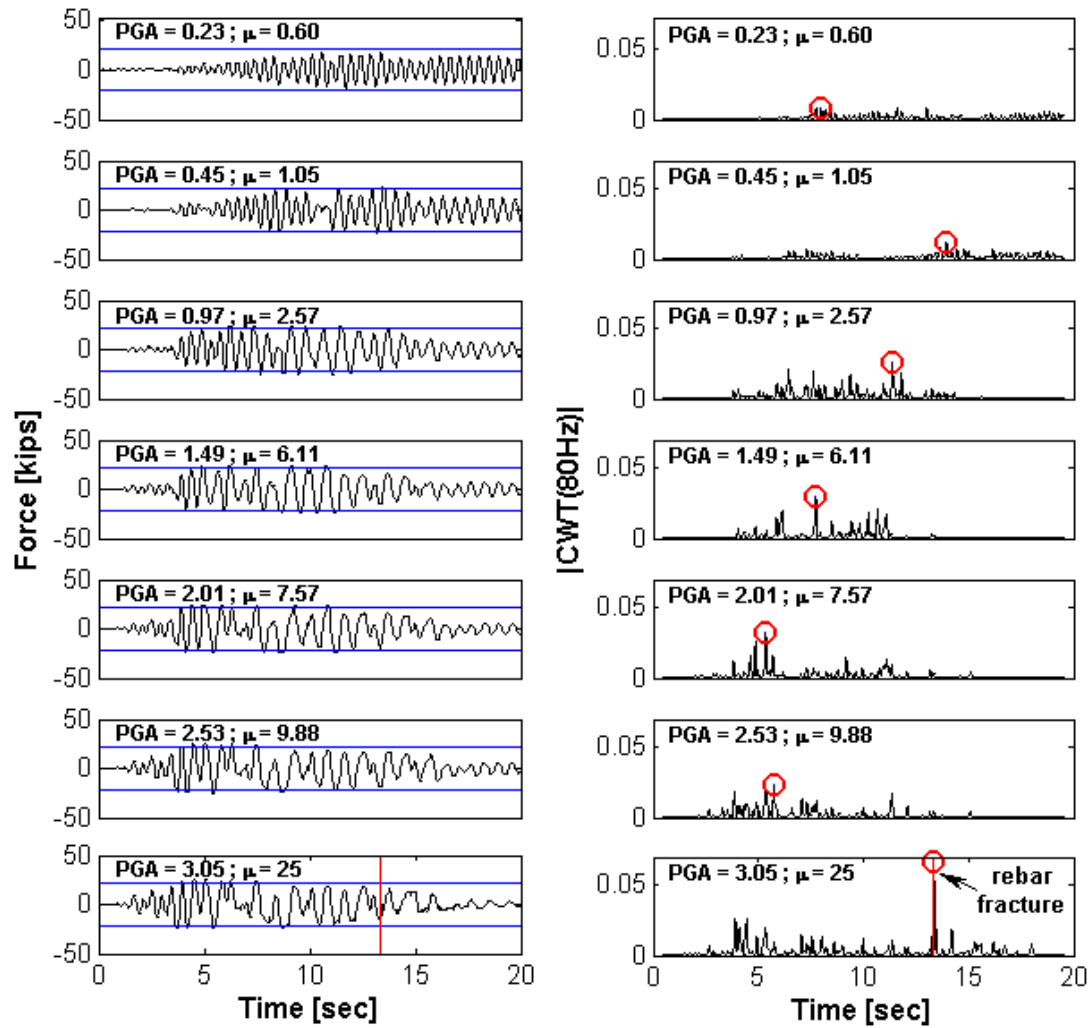


Figure 5-12: CWT - High Frequency analysis showing the coefficients for 80Hz

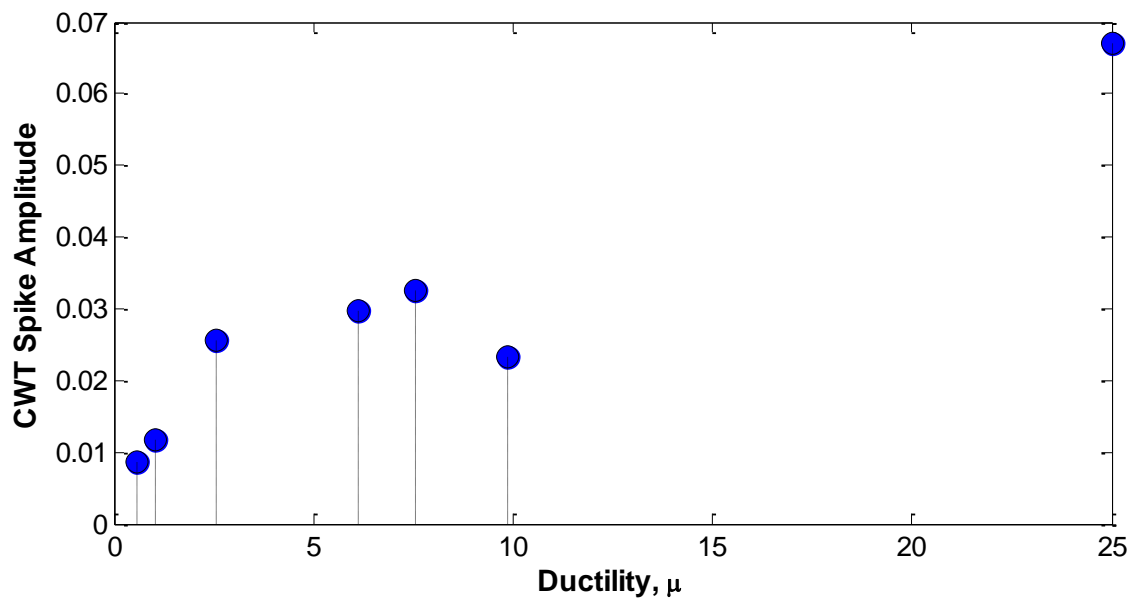


Figure 5-13: CWT Spike Amplitude vs Ductility

5.5.2 White Noise <40Hz

Figures 5-14 to 5-21 illustrate the results for the 40Hz white noise. Figure 5-14 presents the displacement histories for the seven ground motion intensities. Figure 5-15 displays the IDA curve for this dynamic signal. Figure 5-16 shows the time instant when the rebar fracture occurs (i.e. 14.7 seconds) for the last ground motion intensity (PGA = 3.75). The force and acceleration histories are shown in Figure 5-17. The low and high frequency analysis are shown in Figures 5-18 and 5-19. The low frequency analysis was capable of identify the changes in frequencies for the column, but not as clear as for wn20. The results for the high frequency analysis once again were able to partially identify the yield instants. Figure 5-20 illustrates the CWT coefficients for 80Hz. In the last plot the maximum spike does not correspond with the time instant of the rebar fracture. The maximum spikes were identified and plotted in Figure 5-21, but once again no pattern was found.

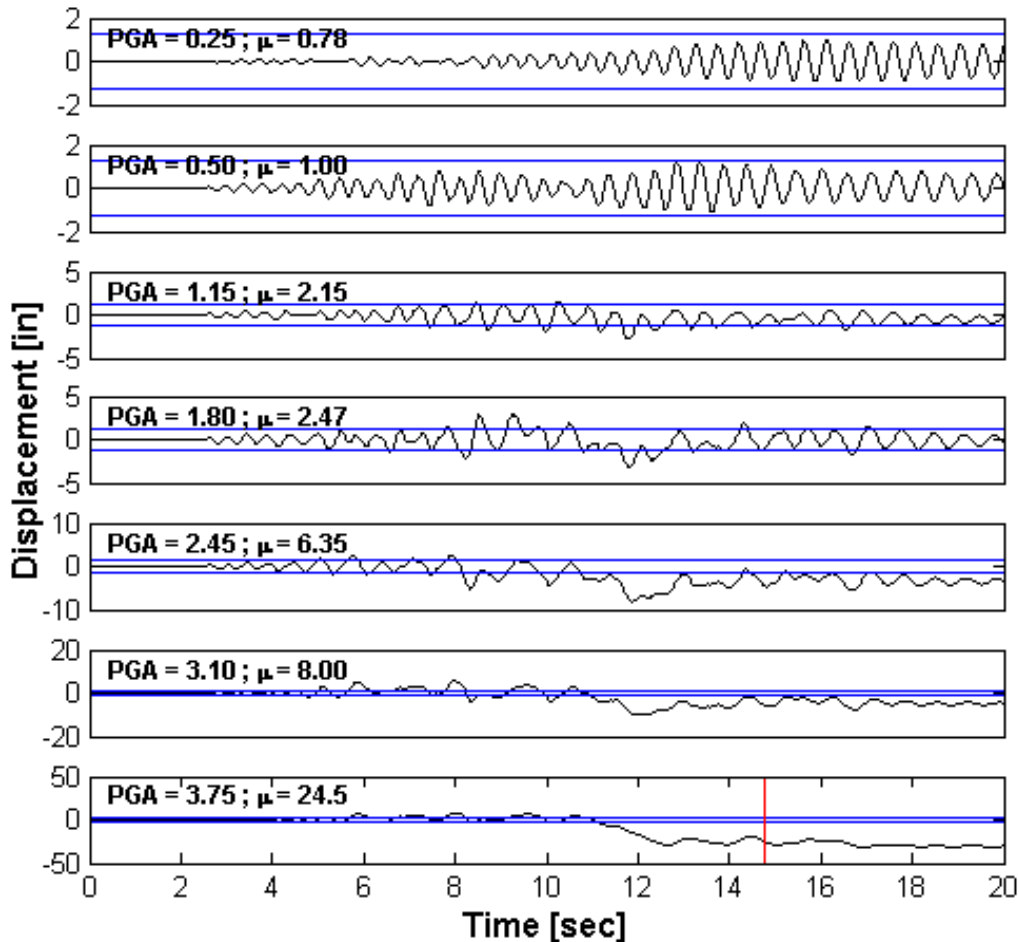


Figure 5-14: Displacement histories for different levels of ground motion intensities

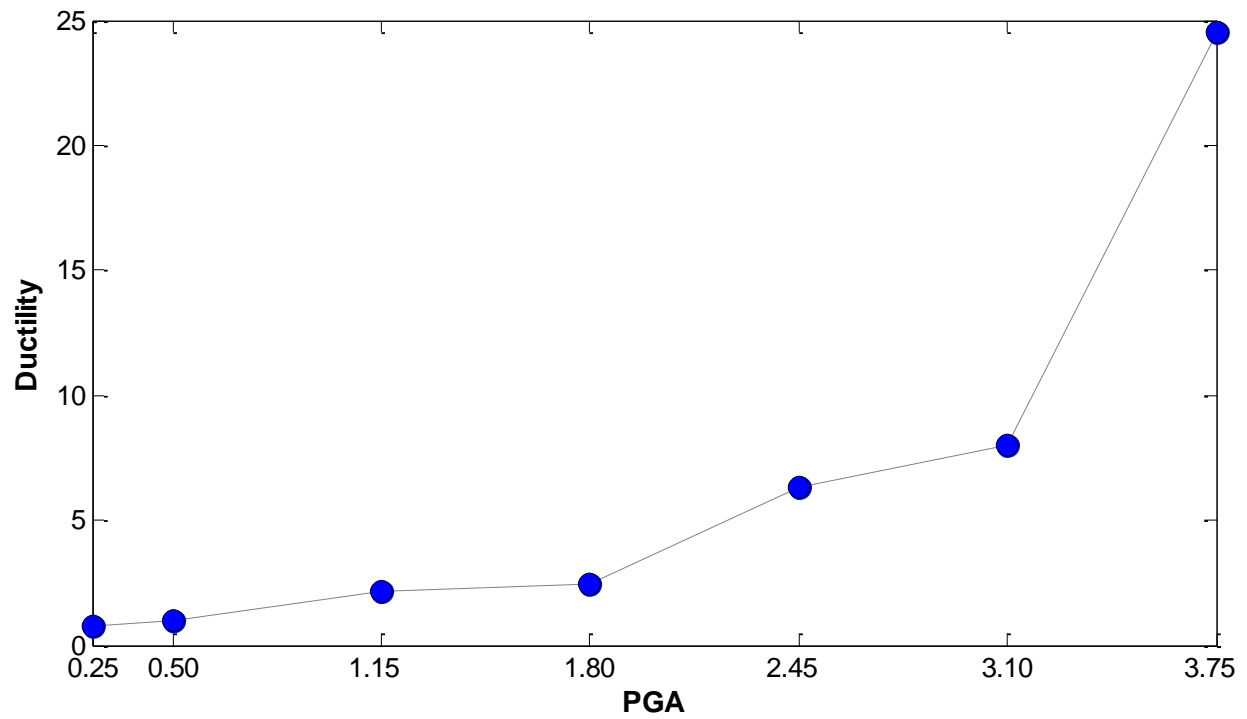


Figure 5-15: White Noise 40Hz - Incremental Dynamic Analysis (IDA curve)

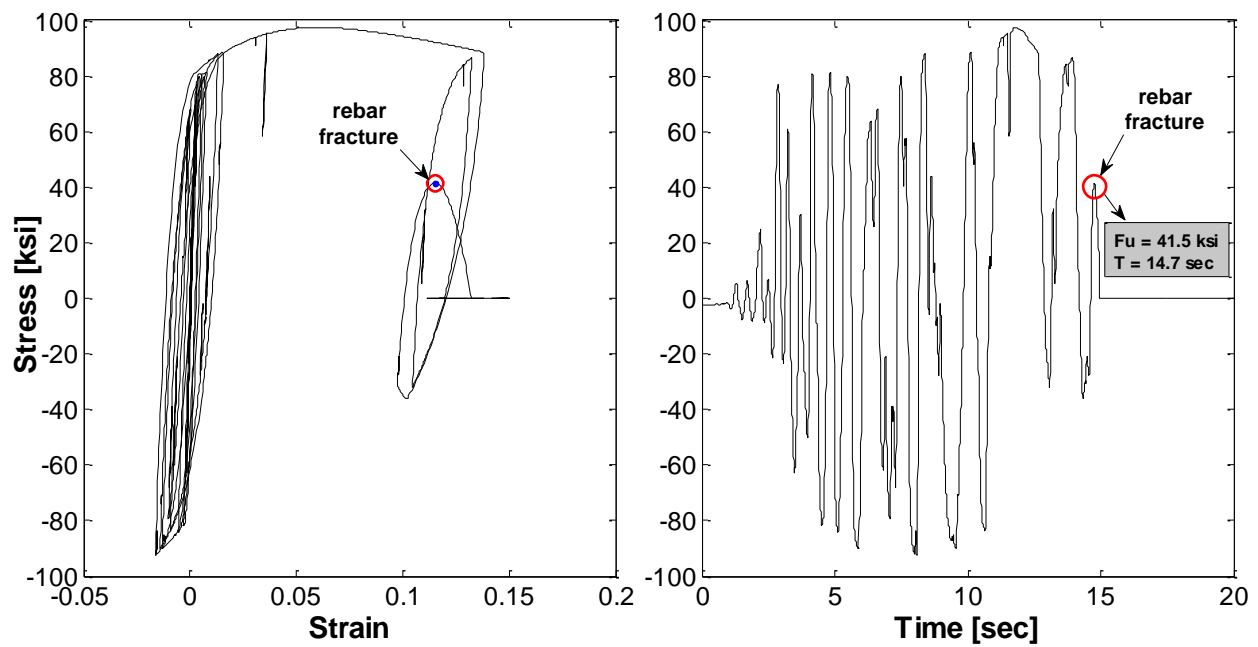


Figure 5-16: (a) Stress - Strain Relationship, (b) Stress - Time Relation

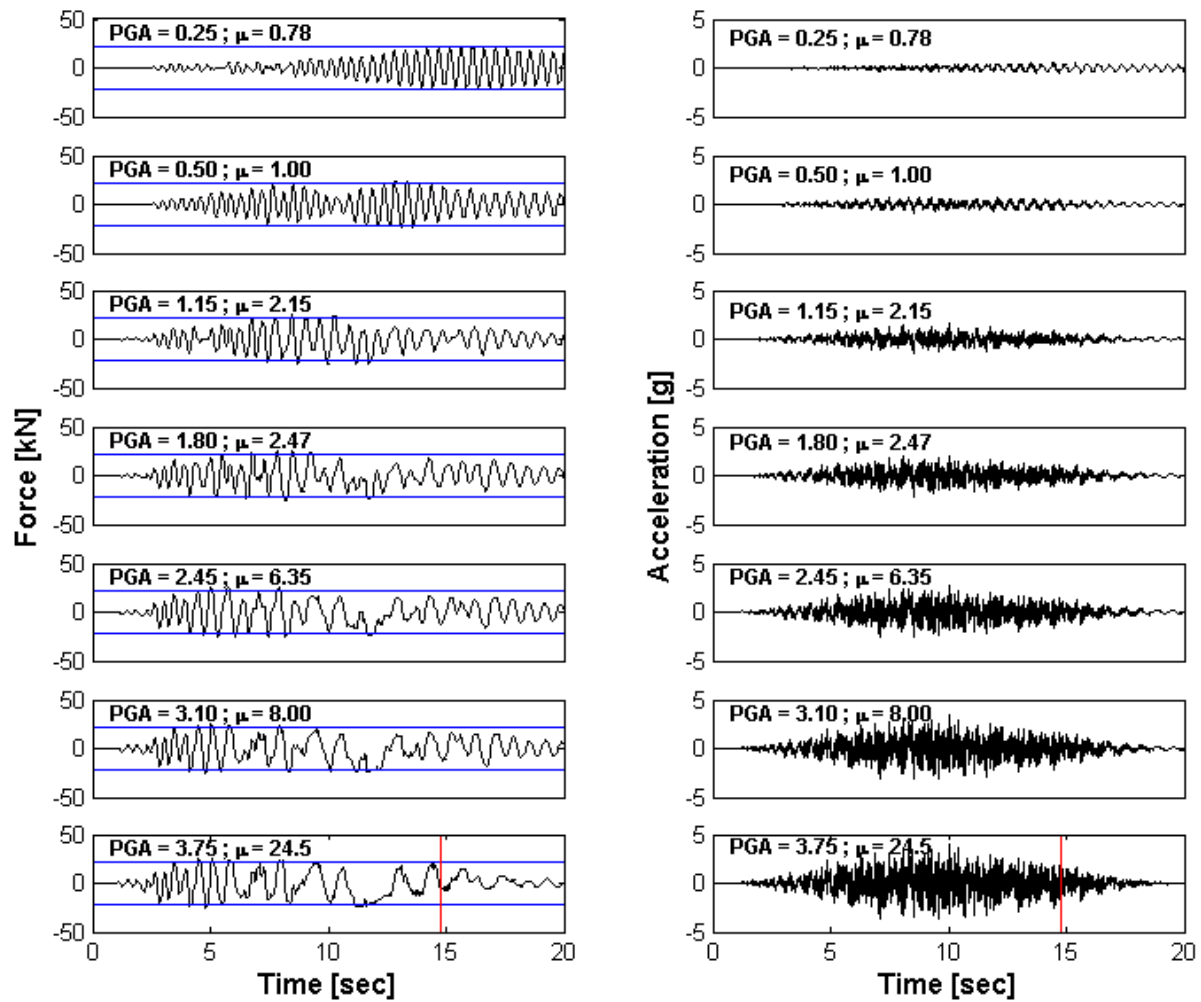


Figure 5-17: Force (left) and Acceleration (right) for different levels of PGA

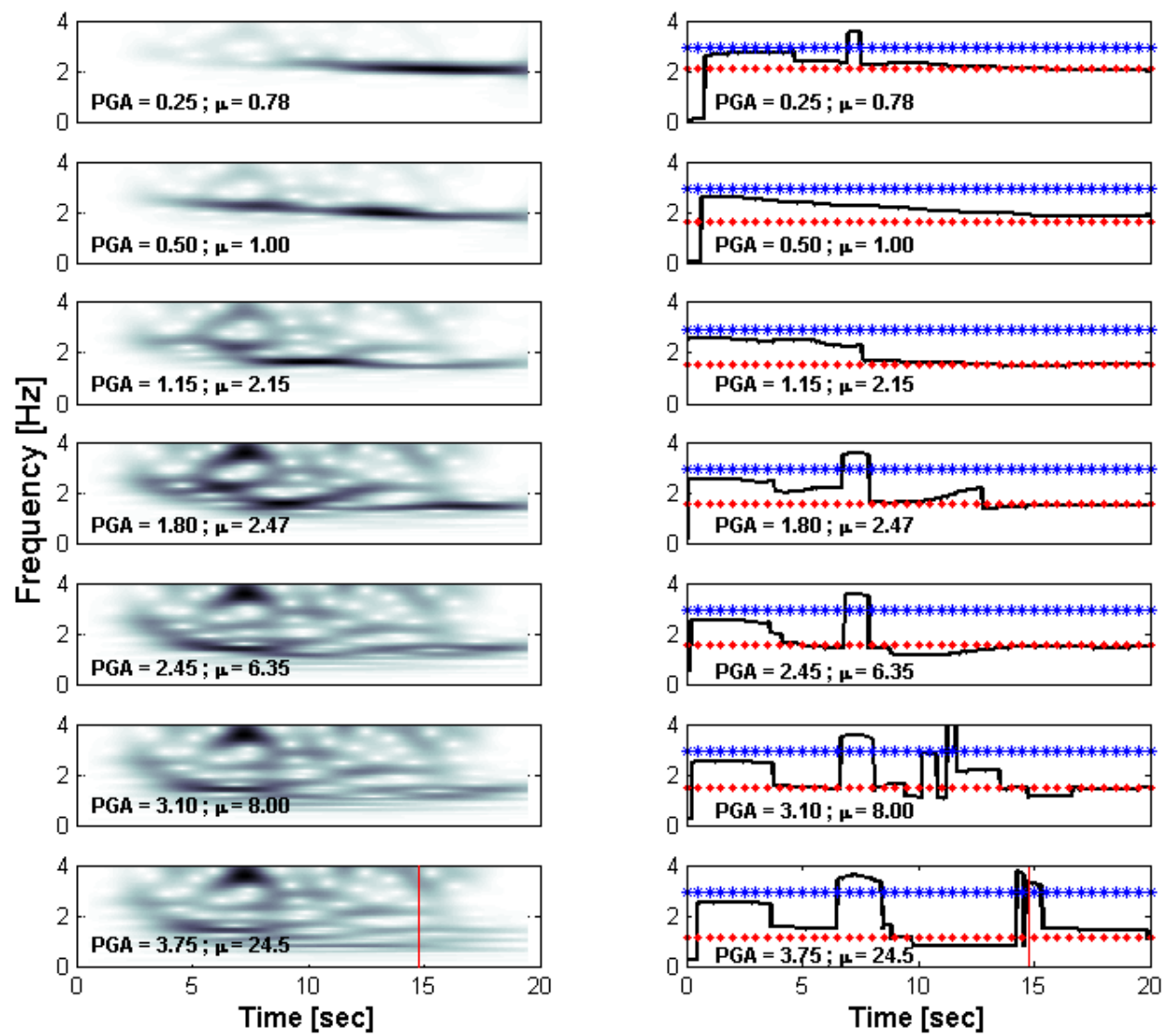


Figure 5-18: CWT - Low Frequency analysis

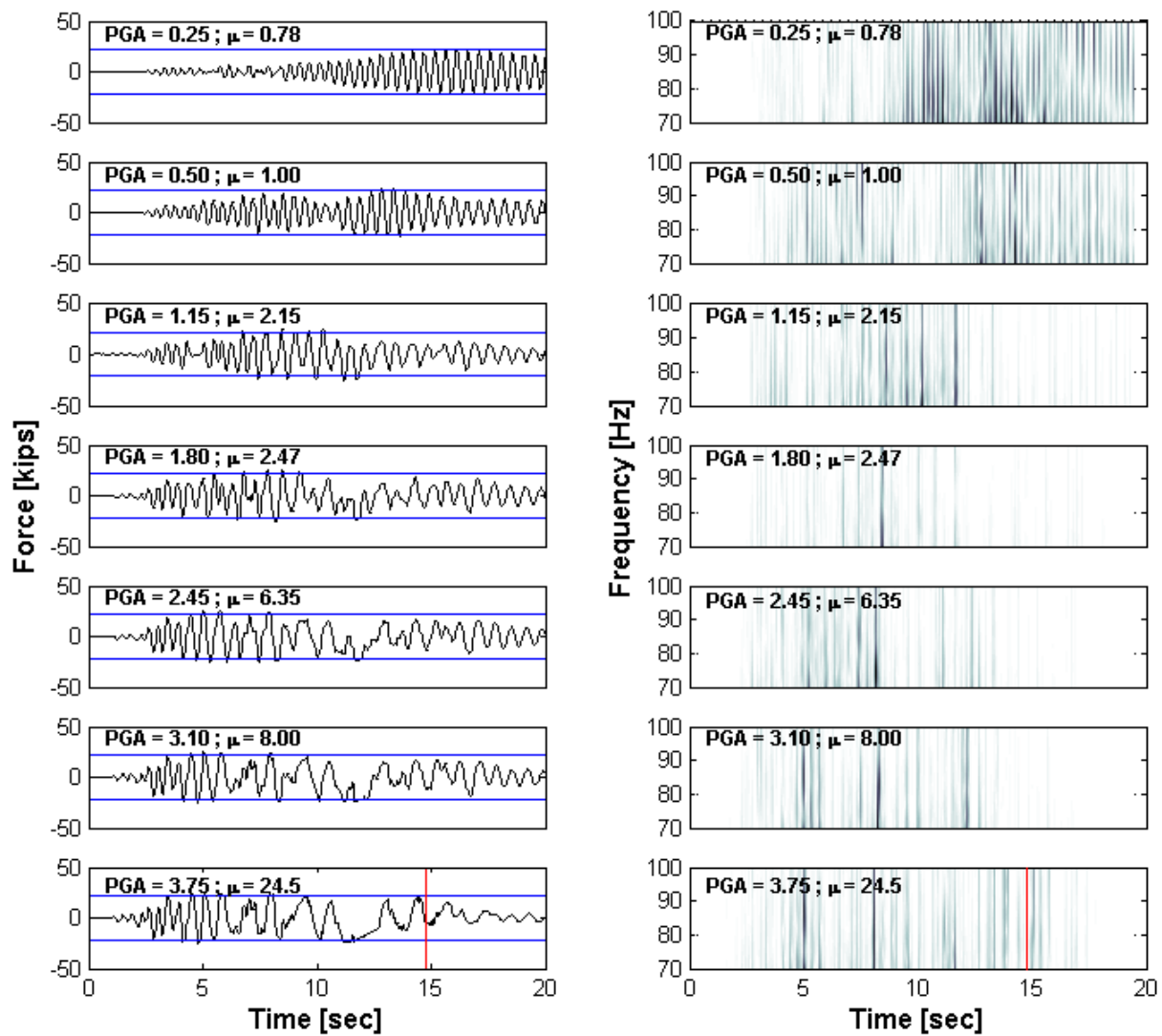


Figure 5-19: CWT - High Frequency analysis

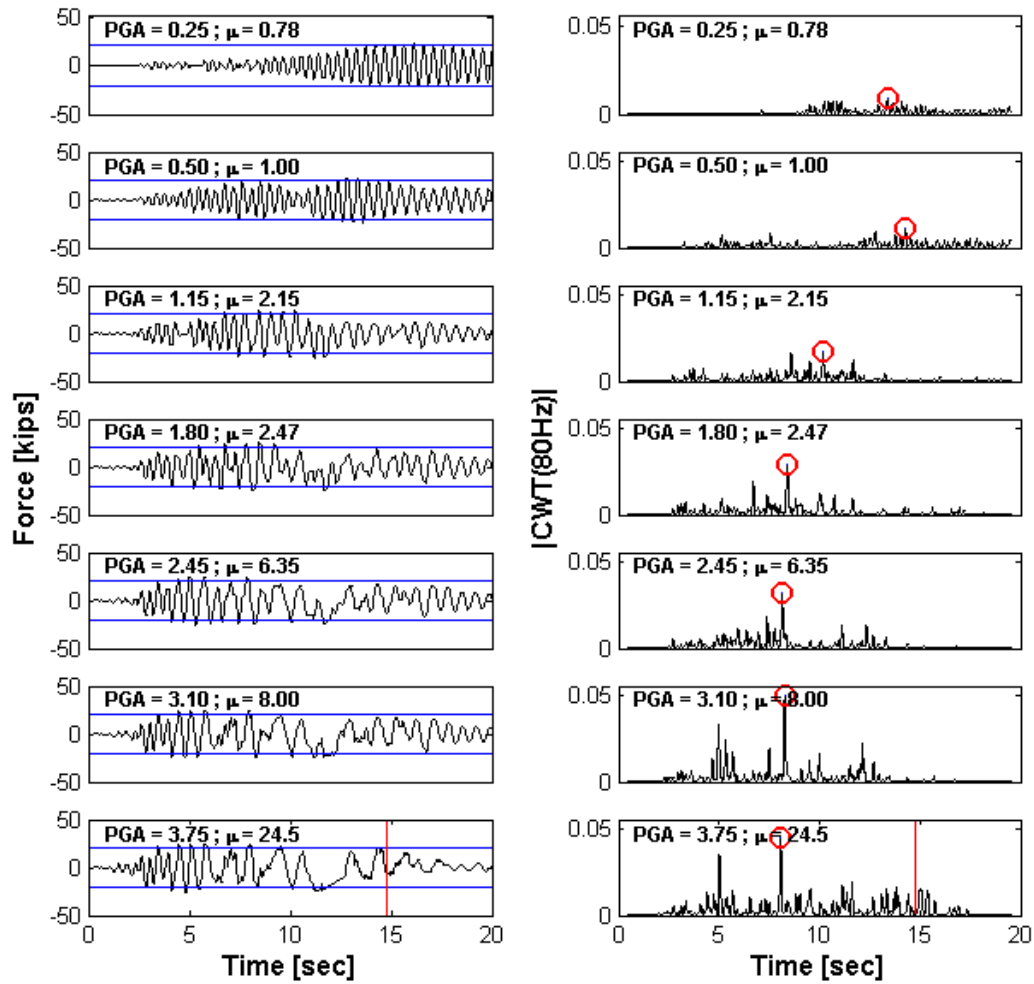


Figure 5-20: CWT - High Frequency analysis showing the coefficients for 80Hz

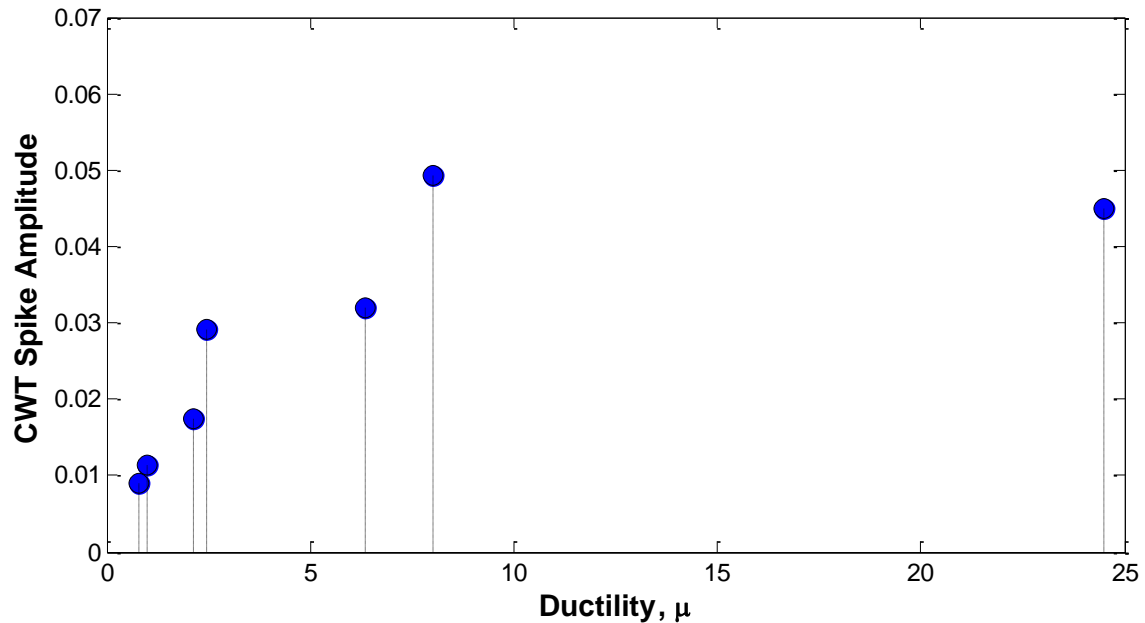


Figure 5-21: CWT Spike Amplitude vs Ductility

5.5.3 Loma Prieta earthquake

Figures 5-23 to 5-29 illustrate the results obtained for the Loma Prieta earthquake. Among these results are the displacement, force and acceleration histories. Also the IDA curve and the stress-strain relationship for the bar that had fracture are shown. Moreover, looking at the low frequency results (Figure 5-26) we can perceive that it were able to detect the changes in frequency for all the PGA. In the high frequency results displayed in Figure 5-27, it mainly shows spurious trends in all the ground motion intensities. Same observation can be made for the 80Hz coefficients in Figure 5- 28. By looking the results in Figure 5-29 is evident that there is no pattern in this plot. Therefore, the high frequency analysis does not present apposite results.

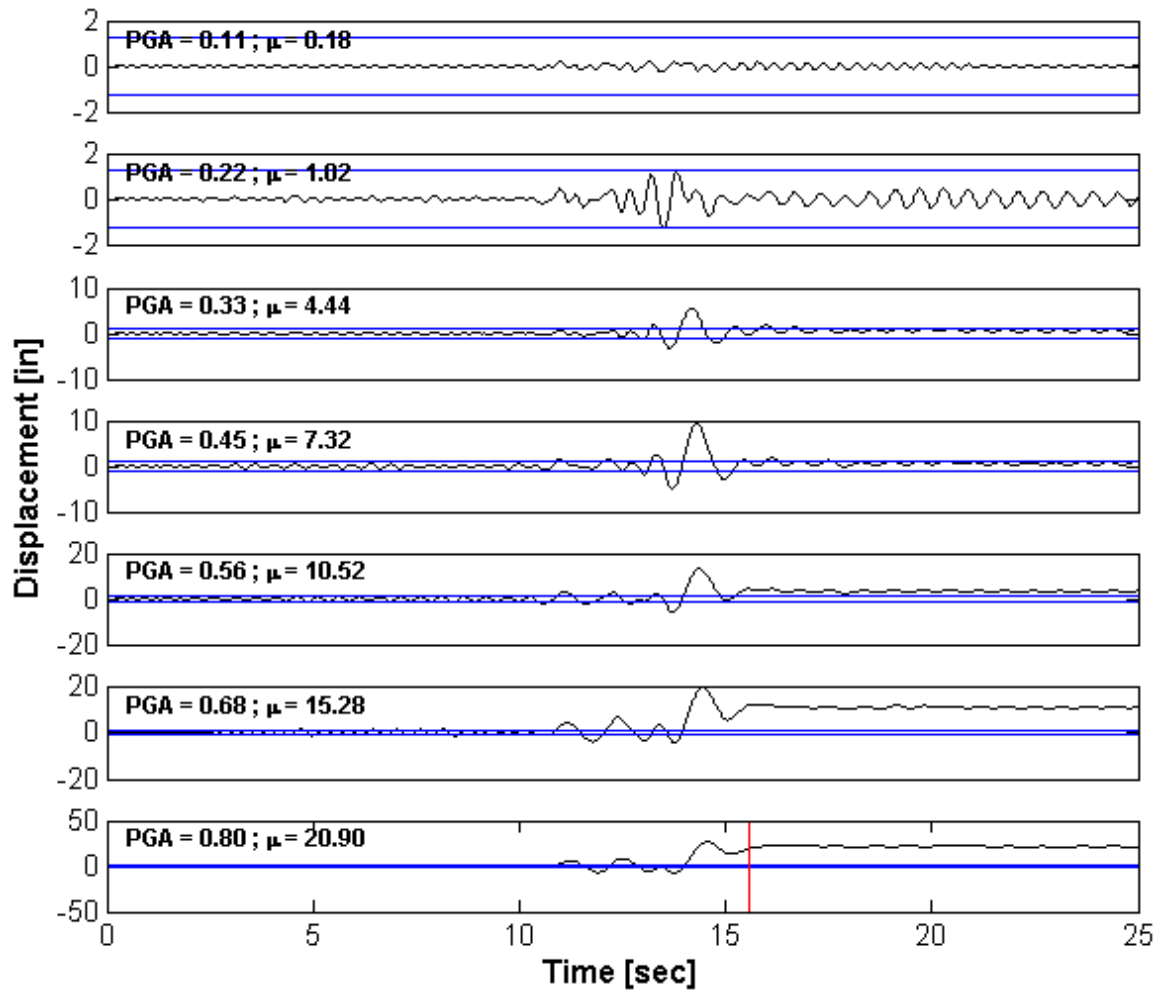


Figure 5-22: Displacement histories for different levels of ground motion intensities

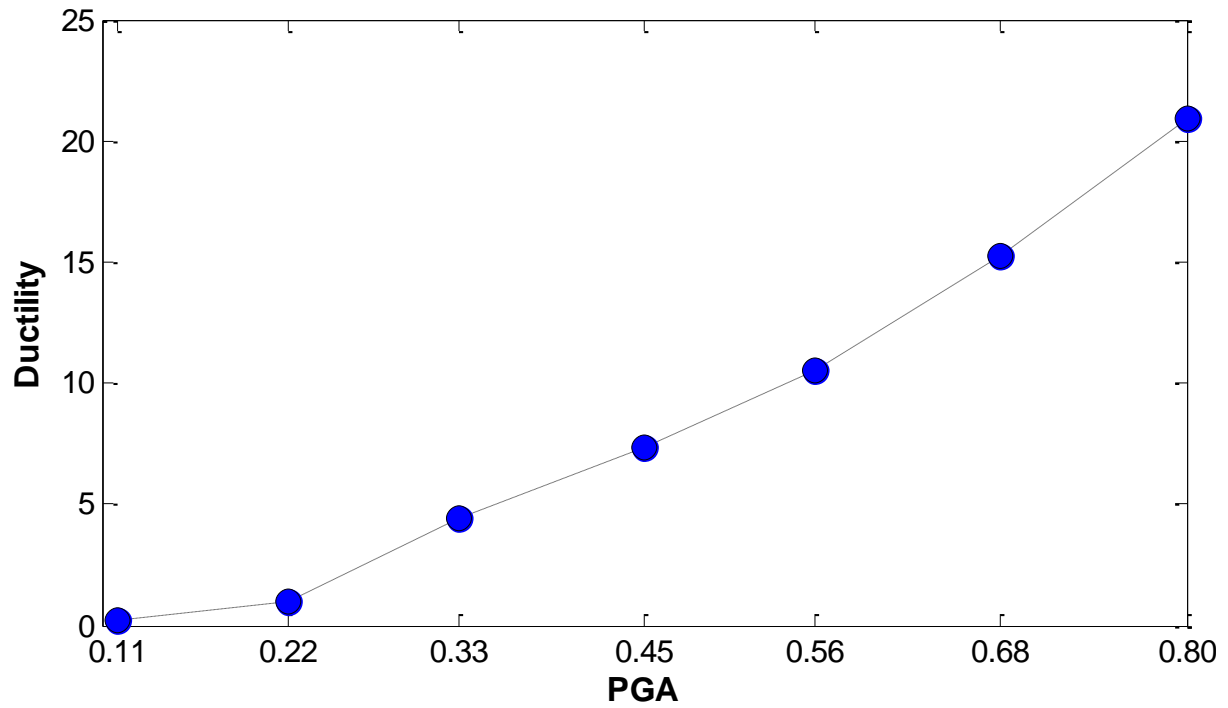


Figure 5-23: Loma Prieta earthquake - Incremental Dynamic Analysis (IDA curve)

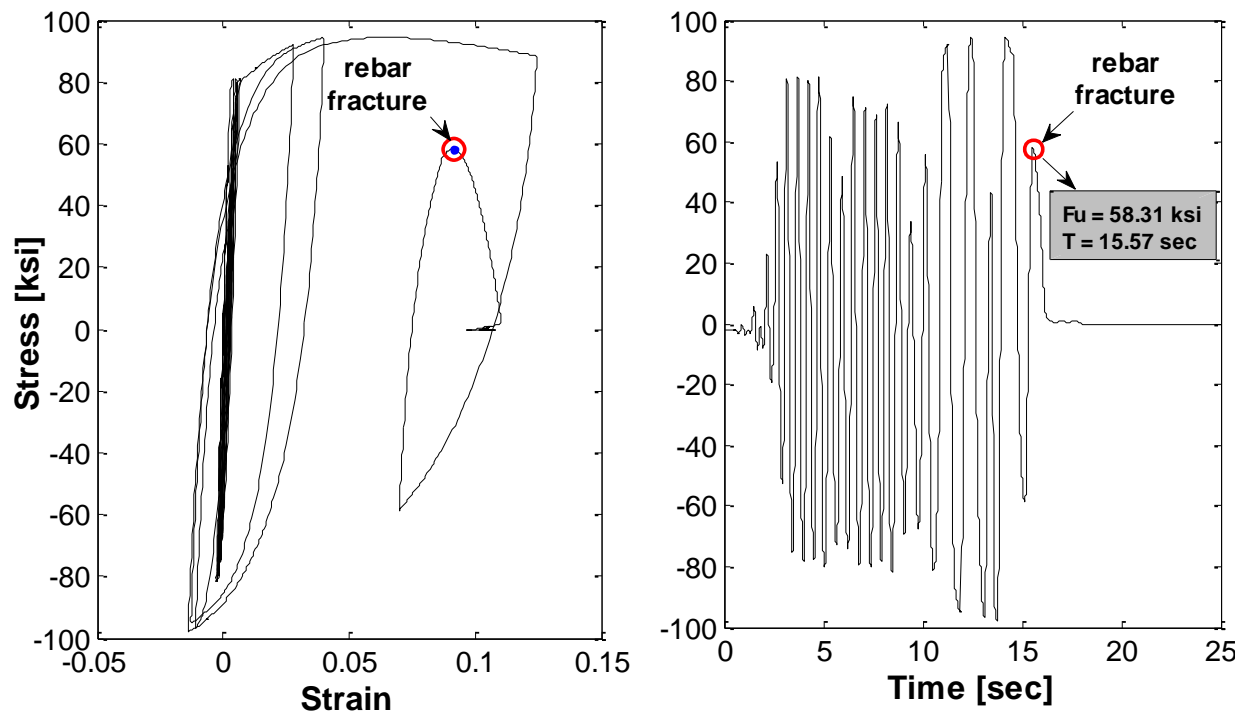


Figure 5-24: (a) Stress-Strain Relationship, (b) Stress-Time Relation

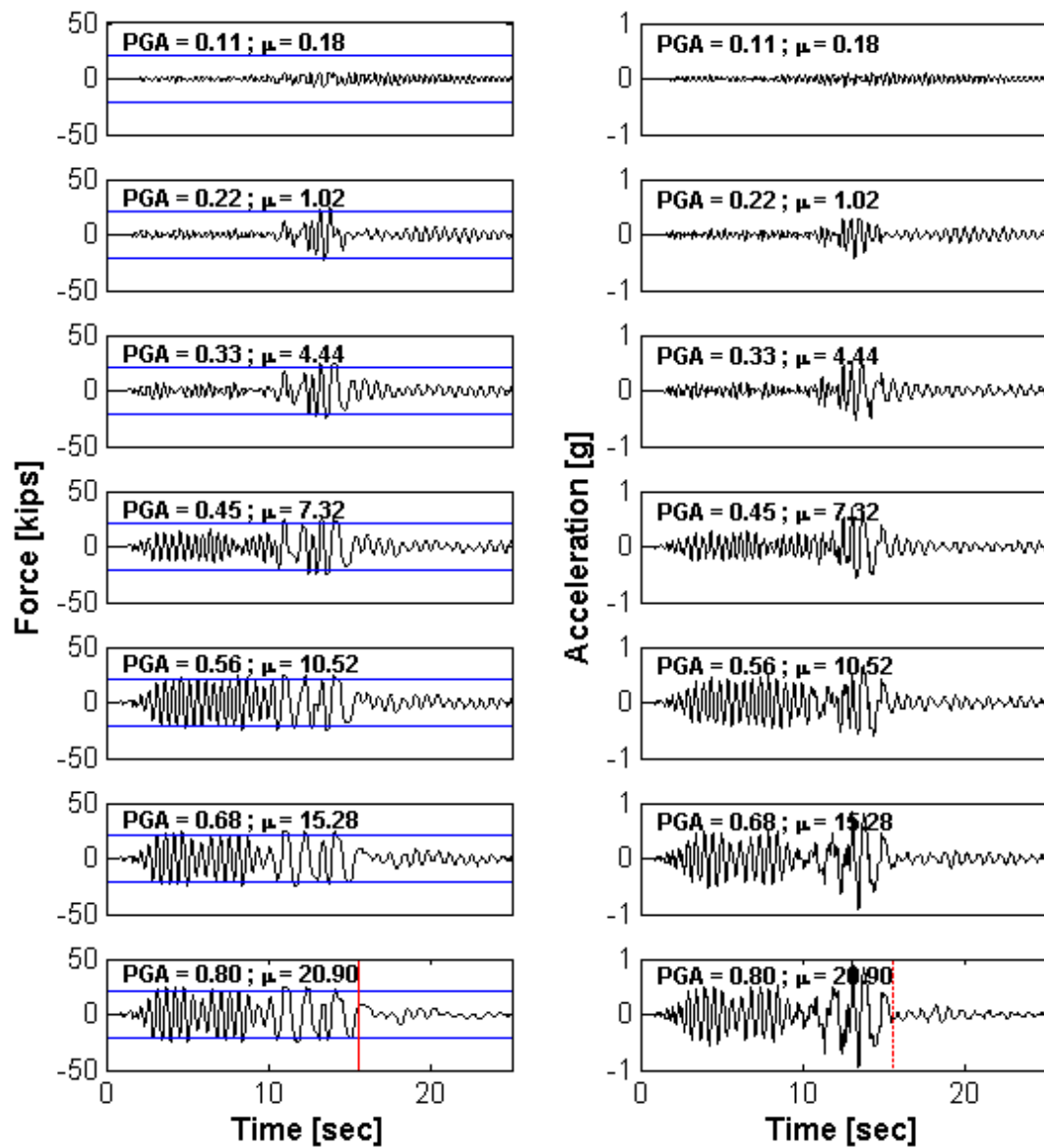


Figure 5-25: Force (left) and Acceleration (right) histories for different levels of PGA

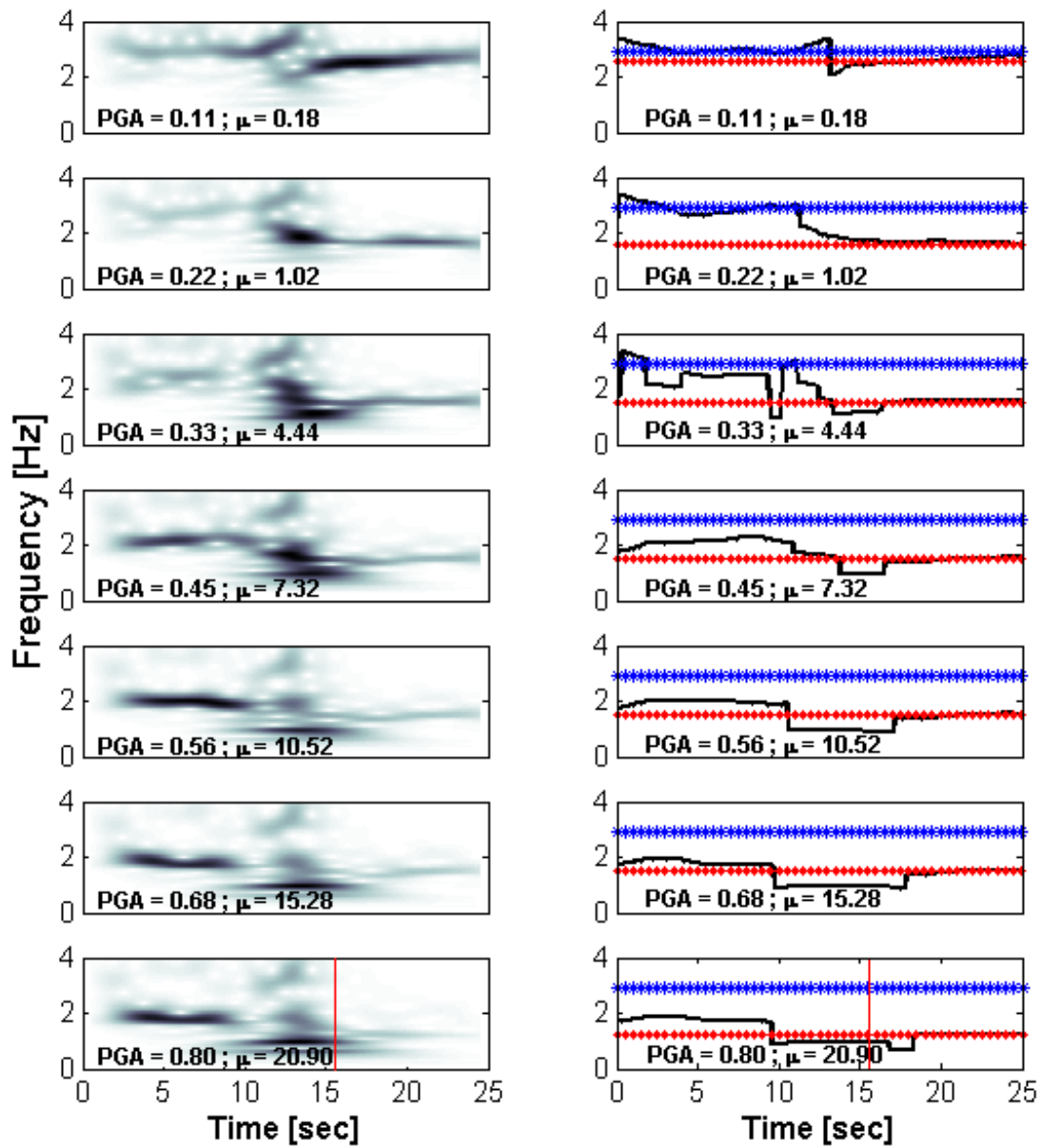


Figure 5-26: CWT - Low Frequency analysis

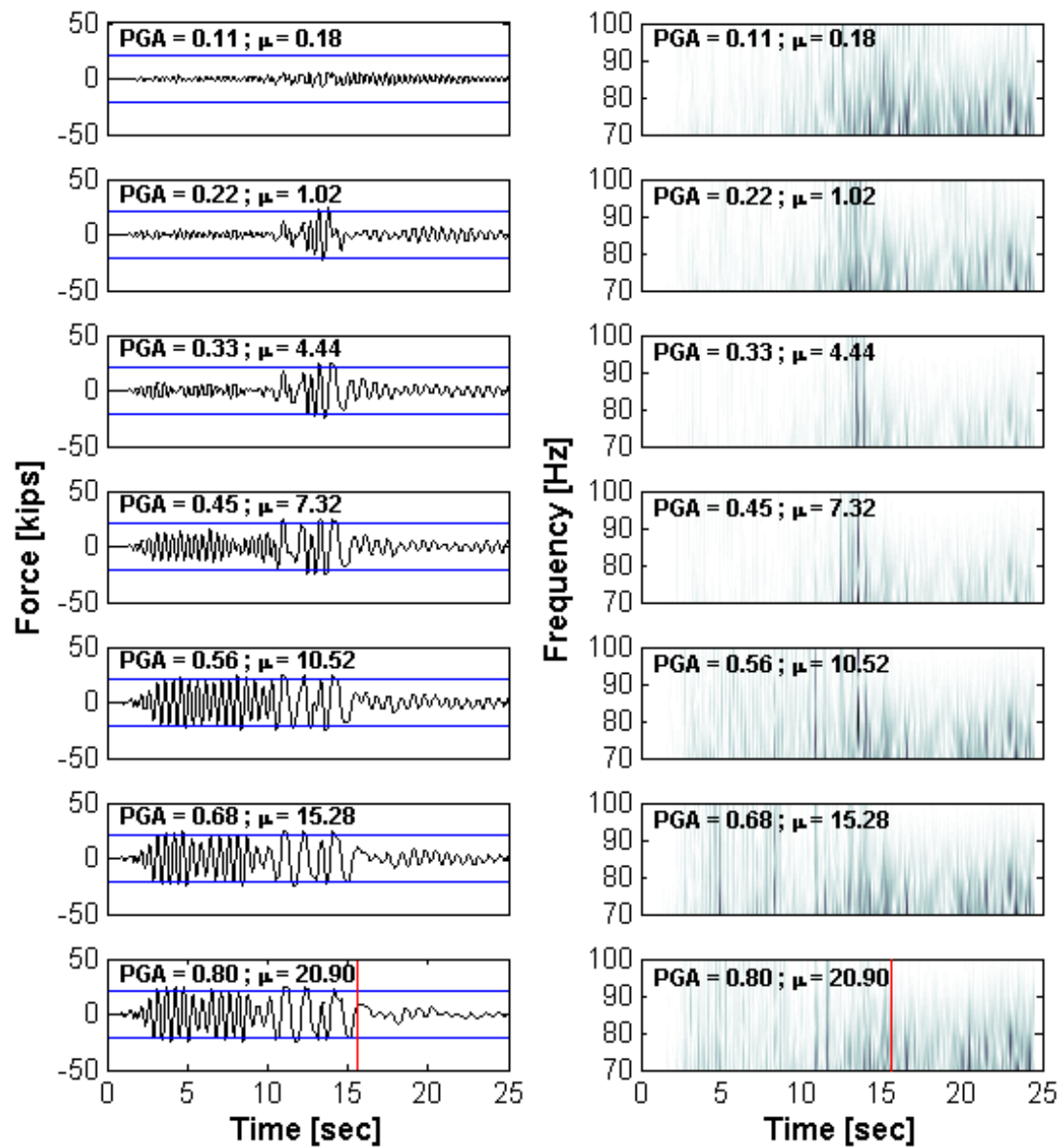


Figure 5-27: CWT - High Frequency analysis

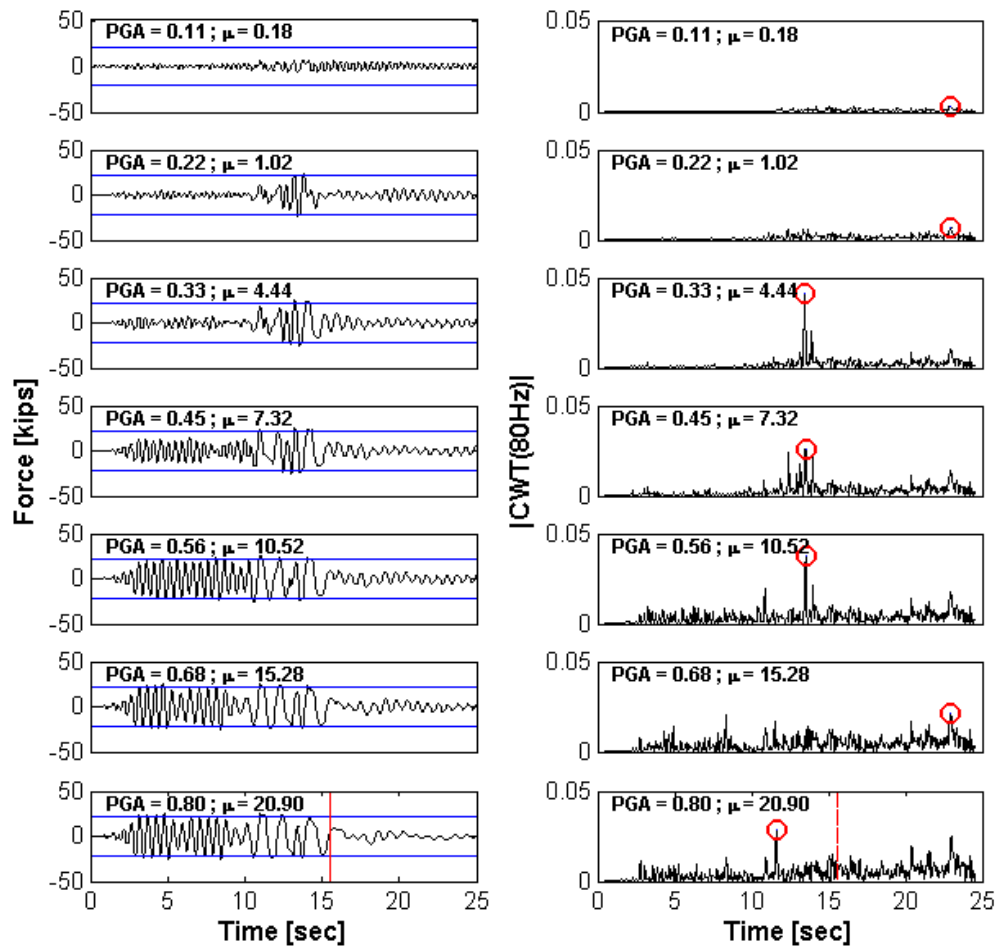


Figure 5-28: CWT - High Frequency analysis showing the coefficients for 80Hz

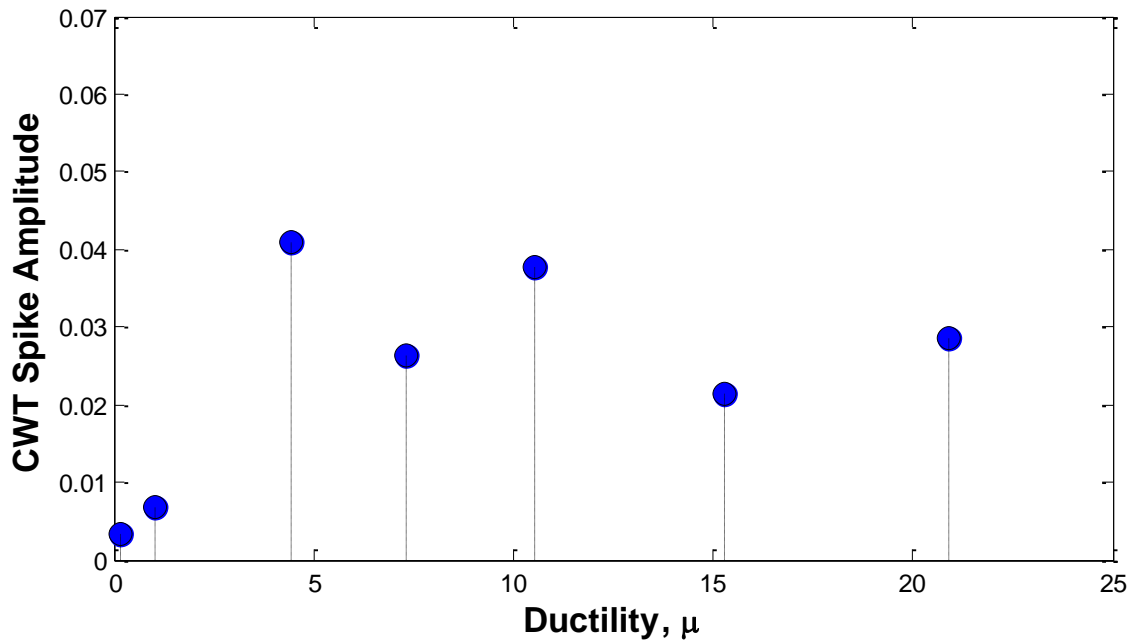


Figure 5-29: CWT Spike Amplitude vs Ductility

5.5.4 Whittier Narrows earthquake

Figures 5-30 to 5-37 present the results for the second earthquake analyzed on this study, i.e. the Whittier Narrows. Figure 5-33 presents the time when occurs the rebar fracture, i.e. around 20.6 seconds. The low frequency results are shown in Figure 5-34; notice that it was possible to identify the changes in frequency. However, such identification is not as clear as for the other cases, we believe due to interference of the frequencies proper of the earthquake. In the high frequency results shown in Figures 5-35 and 5-36 it completely fails in detects the yield instants. In addition, Figure 5-37 presents the CWT spike amplitude that again does not represent any relationship between the spikes amplitude and the level of damage induced.

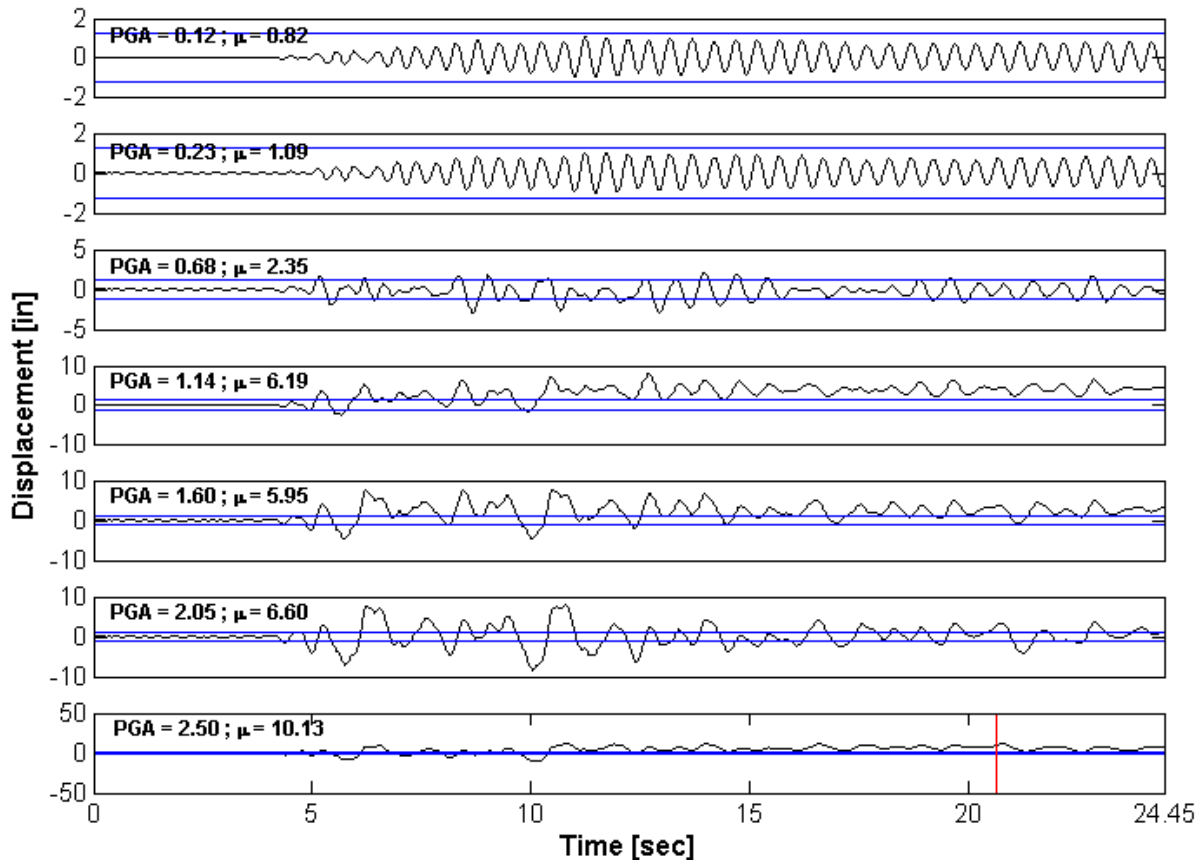


Figure 5-30: Displacement histories for different levels of ground motion intensities

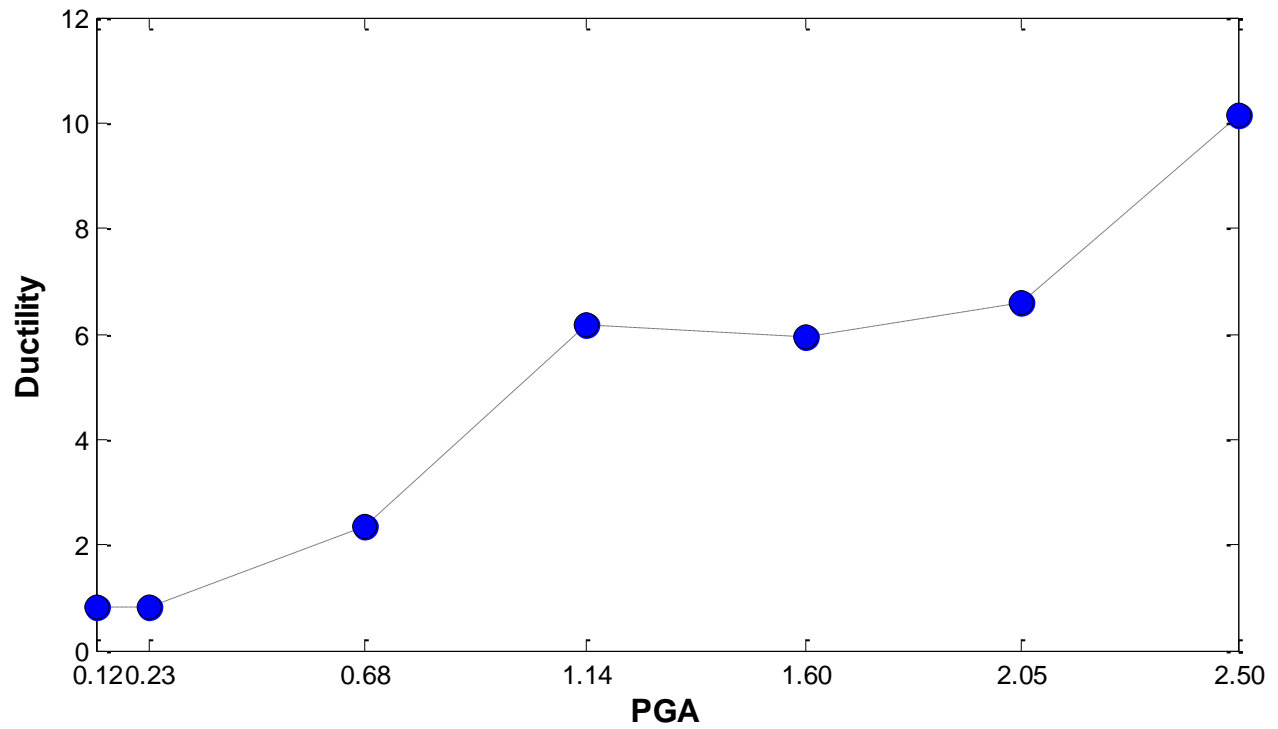


Figure 5-31: Loma Prieta EQ - Incremental Dynamic Analysis (IDA curve)

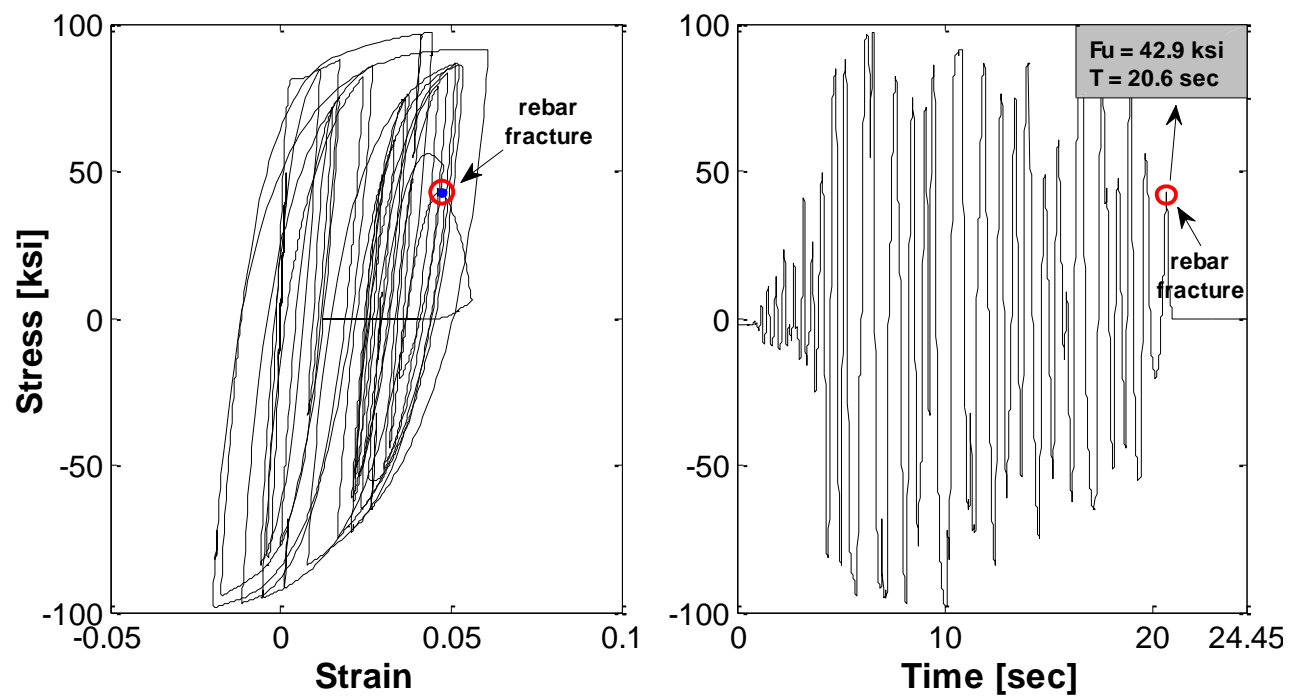


Figure 5-32: (a) Stress-Strain Relationship, (b) Stress-Time Relation

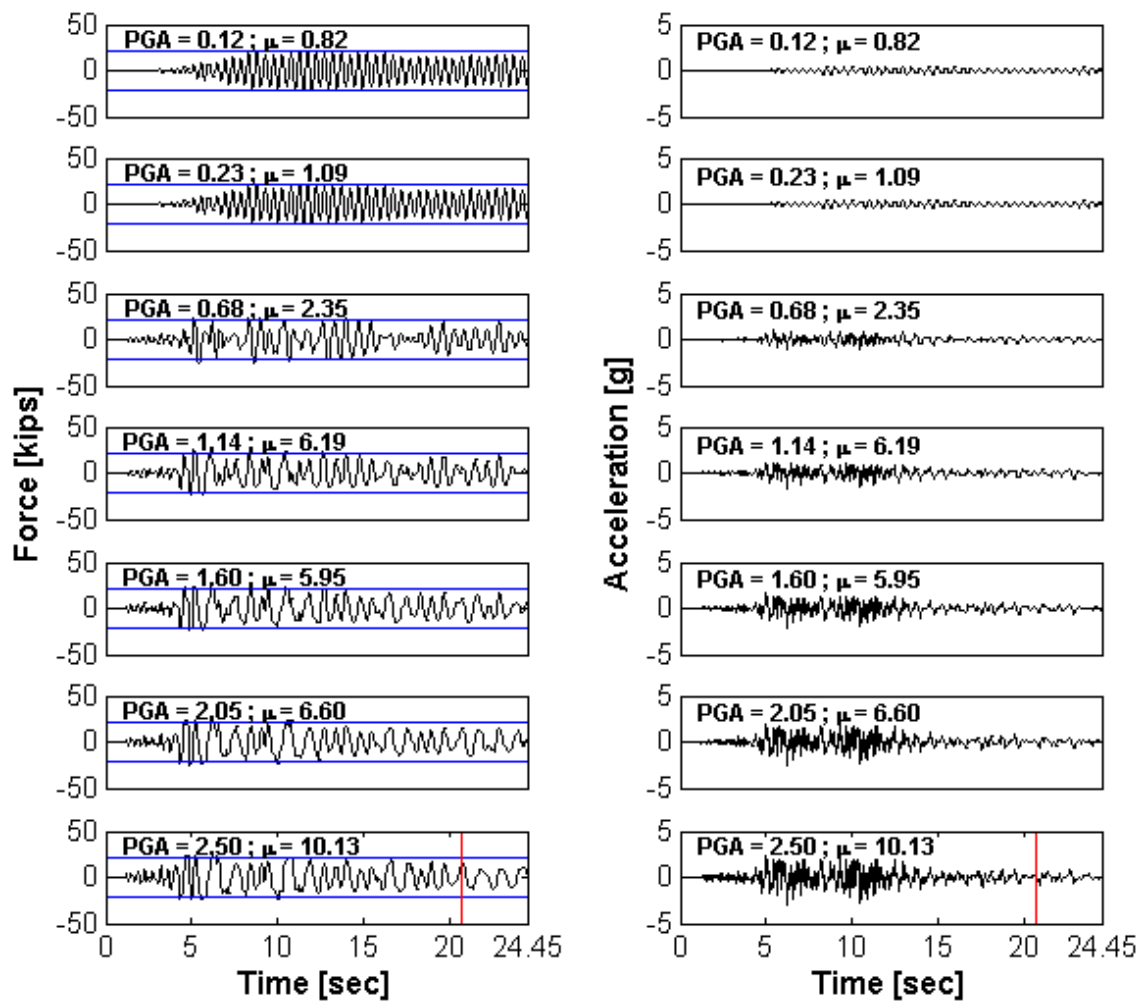


Figure 5-33: Force (left) and Acceleration (right) histories for different levels of PGA

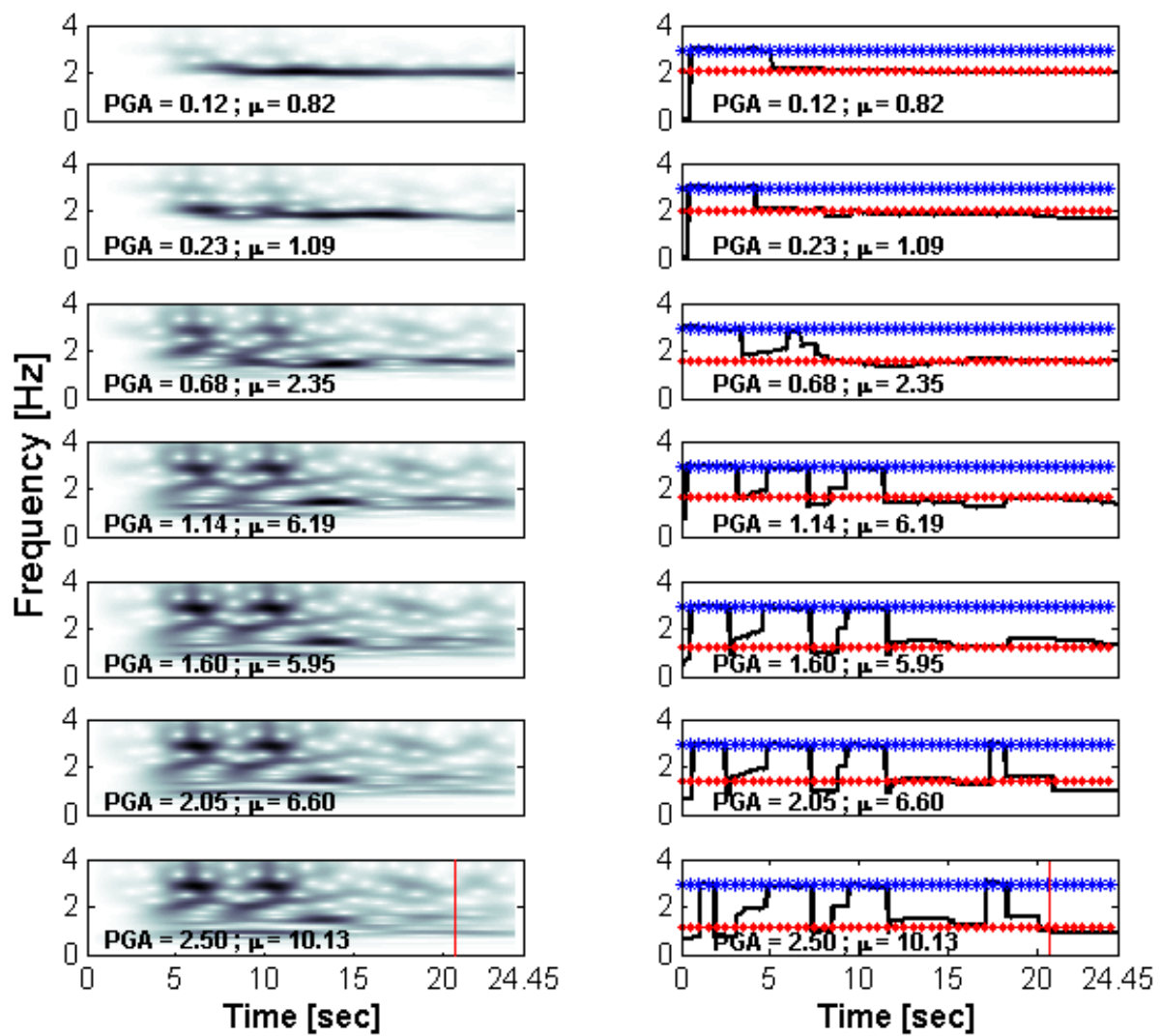


Figure 5-34: CWT - Low Frequency analysis

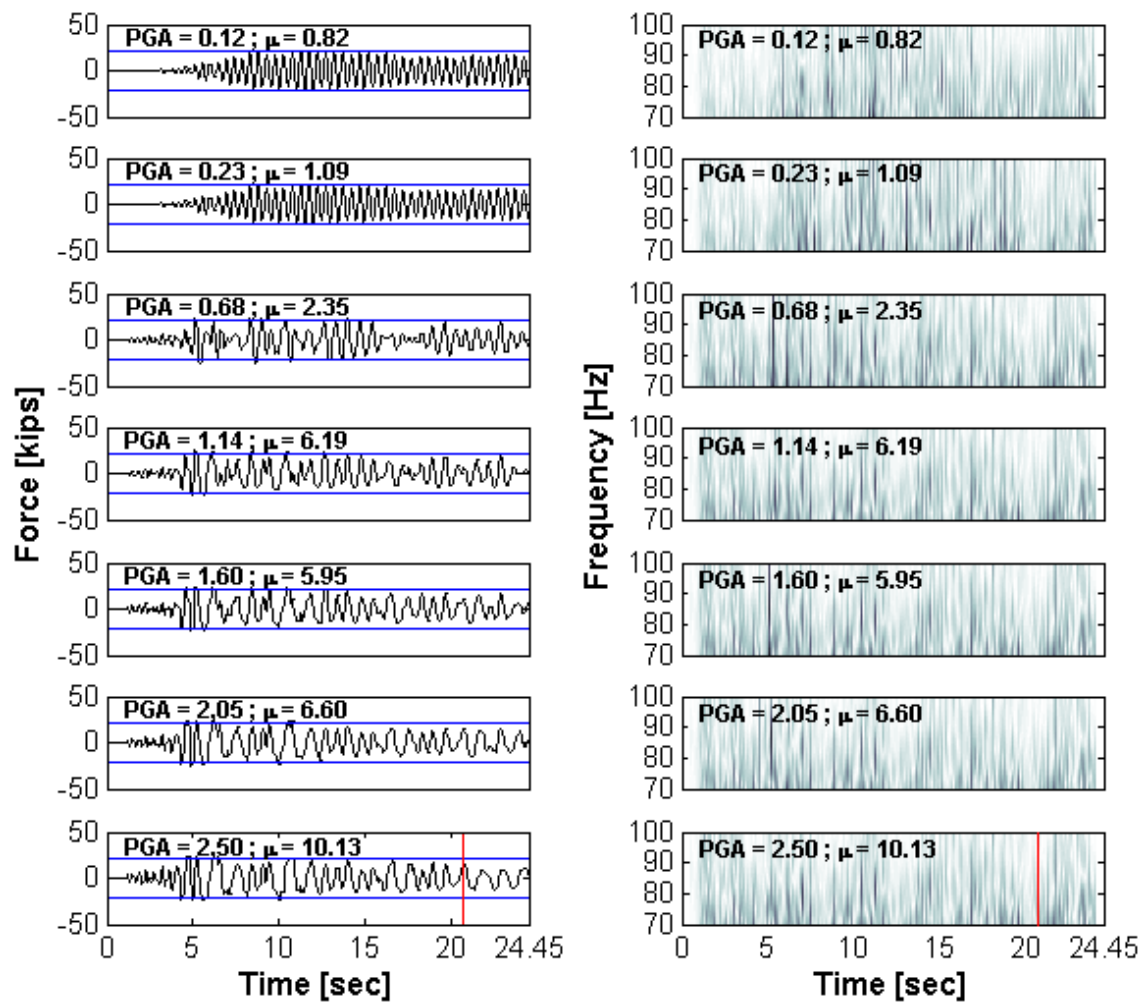


Figure 5-35: CWT - High Frequency analysis

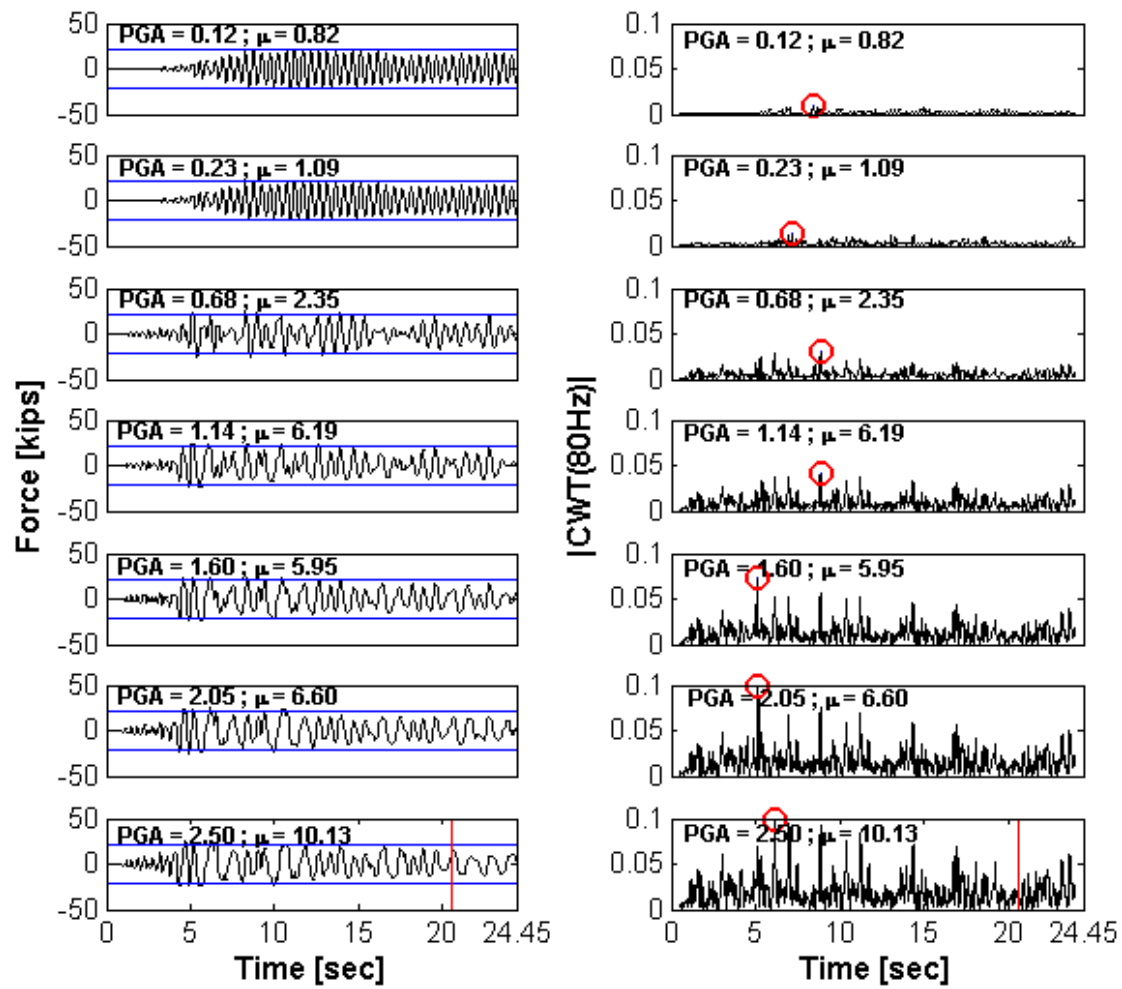


Figure 5-36: CWT - High Frequency analysis showing the coefficients for 80Hz

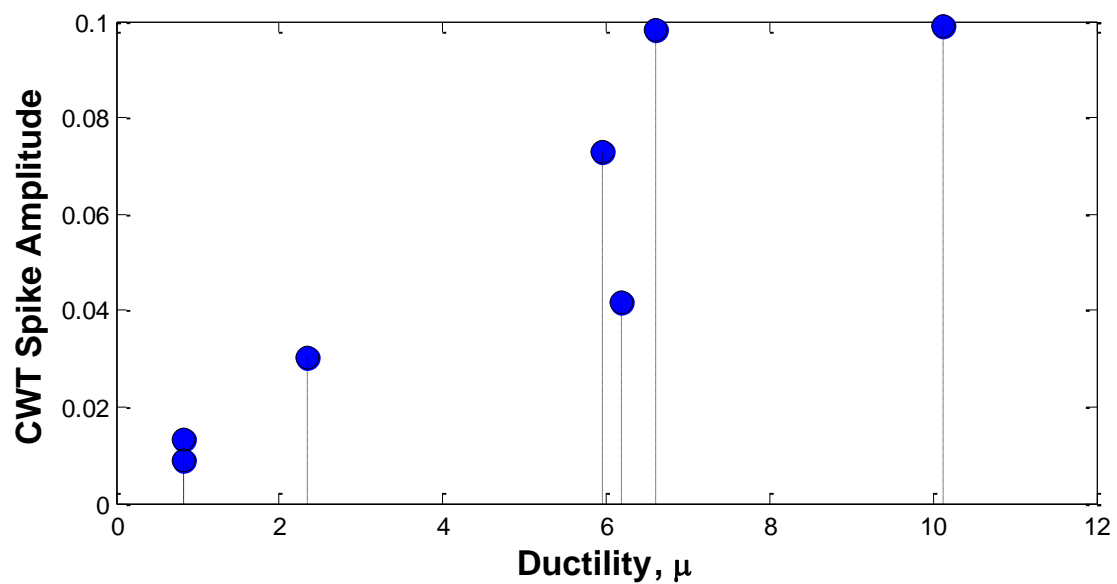


Figure 5-37: CWT Spike Amplitude vs Ductility

5.6 DWT analysis – Single Decomposition

This section presents the DWT results for the incremental dynamic analysis. Next are the results for the four excitation loads.

5.6.1 White Noise <20Hz

The results for the 20Hz white noise are shown in Figure 5-38. It can be note that is difficult to relate the yield instants from the force response in the DWT detail plots because there are a lot of spikes. However, for this particular dynamic excitation, the rebar fracture instant is clear (in the last PGA), being the higher peak (i.e. 13.3 seconds). In Figure 5-39 is plotted the maximum peak amplitude obtained from the DWT detail plots (each one identified with a circle). From this figure we can appreciate a pattern in which can be seen that while the level of ductility demand increases, the spikes amplitude also increases.

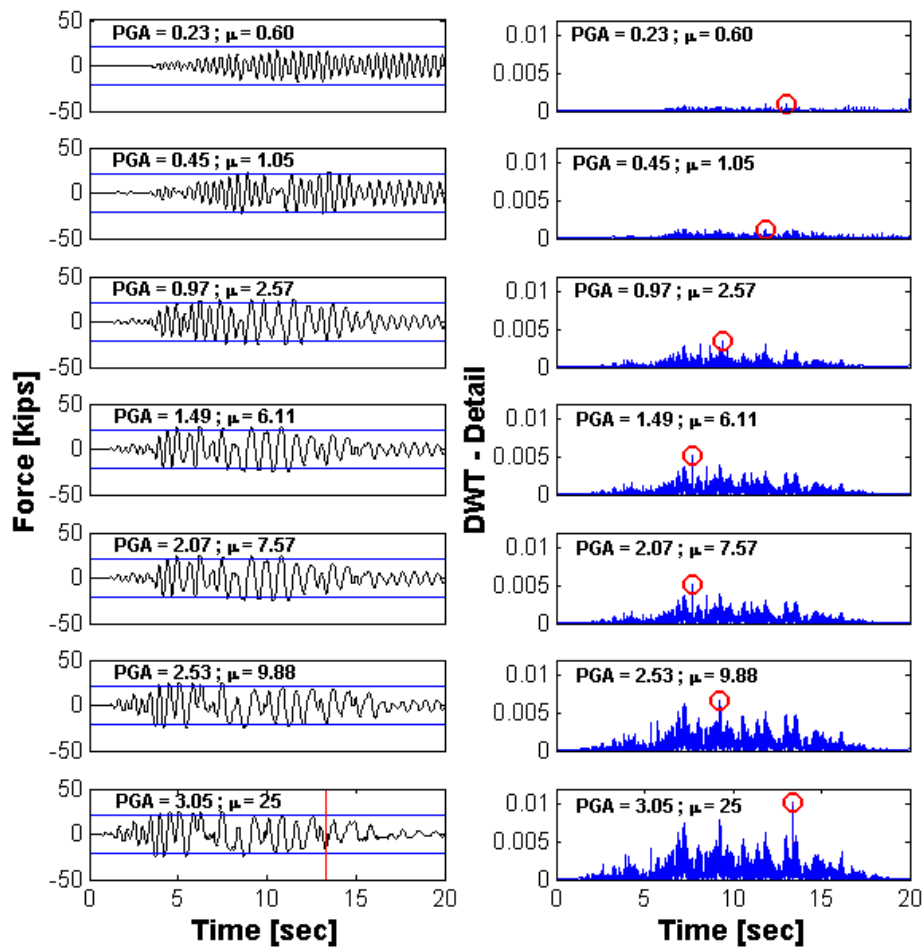


Figure 5-38: WN20 - Force histories (left) and DWT detail analysis (right)

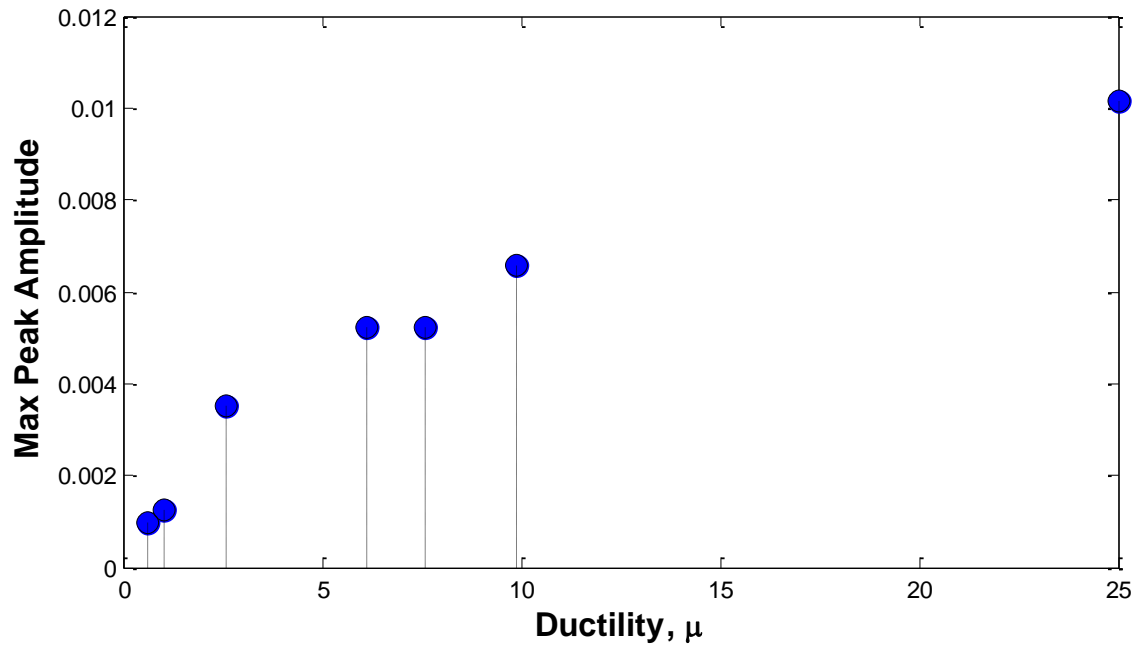


Figure 5-39: WN20 - Maximum Peak Amplitude vs Ductility

5.6.2 White Noise <40Hz

Figure 5-40 displays the results for the 40Hz white noise in which it is very difficult to identify the yield episodes due to the large amount of spikes appearing, many of them not related with the occurrence of inelastic action. Moreover, the higher peak for all the cases is at the middle (i.e. 10 seconds approximately); however, the rebar fracture occurs at 14.7 seconds.

Figure 5-41 shows the relationship between the spikes amplitude with the level of induced damage. Looking at the figure, it is note that as the ductility increases, the spikes amplitude also increases; having a similar pattern like in the previous excitation load (i.e. the 20Hz white noise). It should be note that these results are different than the obtained from the CWT analysis.

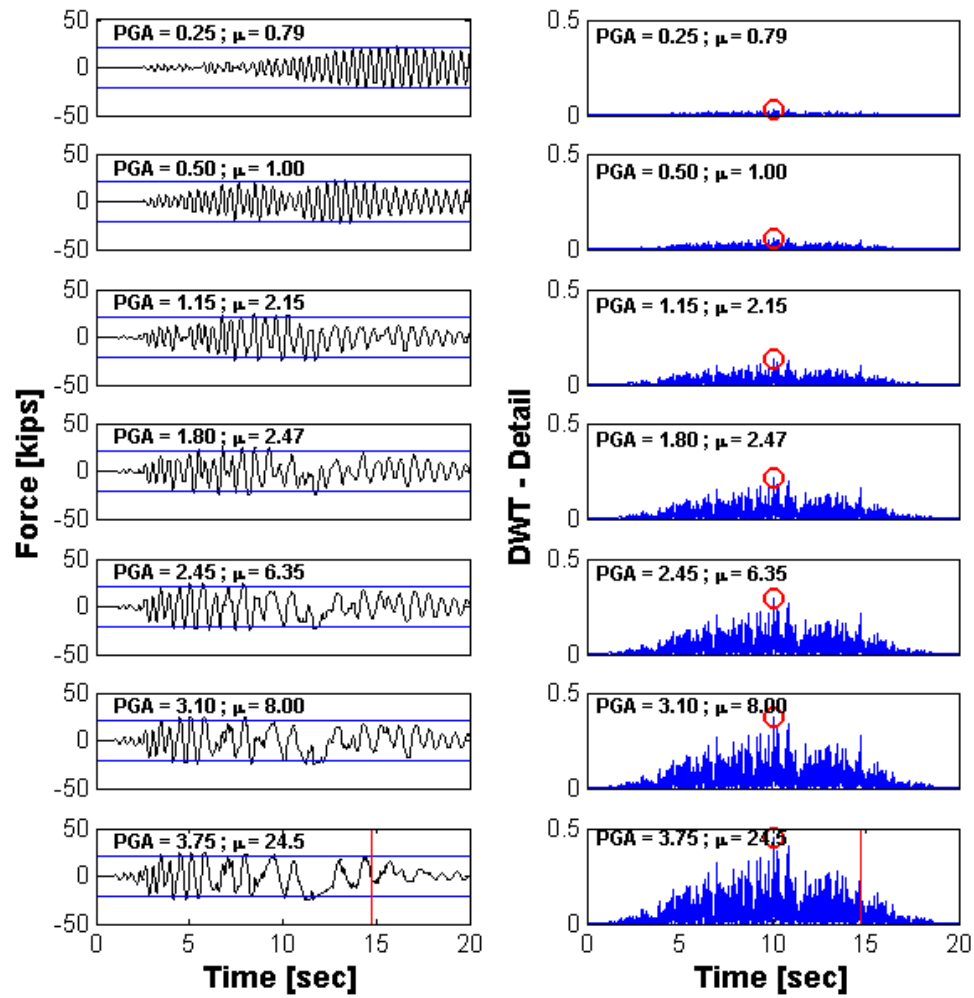


Figure 5-40: WN40 - Force histories (left) and DWT detail analysis (right)

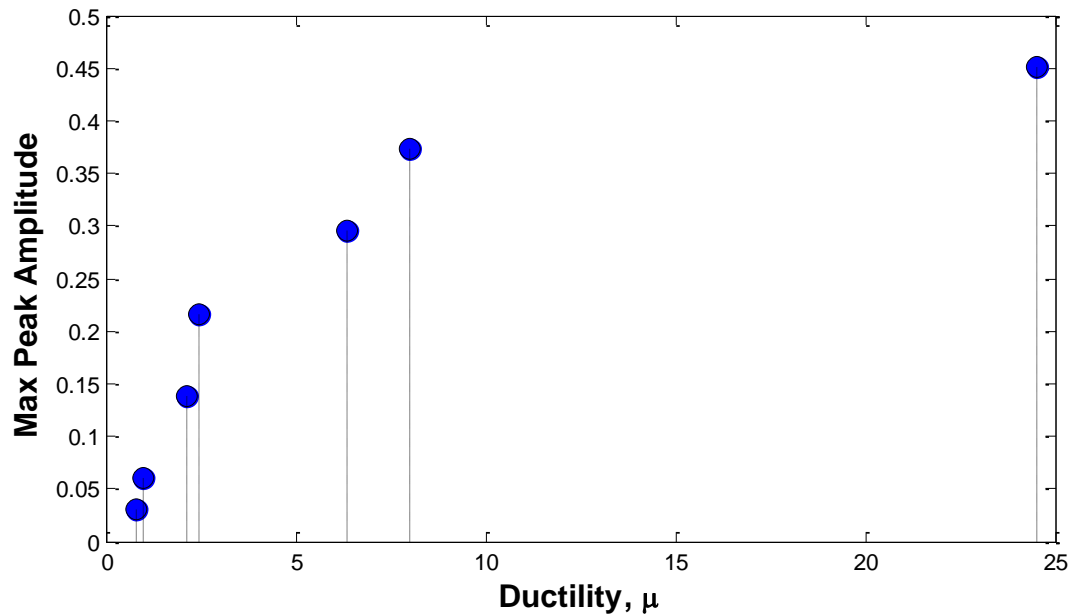


Figure 5-41: WN40 - Maximum Peak Amplitude vs Ductility

5.6.3 Loma Prieta earthquake

Figure 5-42 illustrates the DWT detail results for the narrow-band record. If we see the force responses we can appreciate that the yield instants are at the middle of the force histories and they were identified in the DWT detail plots. However, looking at the Figure 5-43, it can be note that there is no relationship between the spikes amplitude and the level of damage induced.

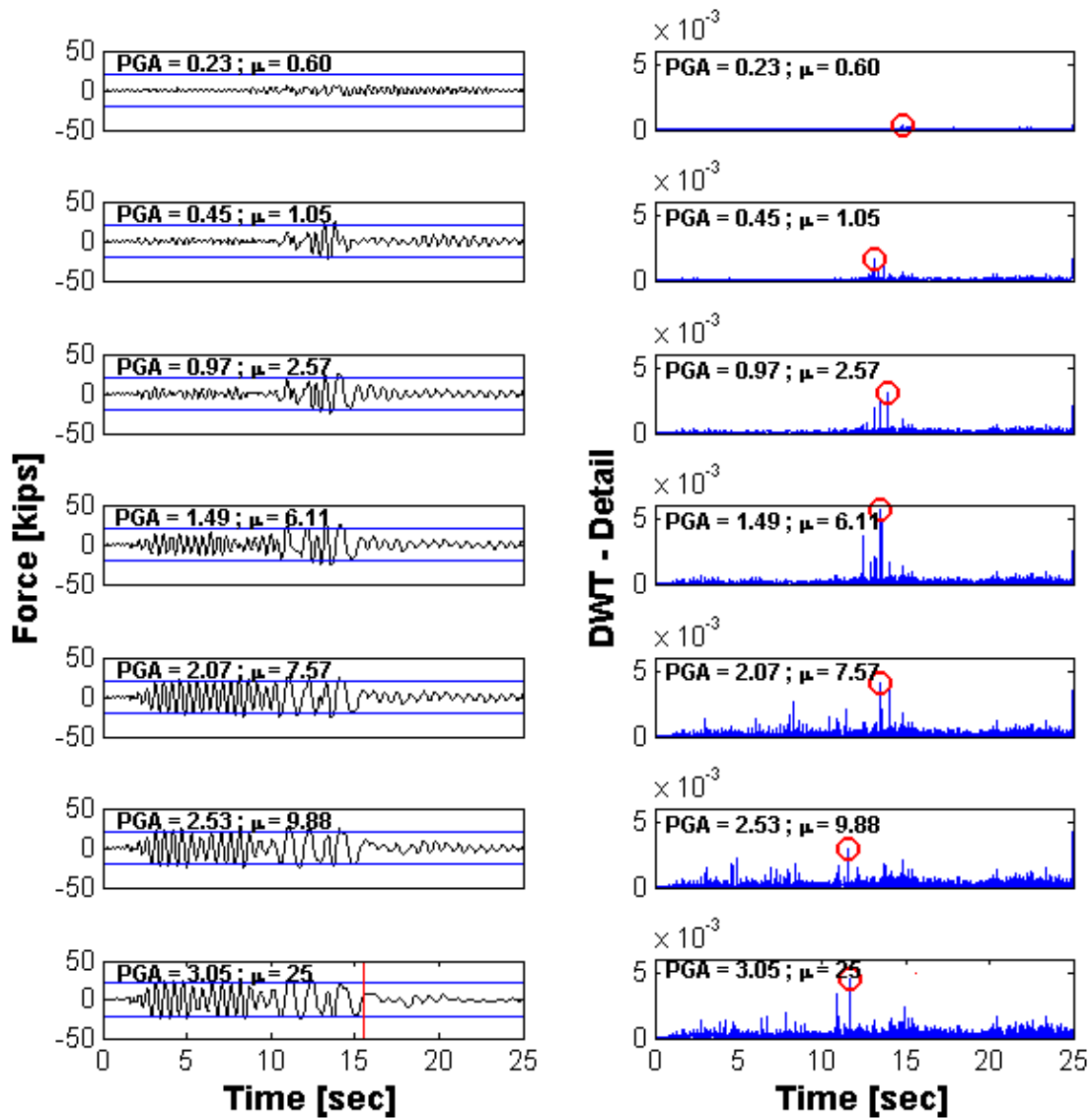


Figure 5-42: Loma Prieta EQ - Force histories (left) and DWT detail analysis (right)

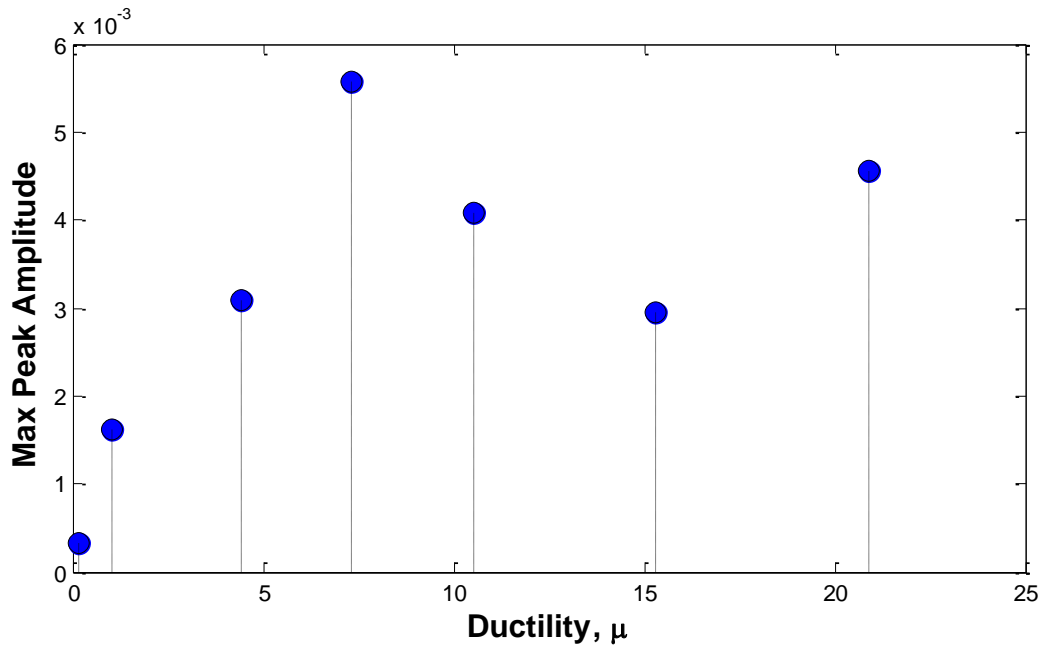


Figure 5-43: Loma Prieta EQ - Maximum Peak Amplitude vs Ductility

5.6.4 Whittier Narrows earthquake

Figure 5-44 shows the results for the wide-band record. It is evident that more spikes are displayed in the DWT detail plots in comparison with the narrow-band record (i.e. Loma Prieta earthquake). Once again the premise of try to get any relationship in the spikes amplitude is rejected by the results in Figure 5-45.

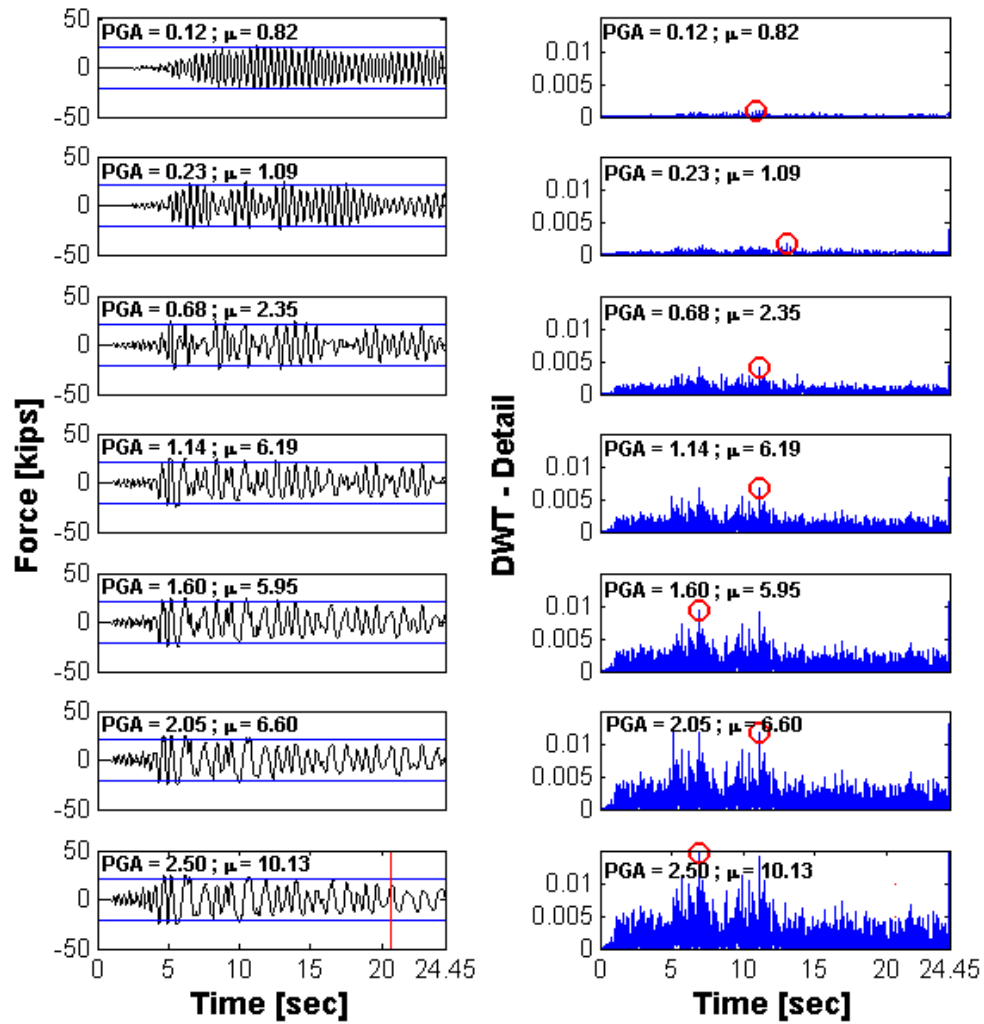


Figure 5-44: Whittier Narrows EQ - Force histories (left) and DWT detail analysis (right)

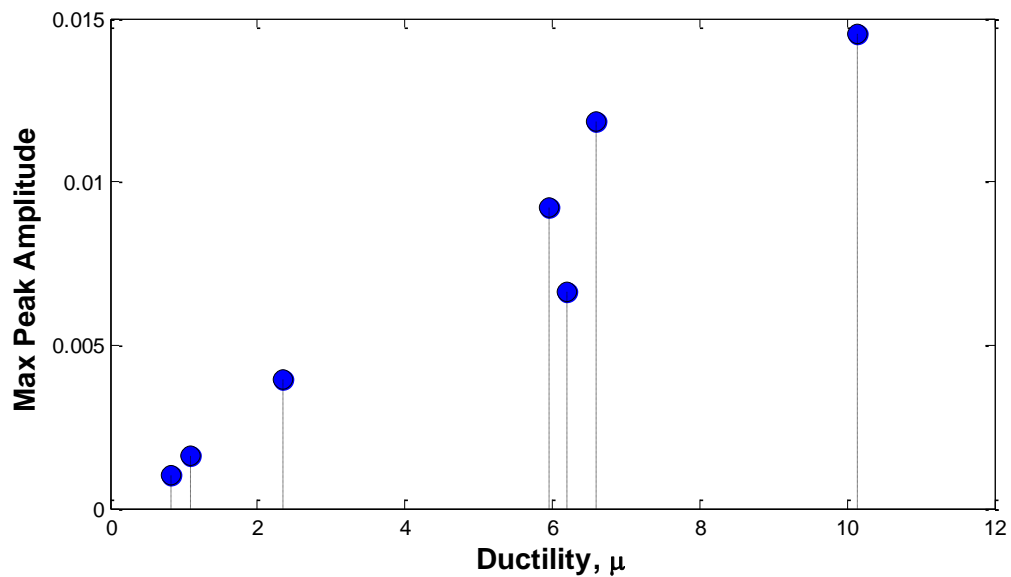


Figure 5-45: Whittier Narrows EQ - Maximum Peak Amplitude vs Ductility

5.7 DWT analysis – Wavelet Package Decomposition

This section shows a Wavelet Package Decomposition (WPD) for the DWT analysis. This decomposition will be performed up to level 3 and only the detail part will be illustrated. As part of the analysis, just the results for the last ground motion intensity (when rebar fracture is present) will be displayed in the sake of brevity. The objective of carry out the WPD is to verify if the high frequencies coming from the excitation can be reduced or removed to stand out the yield instants (or damage events).

Figure 5-46 shows the WPD results for the 20Hz white noise excitation. In the original signal, the time instant when rebar fracture occur is represented with a vertical dash-dotted line. It is appreciate that when the level decomposition goes up, the DWT detail amplitude decrease. In the level 1, we can see the spike corresponding to rebar fracture, but when we decompose up to level 2 and then level 3, this spike becomes to vanish. Hence, no good results were obtained applying the WPD. As consequence, we do not present the other signals decomposition.

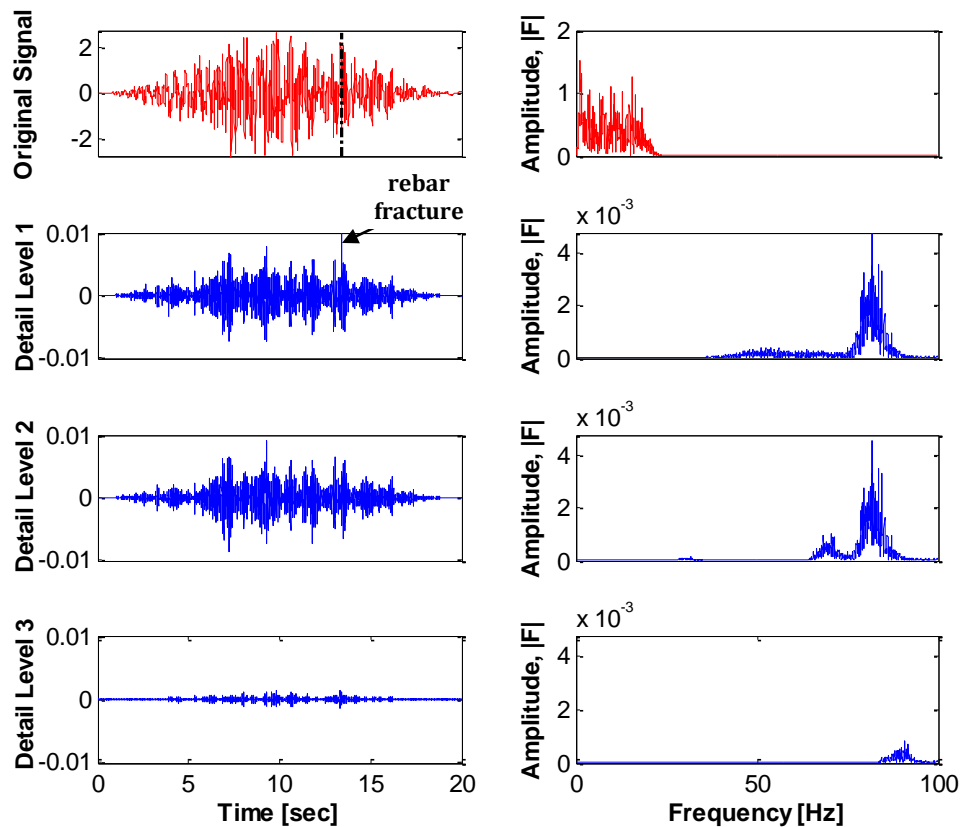


Figure 5-46: WN20 - DWT Detail Decomposition (left) and the Fourier Spectrum (right)

5.8 Proposed Refinements

The proposed refinements aim to isolate the spikes that correspond to yield events (or damage instants) and remove the large amount of spurious peaks that make difficult an explicit identification of the damage instants. In the majority of the cases this interference comes from the base excitation. To avoid the identification of spurious peaks a threshold criterion is adopted, first the spikes (r) at each time instant (j) are normalized according to the rule:

$$z_j = \frac{r_j + \bar{x}}{\sigma} \quad (5-2)$$

where,

\bar{x} : mean of the spike values

σ : standard deviation of the spike values

Any instant (j) where the normalized value (z) is larger than 2 (i.e., the ratio deviates more than 2 standard deviations from the mean value) is treated as a damage instant. An example of the proposed methodology is shown in Figure 5-47. Figure 5-47a presents the results for a CWT analysis performed at high frequencies; the coefficients for the 80Hz frequency are shown. Figure 5-47b illustrates the same plot, but showing the mean (presented with a dotted line), and with a dotted red line, the limit at which we obtained the peaks that principally correspond to the damage instants. Five peaks were identified on this plot. Figure 5-47c shows the result of applying this technique.

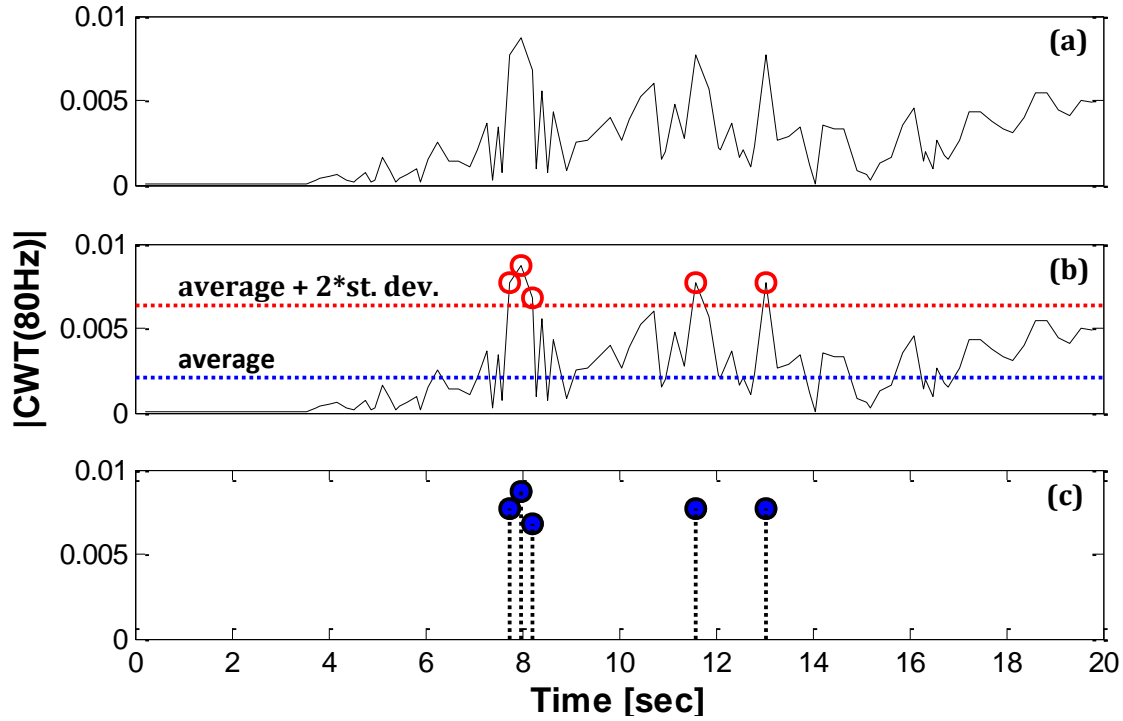


Figure 5-47: (a) CWT coefficients for 80Hz, (b) Proposed methodology, (c) Final results

5.9 CWT analysis – High Frequency

This section presents the CWT results for the proposed methodology refinement previously shown. Each dynamic excitation shows three figures. First, the force response history for the different levels of excitation is compared with the high frequency analysis; the next figure is the same, but now comparing it with the CWT coefficients from 70 to 100Hz. Finally, a 3 plots figure is shown in which the results corresponding to the last ground motion intensity (when rebar fracture is present) are displayed.

5.9.1 White Noise <20Hz

Figure 5-48 and 5-49 display the results obtained for wn20, the first figure is “top view” of the spikes, while the second one is a “front view” where the amplitude of the spikes can be appreciated. We can perceive that the lower peaks were eliminated, allowing a better identification of the yield instants in the column. Figure 5-50 clearly shows the instant (i.e. 13.3 seconds) where rebar fracture occurs. The time instant is evident since it is present

though all the frequency content. Therefore, good results were obtained using the proposed refinement since it was able to clear some spikes in order to have a better damage identification in the column.

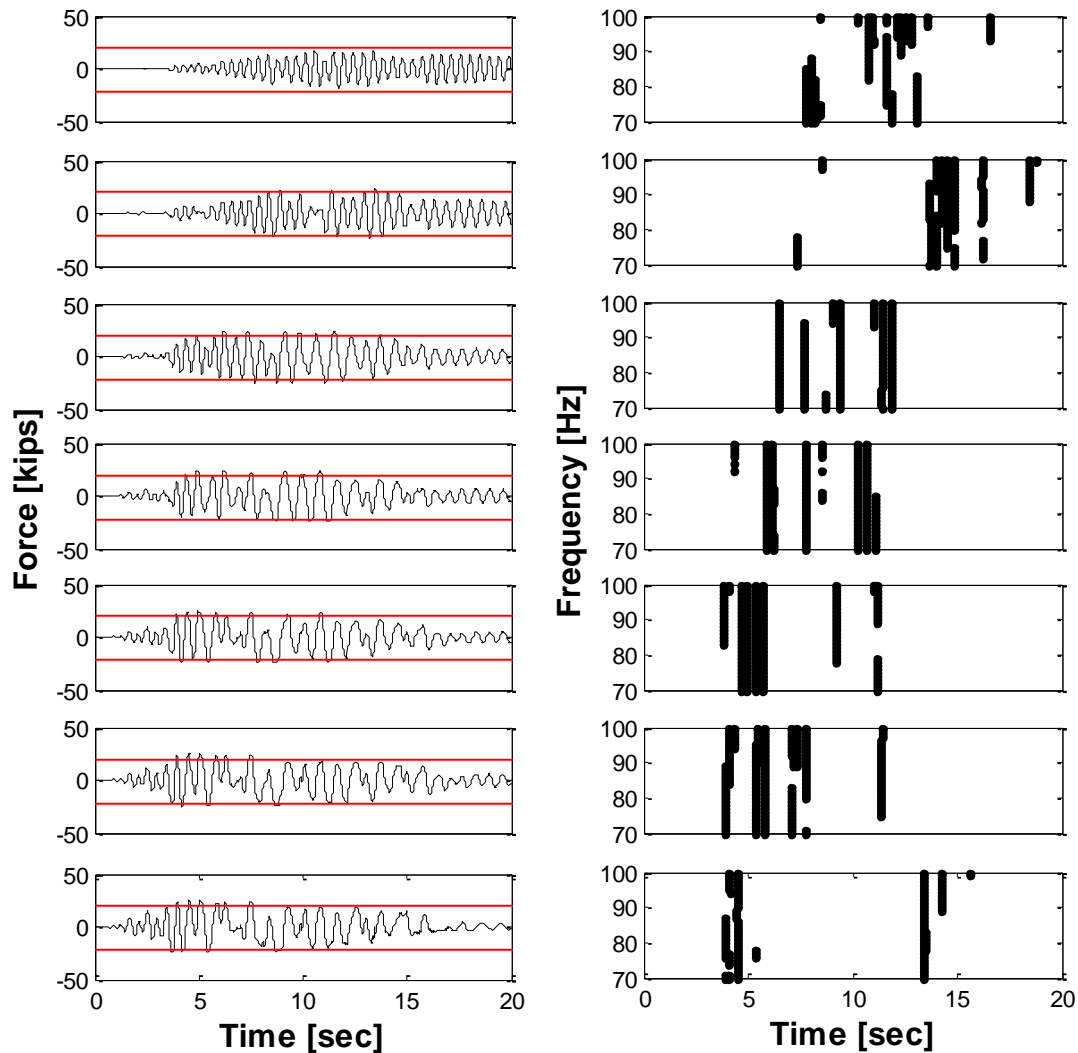


Figure 5-48: WN20 - Force histories (left) and CWT High Frequencies (right) for different PGA

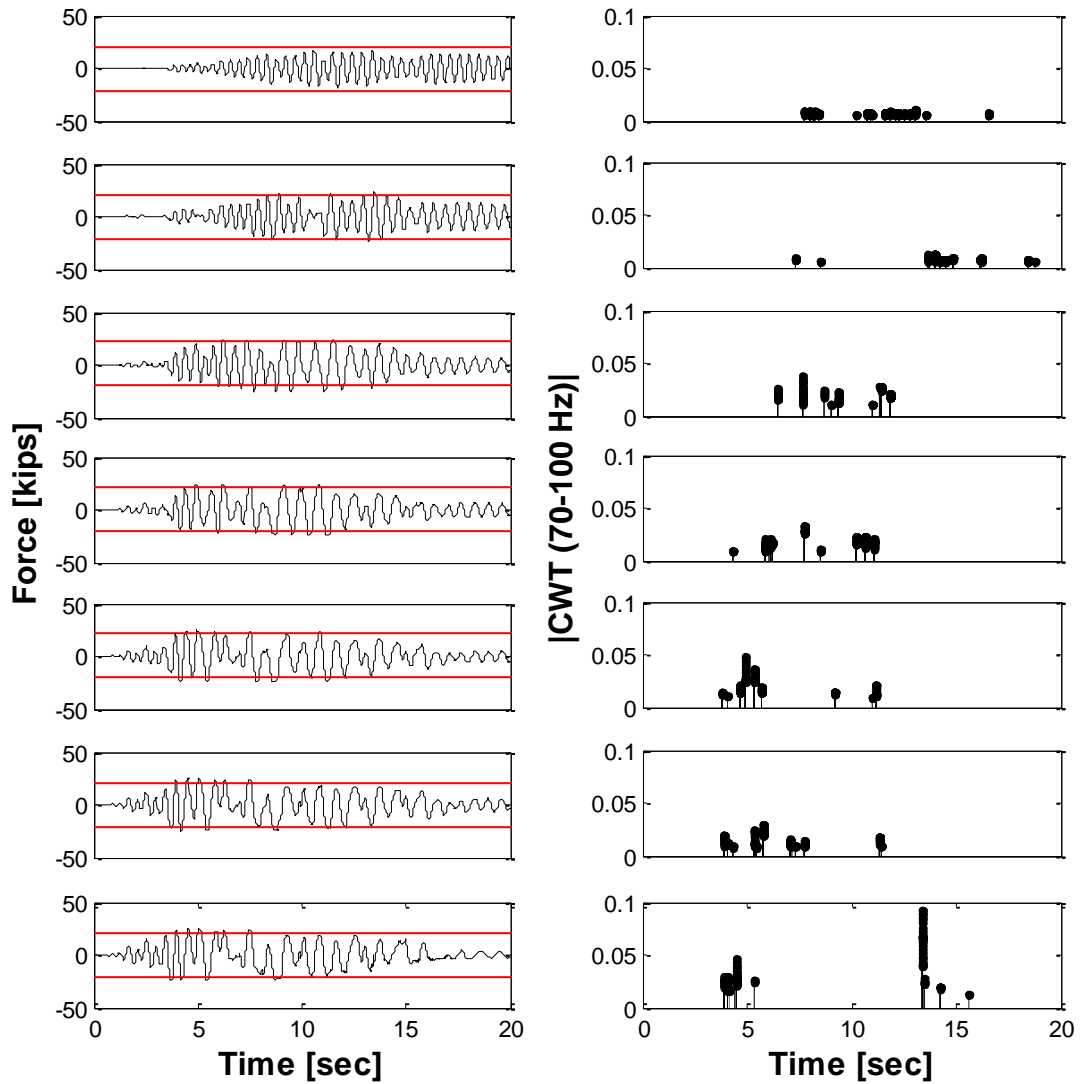


Figure 5-49: WN20 - Force histories (left) and High Frequency coefficients (right) for different PGA

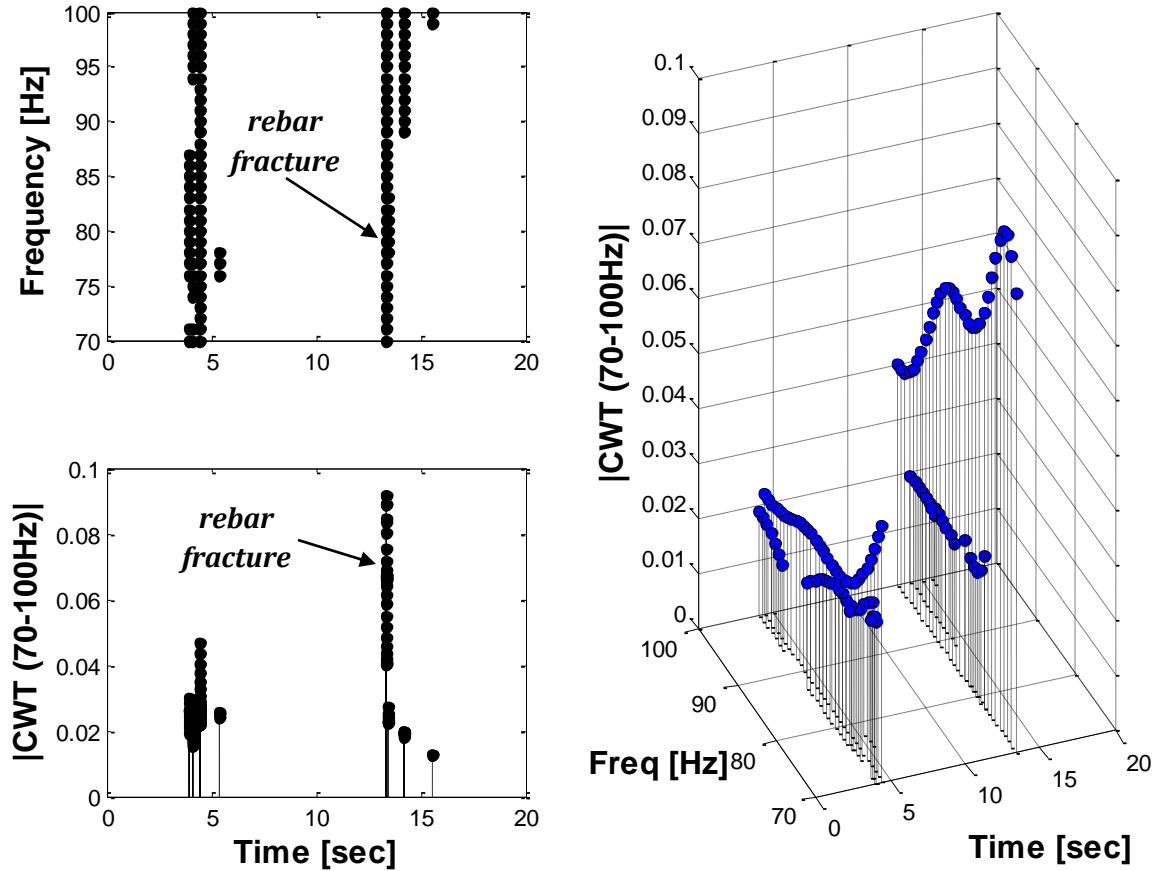


Figure 5-50: WN20 - (a) High Frequency analysis, (b) CWT coefficients, (c) 3D plot

5.9.2 White Noise <40Hz

Figures 5-51 and 5-52 illustrate the results for the 40Hz white noise dynamic excitation. Like in the previous excitation, the results presented for this dynamic load were “cleaned” with the suggested refinement and it was identify the time instant where the damage took place. The time instant where the rebar fracture occurred was around 14.7 seconds. From Figure 5-53, we can appreciate a frequency content from 90 to 100Hz is present at 14 seconds approximately (i.e. 0.7 seconds before the fracture occurs). In other words, we can associate this yield instant as the culprit of the fracture instant. Hence, we can say that the proposed refinement gave good results by allowing a more clear identification of the damaging instants for the two white noises excitation loads.

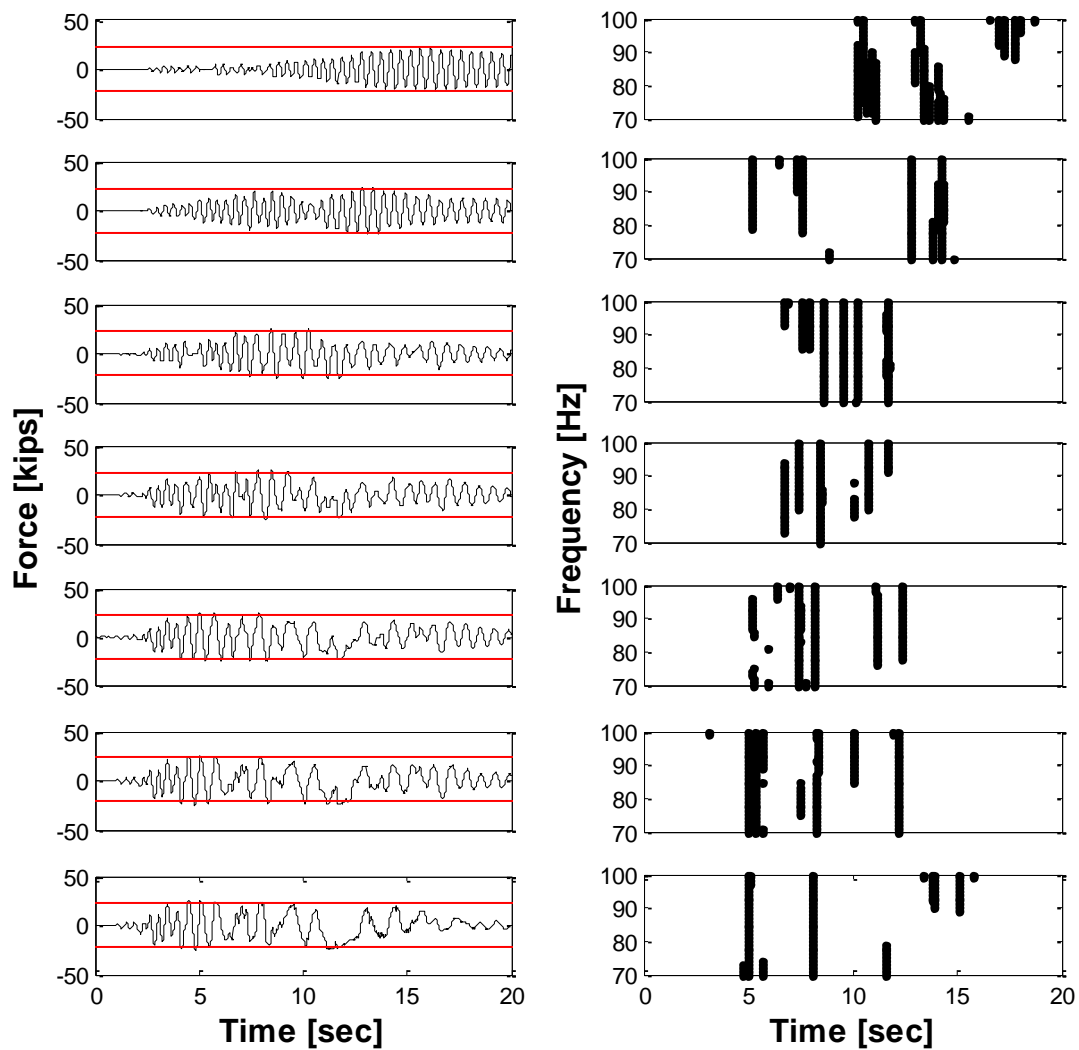


Figure 5-51: WN40 - Force histories (left) and CWT High Frequencies (right) for different PGA

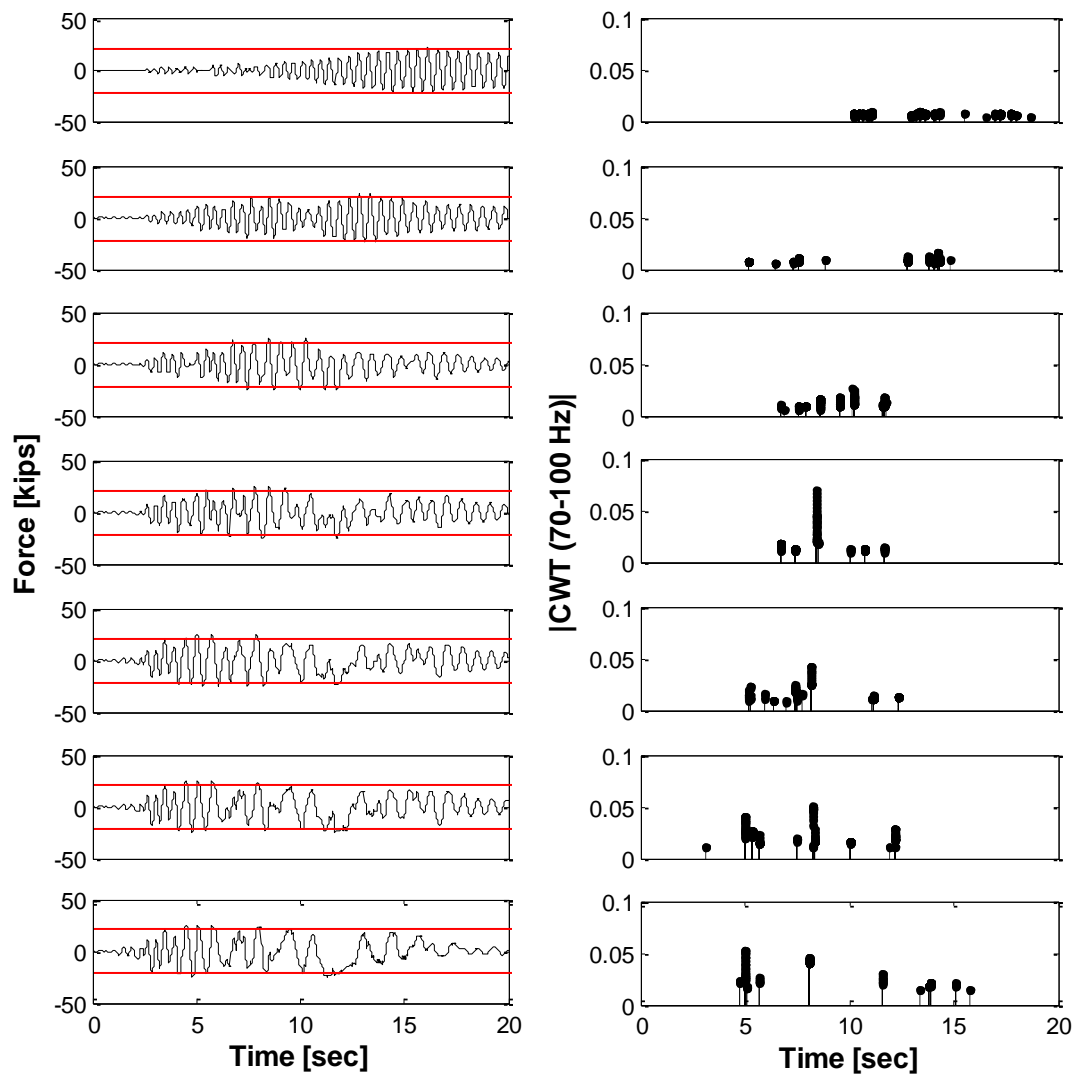


Figure 5-52: WN40 - Force histories (left) and High Frequency coefficients (right) for different PGA

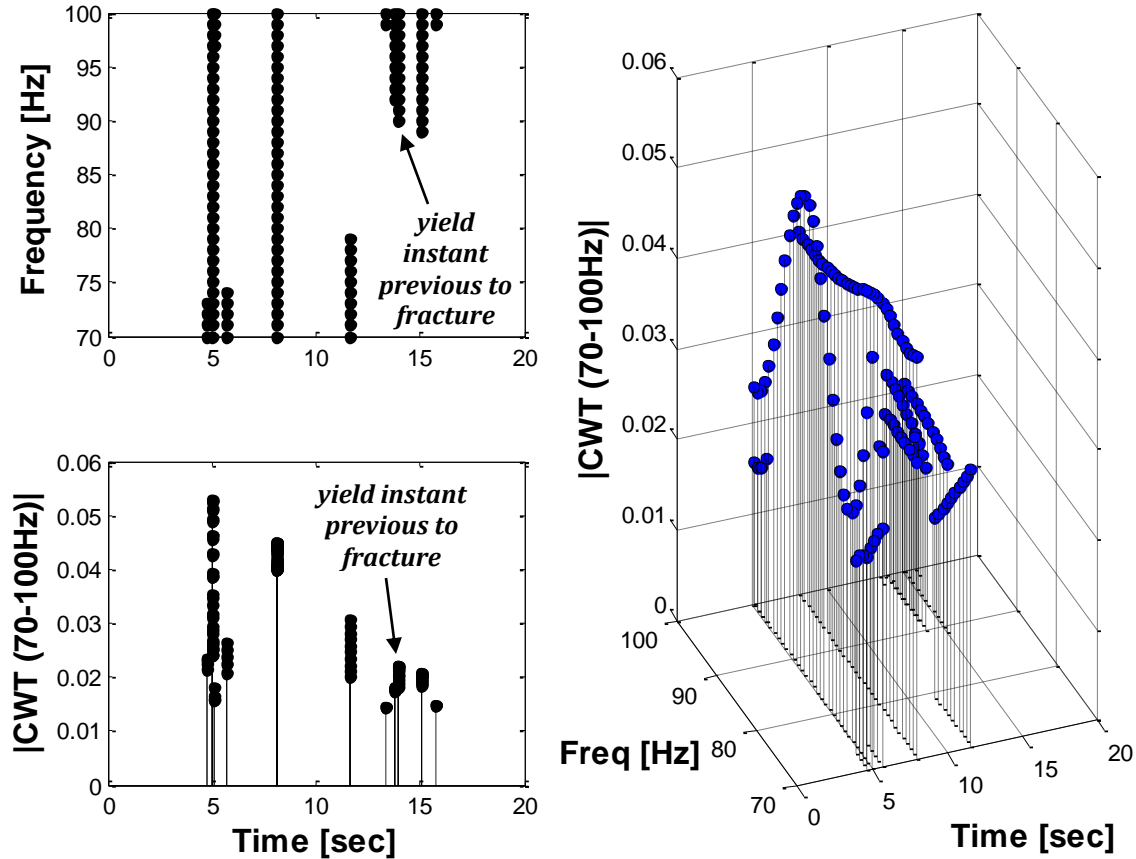


Figure 5-53: WN40 - (a) High Frequency analysis, (b) CWT coefficients, (c) 3D plot

5.9.3 Loma Prieta earthquake

Next we present the results for the narrow-band record in Figures 5-54 and 5-55. From these figures, we can appreciate that the trends are concentrated at the middle for the first four cases. After these cases, the next ones begin to scatter through the entire time domain. If we take a look, there are no trends for the firsts 10 seconds due to the absence of yield episodes in the force response plots. This is good for the methodology since it was able to remove some little peaks that were present before the application of this technique. For example, we can see this argument by comparing the Figure 5-28 with the Figure 5-54.

The rebar fracture was captured once again (Figure 5-56), this time was for frequencies between 72 and 80 Hz approximately. However, notice that some trends are present (from 20 to 25 seconds) without any kind of yield instants in the force response, but remember

that this methodology take into account a parameter (z_j) that can be changed in order to eliminate those points.

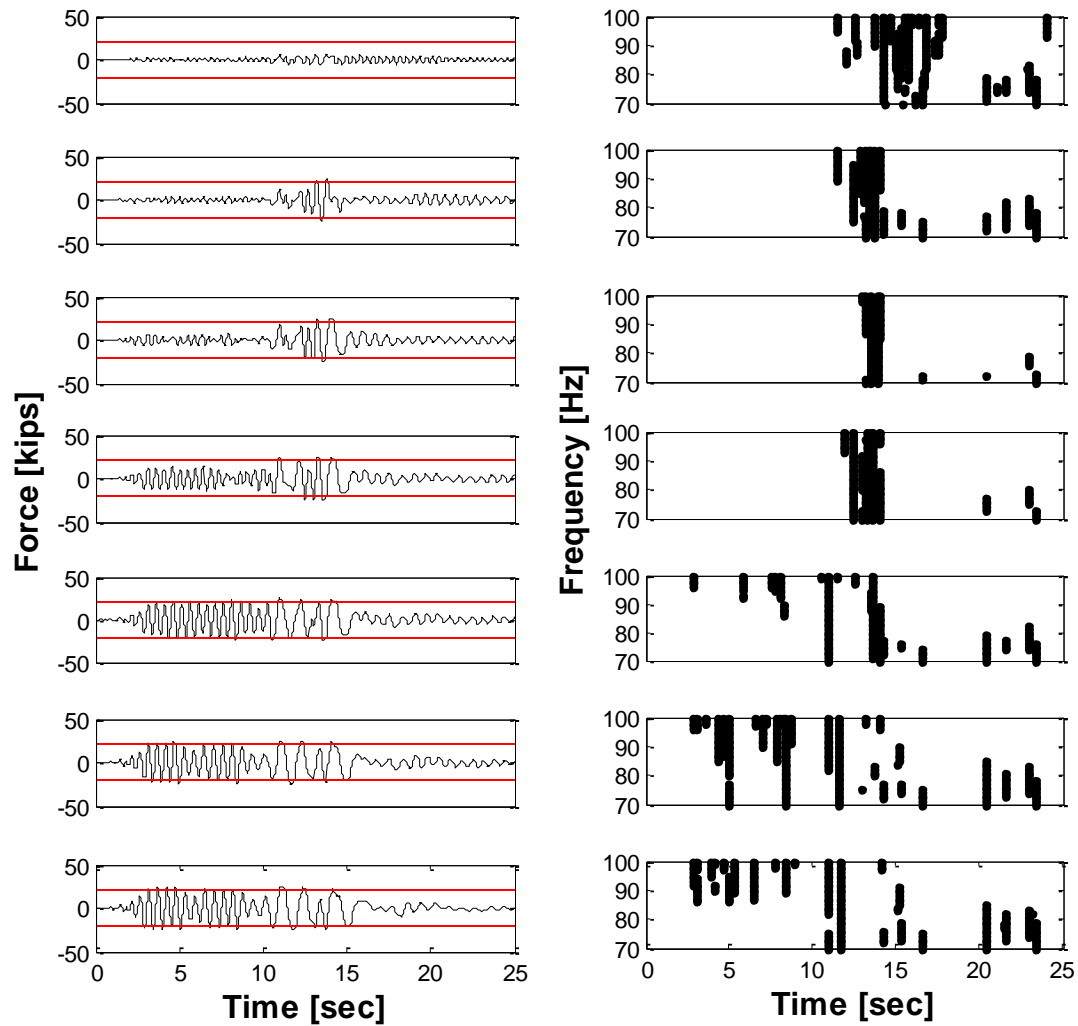


Figure 5-54: Loma Prieta EQ - Force histories (left) and High Frequencies (right) for different PGA

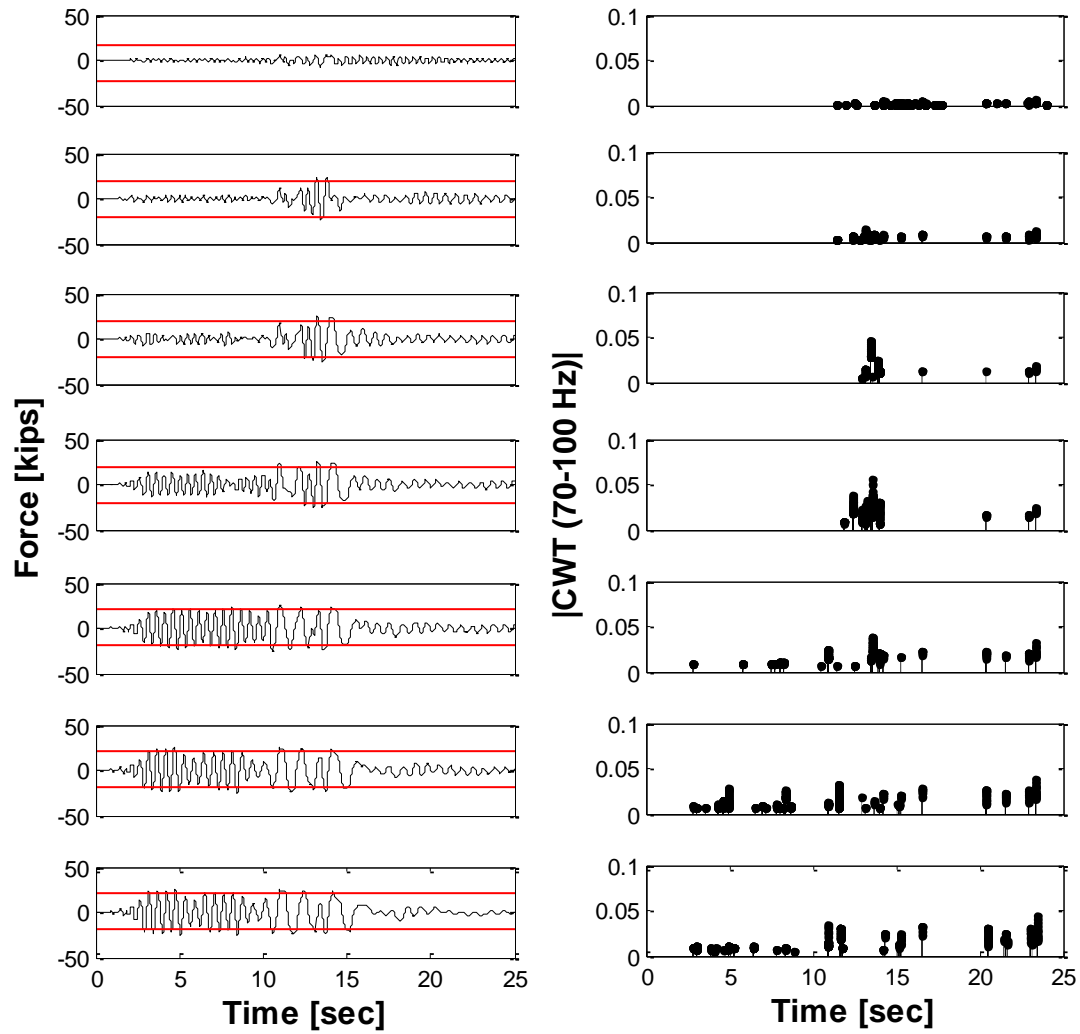


Figure 5-55: Loma Prieta EQ - Force histories (left) and High Frequencies coefficients (right) for different PGA

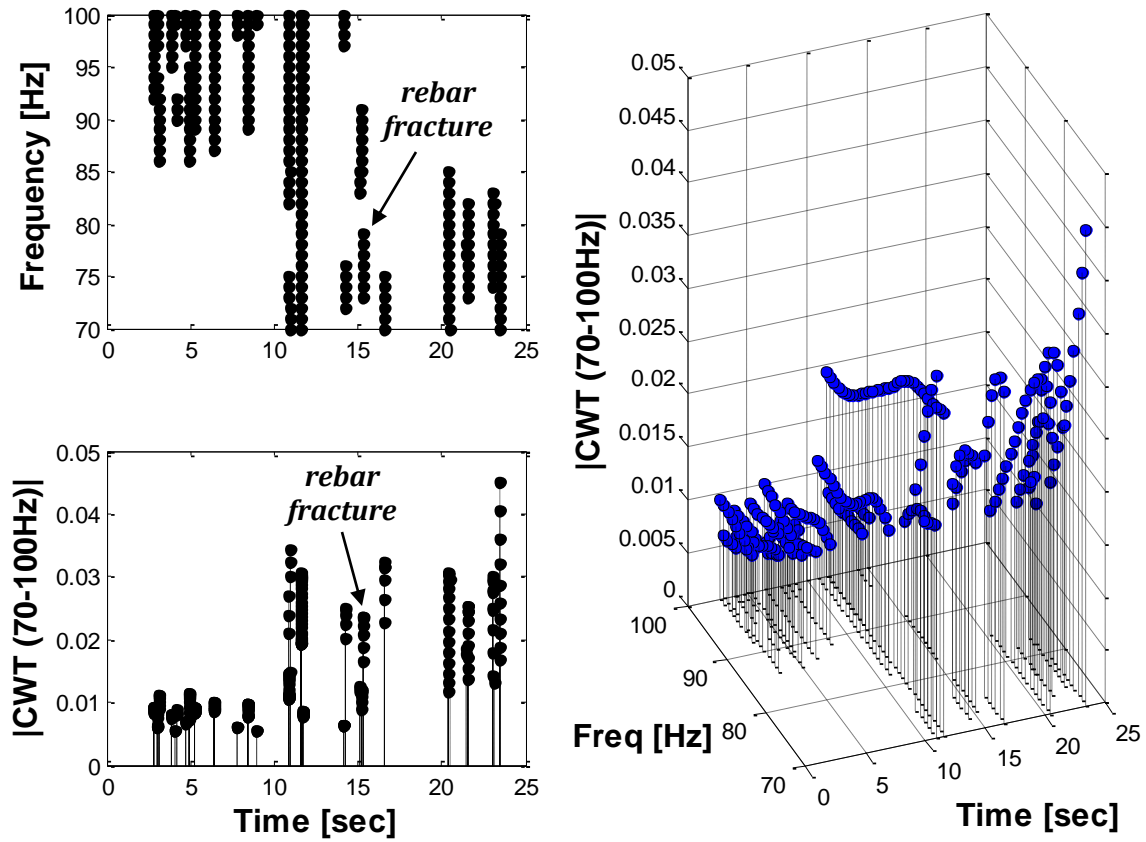


Figure 5-56: Loma Prieta EQ - (a) High Frequency analysis, (b) CWT coefficients, (c) 3D plot

5.9.4 Whittier Narrows earthquake

Now we analyze the wide-band record which is more challenging than the previous earthquake due to it has higher frequency content and it will be reflected in the results. Figures 5-57 and 5-58 show the results for the high frequency and the CWT coefficients for 70-100Hz respectively. The analysis identified a lot of spikes through the entire time domain. However, there are some peaks that are not related to damage. Moreover, the Figure 5-59 presents the results for the last ground motion intensity. In particular for this earthquake, the CWT analysis was not able to identify the time instant where the fracture occurs (i.e. 20.6 seconds).

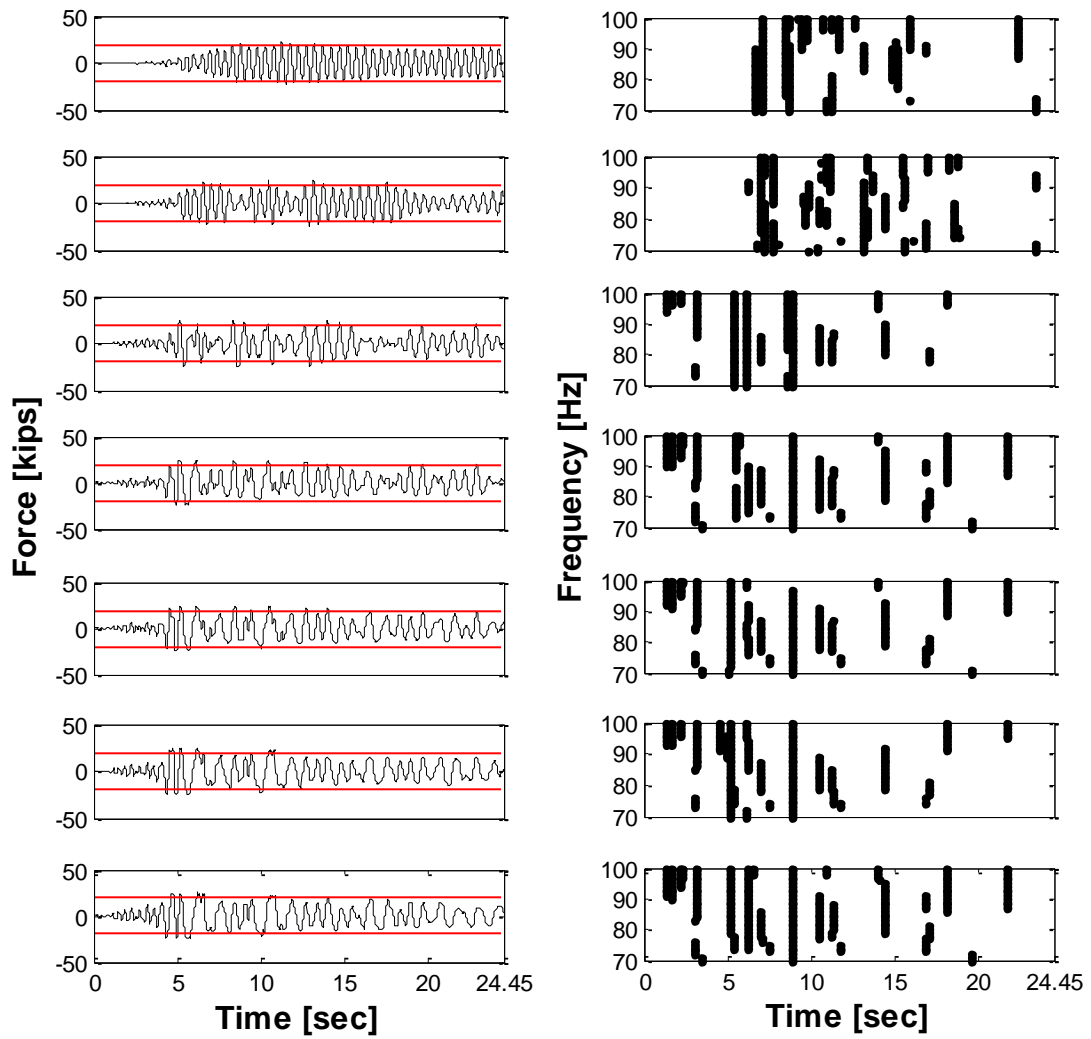


Figure 5-57: Whittier Narrows EQ - Force histories (left) and High Frequencies (right) for different PGA

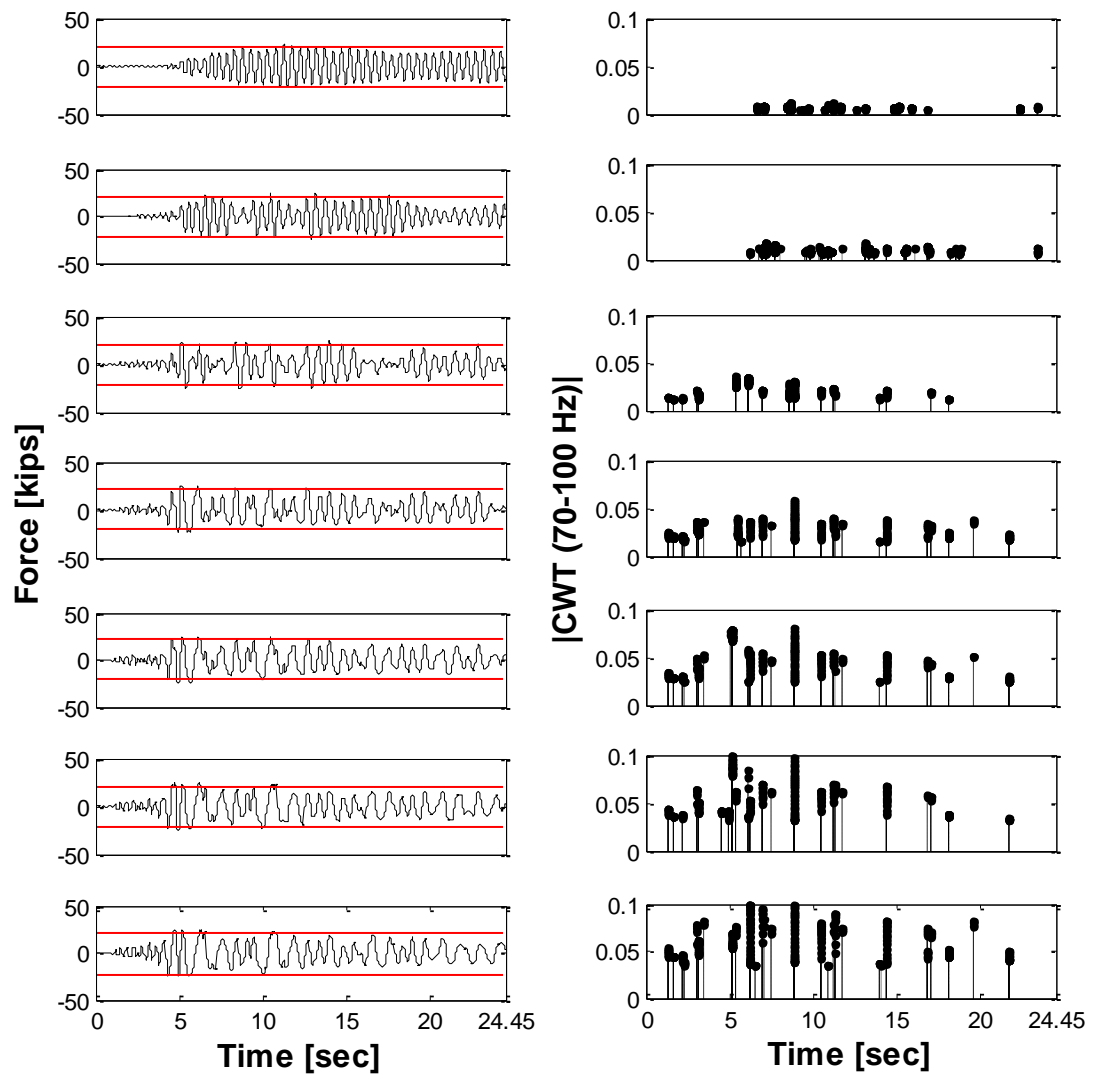


Figure 5-58: Whittier Narrows EQ - Force histories (left) and High Frequencies coefficients (right) for different PGA

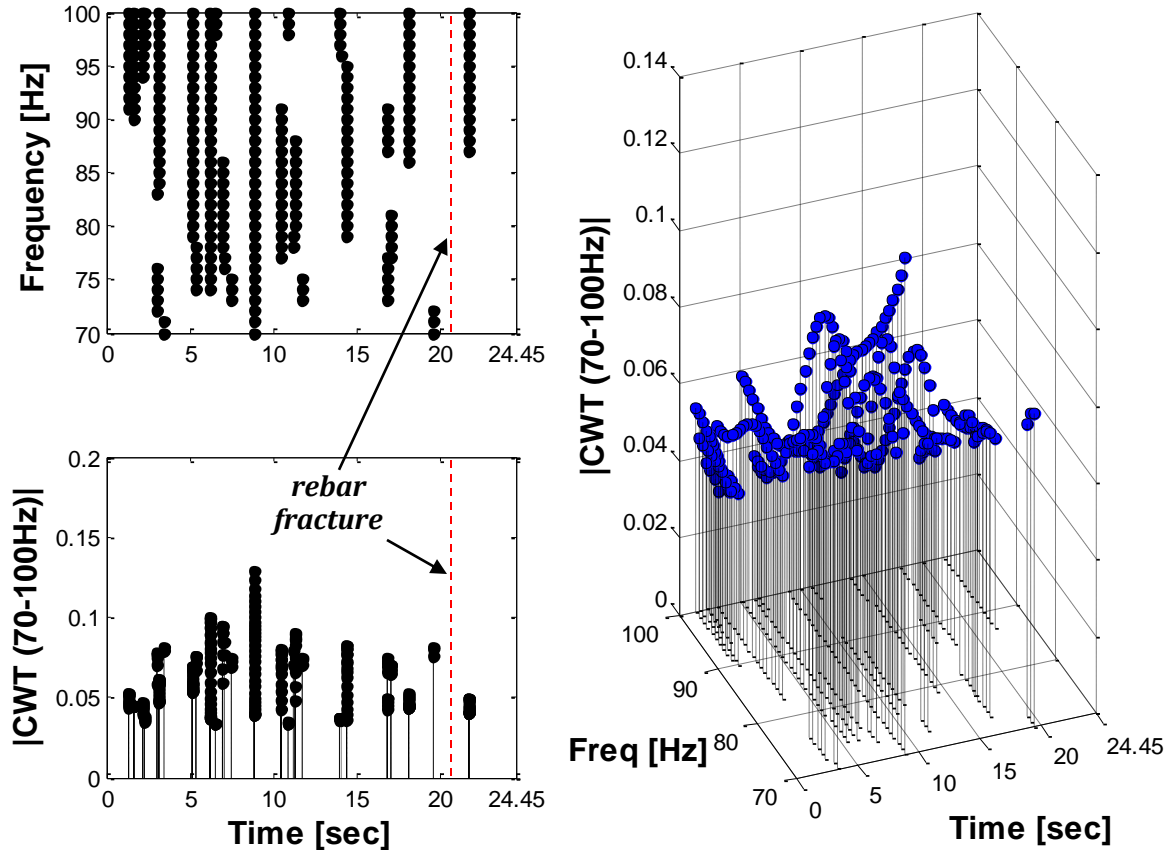


Figure 5-59: Whittier Narrows EQ - (a) High Frequency analysis, (b) CWT coefficients, (c) 3D plot

5.10 DWT analysis results with the proposed refinement

This section presents the proposed methodology results for the DWT analysis. A figure is showed illustrating the force histories comparing them with the DWT detail for the seven amplification factors (or peak ground accelerations) calculated in section 5.4.

5.10.1 White Noise <20Hz

Figure 5-60 displays the results for the first white noise analyzed (i.e. 20 Hz). From this figure we can see that at the beginning and at the end of the time domain there are no spikes in the detail plots. The methodology was able to eliminate all the spikes that were not related to yield for these instants. In addition the time instant (i.e. 13.3 seconds) where the rebar fracture occurs was captured and it was identified in the figure.

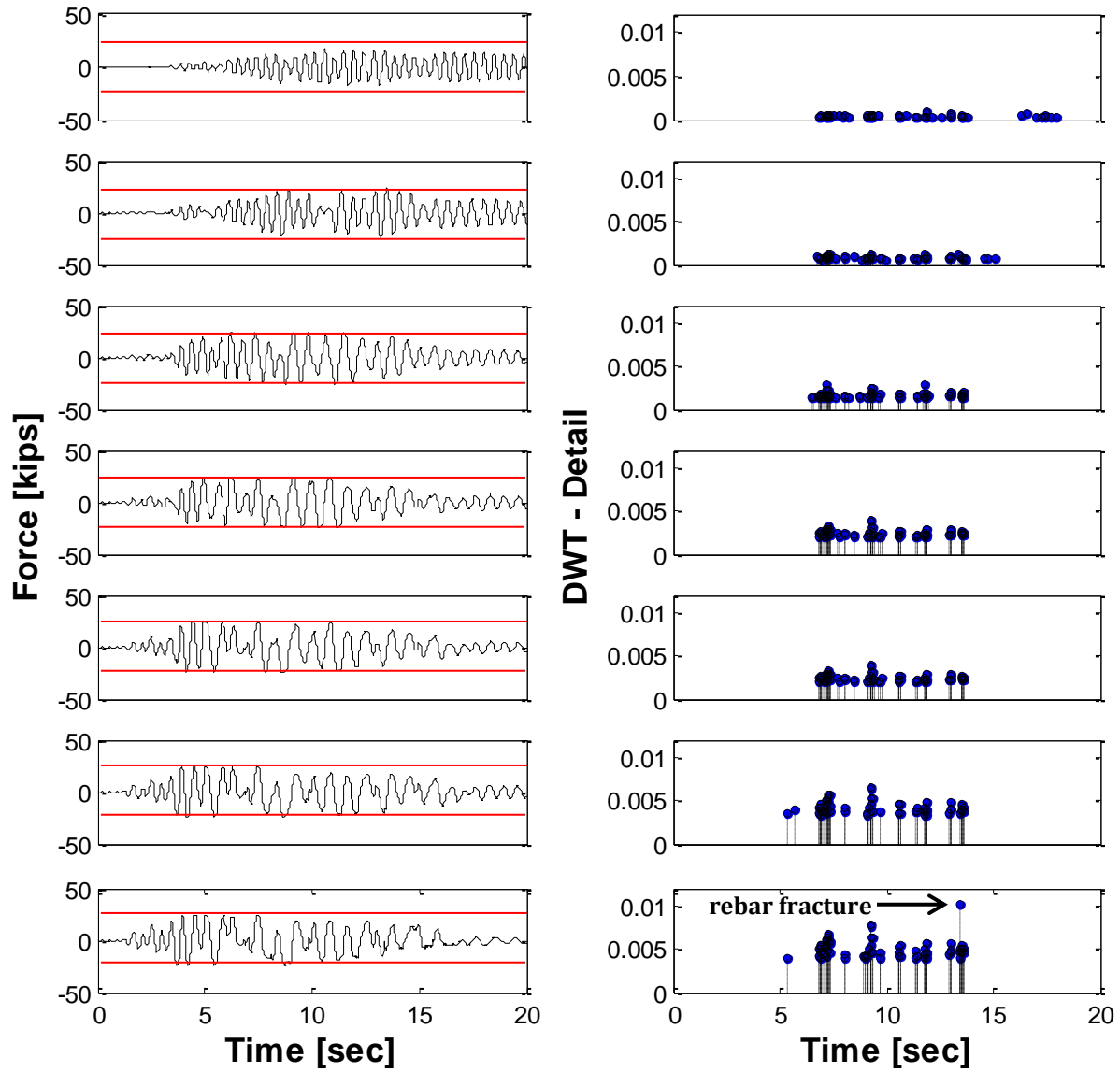


Figure 5-60: White Noise 20Hz - Force histories (left) and DWT detail (right) for different PGA

5.10.2 White Noise <40Hz

For this case (Figure 5-61), it can clearly see the spikes concentration at the center and no spikes are present at both ends. Moreover, the rebar fracture took place at 14.7 seconds and it was identified as a vertical line in the last plot.

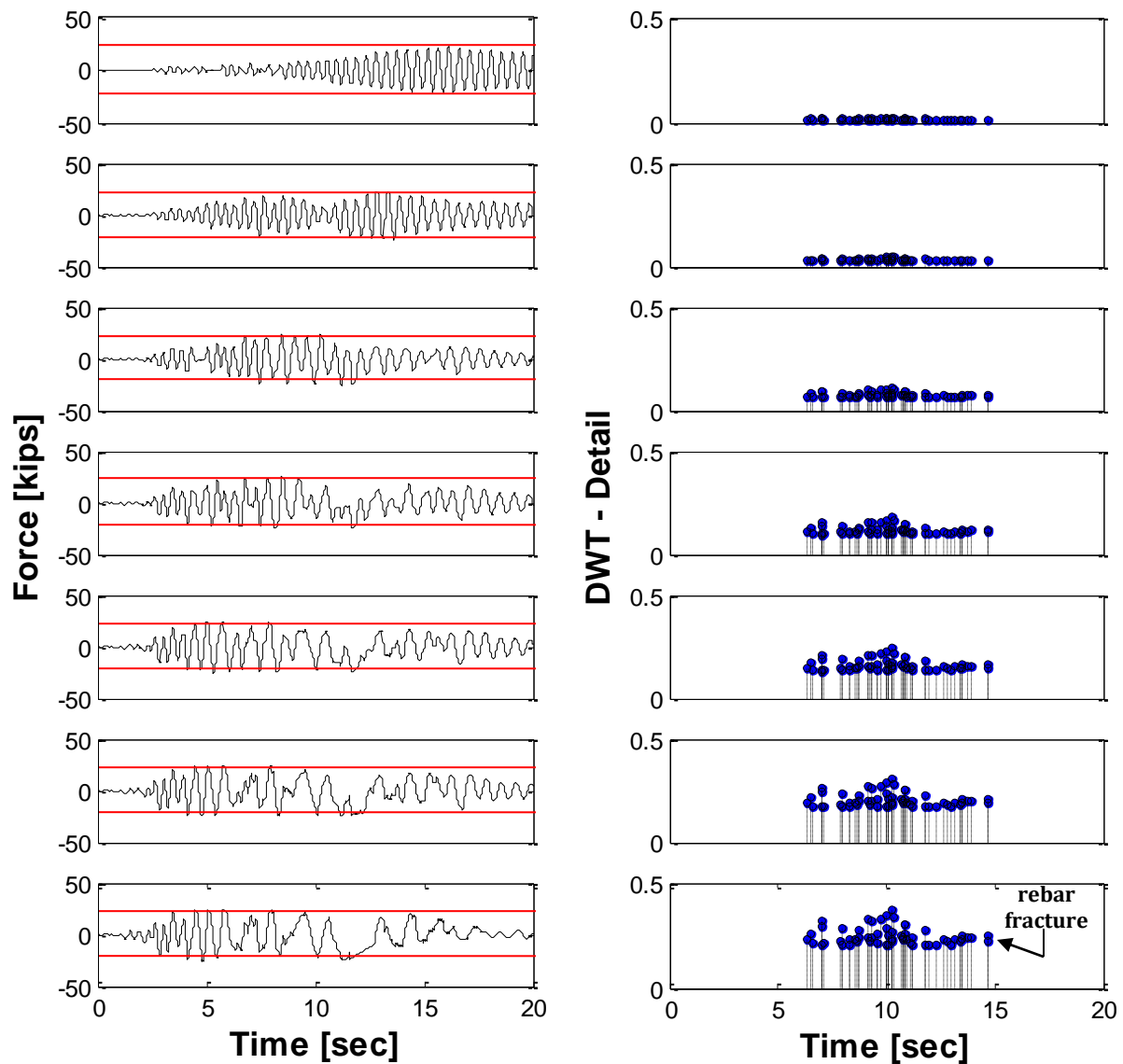


Figure 5-61: White Noise 40Hz - Force histories (left) and DWT detail (right) for different PGA

5.10.3 Loma Prieta earthquake

Figure 5-62 shows the DWT detail analysis results for the narrow-band record. In this particular case, some spurious spikes are present at the end of the results. These spikes can be removed, but some yield instant identified at other parts of the force responses will be eliminated too, and we do not want this. That is why we leave them there, but if we concentrate on the spikes that really stand out, we can associate them to the important yield instants in the force response plots. Moreover, the rebar fracture (occurred at 15.57 seconds) was partially identified in the last plot, but there are a lot of spikes and we can not appreciate very well its time instant in the figure.

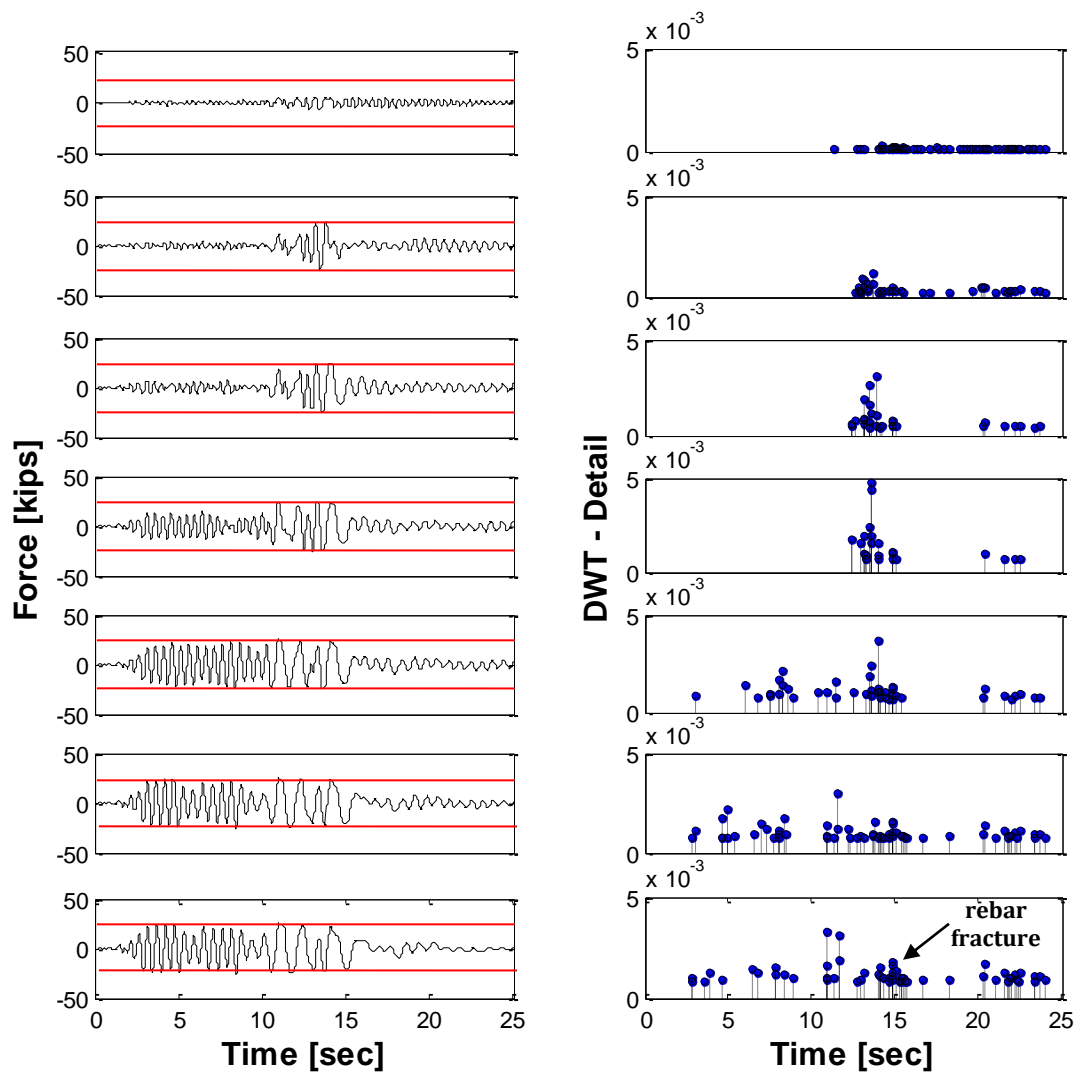


Figure 5-62: Loma Prieta EQ - Force histories (left) and DWT detail (right) for different PGA

5.10.4 Whittier Narrows earthquake

Figure 5-63 illustrates the results for the second earthquake, the wide-band record. This figure shows spurious spikes at the end of the signal. For this particular record, the time instant (i.e. 20.6 seconds) where the rebar fracture took place (identified with a vertical line) was not captured.

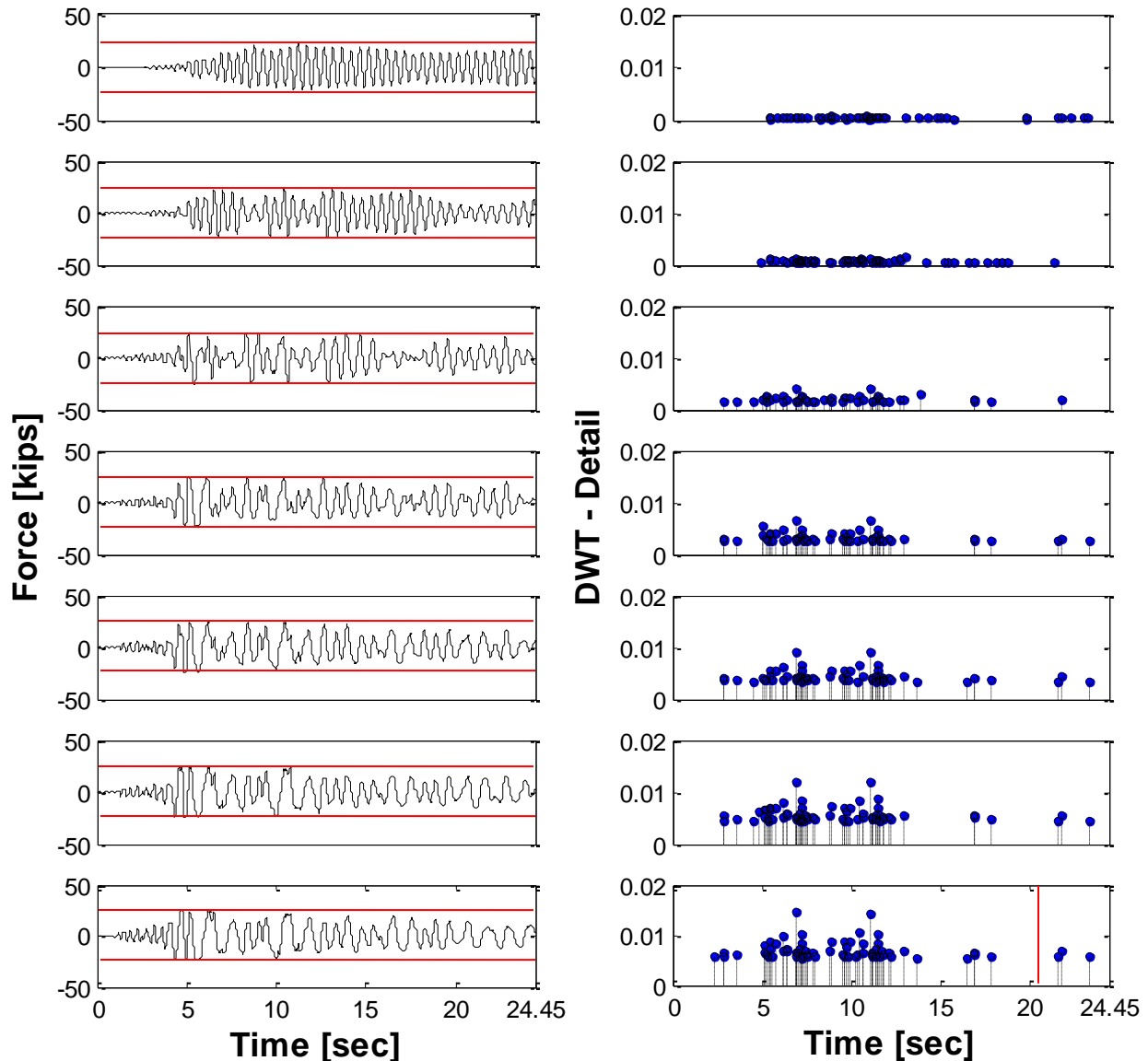


Figure 5-63: Whittier Narrows EQ - Force histories (left) and DWT detail (right) for different PGA

5.11 Conclusions

Based on the problems identified in Chapter IV, especially for the fiber-based model approach where the capability of the damage identification techniques was limited by the frequency content of the load excitation, a methodology refinement was proposed in this chapter. The following comments can be made for the methodology here presented.

1. The proposed methodology had found a better way to present the results efficaciously by partially removing the spikes that are not related with damage (i.e. high frequencies that comes from the base excitation), thus allowing a better identification of the time instants where damage occurred. An example of this argument are the two records, i.e. Loma Prieta (EQ1) and Whittier Narrows (EQ2) earthquakes in which both analyzes (CWT and DWT) without applying it the proposed refinement presented many spikes in the CWT coefficients and DWT details. But when the refinement was applied many of these spikes were removed (Figures 5-64 and 5-67). It should be noted that these figures show the results when there was rebar fracture. In addition, the discrepancy in the spikes amplitude for Figure 5-64 is because Figure (b) shows the coefficients for 80Hz, while Figure (c) displays the coefficients for all the high frequencies analyzed.
2. An incremental dynamic analysis was performed to evaluate the capabilities of wavelet based damage identification techniques to estimate the level of damage in the structure in addition to just detecting the occurrence of damage. The approach followed was to identify the larger peak amplitude resulting from the high frequency analyses and plot them as function of the maximum ductility level reach by the structure. No robust correlation was found between the spike amplitude and the level of damage (inelastic action) induced in the structure. Further research is required to address this important issue.
3. While somehow outside the scope of this work, the results from the IDA also pointed out that damage identification methodologies based solely in the observed frequency shift before and after a damaging event may largely underestimate the actual level of damage in the structure. This can be appreciated from Figures 5-68 to

5-71, where it is seen that an increase in the structure ductility demand is not necessarily reflected in the structure natural frequency of vibration.

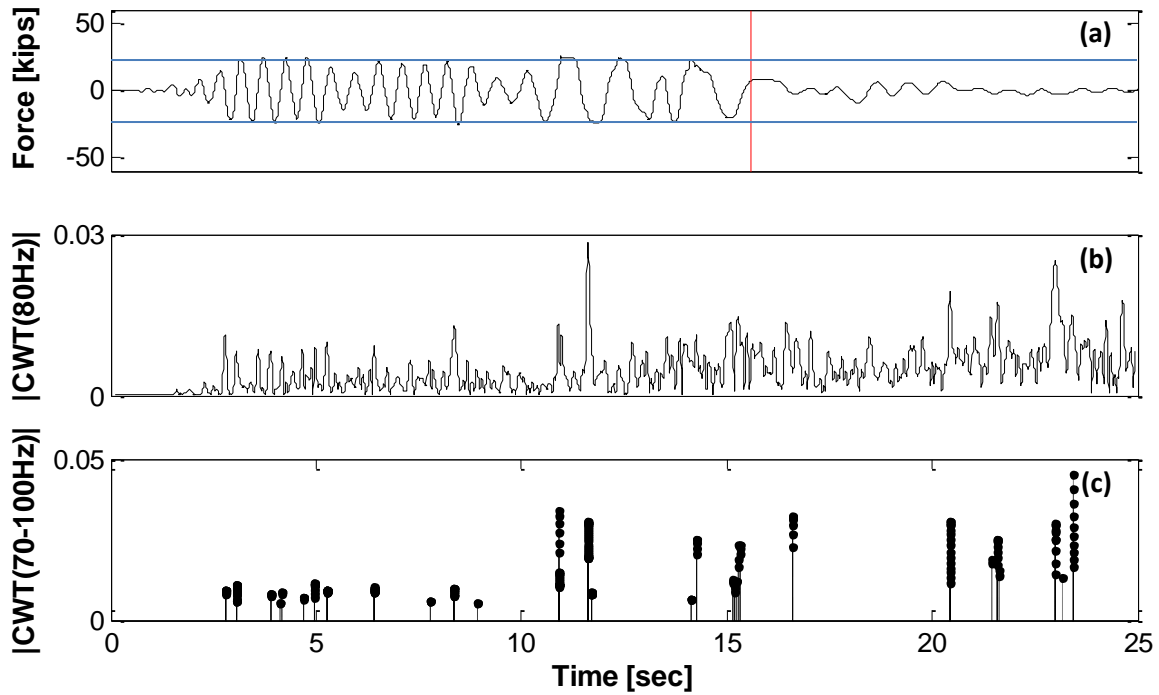


Figure 5-64: EQ1 - (a) Force history, (b) CWT high frequency analysis, (c) Proposed methodology

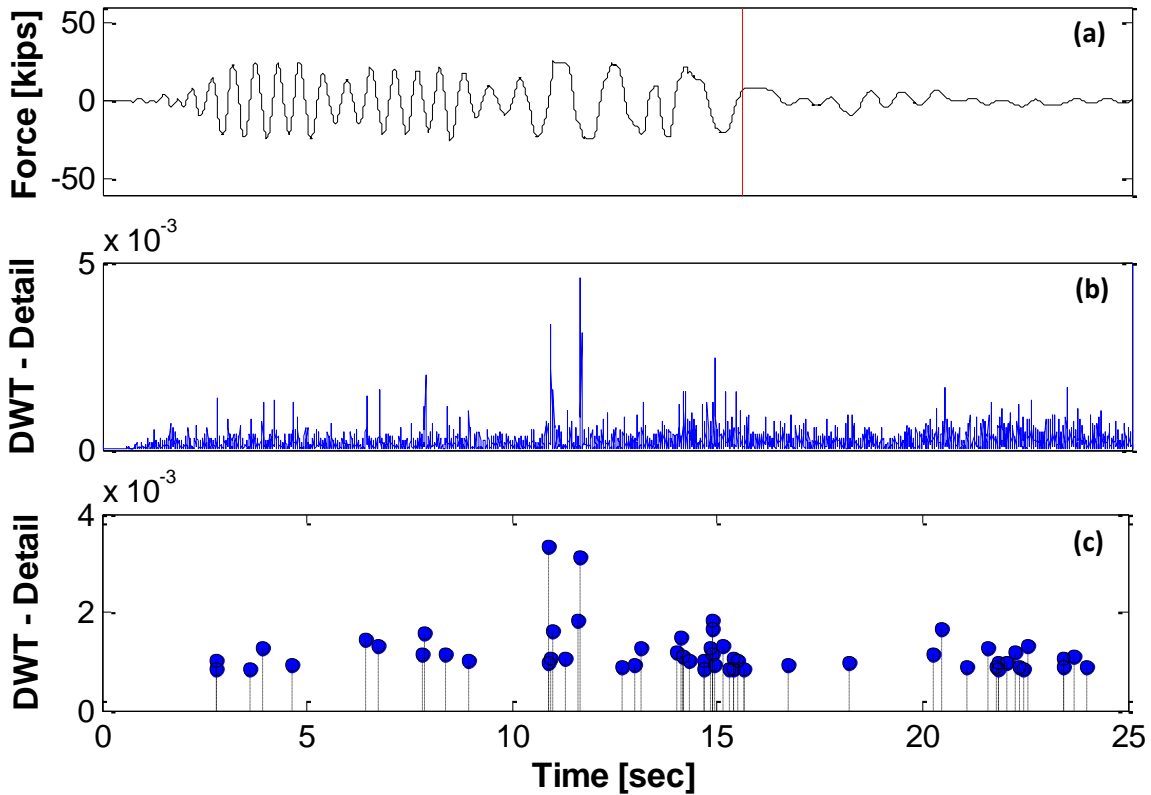


Figure 5-65: EQ1 - (a) Force history, (b) DWT detail analysis, (c) Proposed methodology

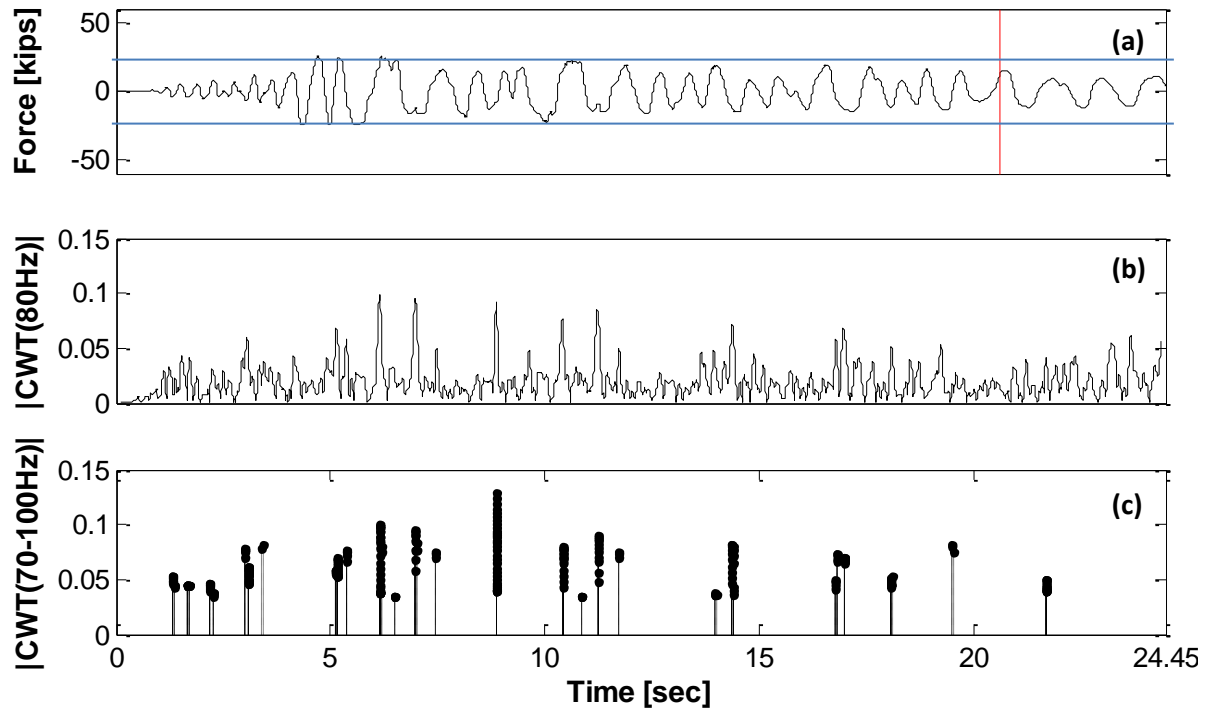


Figure 5-66: EQ2 - (a) Force history, (b) CWT high frequency analysis, (c) Proposed methodology

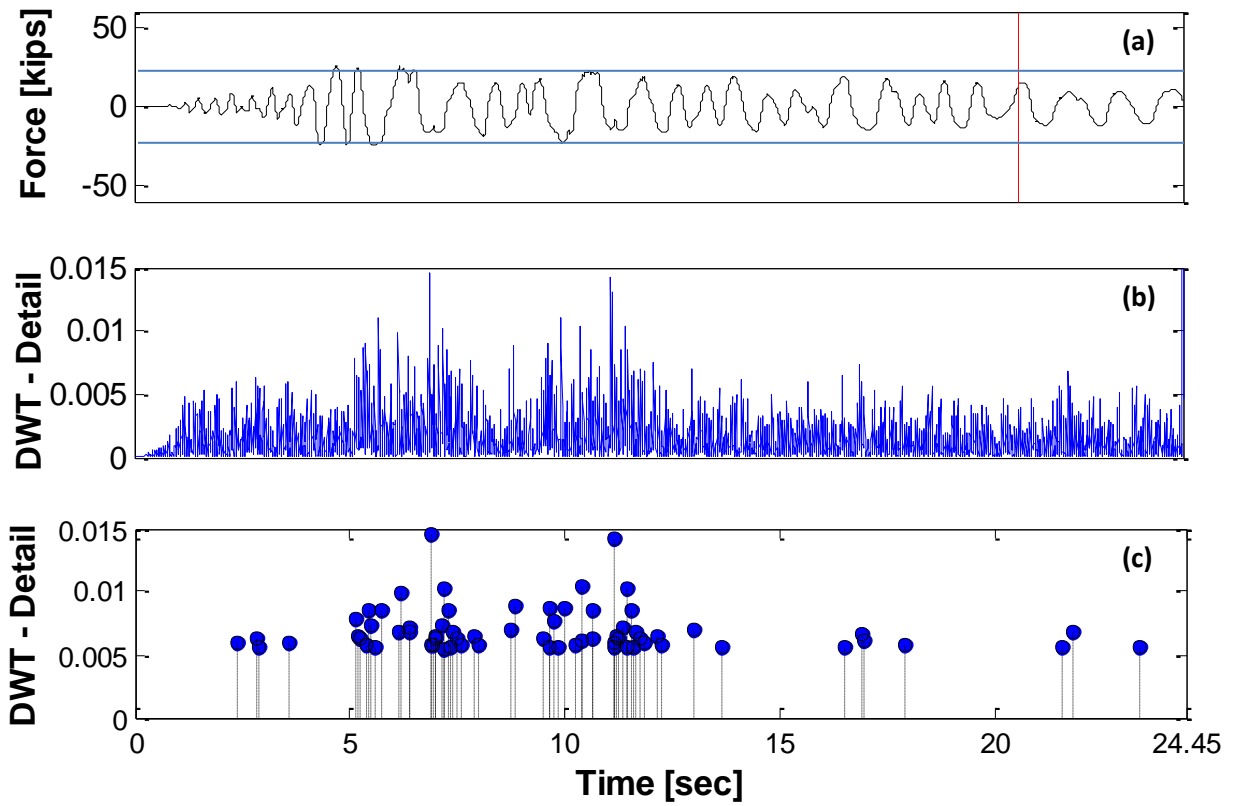


Figure 5-67: EQ2 - (a) Force history, (b) DWT detail analysis, (c) Proposed methodology

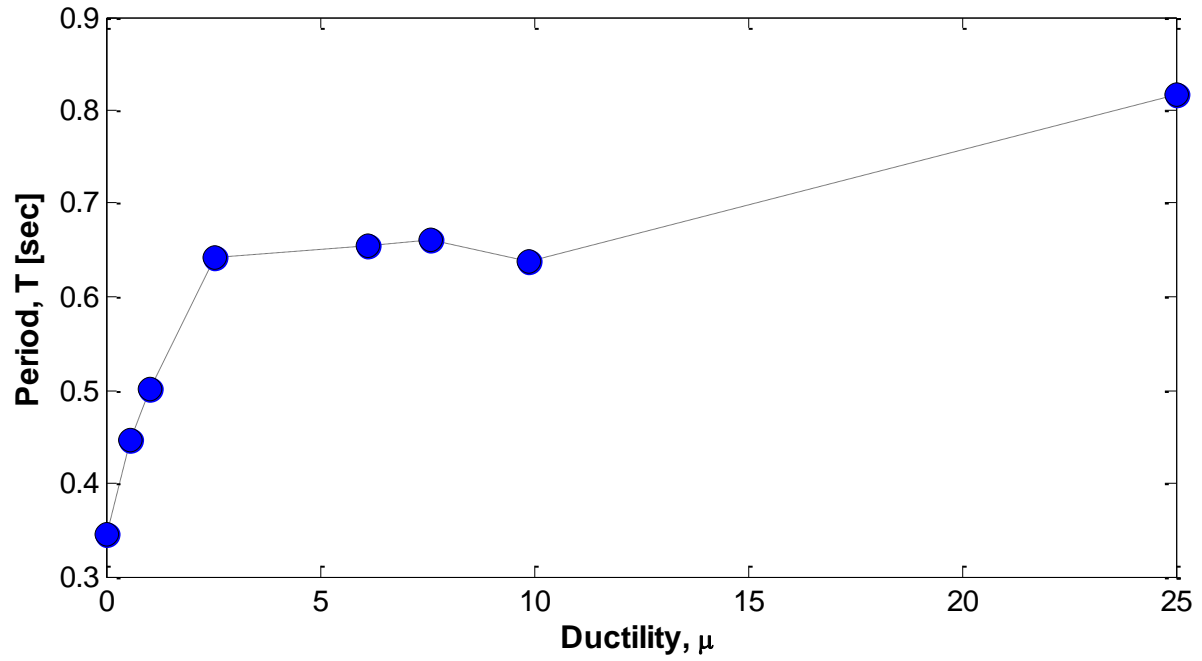


Figure 5-68: White Noise 20Hz - Ductility vs Period

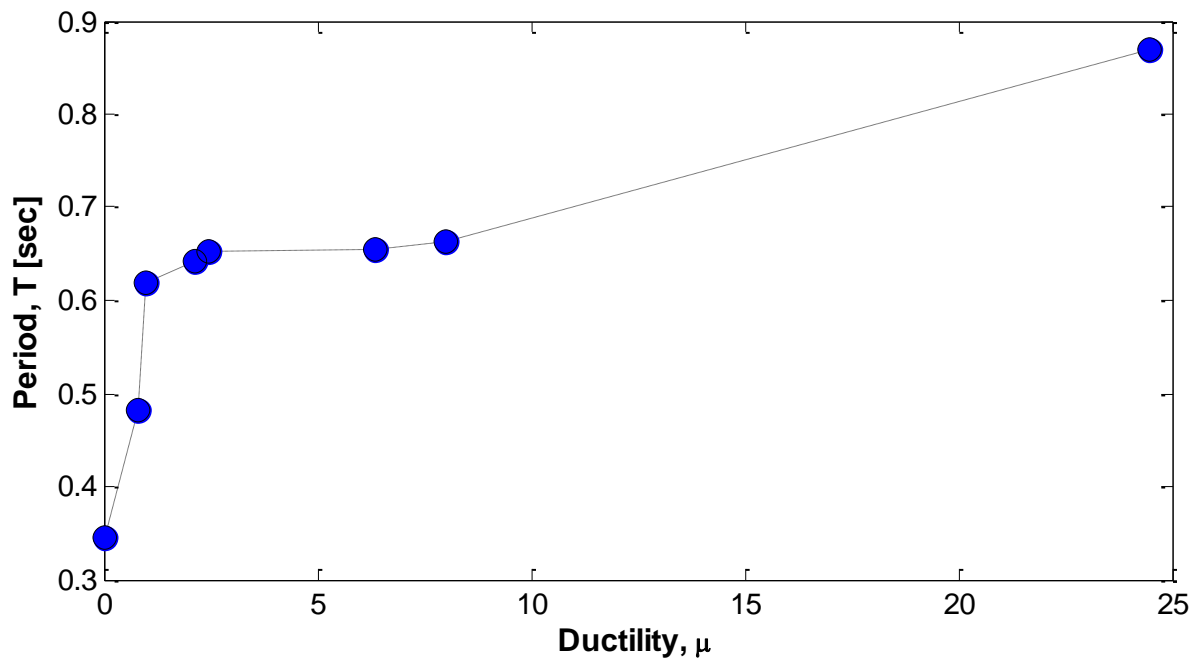


Figure 5-69: White Noise 40Hz - Ductility vs Period

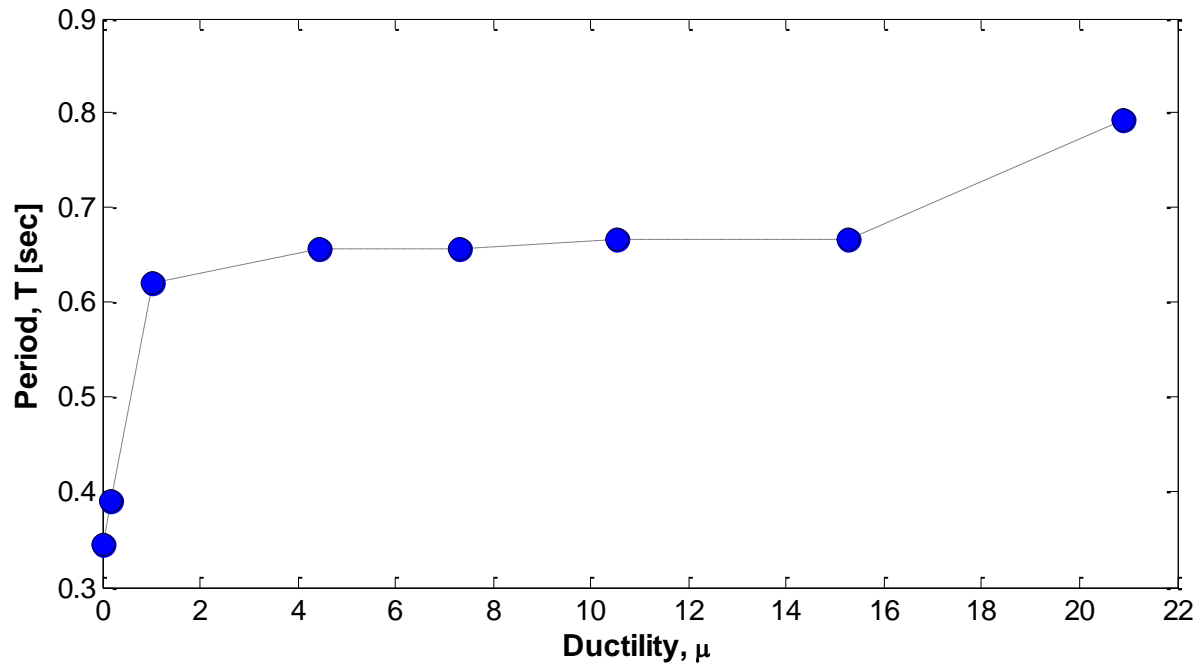


Figure 5-70: Loma Prieta earthquake - Ductility vs Period

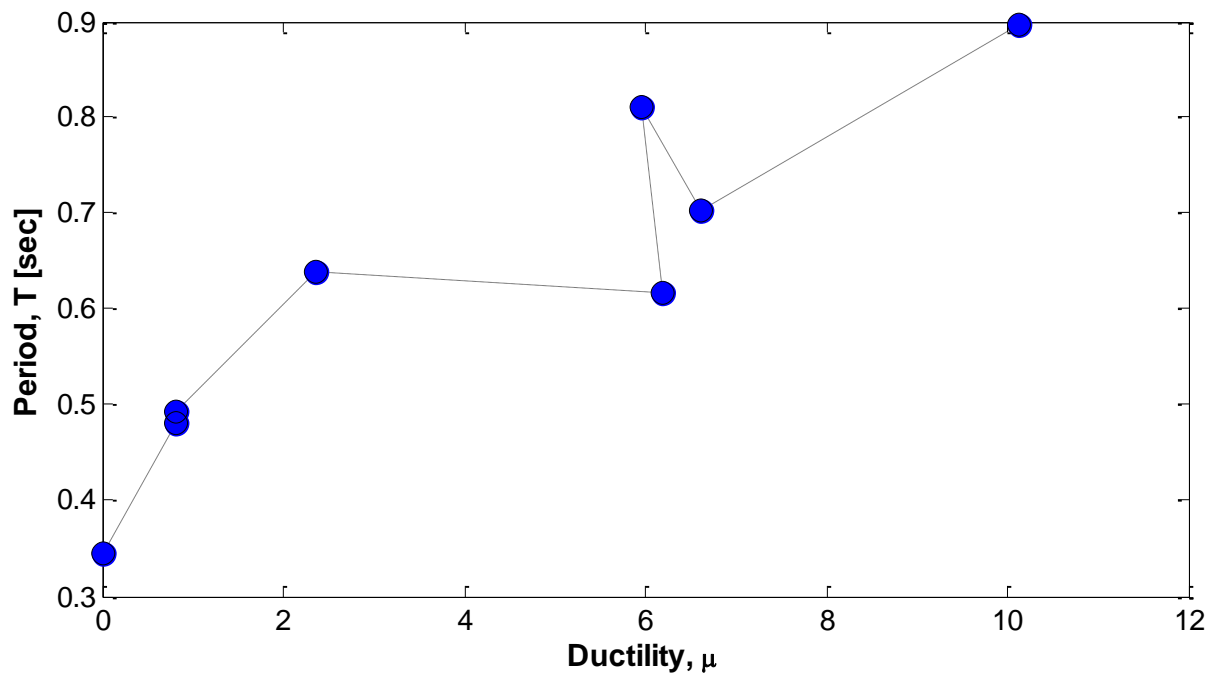


Figure 5-71: Whittier Narrows earthquake - Ductility vs Period

5.12 References

Montejo, L. A. (2010). *"Signal Processing Based Damage Detection in Structures Subjected to Random Excitations"*. Structural Engineering and Mechanics, submitted for publication.

PEER Pacific Earthquake Engineering Research Center (2010), Next Generation Attenuation of Ground Motions NGA database <http://peer.berkeley.edu/nga/index.html>

CHAPTER VI

CONCLUSIONS AND RECOMMENDATIONS

6.1 Summary

This research work had the overall objective of identify the damage (or yield instants) in reinforced concrete (RC) civil structures subjected to earthquake loads. After a large earthquake occurs the assessment of structural damage is required to identify unsafe structures. This thesis focused on methodologies based on the analysis of the nonlinear/nonstationary characteristics of the dynamic response of the structure. The analysis of the structural response registered during the earthquake was performed using an advanced mathematical tool (i.e. Wavelet Transforms) that allows for simultaneous time frequency examination. The occurrence of damage was associated with the changes in the instantaneous frequency (IF) and/or singularities in the high frequency response due to sudden changes in the stiffness parameter.

Since a realistic RC member representation was needed in order to develop and validate the damage identification technique in civil structures, a non-linear fiber-based model approach was adopted. This technique was shown to be superior to other techniques evaluated and based on hysteretic rules (i.e. bilinear, Takeda), since due to their multilinear nature these last ones will always exhibit spurious drastic changes in stiffness. The results from the testing of four large scale RC columns were analyzed in order to validate and calibrate the modeling approach. Such tests included columns subjected to cyclic reversals and column subjected to dynamic base excitations through a shake table. Once the modeling approach was validated we proceed to evaluate and calibrate the different types of damage detection algorithms using wavelet transforms. Both wavelet transforms were implemented, the Continuous Wavelet Transform (CWT) and the Discrete Wavelet Transform (DWT). The CWT was used to perform low frequency analysis (for identification of frequency changes) and high frequency analysis (for detection of sudden stiffness

changes). The DWT was employed for a more time-efficient high frequency analysis. Different kinds of wavelet functions such as Haar, Daubechies, Bior6.8, and Complex Morlet were evaluated. After different examples were conducted using toy signals, two mother wavelets, the Complex Morlet and the Bior6.8, were chosen to implement the CWT and DWT, respectively.

From a first evaluation using different types of dynamic excitations and modeling approaches it was found that wavelet methodologies were limited by the frequency content of the load excitation and modeling approach used. As the high frequency content of the excitation increases and the modeling approach is more realistic, the identification of damage becomes more problematic. Finally, methodology refinements were proposed to precisely tackle this problem. For the application of this methodology only the fiber-based model approach and non-stationary excitation loads were used for evaluation purposes.

6.2 Conclusions

This research work presented a comprehensive evaluation of wavelet based damage detection methodologies when applied to RC structures subjected to base excitations. The work performed was a combination of advanced nonlinear structural modeling, signal processing and algorithm development. It should be noticed that wavelet based approaches have been validated in the past using numerical models in which the characteristic hysteretic and non-linear behavior of the elements of a civil structure is misrepresented by assuming linear or multi-linear behavior at most. The gradual occurrence of damage proper of modern detailed structures has been also misrepresented when the damage is introduced as a sudden loss of stiffness in one of the elements or levels of the structure. This research overcame this limitation by calibrating the detection algorithms with simulated data from state of the art fiber-based nonlinear structural models capable of reproduce the actual nonlinear hysteretic response including the effect of different types of local damage like rebar rupture. The most relevant conclusions resulting from this work are compiled below:

- Wavelet based detection methodologies have been validated in the past using bi-linear or more advanced hysteresis rules like the Takeda model to represent the behavior of reinforced concrete members. While this type of models have been successfully used for years by the structural engineering community to analyze the non-linear behavior of civil structures, their use for validation of damage detection techniques is not adequate due to the unrealistic abrupt change in stiffness proper of any multi-linear hysteretic model.
- A CWT analysis in the low frequency range was generally successful to identify the changes in the structure natural frequency of vibration; however, some problems arise when the dominant frequencies of the excitation are close to the structure natural frequency.
- Detection of singularities from the high frequency range of the response was possible using both, the CWT and DWT. The DWT is more computationally efficient and the magnitude of the spikes appearing in the DWT detail functions seems to relate better with the level of inelastic action induced in the structure. On the other hand, using a projection of the structure high frequency response via the CWT instead of the DWT has the advantage that the frequencies at which the transform operates can be defined by the user, while the frequency bands of the detail functions obtained via DWT are predetermined by the sampling period of the signal.
- Sudden changes in the system stiffness introduces discontinuities in the acceleration response, however such discontinuities are not always related to yield episodes as some of them are just direct consequence of the multilinear nature of the model (if such type of modeling approach is used) or can arise directly from the base excitation.
- When a more realistic modeling approach (i.e. the fiber-based approach) is used to generate the structural model, the efficiency of the detection technique largely diminishes.
- The efficiency of the evaluated methodologies is influenced (i.e. decreases) as the high frequency content of the excitation increases. If the frequency content of the

excitation spans over the frequency range where damage is reflected, the results obtained after a high frequency analysis may include not only spikes due to structural damage but also spikes proper of the excitation. As consequence, better results were obtained for columns that were excited with dynamic loads of limited high frequency content.

- To avoid the identification of spurious peaks a threshold criterion based on the peaks amplitude was proposed to post-process the results. The results obtained show that supplication of this methodology refinement will partially eliminate the spurious peaks.
- While the evaluated methodologies were able to identify the damage instants, an estimation of the level of damage is still uncertain and future research effort should focus in this aspect.
- Since the identification of damage is performed from the direct examination of the nonlinear-nonstationary characteristics of the structure dynamic response, the dependency on large and detailed FE models or on the prior knowledge of the undamaged structure vibration characteristics is partially eliminated.
- Despite the aforementioned challenges, the evaluated methodologies show great potential for identify the damage in civil RC members. If both, high and low frequencies analyzes are used, we can get a more clear idea of the changes undergone by the system being analyzed (Figures 6-1 to 6-8). These figures shows the results for the two white noises (i.e. 20Hz and 40Hz) and the two records analyzed in this research (i.e. EQ1 is the Loma Prieta earthquake and EQ2 is the Whittier Narrows earthquake), both used in Chapter V.

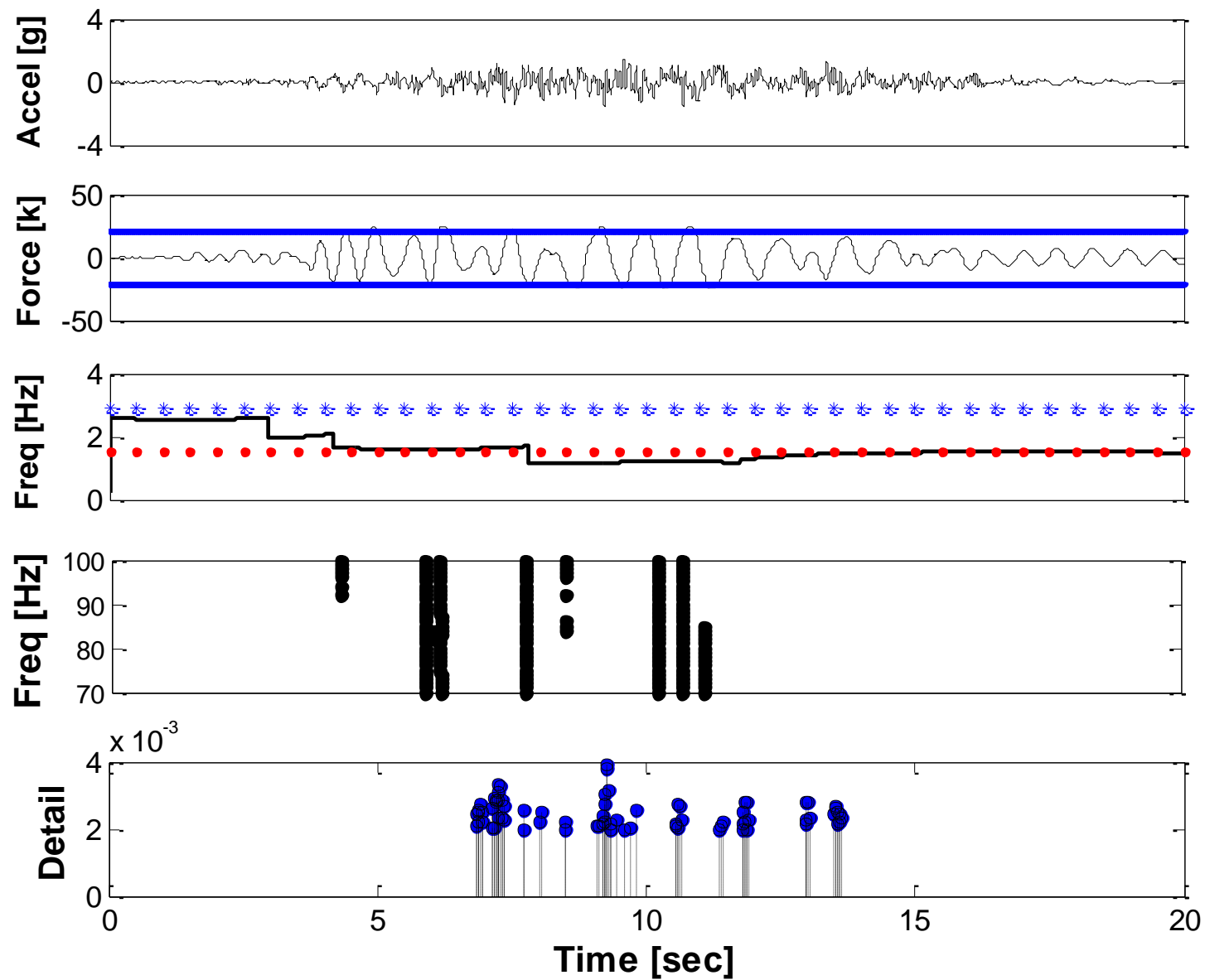


Figure 6-1: WN20 (PGA₄): (a) Acceleration, (b) Force, (c) CWT low-freq, (d) CWT high freq, (e) DWT detail

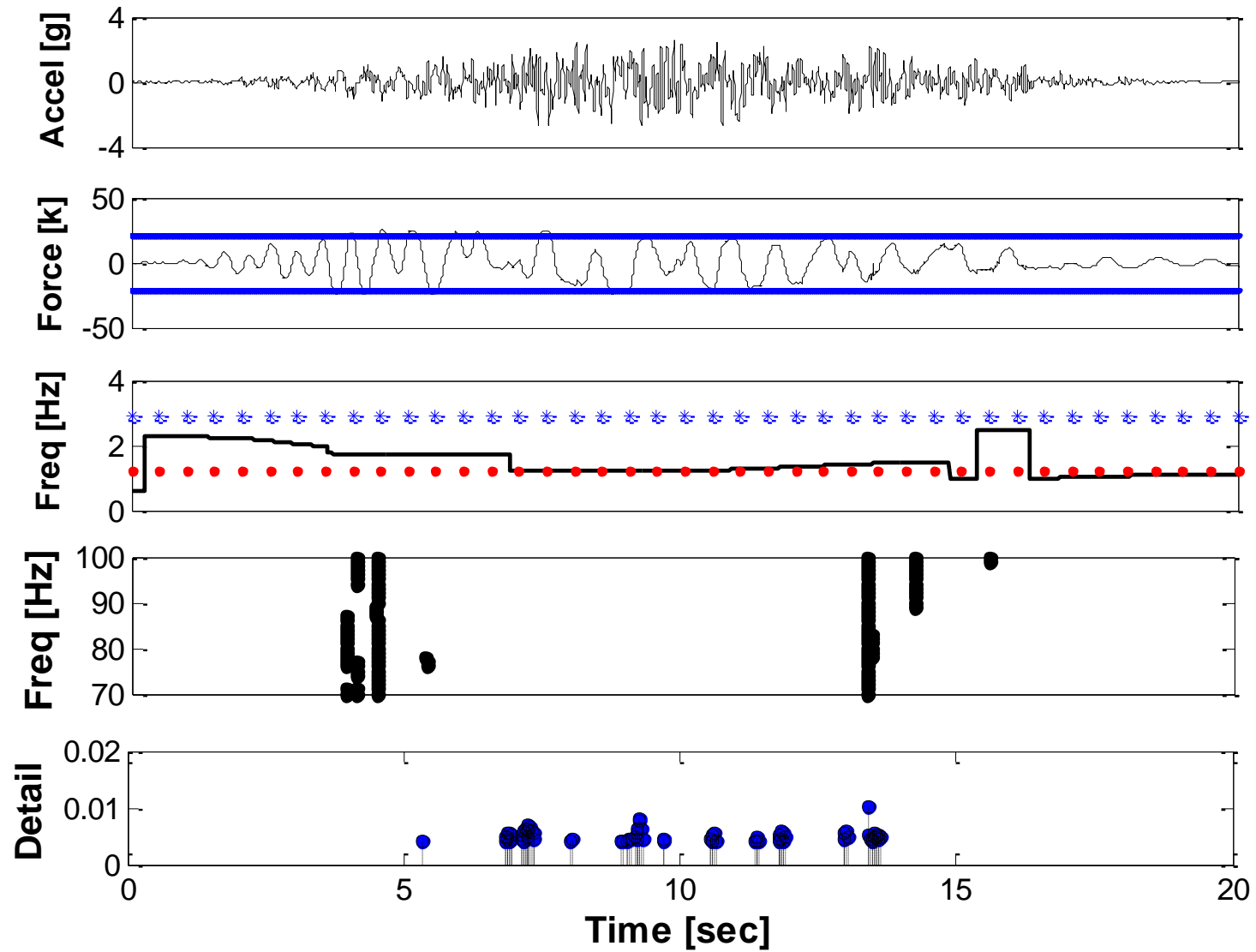


Figure 6-2: WN20 (PGA₇): (a) Acceleration, (b) Force, (c) CWT low-freq, (d) CWT high freq, (e) DWT detail

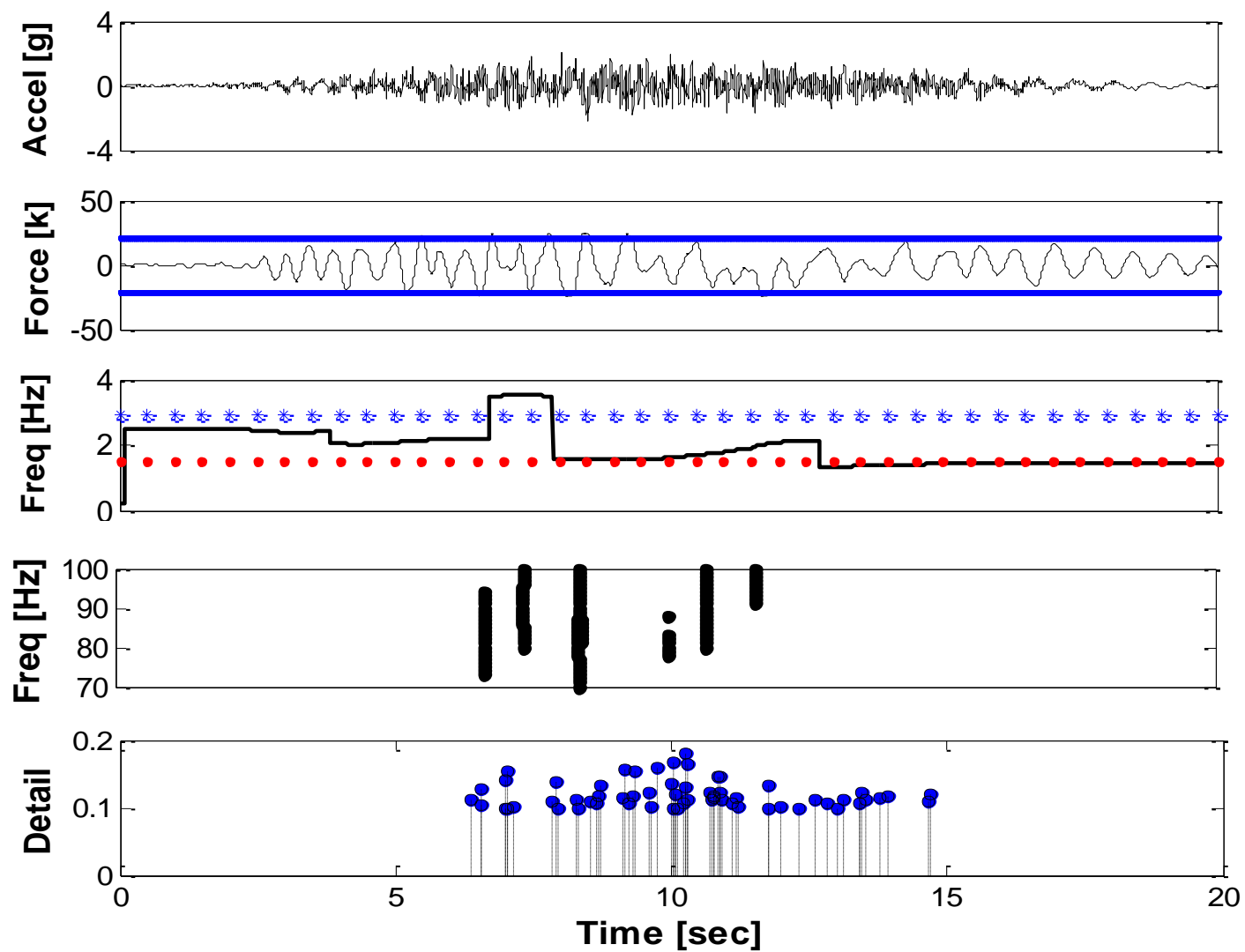


Figure 6-3: WN40 (PGA₄): (a) Acceleration, (b) Force, (c) CWT low-freq, (d) CWT high freq, (e) DWT detail

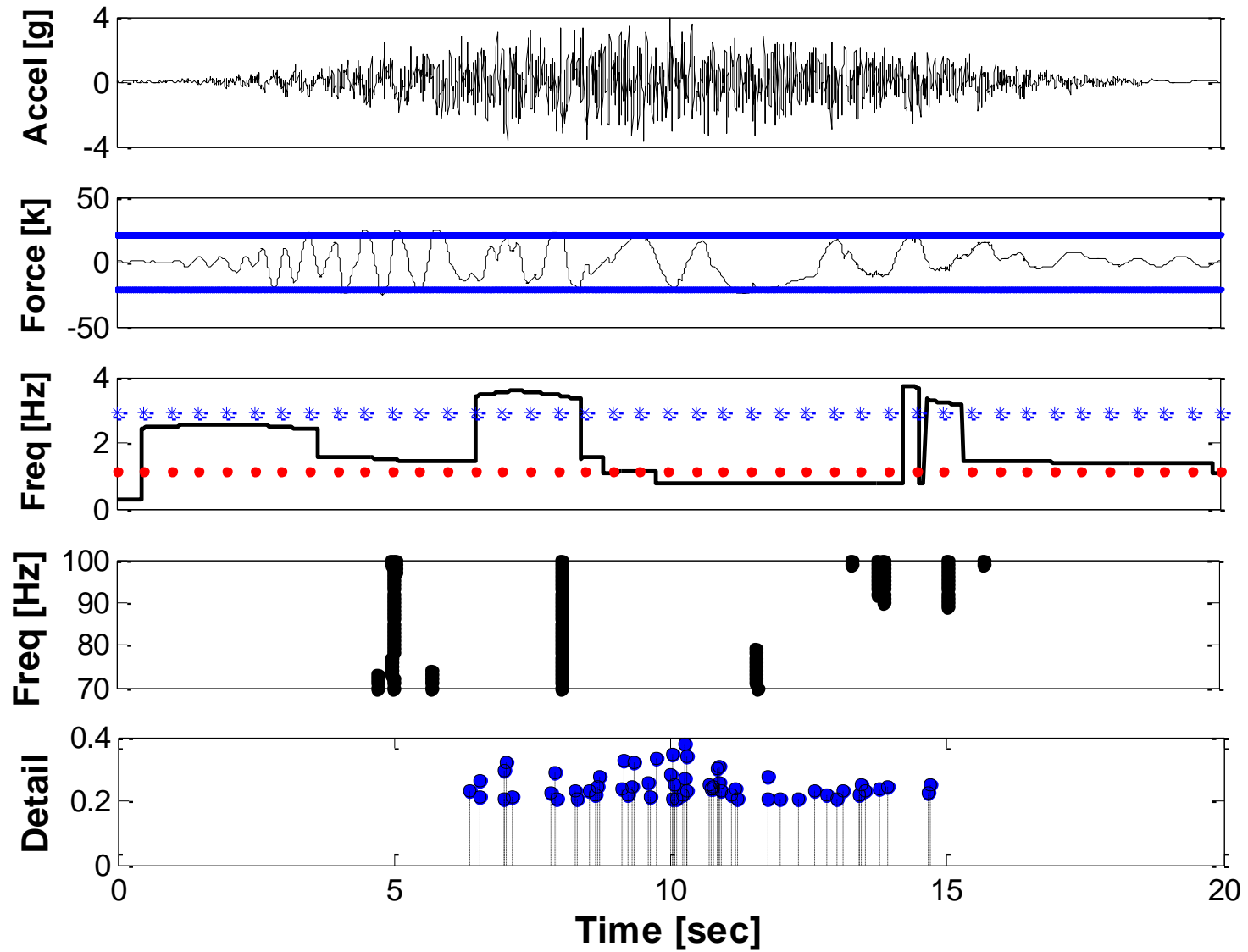


Figure 6-4: WN40 (PGA₇): (a) Acceleration, (b) Force, (c) CWT low-freq, (d) CWT high freq, (e) DWT detail

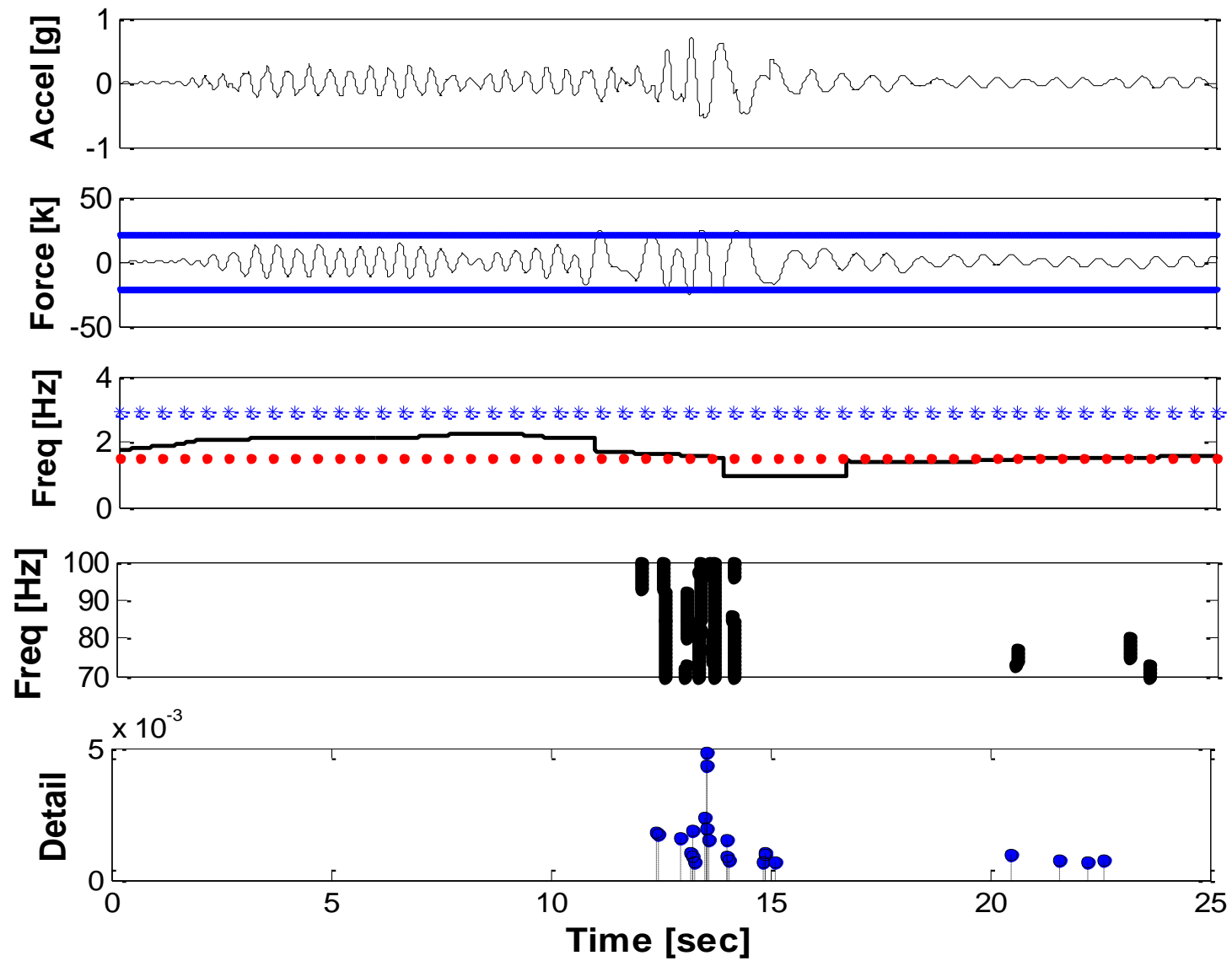


Figure 6-5: EQ1 (PGA₄): (a) Acceleration, (b) Force, (c) CWT low-freq, (d) CWT high freq, (e) DWT detail

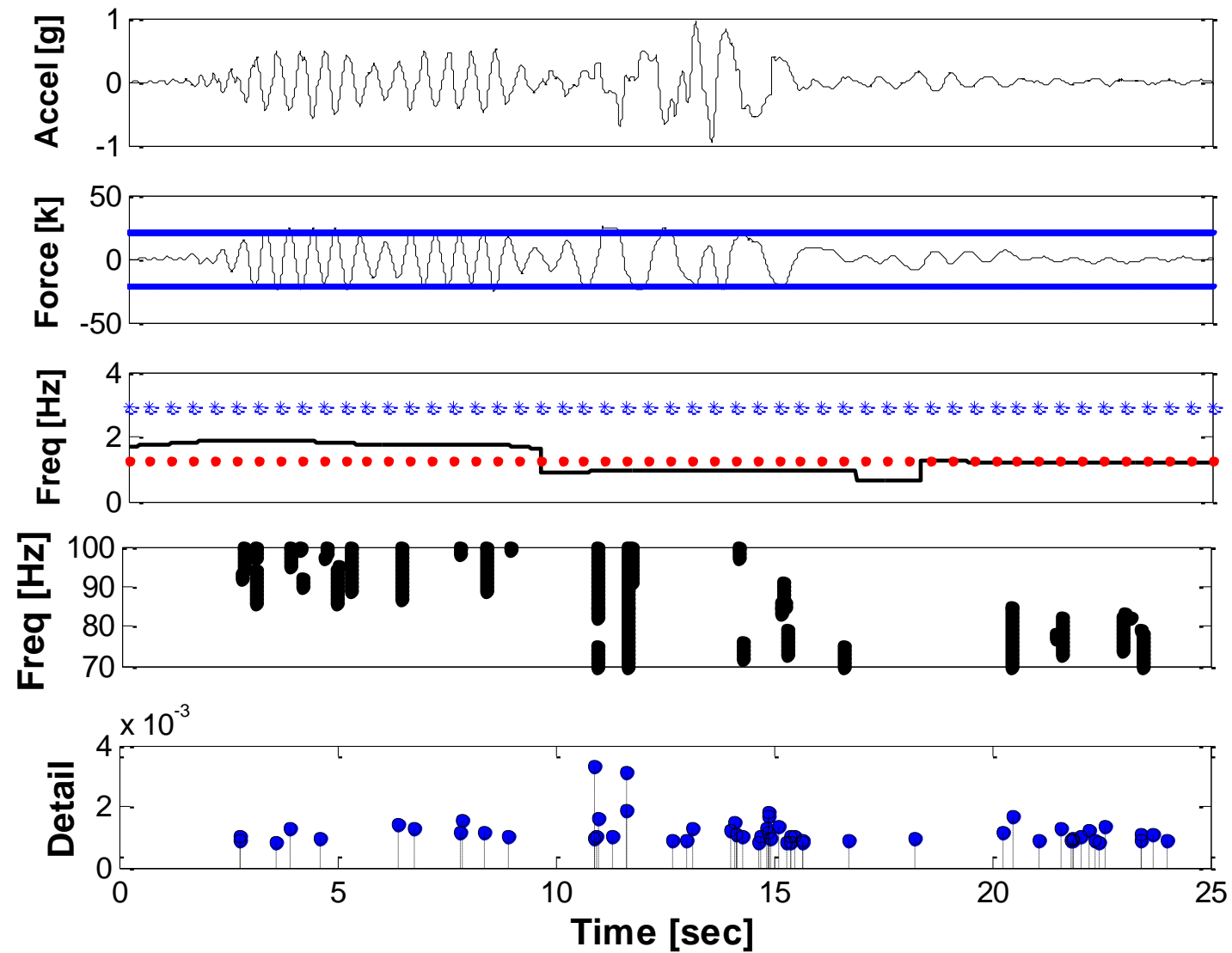


Figure 6-6: EQ1 (PGA₇): (a) Acceleration, (b) Force, (c) CWT low-freq, (d) CWT high freq, (e) DWT detail

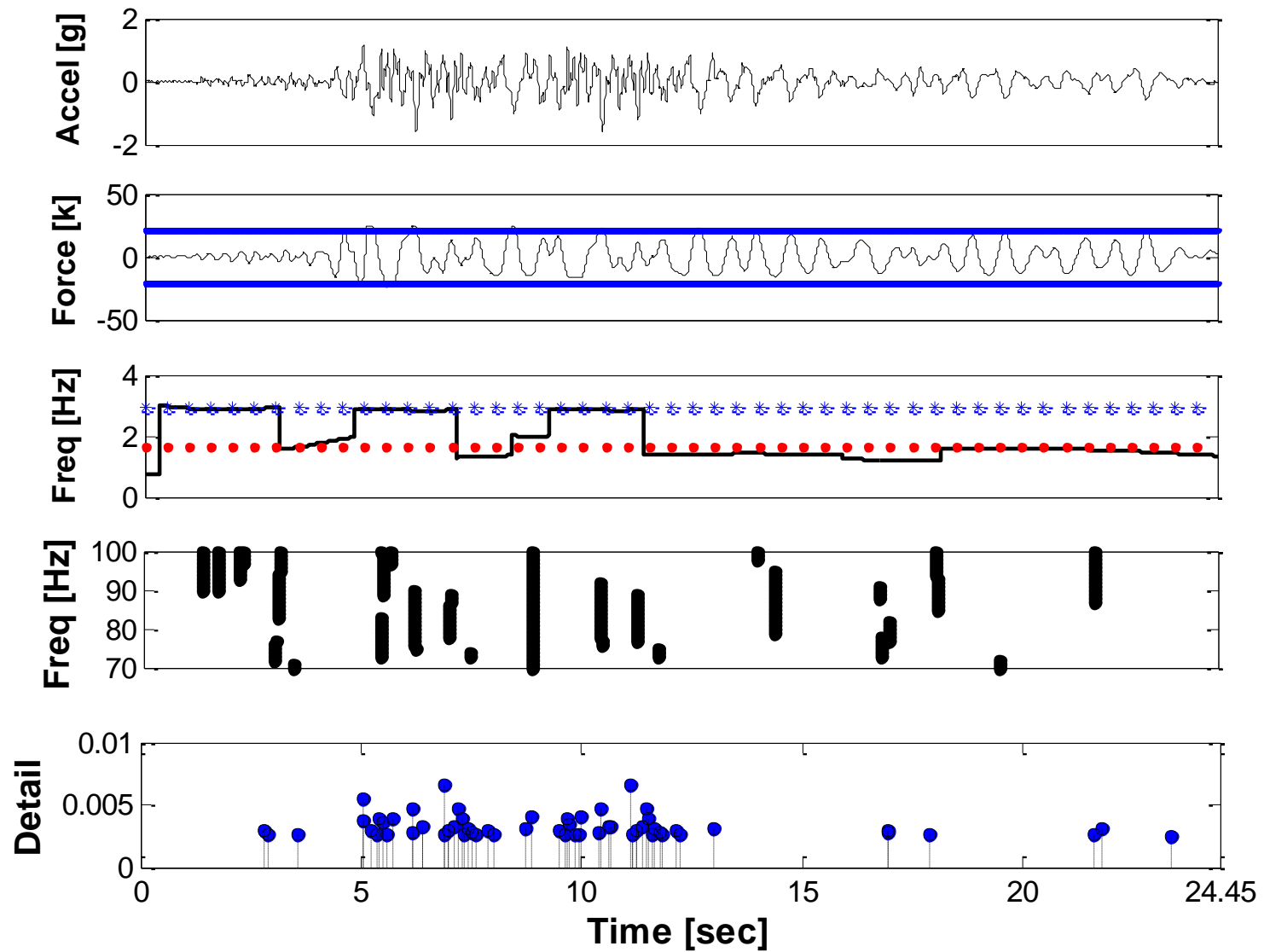


Figure 6-7: EQ2 (PGA₄): (a) Acceleration, (b) Force, (c) CWT low-freq, (d) CWT high freq, (e) DWT detail

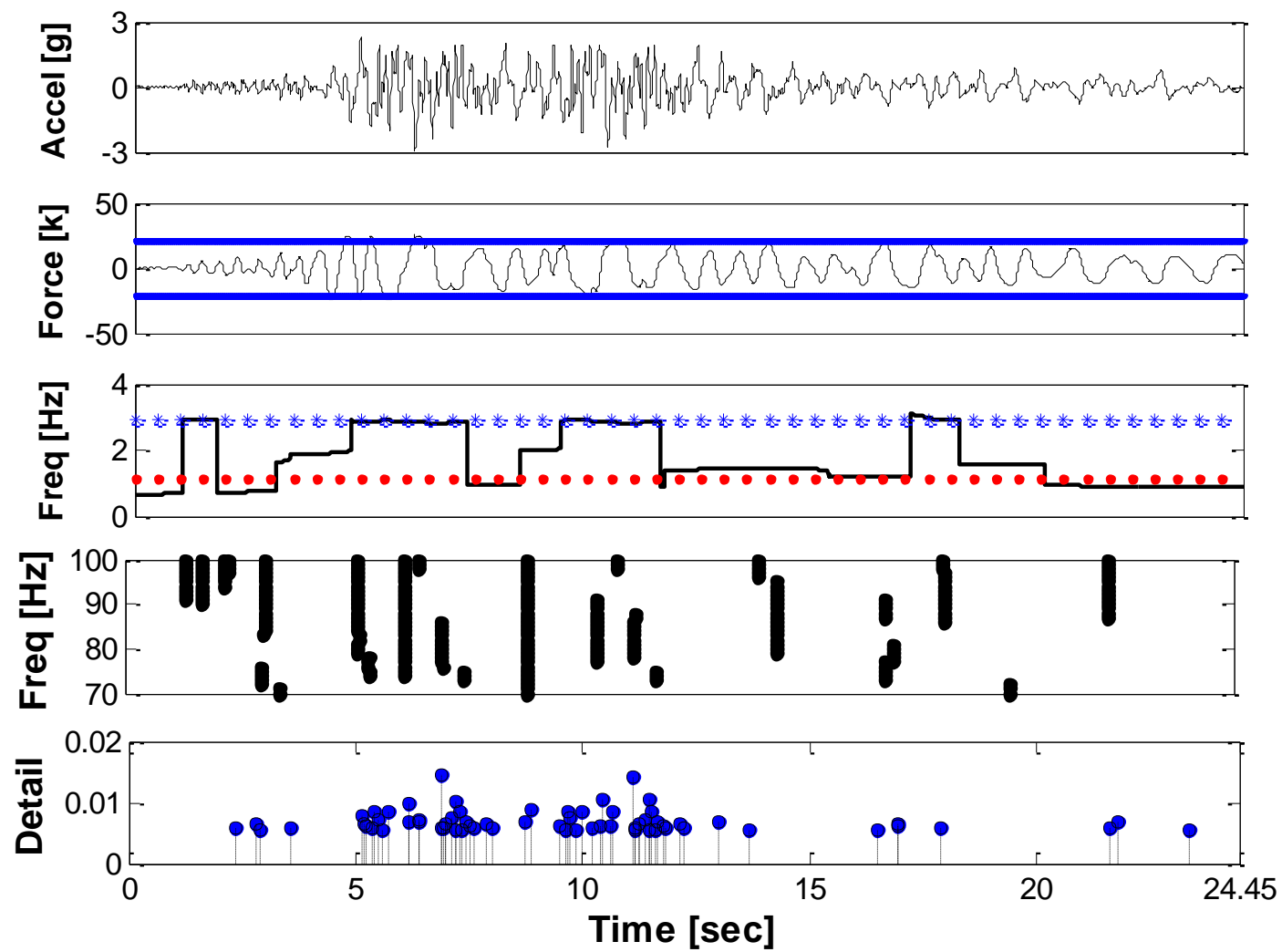


Figure 6-8: EQ2 (PGA₇): (a) Acceleration, (b) Force, (c) CWT low-freq, (d) CWT high freq, (e) DWT detail

6.3 Recommendations for future works

Suggestions for future lines of work that will improve and diversify the implementation of the analytical methodology proposed are presented next:

- Continue the calibration and development of the methodologies evaluated in this analytical research by using experimental data. For example, design and built the RC members and induce some damage while they are been excited with a shaker or a shake table in order to identify the damage. In addition, make emphasis in the effect of different excitation loads and the estimation of the level of damage.
- Further develop the methodology presented in this research to include other kinds of structures, e.g., shear walls, foundations, among others. Additionally, analyze structures of multiple degrees of freedom (MDOF) in contrast to systems with a single degree of freedom (SDOF) as was presented here.
- Instrument structures prone to suffer damage in a seismic event to have real data to validate and further calibrate the detection algorithms.
- Investigate more advanced techniques for the extraction of the ridges from the CWT results. This can certainly improve the results obtained for the structure instant frequency.

APPENDIX A

OPENSEES CODES

A.1 Cantilever Circular Column: FL-89A (bilinear model) used in Chapter II

```
#-----
#                               CANTILEVER CIRCULAR COLUMN FL89A (BILINEAR MODEL)
#                               LUIS R. VELAZQUEZ
#                               luis.velazquez16@gmail.com
#-----

#-----SET UP-----
wipe;                                # create data directory
set dataDir Data/FL89A-BILINEAR;    # set up name of data directory
file mkdir $dataDir;                # create data directory
model BasicBuilder -ndm 2 -ndf 3;    # Define the model builder, ndm=#dimension,
                                     ndf=#dofs

# Units: Kips, in, seg

#-----GEOMETRIC PROPERTIES-----
set LCol 65;                         # column length [in]
set DCol 18;                         # column diameter [in]
set ACol 254.2464;                   # column cross-sectional area [in2]
set IzCol 2628.3455;                 # column moment of inertia [in4]
set Ec 3355;                         # column modulus of elasticity [ksi]
set Weight 51.9308;                  # structure weight [kips]

#-----CALCULATED PARAMETERS-----
set PCol $Weight;                   # nodal dead-load weight per column
set g 386.2204;                     # gravity [in/sec2]
set Mass [expr $PCol/$g];           # nodal mass

#-----NODAL COORDINATES & BOUNDARY CONDITIONS-----
node 1 0 0;                          # node# X, Y
node 2 0 $LCol;

fix 1 1 1 1;                          # node DX, DY, DZ

#-----NODAL MASSES-----
mass 2 $Mass 1e-9 0.;                # node#, Mx My Mz, neglect rotational inertia at
nodes

#-----COLUMN STIFFNESS PARAMETERS-----
set EICol [expr $Ec*$IzCol];          # EI, for moment-curvature relationship
set EACol [expr $Ec*$ACol];           # EA, for axial-force-strain
relationship
set MyCol 4097.895;                   # yield moment
set b 0.0012;                         # strain-hardening ratio
```

```

#-----SECTION MODEL PROPERTIES-----
set ColSecTag 1;          # assign a tag number to the column section tag
set ColMatTagFlex 2;      # assign a tag number to the column flexural
behavior
set ColMatTagAxial 3;     # assign a tag number to the column axial behavior
#-----SECTION GENERATION-----
uniaxialMaterial Steel01 $ColMatTagFlex $MyCol $EICol $b;          # bilinear behavior
for flexure
uniaxialMaterial Elastic $ColMatTagAxial $EACol;                  # this is not used
as a material, this is an axial-force-strain response
section Aggregator $ColSecTag $ColMatTagAxial P $ColMatTagFlex Mz; # combine
axial and flexural behavior

#-----ELEMENTS GENERATION-----
set ColTransfTag 1;      # associate a tag to column transformation
geomTransf Linear $ColTransfTag;
set numIntgrPts 5;       # number of integration points for force-based element
element nonlinearBeamColumn 1 1 2 $numIntgrPts $ColSecTag $ColTransfTag; # self-
explanatory when using variables

#-----RECORDERS-----
recorder Node -file $dataDir/DFree.out -time -node 2 -dof 1 2 3 disp;
# displacements of free nodes
recorder Node -file $dataDir/DBase.out -time -node 1 -dof 1 2 3 disp;
# displacements of support nodes
recorder Node -file $dataDir/RBase.out -time -node 1 -dof 1 2 3 reaction;
# support reaction
recorder Drift -file $dataDir/Drift.out -time -iNode 1 -jNode 2 -dof 1 -perpDirn 2;
# lateral drift
recorder Element -file $dataDir/FCol.out -time -ele 2 globalForce;
# element forces -- column

#-----SET UP PARAMETERS-----
set IDctrlNode 2;        # node where displacement is read for displacement control
set IDctrlDOF 1;         # degree of freedom of displacement read for displacement control
set iPushNode 2;         # define node where lateral load is applied in static lateral
analysis
set iDmax "0.001         0.003         0.007         0.009         0.011         0.011
0.011         0.016         0.016         0.016         0.023         0.023         0.023
0.028         0.028         0.028         0.035         0.035         0.035         0.046
0.046         0.046         0.067         0.067         0.067         0.088         0.089
0.091";                # vector of displacement-cycle peaks, in terms of storey drift
ratio
set Dmax [expr 0.025*$LCol];          # maximum displacement of pushover
set Dincr [expr 0.001*$LCol];         # displacement increment for pushover
set Fact $LCol
set CycleType Full
set Ncycles 1

#-----APPLY GRAVITY LOAD-----
pattern Plain 101 Linear {
    load      2    0 -$PCol 0
}

set Tol 1.0e-8;                    # convergence tolerance for test

```

```

variable constraintsTypeGravity Plain;          # default
if { [info exists RigidDiaphragm] == 1 } {
    if {$RigidDiaphragm=="ON"} {
        variable constraintsTypeGravity Lagrange;      # large model: try
Transformation
    };      # if rigid diaphragm is on
};      # if rigid diaphragm exists
constraints $constraintsTypeGravity ;           # how it handles boundary
conditions
numberer RCM;      # renumber dofs to minimize band-width (optimization)
system BandGeneral; # how to store and solve the system of equations in the analysis
test NormDispIncr $Tol 6; # determine if convergence has been achieved at the end of
an iteration step
algorithm Newton;  # use Newtons solution algorithm: updates tangent stiffness at
every iteration
set NstepGravity 10;      # apply gravity in 10 steps
set DGravity [expr 1./$NstepGravity]; # first load increment
integrator LoadControl $DGravity; # determine the next time step for an analysis
analysis Static;          # define type of analysis static or transient
analyze $NstepGravity;    # apply gravity

loadConst -time 0.0

puts "Model Built"

```

A.2 Cantilever Circular Column: FL-89A (Takeda model) used in Chapter II

```

#-----
#          CANTILEVER CIRCULAR COLUMN FL89A (TAKEDA MODEL)
#          LUIS R. VELAZQUEZ
#          luis.velazquez16@gmail.com
#-----

#-----SET UP-----
wipe;      # create data directory
set dataDir Data/FL89A-TAKEDA;      # set up name of data directory
file mkdir $dataDir;      # create data directory
model BasicBuilder -ndm 2 -ndf 3;      # Define the model builder, ndm=#dimension,
ndf=#dofs
# Units: Kips, in, seg

#-----GEOMETRIC PROPERTIES-----
set LCol 65;      # column length [in]
set DCol 18;      # column diameter [in]
set ACol 254.2464;      # column cross-sectional area [in2]
set IzCol 2628.3455;      # column moment of inertia [in4]
set Ec 3355;      # column modulus of elasticity [ksi]
set Weight 51.9308;      # structure weight [kips]

#-----CALCULATED PARAMETERS-----
set PCol $Weight;      # nodal dead-load weight per column

```

```

set g 386.2204;                # gravity [in/sec2]
set Mass [expr $PCol/$g]; # nodal mass

#-----NODAL COORDINATES & BOUNDARY CONDITIONS-----
node 1 0 0;                    # node# X, Y
node 2 0 $LCol;
fix 1 1 1 1;                   # node DX, DY, DZ

#-----NODAL MASSES-----
mass 2 $Mass 1e-9 0.;         # node#, Mx My Mz, neglect rotational inertia at nodes

#-----COLUMN STIFFNESS PARAMETERS-----
set EACol [expr $Ec*$ACol];    # EA, for axial-force-strain relationship
set Mn 4097.895;              # yield moment
set phynom 0.4021e-3;         # yield curvature
set Mu 4403.778;              # ultimate moment
set phyult 0.018515;          # ultimate curvature

set Mnn -4097.895;            # yield moment
set phynomn -0.4021e-3;       # yield curvature
set Mun -4403.778;           # ultimate moment
set phyultn -0.018515;       # ultimate curvature

set pinchX 1;                # pinching factor for strain (or deformation) during reloading
set pinchY 1;                # pinching factor for stress (or force) during
reloading
set damage1 0.002;           # damage due to ductility: D1(mu-1)
set damage2 0.0015;          # damage due to energy: D2(Eii/Eult)
set beta 0.5;                # power used to determine the degraded unloading
                              # stiffness based on ductility

#-----SECTION MODEL PROPERTIES-----
set ColMatTagFlex 2;          # assign a tag number to the column flexural
                              # behavior
set ColMatTagAxial 3;         # assign a tag number to the column axial behavior
set ColSecTag 1;              # assign a tag number to the column section tag

#-----SECTION GENERATION-----
uniaxialMaterial Hysteretic $ColMatTagFlex $Mn $phynom $Mu $phyult $Mnn $phynomn $Mun
$phyultn $pinchX $pinchY $damage1 $damage2 $beta; # bilinear behavior for flexure

uniaxialMaterial Elastic $ColMatTagAxial $EACol;                # this is not used
as a material, this is an axial-force-strain response

section Aggregator $ColSecTag $ColMatTagAxial P $ColMatTagFlex Mz; # combine
axial and flexural behavior

#-----ELEMENTS GENERATION-----
set ColTransfTag 1;          # associate a tag to column transformation
geomTransf Linear $ColTransfTag;
set numIntgrPts 5;           # number of integration points for force-based element
element nonlinearBeamColumn 1 1 2 $numIntgrPts $ColSecTag $ColTransfTag; # self-
explanatory when using variables

```



```

#-----RECORDERS-----
recorder Node -file $dataDir/DFree.out -time -node 2 -dof 1 2 3 disp;
    # displacements of free nodes
recorder Node -file $dataDir/DBase.out -time -node 1 -dof 1 2 3 disp;
    # displacements of support nodes
recorder Node -file $dataDir/RBase.out -time -node 1 -dof 1 2 3 reaction;
    # support reaction
recorder Drift -file $dataDir/Drift.out -time -iNode 1 -jNode 2 -dof 1 -perpDirn 2;
    # lateral drift
recorder Element -file $dataDir/FCol.out -time -ele 2 globalForce;
    # element forces -- column

#-----SET UP PARAMETERS-----
set IDctrlNode 2;    # node where displacement is read for displacement control
set IDctrlDOF 1;    # degree of freedom of displacement read for displacement control
set iPushNode 2;    # define node where lateral load is applied in static lateral
analysis
set iDmax "0.001      0.003      0.007      0.009      0.011      0.011
0.011      0.016      0.016      0.016      0.023      0.023      0.023
0.028      0.028      0.028      0.035      0.035      0.035      0.046
0.046      0.046      0.067      0.067      0.067      0.088      0.089
0.091";
    # vector of displacement-cycle peaks, in terms of storey drift
ratio
set Dmax [expr 0.025*$LCol];    # maximum displacement of pushover
set Dincr [expr 0.001*$LCol];  # displacement increment for pushover

set Fact $LCol
set CycleType Full
set Ncycles 1

#-----APPLY GRAVITY LOAD-----
pattern Plain 101 Linear {
    load      2      0 -$PCol 0
}

set Tol 1.0e-8;    # convergence tolerance for test
variable constraintsTypeGravity Plain;    # default
if { [info exists RigidDiaphragm] == 1 } {
    if {$RigidDiaphragm=="ON"} {
        variable constraintsTypeGravity Lagrange;    # large model: try
Transformation
    };    # if rigid diaphragm is on
};    # if rigid diaphragm exists
constraints $constraintsTypeGravity ;    # how it handles boundary
conditions
numberer RCM;    # renumber dofs to minimize band-width (optimization)
system BandGeneral ;    # how to store and solve the system of equations in the
analysis (large model: try UmfPack)
test NormDispIncr $Tol 6;    # determine if convergence has been achieved at the end of
an iteration step
algorithm Newton;    # use Newtons solution algorithm: updates tangent
stiffness at every iteration
set NstepGravity 10;    # apply gravity in 10 steps
set DGravity [expr 1./$NstepGravity];    # first load increment

```

```

integrator LoadControl $DGravity;      # determine the next time step for an
                                         analysis
analysis Static;                       # define type of analysis static or transient
analyze $NstepGravity;                 # apply gravity
loadConst -time 0.0
puts "Model Built"

```

A.3 Cantilever Circular Column: FL-89A (Fiber-based model) used in Chapter II

```

#-----
#                               CANTILEVER CIRCULAR COLUMN FL89A (FIBERS-BASED MODEL)
#                               LUIS R. VELAZQUEZ
#                               luis.velazquez16@gmail.com
#-----

#-----SET UP-----
wipe;                                # create data directory
set dataDir Data2/FL89A-FIBERS;      # set up name of data directory
file mkdir $dataDir;                 # create data directory
model BasicBuilder -ndm 2 -ndf 3;     # Define the model builder, ndm=#dimension,
                                         ndf=#dofs

source BuildRCSectionCIR.tcl;        # procedure for definining circular RC fiber
                                         section

# units: Kip, inch, sec

#-----GEOMETRIC PROPERTIES-----
set LCol      65;                    # column length [in]
set DCol      18;                    # column diameter [in]
set numBars    8;                    # number of longitudinal bars
set cover     1.500;                 # cover for longitudinal bars [in]
set Dbar      1.128;                 # longitudinal bar diameter [in]
set barArea   0.995;                 # area of longitudinal bars [in2]
set rsec      9.000;                 # section radius [in]
set rcore     7.688;                 # core section [in]
set rbars     6.938;                 # bar distribution radius [in]
set A         254.469;                # cross-sectional area [in2]
set I         2628.345;                # section moment of inertia [in4]
set E         3355.000;                # section modulus of elasticity [ksi]
set Weight    51.931;                # structure weight [kips]
set Lp        16.300;                # equivalent plastic hinge length [in]

#-----CONCRETE PROPERTIES-----
#------(Concrete 02)-----
set fc1U      -3.100;                # unconfined concrete compressive strength [ksi]
set eps1U     -0.002;                # strain at maximum stress from unconfined concrete
set fc2U      -0.006;                # residual strength for the unconfined concrete [ksi]
set eps2U     -0.006;                # strain at ultimate stress unconfined

set fc1C      -5.270;                # confined concrete compressive strength [ksi]
set eps1C     -0.009;                # strain at maximum stress from confined concrete
set fc2C      -4.427;                # residual strength for the confined concrete [ksi]
set eps2C     -0.045;                # strain at ultimate stress confined

set IDconcCore 1;

```

```

set IDconcCover 2;

uniaxialMaterial Concrete02 $IDconcCore $fc1C $eps1C $fc2C $eps2C;
    # Core concrete (confined)
uniaxialMaterial Concrete02 $IDconcCover $fc1U $eps1U $fc2U $eps2U;
    # Cover concrete (unconfined)

#-----REINFORCING STEEL PROPERTIES-----
#------(Reinforcing Steel Material, Mohle and Kunnath)-----
#------(Coffin-Manson Fatigue and Strength Reduction)-----
set Fy      81.000;      # STEEL yield stress [ksi]
set Fu      102.000;     # STEEL max stress [ksi]
set Es      29000.000;   # STEEL modulus [ksi]
set Esh      726.000;    # Tangent at initial strain hargening [ksi]
set eish      0.008;     # Strain corresponding to initial strain hardening
set eult      0.100;     # Strain at peak stress

set alpha    0.506;      # usually constant for a material type
set Cf        0.340;     # adjust the number of cycles to failure
set Cd        0.600;     # Strength reduction constant

set R1        0.383;
set R2       10.000;
set R3         4.000;

#set Lu        2.350;     # Unsupported Length
#set lsr [expr $Lu/$Dbar]; # Slenderness ratio
#set alpha2 1.000;       # Adjustment Constant usually between 0.75 and 1.0,
                        # Default: alpha2=1.0

#set beta      1.0;      # Amplification factor for the buckled stress strain curve
#set r          0.0;     # Buckling reduction factor
                        # r can be a real number between [0.0 and 1.0]
                        # r=1.0 full reduction (no buckling)
                        # r=0.0 no reduction
#set gama      0.5;      # Buckling constant

set IDSteel    3;
uniaxialMaterial ReinforcingSteel $IDSteel $Fy $Fu $Es $Esh $eish $eult -CMFatigue
$Cf $alpha $Cd -MPCurveParams $R1 $R2 $R3; # -GABuck $lsr $beta $r $gama; #-DMBuck
$lsr $alpha2;

#-----SECTION MODEL PROPERTIES-----
set nfCoreR    10;      # number of radial divisions in the core (number of "rings")
set nfCoreT    20;      # number of theta divisions in the core (number of "wedges")
set nfCoverR    2;      # number of radial divisions in the cover
set nfCoverT    20;      # number of theta divisions in the cover
set ColSecTag    1;

#-----SECTION GENERATION-----
BuildRCSectionCIR $ColSecTag $Dbar $rsec $rcore $rbars $IDconcCore $IDconcCover
$IDSteel $numBars $barArea $nfCoreR $nfCoreT $nfCoverR $nfCoverT;

#-----CALCULATED PARAMETERS-----
set PCol $Weight;      # nodal dead-load weight per column

```

```

set g 386.2204;          # gravity [in/sec2]
set Mass [expr $PCol/$g]; # nodal mass

#-----NODAL COORDINATES & BOUNDARY CONDITIONS-----
node 1 0 0;              # node# X, Y
node 2 0 $LCol;

fix 1 1 1 1;             # node DX, DY, DZ

#-----NODAL MASSES-----
mass 2 $Mass 1e-9 0.;    # node#, Mx My Mz, neglect rotational inertia at
nodes

#-----ELEMENTS GENERATION-----
set ColTransfTag 1;      # associate a tag to column transformation
geomTransf Linear $ColTransfTag;
set numIntgrPts 5;       # number of Gauss integration points for nonlinear
                           curvature distribution
element beamWithHinges 1 1 2 $ColSecTag $Lp $ColSecTag $Lp $E $A $I $ColTransfTag;

#-----RECORDERS-----
recorder Node -file $dataDir/DFree.out -time -node 2 -dof 1 2 3 disp;
    # displacements of free nodes

recorder Node -file $dataDir/RBase.out -time -node 1 -dof 1 2 3 reaction;
    # support reaction

recorder Element -file $dataDir/DefoEle1sec1.out -time -ele 1 section 1 deformation;
    # section deformations, axial and curvature at base

recorder Element -file $dataDir/SteelSSEle1sec1.out -time -ele 1 section 1 fiber -
    $rbars 0 $IDSteel stressStrain; # steel fiber stress-strain at base

recorder Element -file $dataDir/CoreSSEle1sec1.out -time -ele 1 section 1 fiber
    $rcore 0 $IDconcCore stressStrain; # steel fiber stress-strain at base

recorder Element -file $dataDir/CoverSSEle1sec1.out -time -ele 1 section 1 fiber
    $rsec 0 $IDconcCover stressStrain; # steel fiber stress-strain at base

#-----SET UP PARAMETERS-----
set IDctrlNode 2;        # node where displacement is read for displacement control
set IDctrlDOF 1;         # degree of freedom of displacement read for displacement control
set iPushNode 2;         # define node where lateral load is applied in static lateral
                           analysis
set iDmax "0.001         0.003         0.007         0.009         0.011         0.011
0.011         0.016         0.016         0.016         0.023         0.023         0.023
0.028         0.028         0.028         0.035         0.035         0.035         0.046
0.046         0.046         0.067         0.067         0.067         0.088         0.089
0.091";
                           # vector of displacement-cycle peaks, in terms of storey drift
                           ratio
set Dincr 0.013;         # displacement increment for pushover
set Dmax 6.500;          # maximum displacement increment for monotonic pushover

set Fact $LCol
set CycleType Full

```

```

set Ncycles 1
#-----APPLY GRAVITY LOAD-----
pattern Plain 101 Linear {
    load      2    0 -$PCol 0
}

set Tol 1.0e-8;                # convergence tolerance for test
variable constraintsTypeGravity Plain;    # default
if { [info exists RigidDiaphragm] == 1 } {
    if {$RigidDiaphragm=="ON"} {
        variable constraintsTypeGravity Lagrange;    # large model: try
                                                    Transformation
    };    # if rigid diaphragm is on
    # if rigid diaphragm exists
    # how it handles boundary
constraints $constraintsTypeGravity ;
conditions
numberer RCM;    # renumber dofs to minimize band-width (optimization)
system BandGeneral ;    # how to store and solve the system of equations in the
                        analysis
test NormDispIncr $Tol 6; # determine if convergence has been achieved at the end of
                        an iteration step
algorithm Newton;    # use Newtons solution algorithm: updates tangent
                        stiffness at every iteration
set NstepGravity 10;    # apply gravity in 10 steps
set DGravity [expr 1./$NstepGravity];    # first load increment
integrator LoadControl $DGravity;    # determine the next time step for an
                        analysis
analysis Static;    # define type of analysis static or transient
analyze $NstepGravity;    # apply gravity

loadConst -time 0.0
puts "Model Built"

```

A.4 Cantilever Circular Column: SL-P20 (Fiber-based model) used in Chapter II

```

#-----
#    CANTILEVER CIRCULAR COLUMN: SL-P20 (FIBERS-BASED MODEL)
#    LUIS R. VELAZQUEZ
#    luis.velazquez16@gmail.com
#-----
#-----SET UP-----
wipe;    # create data directory
set dataDir Data/SLP20;    # set up name of data directory
file mkdir $dataDir;    # create data directory
model BasicBuilder -ndm 2 -ndf 3;    # Define the model builder, ndm=#dimension,
                        ndf=#dofs
source BuildRCSectionCIR.tcl;    # procedure for definining circular RC fiber
                        section

# units: Kip, inch, sec

#-----GEOMETRIC PROPERTIES-----
set pi 3.141592654;
set lCol 65.000;    # column length [in]

```

```

set DCol      18.000;          # column diameter [in]
set numBars    8;              # number of longitudinal bars
set cover      1.000;          # cover for longitudinal bars [in]
set Dbar       0.625;          # longitudinal bar diameter (bar #5) [in]
set barArea    0.307;          # area of longitudinal bars [in2]
set dbar       0.375;          # transversal bar diameter (bar #3) [in]
set rsec       [expr $DCol/2]; # section radius [in]
set rcore      [expr $rsec-$cover-($dbar/2)]; # core section [in]
set rbars      [expr $rsec-$cover-$dbar-($Dbar/2)]; # bar distribution radius [in]
set A          [expr $pi/4*pow($DCol,2)]; # cross-sectional area [in2]
set I          1016.000;       # section moment of inertia [in4]
set E          4550.000;       # section modulus of elasticity [ksi]
set Weight     0.100;          # structure weight [kips]
set Lp         8.750;          # equivalent plastic hinge length [in]

#-----CONCRETE PROPERTIES-----
#------(Concrete 02)-----
set fc1U      -5.700;          # unconfined concrete compressive strength [ksi]
set eps1U     -0.002;          # strain at maximum stress from unconfined concrete
set fc2U      -0.011;          # residual strength for the unconfined concrete [ksi]
set eps2U     -0.006;          # strain at ultimate stress unconfined

set fc1C      -7.809;          # confined concrete compressive strength [ksi]
set eps1C     -0.006;          # strain at maximum stress from confined concrete
set fc2C      -5.310;          # residual strength for the confined concrete [ksi]
set eps2C     -0.030;          # strain at ultimate stress confined

set IDconcCore 1;
set IDconcCover 2;

uniaxialMaterial Concrete01 $IDconcCore $fc1C $eps1C $fc2C $eps2C;
# Core concrete (confined)
uniaxialMaterial Concrete01 $IDconcCover $fc1U $eps1U $fc2U $eps2U ;
# Cover concrete (unconfined)

#-----REINFORCING STEEL PROPERTIES-----
#------(Reinforcing Steel Material, Mohle and Kunnath)-----
#------(Coffin-Manson Fatigue and Strength Reduction)-----
set Fy        73.000;          # STEEL yield stress [ksi]
set Fu        100.000;         # STEEL max stress [ksi]
set Es        29000.000;        # STEEL modulus [ksi]
set Esh       943.000;          # Tangent at initial strain hargening [ksi]
set eish      0.008;           # Strain corresponding to initial strain hardening
set eult      0.110;           # Strain at peak stress
set alpha     0.506;           # usually constant for a material type
set Cf        0.300;           # adjust the number of cycles to failure
set Cd        0.650;           # Strength reduction constant

set R1        0.484;
set R2        8.000;
set R3        4.000;

set IDSteel    3;
uniaxialMaterial ReinforcingSteel $IDSteel $Fy $Fu $Es $Esh $eish $eult -
MPCurveParams $R1 $R2 $R3 -CMFatigue $Cf $alpha $Cd;

```

```

#-----SECTION MODEL PROPERTIES-----
set nfCoreR    10; # number of radial divisions in the core (number of "rings")
set nfCoreT    20; # number of theta divisions in the core (number of "wedges")
set nfCoverR    2; # number of radial divisions in the cover
set nfCoverT    20; # number of theta divisions in the cover
set ColSecTag   1;

#-----SECTION GENERATION-----
BuildRCSectionCIR $ColSecTag $Dbar $rsec $rcore $rbars $IDconcCore $IDconcCover
$IDSteel $numBars $barArea $nfCoreR $nfCoreT $nfCoverR $nfCoverT;

#-----CALCULATED PARAMETERS-----
set PCol $Weight;          # nodal dead-load weight per column
set g 386.2204;            # gravity [in/sec2]
set Mass [expr $PCol/$g];  # nodal mass

#-----NODAL COORDINATES & BOUNDARY CONDITIONS-----
node 1 0 0;                # node# X, Y
node 2 0 $LCol;

fix 1 1 1 1;               # node DX, DY, DZ

#-----NODAL MASSES-----
mass 2 $Mass 1e-9 0.;      # node#, Mx My Mz, neglect rotational inertia at
nodes

#-----ELEMENTS GENERATION-----
set ColTransfTag 1;        # associate a tag to column transformation
geomTransf Linear $ColTransfTag;
set numIntgrPts 5;         # number of Gauss integration points for nonlinear
                           # curvature distribution
element beamWithHinges 1 1 2 $ColSecTag $Lp $ColSecTag $Lp $E $A $I
$ColTransfTag;

#-----RECORDERS-----
recorder Node -file $dataDir/DFree.out -time -node 2 -dof 1 2 3 disp;
                           # displacements of free nodes

recorder Node -file $dataDir/RBase.out -time -node 1 -dof 1 2 3 reaction;
                           # support reaction

recorder Element -file $dataDir/DefoEle1sec1.out -time -ele 1 section 1 deformation;
                           # section deformations, axial and curvature at base

recorder Element -file $dataDir/SteelSSEle1sec1.out -time -ele 1 section 1 fiber -
$rbars 0 $IDSteel stressStrain; # steel fiber stress-strain at base

recorder Element -file $dataDir/CoreSSEle1sec1.out -time -ele 1 section 1 fiber
$rcore 0 $IDconcCore stressStrain; # steel fiber stress-strain at base

recorder Element -file $dataDir/CoverSSEle1sec1.out -time -ele 1 section 1 fiber
$rsec 0 $IDconcCover stressStrain; # steel fiber stress-strain at base

```

```

#-----SET UP PARAMETERS-----
set IDctrlNode 2;      # node where displacement is read for displacement control
set IDctrlDOF 1;      # degree of freedom of displacement read for displacement control
set iPushNode 2;      # define node where lateral load is applied in static lateral
                        analysis
set iDmax "0.001      0.002      0.003      0.005      0.01      0.01
0.01      0.014      0.014      0.014      0.019      0.019      0.019
0.03      0.03      0.03      0.039      0.039      0.039      0.049
0.049      0.049      0.059      0.059      0.059      0.08      0.08";
# vector of displacement-cycle peaks, in terms of storey drift ratio

set Dincr 0.013;      # displacement increment for pushover
set Dmax 6.500;      # maximum displacement increment for monotonic
                        pushover

set Fact $LCol
set CycleType Full
set Ncycles 1

#-----APPLY GRAVITY LOAD-----
pattern Plain 101 Linear {
    load      2      0 -$PCol 0
}

set Tol 1.0e-8;      # convergence tolerance for test
variable constraintsTypeGravity Plain;      # default
if { [info exists RigidDiaphragm] == 1 } {
    if {$RigidDiaphragm=="ON"} {
        variable constraintsTypeGravity Lagrange;      # large model: try
Transformation
    };
};      # if rigid diaphragm is on
      # if rigid diaphragm exists
constraints $constraintsTypeGravity ;      # how it handles boundary conditions
numberer RCM;      # renumber dofs to minimize band-width (optimization)
system BandGeneral ;      # how to store and solve the system of equations in the
                        analysis
test NormDispIncr $Tol 6 ;# determine if convergence has been achieved at the end of
                        an iteration step
algorithm Newton;      # use Newtons solution algorithm: updates tangent
                        stiffness at every iteration
set NstepGravity 10;      # apply gravity in 10 steps
set DGravity [expr 1./$NstepGravity];      # first load increment
integrator LoadControl $DGravity;      # determine the next time step for an
                        analysis
analysis Static;      # define type of analysis static or transient
analyze $NstepGravity;      # apply gravity

loadConst -time 0.0
puts "Model Built"

```

A.5 Cantilever Circular Column: EUCENTRE (Fiber-based model) used in Chapter II

```

#-----
#          CANTILEVER CIRCULAR COLUMN FIBERS ELEMENTS - EUCENTRE TEST
#          LUIS R. VELAZQUEZ

```



```

#                               luis.velazquez16@gmail.com
#-----
#-----SET UP-----
wipe;                               # create data directory
set dataDir Data/EUCENTRE;         # set up name of data directory
file mkdir $dataDir;               # create data directory
model BasicBuilder -ndm 2 -ndf 3;   # Define the model builder, ndm=#dimension,
                                   ndf=#dofs
source BuildRCSectionCIR.tcl;       # procedure for definining hollow circular RC
                                   fiber section

# units: Kip, inch, sec

#-----GEOMETRIC PROPERTIES-----
set LCol      80.00;                # column length [in]
set DCol      18.00;                # column diameter [in]
set numBars   18;                   # number of longitudinal bars
set cover     1.000;                # cover for longitudinal bars [in]
set Dbar      0.394;                # longitudinal bar diameter [in]
set barArea   0.125;                # area of longitudinal bars [in2]
set rsec      9.000;                # section radius [in]
set rcore     8.125;                # core section [in]
set rbars     7.550;                # bar distribution radius [in]
set A         254.000;              # cross-sectional area [in2]
set I         1226.000;              # section moment of inertia [in4]
set E         3916.000;              # section modulus of elasticity [ksi]
set Weight    17.200;               # structure weight [kips]
set Lp        10.700;               # equivalent plastic hinge length [in]

#-----CONCRETE PROPERTIES-----
#------(Concrete 02)-----
set fc1U      -5.656;                # unconfined concrete compressive strength [ksi]
set eps1U     -0.002;                # strain at maximum stress from unconfined concrete
set fc2U      -0.006;                # residual strength for the unconfined concrete [ksi]
set eps2U     -0.006;                # strain at ultimate stress unconfined

set fc1C      -7.491;                # confined concrete compressive strength [ksi]
set eps1C     -0.005;                # strain at maximum stress from confined concrete
set fc2C      -4.467;                # residual strength for the confined concrete [ksi]
set eps2C     -0.026;                # strain at ultimate stress confined

set IDconcCore 1;
set IDconcCover 2;

uniaxialMaterial Concrete01 $IDconcCore $fc1C $eps1C $fc2C $eps2C;
# Core concrete (confined)
uniaxialMaterial Concrete01 $IDconcCover $fc1U $eps1U $fc2U $eps2U;
# Cover concrete (unconfined)

#-----REINFORCING STEEL PROPERTIES-----
#------(Reinforcing Steel Material, Mohle and Kunnath)-----
#------(Coffin-Manson Fatigue and Strength Reduction)-----
set Fy        75.000;                # STEEL yield stress [ksi]
set Fu        104.500;                # STEEL max stress [ksi]
set Es       29000.000;                # STEEL modulus [ksi]
set Esh       726.000;                # Tangent at initial strain hargening [ksi]

```

```

set eish 0.008; # Strain corresponding to initial strain hardening
set eult 0.100; # Strain at peak stress
set alpha 0.506; # usually constant for a material type
set Cf 0.250; # adjust the number of cycles to failure
set Cd 0.500; # Strength reduction constant
set R1 0.383;
set R2 16.000;
set R3 8.000;

set IDSteel 3;

uniaxialMaterial ReinforcingSteel $IDSteel $Fy $Fu $Es $Esh $eish $eult -
MPCurveParams $R1 $R2 $R3 -CMFatigue $Cf $alpha $Cd;

#-----SECTION MODEL PROPERTIES-----
set nfCoreR 20; # number of radial divisions in the core (number of "rings")
set nfCoreT 40; # number of theta divisions in the core (number of "wedges")
set nfCoverR 4; # number of radial divisions in the cover
set nfCoverT 40; # number of theta divisions in the cover
set ColSecTag 1;

#-----SECTION GENERATION-----
BuildRCSectionCIR $ColSecTag $Dbar $rsec $rcore $rbars $IDconcCore $IDconcCover
$IDSteel $numBars $barArea $nfCoreR $nfCoreT $nfCoverR $nfCoverT;

#-----CALCULATED PARAMETERS-----
set PCol $Weight; # nodal dead-load weight per column
set g 386.2204; # gravity [in/sec2]
set Mass [expr $PCol/$g]; # nodal mass

#-----NODAL COORDINATES & BOUNDARY CONDITIONS-----
node 1 0 0; # node# X, Y
node 2 0 $LCol;

fix 1 1 1 1; # node DX, DY, DZ

#-----NODAL MASSES-----
mass 2 $Mass 1e-9 0.0; # node#, Mx My Mz, neglect rotational inertia at
nodes

#-----ELEMENTS GENERATION-----
set ColTransfTag 1; # associate a tag to column transformation
geomTransf Linear $ColTransfTag;
set numIntgrPts 5; # number of Gauss integration points for nonlinear
curvature distribution

element beamWithHinges 1 1 2 $ColSecTag $Lp $ColSecTag $Lp $E $A $I
$ColTransfTag;

#-----RECORDERS-----
recorder Node -file $dataDir/DFree.out -time -node 2 -dof 1 2 3 disp;
# displacements of free nodes

recorder Node -file $dataDir/RBase.out -time -node 1 -dof 1 2 3 reaction;
# support reaction

```

```

recorder Element -file $dataDir/DefoEle1sec1.out -time -ele 1 section 1 deformation;
                    # section deformations, axial and curvature at base

recorder Element -file $dataDir/SteelSSEle1sec1.out -time -ele 1 section 1 fiber -
$rbars 0 $IDSteel stressStrain; # steel fiber stress-strain at base

recorder Element -file $dataDir/CoreSSEle1sec1.out -time -ele 1 section 1 fiber
$rcore 0 $IDconcCore stressStrain; # steel fiber stress-strain at base

recorder Element -file $dataDir/CoverSSEle1sec1.out -time -ele 1 section 1 fiber
$rsec 0 $IDconcCover stressStrain; # steel fiber stress-strain at base

#-----SET UP PARAMETERS-----
set IDctrlNode 2; # node where displacement is read for displacement control
set IDctrlDOF 1; # degree of freedom of displacement read for displacement control
set iPushNode 2; # define node where lateral load is applied in static lateral
analysis
set iDmax "0.000419      0.000419      0.000419      0.000851      0.000851
0.000851      0.00726      0.00726      0.00726      0.017      0.017
0.017      0.00849      0.034      0.034      0.034      0.00849      0.049
0.049      0.049"; # vector of displacement-cycle peaks, in terms of
storey drift ratio

set Dincr 0.0002; # displacement increment for pushover
#set Dmax 5.000; # maximum displacement increment for monotonic pushover

set Fact $LCol
set CycleType Full
set Ncycles 1

#-----APPLY GRAVITY LOAD-----
pattern Plain 101 Linear {
    load      2      0 -$PCol 0
}
set Tol 1.0e-8; # convergence tolerance for test
variable constraintsTypeGravity Plain; # default
if { [info exists RigidDiaphragm] == 1 } {
    if {$RigidDiaphragm=="ON"} {
        variable constraintsTypeGravity Lagrange; # large model: try
Transformation
    }; # if rigid diaphragm is on
}; # if rigid diaphragm exists
constraints $constraintsTypeGravity ; # how it handles boundary conditions
numberer RCM; # renumber dofs to minimize band-width (optimization)
system BandGeneral ; # how to store and solve the system of equations in the
analysis
test NormDispIncr $Tol 6; # determine if convergence has been achieved at the end of
an iteration step
algorithm Newton; # use Newtons solution algorithm: updates tangent
stiffness at every iteration
set NstepGravity 10; # apply gravity in 10 steps
set DGravity [expr 1./$NstepGravity]; # first load increment
integrator LoadControl $DGravity; # determine the next time step for an
analysis

```

```

analysis Static;                # define type of analysis static or transient
analyze $NstepGravity;          # apply gravity
loadConst -time 0.0
puts "Model Built"

```

A.6 Cantilever Circular Column: UCSD (Fiber-based model) used in Chapter II

```

#-----
#   CANTILEVER CIRCULAR COLUMN FIBERS ELEMENTS - UCSD BRIDGE COLUMN CONTEST 2010
#   LUIS R. VELAZQUEZ
#   luis.velazquez16@gmail.com
#-----
#-----SET UP-----
wipe;                # create data directory
set dataDir Data/UCSD;    # set up name of data directory
file mkdir $dataDir;      # create data directory
model BasicBuilder -ndm 2 -ndf 3;    # Define the model builder, ndm=#dimension,
                                   ndf=#dofs
source BuildRCSectionCIR.tcl;    # procedure for definining circular RC fiber
                                   section
# units: Kip, inch, sec

#-----GEOMETRIC PROPERTIES-----
set pi 3.141592654;

set LCol 288.000;      # column length [in]
set DCol 48.000;       # column diameter [in]
set numBars 18;        # number of longitudinal bars
set cover 2.000;       # cover for longitudinal bars [in]
set Dbar 1.410;        # longitudinal bar diameter (#11) [in]
set barArea 1.560;     # area of longitudinal bars [in2]
set dbar 0.889;        # transversal bar diameter (2#5 -->
equivalent diameter) [in]
set rsec [expr $DCol/2];    # section radius [in]
set rcore [expr $rsec-$cover-($dbar/2)];    # core section [in]
set rbars [expr $rsec-$cover-$dbar-($Dbar/2)];    # bar distribution radius [in]
set A [expr $pi/4*pow($DCol,2)];    # cross-sectional area [in2]
set I 88252.000;        # section moment of inertia [in4]
set E 4411.000;         # section modulus of elasticity [ksi]
set Weight 521.500;     # structure weight [kips]
set Lp 36.930;          # equivalent plastic hinge length [in]

#-----CONCRETE PROPERTIES-----
#----- (Concrete 02)-----
set fc1U -5.366;        # unconfined concrete compressive strength [ksi]
set eps1U -0.002;       # strain at maximum stress from unconfined concrete
set fc2U -0.1450;       # residual strength for the unconfined concrete [ksi]
set eps2U -0.0063;      # strain at ultimate stress unconfined

set fc1C -6.984;        # confined concrete compressive strength [ksi]
set eps1C -0.005;       # strain at maximum stress from confined concrete
set fc2C -4.5617;       # residual strength for the confined concrete [ksi]
set eps2C -0.0263;      # strain at ultimate stress confined

```

```

set IDconcCore 1;
set IDconcCover 2;

uniaxialMaterial Concrete01 $IDconcCore $fc1C $eps1C $fc2C $eps2C;
    # Core concrete (confined)
uniaxialMaterial Concrete01 $IDconcCover $fc1U $eps1U $fc2U $eps2U;
    # Cover concrete (unconfined)

#-----REINFORCING STEEL PROPERTIES-----
#------(Reinforcing Steel Material, Mohle and Kunnath)-----
#------(Coffin-Manson Fatigue and Strength Reduction)-----
set Fy 75.200; # STEEL yield stress [ksi]
set Fu 102.400; # STEEL max stress [ksi]
set Es 29000.000; # STEEL modulus [ksi]
set Esh 726.000; # Tangent at initial strain hargening [ksi]
set eish 0.008; # Strain corresponding to initial strain hardening
set eult 0.100; # Strain at peak stress
set alpha 0.506; # usually constant for a material type
set Cf 0.300; # adjust the number of cycles to failure
set Cd 0.600; # Strength reduction constant

set R1 0.383;
set R2 16.000;
set R3 8.000;

set IDSteel 3;

uniaxialMaterial ReinforcingSteel $IDSteel $Fy $Fu $Es $Esh $eish $eult
-MPCurveParams $R1 $R2 $R3 -CMFatigue $Cf $alpha $Cd;

#-----SECTION MODEL PROPERTIES-----
set nfCoreR 20; # number of radial divisions in the core (number of "rings")
set nfCoreT 40; # number of theta divisions in the core (number of "wedges")
set nfCoverR 4; # number of radial divisions in the cover
set nfCoverT 40; # number of theta divisions in the cover
set ColSecTag 1;

#-----SECTION GENERATION-----
BuildRCSectionCIR $ColSecTag $Dbar $rsec $rcore $rbars $IDconcCore $IDconcCover
$IDSteel $numBars $barArea $nfCoreR $nfCoreT $nfCoverR $nfCoverT;

#-----CALCULATED PARAMETERS-----
set PCol $Weight; # nodal dead-load weight per column
set g 386.2204; # gravity [in/sec2]
set Mass [expr $PCol/$g]; # nodal mass

#-----NODAL COORDINATES & BOUNDARY CONDITIONS-----
node 1 0 0; # node# X, Y
node 2 0 $LCol;

fix 1 1 1 1; # node DX, DY, DZ

#-----NODAL MASSES-----
mass 2 $Mass 1e-9 0.; # node#, Mx My Mz, neglect rotational inertia at
nodes

```

```

#-----ELEMENTS GENERATION-----
set ColTransfTag 1;          # associate a tag to column transformation
geomTransf PDelta $ColTransfTag;
set numIntgrPts 5;          # number of Gauss integration points for nonlinear
                             curvature distribution

element beamWithHinges 1 1 2 $ColSecTag $Lp $ColSecTag $Lp $E $A $I
$ColTransfTag;

#-----RECORDERS-----
recorder Node -file $dataDir/DFree.out -time -node 2 -dof 1 2 3 disp;
                             # displacements of free nodes

recorder Node -file $dataDir/RBase.out -time -node 1 -dof 1 2 3 reaction;
                             # support reaction

recorder Element -file $dataDir/DefoEle1sec1.out -time -ele 1 section 1 deformation;
                             # section deformations, axial and curvature at base

recorder Element -file $dataDir/SteelSSEle1sec1.out -time -ele 1 section 1 fiber -
$rbars 0 $IDSteel stressStrain; # steel fiber stress-strain at base

recorder Element -file $dataDir/CoreSSEle1sec1.out -time -ele 1 section 1 fiber
$core 0 $IDconcCore stressStrain; # steel fiber stress-strain at base

recorder Element -file $dataDir/CoverSSEle1sec1.out -time -ele 1 section 1 fiber
$rsec 0 $IDconcCover stressStrain; # steel fiber stress-strain at base

#-----SET UP PARAMETERS-----
set IDctrlNode 2; # node where displacement is read for displacement control
set IDctrlDOF 1; # degree of freedom of displacement read for displacement control
set iPushNode 2; # define node where lateral load is applied in static lateral
analysis
set iDmax "0.007      0.007      0.007      0.013      0.013      0.013
0.026      0.026      0.026      0.052      0.052      0.052      0.079
0.079      0.079      0.092      0.092      0.092"; # vector of
displacement-cycle peaks, in terms of storey drift ratio

set Dincr 0.0035; # displacement increment for pushover
#set Dmax 5.000; # maximum displacement increment for monotonic pushover

set Fact $LCol
set CycleType Full
set Ncycles 1

#-----APPLY GRAVITY LOAD-----
pattern Plain 101 Linear {
    load      2      0 -$PCol 0
}

set Tol 1.0e-8; # convergence tolerance for test
variable constraintsTypeGravity Plain; # default
if { [info exists RigidDiaphragm] == 1 } {

```

```

        if {$RigidDiaphragm=="ON"} {
            variable constraintsTypeGravity Lagrange;      # large model: try
Transformation
        };                                              # if rigid diaphragm is on
    };                                              # if rigid diaphragm exists
constraints $constraintsTypeGravity ;                # how it handles boundary
conditions
numberer RCM;          # renumber dofs to minimize band-width (optimization)
system BandGeneral ;   # how to store and solve the system of equations in the
                        analysis
test NormDispIncr $Tol 6 ;# determine if convergence has been achieved at the end of
                        an iteration step
algorithm Newton;      # use Newtons solution algorithm: updates tangent
                        stiffness at every iteration
set NstepGravity 10;   # apply gravity in 10 steps
set DGravity [expr 1./$NstepGravity]; # first load increment
integrator LoadControl $DGravity;      # determine the next time step for an
analysis
analysis Static;          # define type of analysis static or transient
analyze $NstepGravity;    # apply gravity

loadConst -time 0.0

puts "Model Built"

```

A.7 Cantilever Circular Column: FL-89A (Fiber-based model) used in Chapter V

```

=====
#                                CANTILEVER CIRCULAR COLUMN FL89A FIBERS ELEMENTS
#                                LUIS R. VELAZQUEZ
#                                luis.velazquez16@gmail.com
=====
#==SETUP
=====
wipe;                                # create data directory
set dataDir Data5/FL89A;            # set up name of data directory
file mkdir $dataDir;                # create data directory
model BasicBuilder -ndm 2 -ndf 3;    # Define the model builder, ndm=#dimension
source BuildRCSectionCIR.tcl;        # procedure for defining circular RC fiber section

# units: Kip, inch, sec
set pi 3.141592654;

#=====
#== COLUMN GEOMETRIC PROPERTIES
#=====
set LCol      90;                    # column length [in]
set DCol      18;                    # column diameter [in]
set numBars    8;                    # number of longitudinal bars
set cover     1.500;                 # cover for longitudinal bars [in]
set Dbar      0.875;                 # longitudinal bar diameter [in]
set barArea   0.600;                 # area of longitudinal bars [in2]
set dbar      0.375;                 # transversal bar diameter (#3) [in]
set rsec      [expr $DCol/2];        # section radius [in]

```

```

set rcore    [expr $rsec-$cover-($dbar/2)];      # core section [in]
set rbars    [expr $rsec-$cover-$dbar-($Dbar/2)]; # bar distribution radius [in]
set A        [expr $pi/4*pow($DCol,2)];          # cross-sectional area [in2]
set I        1958.000;                            # section moment of inertia [in4]
set E        3355.000;                            # section modulus of elasticity [ksi]
set Weight   52.000;                              # structure weight [kips]
set Lp       21.500;                              # equivalent plastic hinge length [in]

```

```
puts "Geometric Properties --> OK"
```

```

#=====
#== CONCRETE PROPERTIES ==> (Concrete01)
#=====
#== Unconfined Concrete on column

```

```

=====
set fc1U    -3.100;      # unconfined concrete compressive strength [ksi]
set eps1U    -0.002;     # strain at maximum stress from unconfined concrete
set fc2U    -0.006;     # residual strength for the unconfined concrete [ksi]
set eps2U    -0.006;     # strain at ultimate stress unconfined

```

```
#== Confine Concrete on column
```

```

=====
set fc1C    -3.887;      # confined concrete compressive strength [ksi]
set eps1C    -0.0045;    # strain at maximum stress from confined concrete
set fc2C    -2.789;     # residual strength for the confined concrete [ksi]
set eps2C    -0.025;     # strain at ultimate stress confined

```

```

set IDconcCore 1;
set IDconcCover 2;

```

```

uniaxialMaterial Concrete01 $IDconcCore $fc1C $eps1C $fc2C $eps2C; # $lambda $ftC
$Ets; # Core concrete (confined)
uniaxialMaterial Concrete01 $IDconcCover $fc1U $eps1U $fc2U $eps2U; # $lambda $ftU
$Ets; # Cover concrete (unconfined)

```

```
puts "Concrete Properties --> OK"
```

```

#=====
#== REINFORCING STEEL PROPERTIES
#=====

```

```

set Fy    81.000; # STEEL yield stress [ksi]
set Fu    102.000; # STEEL max stress [ksi]

```

```
set IDSteel 3;
```

```

#=====
#== (Reinforcing Steel Material, Mohle and Kunnath)
#== (Coffin-Manson Fatigue and Strength Reduction)
#=====

```

```

set Es 29000.000; # STEEL modulus [ksi]
set Esh 726.000; # Tangent at initial strain hardening [ksi]
set eish 0.008; # Strain corresponding to initial strain hardening
set eult 0.100; # Strain at peak stress

```

```
set alpha 0.480; # usually constant for a material type
```



```

set Cf      0.150;    # adjust the number of cycles to failure
set Cd      0.380;    # Strength reduction constant

set R1      0.383;
set R2      10.000;
set R3      4.000;

uniaxialMaterial ReinforcingSteel $IDSteel $Fy $Fu $Es $Esh $eish $eult -CMFatigue
$Cf $alpha $Cd -MPCurveParams $R1 $R2 $R3;

puts "Reinforcing Steel Properties --> OK"

#=====
#== SECTION MODEL PROPERTIES
#=====
set nfCoreR  10;    # number of radial divisions in the core (number of "rings")
set nfCoreT  20;    # number of theta divisions in the core (number of "wedges")
set nfCoverR  2;    # number of radial divisions in the cover
set nfCoverT 20;    # number of theta divisions in the cover

set ColSecTag 1;

#=====
#== SECTION GENERATION
#=====
BuildRCSectionCIR $ColSecTag $Dbar $rsec $rcore $rbars $IDconcCore $IDconcCover
$IDSteel $numBars $barArea $nfCoreR $nfCoreT $nfCoverR $nfCoverT;

puts "Section Generation --> OK"

#=====
#== CALCULATED PARAMETERS
#=====
set PCol $Weight;      # nodal dead-load weight per column
set g 386.4;           # gravity [in/sec2]
set Mass [expr $PCol/$g]; # nodal mass

#=====
#== NODAL COORDINATES & BOUNDARY CONDITIONS
#=====
node 1 0 0;            # node# X, Y
node 2 0 $LCol;

fix 1 1 1 1;           # node DX, DY, DZ

#=====
#== NODAL MASSES
#=====
mass 2 $Mass $Mass 0.; # node#, Mx My Mz, neglect rotational inertia at
nodes

puts "Mass & Nodal Coordinates --> OK"

#=====
#== ELEMENTS GENERATION

```

```

=====
set ColTransfTag 1;          # associate a tag to column transformation
geomTransf PDelta $ColTransfTag;
set numIntgrPts 5;          # number of Gauss integration points for nonlinear
curvature distribution

element beamWithHinges 1 1 2 $ColSecTag $Lp $ColSecTag $Lp $E $A $I
$ColTransfTag;

puts "Element Generation --> OK"

=====
#== RECORDERS
=====
recorder Node -file $dataDir/DFree.out -time -node 2 -dof 1 2 3 disp;
      # displacements of free nodes

recorder Node -file $dataDir/RBase.out -time -node 1 -dof 1 2 3 reaction;
      # support reaction

recorder Element -file $dataDir/ForceEle1sec1.out -time -ele 1 section 1 force;
      # section force, axial and moment at base

recorder Element -file $dataDir/DefoEle1sec1.out -time -ele 1 section 1 deformation;
      # section deformations, axial and curvature at base

recorder Element -file $dataDir/SteelSSEle1sec1a.out -time -ele 1 section 1 fiber
$rbars 0 $IDSteel stressStrain; # steel fiber stress-strain at base

recorder Element -file $dataDir/CoreSSEle1sec1a.out -time -ele 1 section 1 fiber
$rcore 0 $IDconcCore stressStrain; # steel fiber stress-strain at base

recorder Element -file $dataDir/CoverSSEle1sec1a.out -time -ele 1 section 1 fiber
$rsec 0 $IDconcCover stressStrain; # steel fiber stress-strain at base

recorder Element -file $dataDir/SteelSSEle1sec1b.out -time -ele 1 section 1 fiber -
$rbars 0 $IDSteel stressStrain; # steel fiber stress-strain at base

recorder Element -file $dataDir/CoreSSEle1sec1b.out -time -ele 1 section 1 fiber -
$rcore 0 $IDconcCore stressStrain; # steel fiber stress-strain at base

recorder Element -file $dataDir/CoverSSEle1sec1b.out -time -ele 1 section 1 fiber -
$rsec 0 $IDconcCover stressStrain; # steel fiber stress-strain at base

puts "Recorders --> OK"

=====
#== SET UP PARAMETERS
=====
set IDctrlNode 2; # node where displacement is read for displacement control
set IDctrlDOF 1; # degree of freedom of displacement read for displacement control
set iPushNode 2; # define node where lateral load is applied in static lateral
analysis
set iDmax "0.0035 0.0071 0.0106 0.0141 0.0141 0.0141
0.0283 0.0283 0.0283 0.0424 0.0424 0.0424 0.0566

```

```

0.0566      0.0566      0.0707      0.0707      0.0707      0.0849      0.0849
0.0849      0.0990      0.0990      0.0990"; # vector of displacement-cycle
peaks, in terms of storey drift ratio
set Dincr 0.01;      # displacement increment for pushover
set Dmax 10;         # maximum displacement increment for monotonic pushover

set Fact $LCol
set CycleType Full
set Ncycles 1

puts "Parameters for Pushover Analysis --> OK"

#=====
#== APPLY GRAVITY LOAD
#=====
pattern Plain 101 Linear {
    load      2      0 -$PCol 0
}

set Tol 1.0e-8;      # convergence tolerance for test
variable constraintsTypeGravity Plain;      # default
if { [info exists RigidDiaphragm] == 1 } {
    if {$RigidDiaphragm=="ON"} {
        variable constraintsTypeGravity Lagrange;      # large model: try
                                                    Transformation
    };      # if rigid diaphragm is on
            # if rigid diaphragm exists
};
constraints $constraintsTypeGravity ;      # how it handles boundary conditions
numberer RCM;      # renumber dofs to minimize band-width (optimization)
system BandGeneral ;      # how to store and solve the system of equations in the
analysis
test NormDispIncr $Tol 6 ;# determine if convergence has been achieved at the end of
an iteration step
algorithm Newton;      # use Newtons solution algorithm: updates tangent
stiffness at every iteration
set NstepGravity 10;      # apply gravity in 10 steps
set DGravity [expr 1./$NstepGravity];      # first load increment
integrator LoadControl $DGravity;      # determine the next time step for an
analysis
analysis Static;      # define type of analysis static or transient
analyze $NstepGravity;      # apply gravity

loadConst -time 0.0

puts "Apply Gravity Load --> OK"
puts "Model Built!"

```

A.8 Build Reinforced Concrete Circular Section code

```

proc BuildRCSectionCIR {id Dbar rsec rcore rbars coreID coverID steelID numBarsSec
barAreaSec nfCoreR nfCoreT nfCoverR nfCoverT} {
    #####
    # BuildRCrectSectionCIR $id $Dbar $rsec $rcore $rbars $coreID $coverID
    $steelID $numBarsSec $barAreaSec $nfCoreR $nfCoreT $nfCoverR $nfCoverT
}

```

```
#####
# Generate a circular reinforced concrete section with one layer of steel
# evenly distributed around the perimeter and a confined core.
# confined core.
#   by: Michael H. Scott, 2003

#   id - tag for the section that is generated by this procedure
#   Dbar - bar diameter
#   rsec - section radius
#   rcore - core radius
#   rbars - bars distribution ratio
#   coreID - material tag for the core patch
#   coverID - material tag for the cover patches
#   steelID - material tag for the reinforcing steel
#   numBarsSec - number of uniformly-distributed longitudinal-reinforcement
bars
#   barAreaSec - area of longitudinal-reinforcement bars
#   nfCoreR - number of radial divisions in the core (number of "rings")
#   nfCoreT - number of theta divisions in the core (number of "wedges")
#   nfCoverR - number of radial divisions in the cover
#   nfCoverT - number of theta divisions in the cover

set ri 0.0;   # inner radius of the section, only for hollow sections

# Define the fiber section
section fiberSec $id {
patch circ $coreID $nfCoreT $nfCoreR 0 0 $ri $rcore 0 360;
    # Define the core patch

patch circ $coverID $nfCoverT $nfCoverR 0 0 $rcore $rsec 0 360;
    # Define the cover patch

set theta [expr 360.0/$numBarsSec];
    # Determine angle increment between bars

layer circ $steelID $numBarsSec $barAreaSec 0 0 $rbars $theta 360;
    # Define the reinforcing layer

};   # end of fibersection definition
};   # end of procedure
```

A.9 Static Reversed-Cyclic Analysis (used in Chapter II)

```
# -----
# Static Reversed-Cyclic Analysis
#
# execute this file after you have built the model, and after you apply gravity
#

set LunitTXT "in";           # define basic-unit text for output

# create load pattern for lateral pushover load

pattern Plain 200 Linear {};   # define load pattern -- generalized
```

```

        foreach PushNode $iPushNode {
            load $PushNode $PCol 0.0 0.0 0.0 0.0 0.0
        }
    }
# ----- set up analysis parameters
source LibAnalysisStaticParameters.tcl;# constraintsHandler,DofNumberer,system-
ofequations,convergenceTest,solutionAlgorithm,integrator

# ----- perform Static Cyclic Displacements Analysis
source LibGeneratePeaks.tcl
set fmt1 "%s Cyclic analysis: CtrlNode %.3i, dof %.1i, Disp=%.4f %s"; # format for
screen/file output of DONE/PROBLEM analysis
foreach Dmax $iDmax {
    set iDstep [GeneratePeaks $Dmax $Dincr $CycleType $Fact]; # this proc is
defined above
    for {set i 1} {$i <= $Ncycles} {incr i 1} {
        set zeroD 0
        set D0 0.0
        foreach Dstep $iDstep {
            set D1 $Dstep
            set Dincr [expr $D1 - $D0]
            integrator DisplacementControl $IDctrlNode $IDctrlDOF $Dincr
            analysis Static
            # -----first analyze
command-----
            set ok [analyze 1]
            # -----if convergence
failure-----
            if {$ok != 0} {
                # if analysis fails, we try some other stuff
                # performance is slower inside this loop      global
maxNumIterStatic; # max no. of iterations performed before "failure to
converge" is ret'd
                if {$ok != 0} {
                    puts "Trying Newton with Initial Tangent .."
                    test NormDispIncr $Tol 2000 0
                    algorithm Newton -initial
                    set ok [analyze 1]
                    test $testTypeStatic $TolStatic
                    $maxNumIterStatic 0
                    algorithm $algorithmTypeStatic
                }
                if {$ok != 0} {
                    puts "Trying Broyden .."
                    algorithm Broyden 8
                    set ok [analyze 1]
                    algorithm $algorithmTypeStatic
                }
                if {$ok != 0} {
                    puts "Trying NewtonWithLineSearch .."
                    algorithm NewtonLineSearch 0.8
                    set ok [analyze 1]
                    algorithm $algorithmTypeStatic
                }
                if {$ok != 0} {

```

```

                                set putout [format $fmt1 "PROBLEM" $IDctrlNode
$IDctrlDOF [nodeDisp $IDctrlNode $IDctrlDOF] $LunitTXT]
                                puts $putout
                                return -1
                                }; # end if
                                }; # end if
                                # -----
-----
                                set D0 $D1;                                # move to next step
                                }; # end Dstep
                                }; # end i
                                }; # end of iDmaxCycl
                                # -----
-----
if {$ok != 0 } {
    puts [format $fmt1 "PROBLEM" $IDctrlNode $IDctrlDOF [nodeDisp $IDctrlNode
$IDctrlDOF] $LunitTXT]
} else {
    puts [format $fmt1 "DONE" $IDctrlNode $IDctrlDOF [nodeDisp $IDctrlNode
$IDctrlDOF] $LunitTXT]
}

puts "Static Reversed-Cyclic Analysis --> DONE!"

```

A.10 Static Cyclic Analysis Parameters (needed for the Static Reversed-Cyclic Analysis code)

```

# -----
# static analysis parameters
# I am setting all these variables as global variables (using variable rather than
# set command)
# so that these variables can be uploaded by a procedure
#
# Silvia Mazzoni & Frank McKenna, 2006
#

# CONSTRAINTS handler -- Determines how the constraint equations are enforced in the
# analysis (http://opensees.berkeley.edu/OpenSees/manuals/usermanual/617.htm)
# Plain Constraints -- Removes constrained degrees of freedom from the
# system of equations (only for homogeneous equations)
# Lagrange Multipliers -- Uses the method of Lagrange multipliers to enforce
# constraints
# Penalty Method -- Uses penalty numbers to enforce constraints --good for
# static analysis with non-homogeneous eqns (rigidDiaphragm)
# Transformation Method -- Performs a condensation of constrained degrees of
# freedom
variable constraintsTypeStatic Plain;                                # default;
if { [info exists RigidDiaphragm] == 1 } {
    if {$RigidDiaphragm=="ON"} {
        variable constraintsTypeStatic Lagrange;                                # for large model, try
Transformation
    }; # if rigid diaphragm is on
}; # if rigid diaphragm exists
constraints $constraintsTypeStatic

```

```

# DOF NUMBERER (number the degrees of freedom in the domain):
(http://opensees.berkeley.edu/OpenSees/manuals/usermanual/366.htm)
#   determines the mapping between equation numbers and degrees-of-freedom
#       Plain -- Uses the numbering provided by the user
#       RCM -- Renumbers the DOF to minimize the matrix band-width using the
Reverse Cuthill-McKee algorithm
set numbererTypeStatic RCM
numberer $numbererTypeStatic

# SYSTEM (http://opensees.berkeley.edu/OpenSees/manuals/usermanual/371.htm)
#   Linear Equation Solvers (how to store and solve the system of equations in the
analysis)
#   -- provide the solution of the linear system of equations  $Ku = P$ . Each solver is
tailored to a specific matrix topology.
#       ProfileSPD -- Direct profile solver for symmetric positive definite
matrices
#       BandGeneral -- Direct solver for banded unsymmetric matrices
#       BandSPD -- Direct solver for banded symmetric positive definite matrices
#       SparseGeneral -- Direct solver for unsymmetric sparse matrices
#       SparseSPD -- Direct solver for symmetric sparse matrices
#       UmfPack -- Direct UmfPack solver for unsymmetric matrices
set systemTypeStatic BandGeneral;          # try UmfPack for large model
system $systemTypeStatic

# TEST: # convergence test to
# Convergence TEST (http://opensees.berkeley.edu/OpenSees/manuals/usermanual/360.htm)
#   -- Accept the current state of the domain as being on the converged solution path
#   -- determine if convergence has been achieved at the end of an iteration step
#       NormUnbalance -- Specifies a tolerance on the norm of the unbalanced load
at the current iteration
#       NormDispIncr -- Specifies a tolerance on the norm of the displacement
increments at the current iteration
#       EnergyIncr -- Specifies a tolerance on the inner product of the unbalanced
load and displacement increments at the current iteration
#       RelativeNormUnbalance --
#       RelativeNormDispIncr --
#       RelativeEnergyIncr --
variable TolStatic 1.e-8;                  # Convergence Test: tolerance
variable maxNumIterStatic 6;              # Convergence Test: maximum number of
iterations that will be performed before "failure to converge" is returned
variable printFlagStatic 0;               # Convergence Test: flag used to print
information on convergence (optional)     # 1: print information on each step;
variable testTypeStatic EnergyIncr ;      # Convergence-test type
test $testTypeStatic $TolStatic $maxNumIterStatic $printFlagStatic;
# for improved-convergence procedure:
    variable maxNumIterConvergeStatic 2000;
    variable printFlagConvergeStatic 0;

# Solution ALGORITHM: -- Iterate from the last time step to the current
(http://opensees.berkeley.edu/OpenSees/manuals/usermanual/682.htm)
# Linear -- Uses the solution at the first iteration and continues
# Newton -- Uses the tangent at the current iteration to iterate to convergence
# ModifiedNewton -- Uses the tangent at the first iteration to iterate to convergence

```

```

# NewtonLineSearch --
# KrylovNewton --
# BFGS --
# Broyden --
variable algorithmTypeStatic Newton
algorithm $algorithmTypeStatic;

# Static INTEGRATOR: -- determine the next time step for an analysis
(http://opensees.berkeley.edu/OpenSees/manuals/usermanual/689.htm)
#          LoadControl -- Specifies the incremental load factor to be applied to the
loads in the domain
#          DisplacementControl -- Specifies the incremental displacement at a
specified DOF in the domain
#          Minimum Unbalanced Displacement Norm -- Specifies the incremental load
factor such that the residual displacement norm is minimized
#          Arc Length -- Specifies the incremental arc-length of the load-
displacement path
# Transient INTEGRATOR: -- determine the next time step for an analysis including
inertial effects
#          Newmark -- The two parameter time-stepping method developed by Newmark
#          HHT -- The three parameter Hilbert-Hughes-Taylor time-stepping method
#          Central Difference -- Approximates velocity and acceleration by centered
finite differences of displacement
integrator DisplacementControl $IDctrlNode $IDctrlDOF $Dincr

# ANALYSIS -- defines what type of analysis is to be performed
(http://opensees.berkeley.edu/OpenSees/manuals/usermanual/324.htm)
#          Static Analysis -- solves the KU=R problem, without the mass or damping
matrices.
#          Transient Analysis -- solves the time-dependent analysis. The time step in
this type of analysis is constant. The time step in the output is also constant.
#          variableTransient Analysis -- performs the same analysis type as the
Transient Analysis object. The time step, however, is variable. This method is used
when
#          there are convergence problems with the Transient Analysis object
at a peak or when the time step is too small. The time step in the output is also
variable.
set analysisTypeStatic Static
analysis $analysisTypeStatic

```

A.11 Dynamic Analysis (used in Chapters II, IV and V)

```

# -----
# Dynamic Earthquake Analysis
# Silvia Mazzoni & Frank McKenna, 2006
# execute this file after you have built the model, and after you apply gravity

# Uniform Earthquake ground motion (uniform acceleration input at all support nodes)

set GMdirection 1;          # ground-motion direction
set GMfile "DYNAMIC LOAD NAME" ;  # ground-motion filename
set GMfact 1.00;           # ground-motion scaling factor
set dt 0.005;              # time step for input ground motion

```



```

set DtAnalysis      0.005;                # time-step Dt for lateral analysis
set TmaxAnalysis 55.05;                  # maximum duration of ground-motion analysis
-- should be 50*$sec

source LibAnalysisDynamicParameters.tcl;    #
constraintsHandler,DOFnumberer,system-
ofequations,convergenceTest,solutionAlgorithm,integrator

# ----- define & apply damping
# RAYLEIGH damping parameters, Where to put M/K-prop damping, switches
(http://opensees.berkeley.edu/OpenSees/manuals/usermanual/1099.htm)
#      D= $\alpha M + \beta K_{curr} K_{current} + \beta K_{comm} K_{lastCommit} +$ 
 $\beta K_{beatKinit} K_{Kinit}$ 

set xDamp 0.005;                        # damping ratio

set MpropSwitch 0.0;
set KcurrSwitch 0.0;
set KcommSwitch 1.0;
set KinitSwitch 0.0;

set nEigenI 1;                          # mode 1
set nEigenJ 1;                          # mode 1

set lambdaN [eigen [expr $nEigenJ]];    # eigenvalue analysis for
nEigenJ modes
set lambdaI [lindex $lambdaN [expr $nEigenI-1]]; # eigenvalue mode i
set lambdaJ [lindex $lambdaN [expr $nEigenJ-1]]; # eigenvalue mode j
set omegaI [expr pow($lambdaI,0.5)];
set omegaJ [expr pow($lambdaJ,0.5)];

set To [expr 2*3.1416/$omegaI]

set alphaM [expr $MpropSwitch*$xDamp*(2*$omegaI*$omegaJ)/($omegaI+$omegaJ)];
# M-prop. damping; D =  $\alpha M$ 
set betaKcurr [expr $KcurrSwitch*2.*$xDamp/($omegaI)]; #
current-K;      +beatKcurr*KCurrent
set betaKcomm [expr $KcommSwitch*2.*$xDamp/($omegaI)]; # last-
committed K;    +betaKcomm*KlastCommitt
set betaKinit [expr $KinitSwitch*2.*$xDamp/($omegaI+$omegaJ)]; #
initial-K;      +beatKinit*Kini

rayleigh $alphaM $betaKcurr $betaKinit $betaKcomm; # RAYLEIGH
damping

set IDloadTag 401;                        # load tag
set GMfatt [expr $g*$GMfact];            # data in
input file is in g Units -- ACCELERATION TH
set AccelSeries "Series -dt $dt -filePath $GMfile -factor $GMfatt"; # time
series information
pattern UniformExcitation $IDloadTag $GMdirection -accel $AccelSeries; #
create Uniform excitation

```

```

set Nsteps [expr int($TmaxAnalysis/$DtAnalysis)];
set ok [analyze $Nsteps $DtAnalysis];                                     # actually
perform analysis; returns ok=0 if analysis was successful

if {$ok != 0} {                                                           # analysis
    was not successful.
    # -----
    -----
    # change some analysis parameters to achieve convergence
    # performance is slower inside this loop
    # Time-controlled analysis
    set ok 0;
    set controlTime [getTime];
    while {$controlTime < $TmaxAnalysis && $ok == 0} {
        set controlTime [getTime]
        set ok [analyze 1 $DtAnalysis]
        if {$ok != 0} {
            puts "Trying Newton with Initial Tangent .."
            test NormDispIncr $Tol 1000 0
            algorithm Newton -initial
            set ok [analyze 1 $DtAnalysis]
            test $testTypeDynamic $TolDynamic $maxNumIterDynamic 0
            algorithm $algorithmTypeDynamic
        }
        if {$ok != 0} {
            puts "Trying Broyden .."
            algorithm Broyden 8
            set ok [analyze 1 $DtAnalysis]
            algorithm $algorithmTypeDynamic
        }
        if {$ok != 0} {
            puts "Trying NewtonWithLineSearch .."
            algorithm NewtonLineSearch .8
            set ok [analyze 1 $DtAnalysis]
            algorithm $algorithmTypeDynamic
        }
    }
}; # end if ok != 0

puts "Ground Motion Done. End Time: [getTime]"
puts "Vibration Period. [$To]"
puts "Dynamic Analysis ---> DONE!"

```

A.12 Dynamic Analysis Parameters (needed for the Dynamic Analysis code)

```

# -----
# dynamic-analysis parameters
# I am setting all these variables as global variables (using variable rather than
# set command)
# so that these variables can be uploaded by a procedure
#
# Silvia Mazzoni & Frank McKenna, 2006

# Set up Analysis Parameters -----

```

```

# CONSTRAINTS handler -- Determines how the constraint equations are enforced in the
analysis (http://opensees.berkeley.edu/OpenSees/manuals/usermanual/617.htm)
#      Plain Constraints -- Removes constrained degrees of freedom from the
system of equations
#      Lagrange Multipliers -- Uses the method of Lagrange multipliers to enforce
constraints
#      Penalty Method -- Uses penalty numbers to enforce constraints
#      Transformation Method -- Performs a condensation of constrained degrees of
freedom
variable constraintsTypeDynamic Transformation;
constraints $constraintsTypeDynamic ;

# DOF NUMBERER (number the degrees of freedom in the domain):
(http://opensees.berkeley.edu/OpenSees/manuals/usermanual/366.htm)
#      determines the mapping between equation numbers and degrees-of-freedom
#      Plain -- Uses the numbering provided by the user
#      RCM -- Renumbers the DOF to minimize the matrix band-width using the
Reverse Cuthill-McKee algorithm
variable numbererTypeDynamic RCM
numberer $numbererTypeDynamic

# SYSTEM (http://opensees.berkeley.edu/OpenSees/manuals/usermanual/371.htm)
#      Linear Equation Solvers (how to store and solve the system of equations in the
analysis)
#      -- provide the solution of the linear system of equations  $Ku = P$ . Each solver is
tailored to a specific matrix topology.
#      ProfileSPD -- Direct profile solver for symmetric positive definite
matrices
#      BandGeneral -- Direct solver for banded unsymmetric matrices
#      BandSPD -- Direct solver for banded symmetric positive definite matrices
#      SparseGeneral -- Direct solver for unsymmetric sparse matrices (-piv
option)
#      SparseSPD -- Direct solver for symmetric sparse matrices
#      UmfPack -- Direct UmfPack solver for unsymmetric matrices
variable systemTypeDynamic BandGeneral; # try UmfPack for large problems
system $systemTypeDynamic

# TEST: # convergence test to
# Convergence TEST (http://opensees.berkeley.edu/OpenSees/manuals/usermanual/360.htm)
#      -- Accept the current state of the domain as being on the converged solution path
#      -- determine if convergence has been achieved at the end of an iteration step
#      NormUnbalance -- Specifies a tolerance on the norm of the unbalanced load
at the current iteration
#      NormDispIncr -- Specifies a tolerance on the norm of the displacement
increments at the current iteration
#      EnergyIncr-- Specifies a tolerance on the inner product of the unbalanced
load and displacement increments at the current iteration
#      RelativeNormUnbalance --
#      RelativeNormDispIncr --
#      RelativeEnergyIncr --
variable TolDynamic 1.e-8; # Convergence Test: tolerance
variable maxNumIterDynamic 10; # Convergence Test: maximum number of
iterations that will be performed before "failure to converge" is returned
variable printFlagDynamic 0; # Convergence Test: flag used to print
information on convergence (optional) # 1: print information on each step;

```

```

variable testTypeDynamic EnergyIncr;    # Convergence-test type
test $testTypeDynamic $TolDynamic $maxNumIterDynamic $printFlagDynamic;
# for improved-convergence procedure:
    variable maxNumIterConvergeDynamic 2000;
    variable printFlagConvergeDynamic 0;

# Solution ALGORITHM: -- Iterate from the last time step to the current
(http://opensees.berkeley.edu/OpenSees/manuals/usermanual/682.htm)
#     Linear -- Uses the solution at the first iteration and continues
#     Newton -- Uses the tangent at the current iteration to iterate to
convergence
#     ModifiedNewton -- Uses the tangent at the first iteration to iterate to
convergence
#     NewtonLineSearch --
#     KrylovNewton --
#     BFGS --
#     Broyden --
variable algorithmTypeDynamic ModifiedNewton
algorithm $algorithmTypeDynamic;

# Static INTEGRATOR: -- determine the next time step for an analysis
(http://opensees.berkeley.edu/OpenSees/manuals/usermanual/689.htm)
#     LoadControl -- Specifies the incremental load factor to be applied to the
loads in the domain
#     DisplacementControl -- Specifies the incremental displacement at a
specified DOF in the domain
#     Minimum Unbalanced Displacement Norm -- Specifies the incremental load
factor such that the residual displacement norm is minimized
#     Arc Length -- Specifies the incremental arc-length of the load-
displacement path
# Transient INTEGRATOR: -- determine the next time step for an analysis including
inertial effects
#     Newmark -- The two parameter time-stepping method developed by Newmark
#     HHT -- The three parameter Hilbert-Hughes-Taylor time-stepping method
#     Central Difference -- Approximates velocity and acceleration by centered
finite differences of displacement
variable NewmarkGamma 0.5;# Newmark-integrator gamma parameter (also HHT)
variable NewmarkBeta 0.25;# Newmark-integrator beta parameter
variable integratorTypeDynamic Newmark;
integrator $integratorTypeDynamic $NewmarkGamma $NewmarkBeta

# ANALYSIS -- defines what type of analysis is to be performed
(http://opensees.berkeley.edu/OpenSees/manuals/usermanual/324.htm)
#     Static Analysis -- solves the KU=R problem, without the mass or damping
matrices.
#     Transient Analysis -- solves the time-dependent analysis. The time step in
this type of analysis is constant. The time step in the output is also constant.
#     variableTransient Analysis -- performs the same analysis type as the
Transient Analysis object. The time step, however, is variable. This method is used
when
#         there are convergence problems with the Transient Analysis object
at a peak or when the time step is too small. The time step in the output is also
variable.
variable analysisTypeDynamic Transient
analysis $analysisTypeDynamic

```